Cyclohexane/Water Dispersion Behaviour Including Benzoic Acid Mass Transfer by Influence of Different Types of Stirrers – Experiments and CFD Simulation

(Cyclohexan/Wasser Dispergierverhalten einschließlich Benzoesäure-Stoffaustausch unter dem Einfluss verschiedener Rührertypen – Experimente und CFD-Simulation)

by

Laila Mahmod Nabhan Abu-Farah (Jordan-Zarqa)

Thesis submitted to the Institute of Chemical Engineering,
Faculty of Chemistry at Universität Duisburg-Essen, in partial
fulfilment of the requirements of the degree of
Dr. rer. nat.

Approved by the examination committee on July 14, 2010:

Chair : Prof. Dr. G. Jansen

Advisor : Prof. Dr. A. Schönbucher

Reviewer : Prof. Dr. F. Bandermann

Essen, 2010

Declaration

I declare here that I have written this thesis on my own. The literature and technical aids used have been completely indicated.

Essen, 28.05.2010 Signature:

Acknowledgements

First, I wish to express my deep gratitude and appreciation to my advisor Prof. Dr. Axel Schönbucher for his guidance and support in the course of this work. He has given me helpful advice on approaching and performing challenging tasks.

I am very grateful to Prof. Dr. F. Bandermann for his accepting the task of co-examiner of this thesis and for investing time in reading and discussion this thesis, I appreciate him for providing me with valuable ideas and useful information.

I am obliged to Prof. Dr. G. Jansen for taking over the position of chairman of the examination board.

I would like to thank Dr. Wolfgang Laarz for his support and advice as well as his help to build up the experimental setup. I would like to thank Peter Sudhoff for his help with the computer cluster and the staff of the Institute. Also my thanks go to Mrs. Lieselotte Schröder for her help in the administrative matters and her support in many other things.

Especial hearty and gratitude thanks go to my husband Dr.rer.nat.-Eng. Fawzi Al-Qaessi for his endless help, advice, encouragement and support through my project work and patience during the course of my life. Also, to our sons Sadid and Noor for providing me so much love. I was always glad to know that they are with me.

I want to thank my parents, brothers and sisters for giving me support in any way I needed it before and during the time of this work. Their love and strong belief in me has always strengthened my self-confidence.

Table of Contents

Abstract

The dispersion behaviour of cyclohexane (dispersed phase) into water (continuous phase) in a stirred unbaffled batch vessel is studied experimentally and with computational fluid dynamic (CFD) simulation. The important aspects and fundamentals in liquid-liquid systems including mass transfer are described.

The dispersion and distribution of cyclohexane into water is visualized by a red colour tracer and registered with a video camera. Different types of stirrers are used such as anchor impeller (tangential flow), 3-bladed propeller (axial flow), 4-bladed pitched blade turbine PBT (combined flow) and 6-bladed rushton turbine impeller RTI (radial flow). The minimum stirrer velocities for complete and uniform dispersion are determined by tracking the red layer of cyclohexane. The shape and size of the cyclohexane droplets are measured by using the particle vision microscope (PVM). The axial and radial profiles of cyclohexane volume fractions at different stirrer velocities are measured by using sampling withdrawal method. The minimum stirrer velocities are also determined from this method. Mass transfer of the solute (benzoic acid) from water to cyclohexane is used as an indirect method to calculate the volumetric mass transfer coefficient k_cA between the two phases –from the measured transient concentrations of benzoic acid in water– by using the chemical acid-base titration method. The flow velocity fields produced by RTI and propeller impeller are measured by using photographic-light cut method with the help of tracer particles and MathCAD software.

For the 3D steady and transient CFD simulations (using ANSYS CFX-11 and ICEM CFD-11), the geometry and the unstructured mesh generation for the anchor and RTI as well as all used submodels, the initial and boundary conditions and also the solution algorithm, are described. The submodels are: Eulerian-Eulerian multi-fluid model, the k-ε turbulent model, algebraic slip (ASM) and Ishii-Zuber models, buoyancy model, the standard free surface flow

model, particle model and the sliding mesh model.

It is found many vortices and symmetric flow around the impellers. With anchor impeller, large axial vortex is formed in the water phase and large symmetrical vortex of cyclohexane is concentrated around the shaft of the anchor impeller. Whereas a radial flow with two circulations above and below the RTI is formed.

The shape of the cyclohexane droplets is found to be spherical. Mean Sauter droplet diameter d_{32} is ordered referring to the type of the impeller as $d_{32,RTI}$ (409 μm) > $d_{32,anchor}$ (388 μm) > $d_{32,propeller}$ (376 μm) > $d_{32,PBT}$ (343 μm), referring to the percentage volume of cyclohexane with RTI as $d_{32,20\ vol\%}$ (399 μm) > $d_{32,10\ vol\%}$ (348 μm) and referring to the RTI bottom clearance as $d_{32,4.1\ cm}$ (409 μm) > $d_{32,3.2\ cm}$ (399 μm). For better understanding, a droplet size distribution is also analyzed by the number frequency diagram. The anchor impeller gives a bi-modal distribution, whereas the other stirrers give a uni-modal one.

The CFD predicted axial and radial profiles of cyclohexane volumetric fractions are in a good agreement with that measured from the sampling method. The ASM is able to predict the axial and radial profiles of cyclohexane volume fractions in case of the RTI, whereas Ishii-Zuber model is suitable in case of the anchor impeller. The grid size should not exceed 0.001 m for good predictions.

Increasing the bottom clearance of RTI reduces the minimum velocity for complete dispersion in the order of 5.5 cm (400 rpm) < 4.1 cm (500 rpm) < 3.2 cm (550 rpm). The minimum RTI velocity to get a uniform dispersion of cyclohexane is 750 rpm, it is independent on the RTI clearance.

The minimum velocity for complete dispersion referring to the stirrer type is ordered as anchor (350 rpm) < propeller (400 rpm) < PBT (450) < RTI (500 rpm). Non uniform distribution of cyclohexane in the axial and radial distances is found with anchor impeller. The dispersion of cyclohexane becomes uniform at PBT velocity of 550 rpm. For propeller impeller, the dispersion

becomes nearly uniform at a minimum velocity of 650 rpm, especially in the region of the axial circulation. The level of the total liquid phases remains nearly constant with all types of the stirrers except that for anchor impeller. The dispersion behaviour obtained by propeller and anchor impellers is similar. Another similarity exists between RTI and PBT impeller. The dispersion of cyclohexane/water and the minimum stirrer velocities from the visualisation with red tracer coincide with those obtained from the measured axial and radial profiles of cyclohexane volume fractions, and show a good agreement with the CFD predictions.

The interfacial area A between the two phases is calculated from the measured droplet diameters and the CFD predicted averaged volumetric fractions of cyclohexane. From the measured k_c A, the k_c is then determined. It is found that k_c increases approximately as the 4.23 power of the RTI velocity and 2.95 of the anchor velocity, whereas A increases as the 2.62 power of RTI velocity and 0.75 power of anchor velocity.

The k_c A is influenced by the stirrer type (flow pattern) in the order of $(k_cA)_{anchor} > (k_cA)_{propeller} > (k_cA)_{PBT} > (k_cA)_{RTI}$. The propeller impeller gives the maximum volumetric mass transfer coefficient of 0.00003 m^3/s at a minimum velocity of 500 rpm, whereas the PBT impeller gives the same value at 600 rpm. The RTI gives the maximum value of 0.00002 m^3/s at velocity of 550 rpm.

Increasing RTI bottom clearance enhances the mass transfer of benzoic acid for RTI velocities $\leq$ 450 rpm, but it has no significant effect on k_c A. High mass transfer occurs when cyclohexane is completely dispersed and enhanced when a uniform dispersion is achieved. The surface renewal of the dispersed phase by diffusion and turbulence is responsible for mass transfer of the solute. Increasing the initial volume (percentage) of cyclohexane in case of anchor impeller increases k_c A.

The equilibrium concentrations are similar for all types of stirrers. The anchor impeller gives the minimum equilibrium time of 30 s at a minimum velocity of 350 rpm, whereas the RTI and PBT both reach the equilibrium concentration at the same equilibrium time of 300 s at velocities of 500 and 400 rpm, respectively. The RTI and propeller impeller reach the equilibrium concentration at the same velocity of 500 rpm but at different equilibrium times of 300 s and 60 s, respectively.

The predicted radial flow velocities are higher than the axial one in case of the RTI, whereas the axial velocities are higher than the radial one in case of the anchor impeller. The turbulence is high near the impeller, minimum at the free surface and bottom of the vessel and intermediate between these locations. The CFD predicted turbulent flow velocity distributions are in agreement to that obtained by photographic light-cut method and with the cyclohexane volumetric fraction distribution from sampling and visualization methods.

Nomenclature

Latin letters

A	$[m^2]$	Interfacial area
A_p	$[m^2]$	Droplet area
$A_{\alpha\beta}$	[1/m]	Interfacial area density
a	$[m^2/ m^3]$	Interfacial area per unit volume of the mixed phases
B	[m]	Bottom clearance
b	[m]	Blade width of rushton turbine impeller
C	[m]	Wall clearance
C_A	$[mol/ m^3]$	Concentration of solute A at time t
C_{A0}	$[mol/ m^3]$	Concentration of solute A at time t = 0
C_{BA}	$[mol/ m^3]$	Concentration of benzoic acid
$C_{BA/W}$	$[mol/ m^3]$	Concentration of benzoic acid in water
$C_{BA/CH}$	$[mol/ m^3]$	Concentration of benzoic acid in cyclohexane
$C_{BA.eq./W}$	$[mol/ m^3]$	Equilibrium concentration of benzoic acid in water
C_D	[–]	Drag coefficient
$C_{eq.}$	$[mol/ m^3]$	Concentration of solute at equilibrium
C_t	$[mol/ m^3]$	Concentration of solute at time t
C_{t0}	$[mol/ m^3]$	Concentration of solute at time t = 0
D	[m]	Stirrer diameter
D_p	[N]	Drag force by a single droplet
$D_{\alpha\beta}$	[N]	Total drag force by a number of droplets
d	[m]	Mean droplet diameter
d_{32}	[m]	Sauter mean droplet diameter
d_d	[m]	disk diameter
d_i	[m]	Diameter of drops in size class i
d_v	[m]	Vessel diameter

F_α	[N/m^3]	Volumetric buoyancy force
g	[m/s^2]	Acceleration due to gravity
H	[m]	Vessel height
H_i	[m]	Impeller height
H_l	[m]	Total liquid height
K	[m]	Blade thickness of anchor impeller
k	[m/s]	Mass transfer coefficient
k	[m^2/s^2]	Turbulent kinetic energy
k_c	[m/s]	Mass transfer coefficient
k_cA	[m^3/s]	Volumetric mass transfer coefficient
M	[Nm]	Torque of the stirrer
M_{BA}	[kg]	Mass of benzoic acid
M_w	[kg/mol]	Molar mass of benzoic acid
m	[–]	Number of size classes
$\dot{m}_A$	[mol/s]	Mass transfer rate of species A
M_α	[N/m^3]	Momentum transfer with other phases
$M_{\alpha\beta}^{D}$	[N/m^3]	Momentum transfer due to drag force
$M_{\alpha\beta}^{L}$	[N/m^3]	Momentum transfer due to lift force
$M_{\alpha\beta}^{LUB}$	[N/m^3]	Momentum transfer due to wall lubrication force
$M_{\alpha\beta}^{VM}$	[N/m^3]	Momentum transfer due to mass force
$M_{\alpha\beta}^{TD}$	[N/m^3]	Momentum transfer due to turbulent disperse force
N_P	[–]	Total number of phases
n_i	[–]	Number of drops
n_p	[–]	Number of particles per unit volume
p	[Pa]	Pressure
P_k	[kg/(m s^3)]	Turbulence production due to viscous and buoyancy forces

P_{kb}	[kg/(m s^3)]	Buoyancy production term
$P_{\varepsilon b}$	[kg/(m s^3)]	Buoyancy dissipation term
$\mathrm{ROMT}_{BA/CH}$	[mol/(L min)]	Rate of mass transfer of benzoic acid to cyclohexane
r	[m]	Radial direction
r_α	[-]	Volume fraction of phase α
r_β	[-]	Volume fraction of phase β
r_d	[-]	Volume fraction of the dispersed phase
S	[m]	Shaft diameter
$S_{MS\alpha}$	[kg/(m^{3}s)]	Mass source in continuity equation
T	[K]	Temperature
t	[s]	Time
t_0	[s]	Initial time
$t_{eq.}$	[s]	Equilibrium time
U	[m/s]	Vector of velocity $\begin{pmatrix}u_x\\u_y\\u_z\end{pmatrix}$ in bulk liquid
U_α	[m/s]	Vector of velocity $\begin{pmatrix}u_x\\u_y\\u_z\end{pmatrix}$ in phase α
U_β	[m/s]	Vector of velocity $\begin{pmatrix}u_x\\u_y\\u_z\end{pmatrix}$ in phase β
U_{Wall}	[m/s]	Velocity at the wall
u_m	[m/s]	mixture velocity
$\begin{pmatrix}u_x\\u_y\\u_z\end{pmatrix}$	[m/s]	Velocity in the coordinate directions x, y, z
u^i_C	[m/s]	Velocity of component i in continuous phase C
$u^i_{D\alpha}$	[m/s]	Drift velocity of component i in phase α
u^i_m	[m/s]	Velocity of component i in the mixture m

$u^i_{S\alpha}$	[m/s]	Slip velocity of component i in phase α
u^i_α	[m/s]	Velocity of component i in phase α
V	[m^3]	Volume of the mixed phases in the vessel
V_c	[m^3]	Volume of the continuous phase
V_p	[m^3]	Volume of a droplet
V_s	[m^3]	Volume of the sample
V_{SH}	[m^3]	Volume of sodium hydroxide
W	[m]	Blade thickness of rushton turbine impeller
w	[m]	Blade width of anchor impeller
x, y, z	[m]	Cartesian coordinates

Greek letters

ε	[m^2/s^3]	Turbulent energy dissipation
ϕ	[–]	Volume fraction of the dispersed phase
$\Gamma_{\alpha\beta}$	[kg/(m^{3}s)]	Interphase mass transfer
μ_α	[Pa s]	Dynamic viscosity of phase α
μ_t	[Pa s]	Turbulence viscosity
ν	[m^2/s]	Kinematic viscosity
$\nu_{\alpha\tau}$	[m^2/s]	Turbulent kinematic viscosity of phase α
ρ	[kg/m^3]	Density
ρ_i	[kg/m^3]	Density of the component i
ρ_α	[kg/m^3]	Density of phase α
σ	[N/m]	Surface tension coefficient
σ_τ	[–]	Turbulent Schmidt number
τ	[N/m^2]	Shear stress
ω	[rpm]	Stirrer velocity

Indices

α	Phase α
β	Phase β
D	Drift
i	Components i = A, B, … N
j	x,y,z- coordinates
m	Mixture
ref	Reference state

Abbreviations

ASM	Algebraic slip model
BA	Benzoic acid
C1, C2, C3	Stirrer bottom clearance
CAM	Video camera
CCD	Charge-coupled device camera
CEL	Command expression language
CFD	Computational fluid dynamics
CH	Cyclohexane
CHVF	Cyclohexane volume fractions
CS	Cell size
DSD	Drop size distribution
FD	Finite difference method
FE	Finite element method
FV	Finite volume method
LDA	Laser doppler anemometry
LDV	Laser doppler velocimetry
LES	Large eddy simulation
MRF	Multiple reference frames
PIV	Particle image velocimetry

PBT	Pitched blade turbine impeller
PVM	Particle vision microscope
RANS	Reynolds average Navier Stokes
ROMT	Rate of mass transfer
rpm	Revolution per minute
RTI	Rushton turbine impeller
SST	Shear stress turbulent
W	Water

1. INTRODUCTION

Immiscible liquid-liquid dispersions are encountered in chemical, petroleum, pharmaceutical and biochemical processes such as liquid-liquid extraction, suspension polymerization and other chemical reactions with the objective to increase the contact area between the two phases [1][2]. Dispersions are defined as mixtures of two immiscible fluids with one dispersed as drops in a second fluid which forms a continuous phase [3]. The purpose of this operation is to mix two phases and increase the interfacial area and to enhance the mass transfer between the two phases [1]. When two immiscible liquids are combined in a mixing vessel, it is required to know the minimum mixing stirrer velocity for both complete and uniform dispersion of one liquid in the other [4]. This can be determined when the dispersed phase visually disappears from the vessel and becomes completely incorporated into the bulk of the liquid [5]. In this study when the local volume fraction of the dispersed phase remains constant with the same value at different positions in the vessel, then the complete and uniform dispersion is achieved. The knowledge of the dispersion and distribution of the dispersed phase is essential in determination the rates of mass transfer and for the design and scale up of the mixing equipment [6].

Mass transfer across the interface between two liquids in a mixing vessel is dependent upon the concentration difference, the interfacial area between the two liquids and the mass transfer coefficient [7]. These parameters are very important in the design of mixing processes because of their role in the control of the rates of heat and mass transfer and also the reaction rate. The interfacial area is affected by different variables such as volume fraction of the dispersed phase, fluid properties of the continuous and dispersed phases and the mechanical mixing conditions like the vessel size, stirrer size and velocity [8].

Insufficient understanding of these mixing processes causes the continuous loss of a large amount of money. Flows in industrial mixing vessels have many complications arising from the complex design of the impeller/vessel arrangement (small clearance impellers (e.g. helical ribbon and anchor impellers) and rounded bottom vessel) and from the complex rheological behaviour of the stirred fluid [5]. Many problems are found in the industrial applications of immiscible liquid–liquid systems caused by the failure to achieve the required interfacial area due to effects of coalescence, drop size distribution and process heat transfer. Liquid–liquid dispersion faces some complication when making scale up because it is accompanied by heat/mass transfer and chemical reaction.

Drop size distribution, the physical and interfacial properties between the two liquid phases are affected by stirrer type- and velocity, the flow field, shear forces, turbulence intensity and dispersion time [9]. Few studies have been done on the experimental investigation and numerical prediction of the immiscible liquid-liquid dispersion in stirred vessel, and they focused on the measurements of the drop size distribution [1][10][11]. Previous investigations focused on the multiphase mixing processes of gas-liquid and solid-liquid systems [12][13].

Stirred vessels are often used as an industrial process equipment to study the phase behaviour. Immiscible liquid–liquid systems are processed in batch and continuous modes. Different types of stirrers with different flow field patterns are used in this study such as anchor stirrer which gives tangential with secondary flow mainly axial for low viscosity liquids [14], propeller and PBT impellers give an axial flow field whereas the RTI gives the radial flow, and they are widely used for the mixing of solid-liquid, gas-liquid and liquid-liquid multiphase systems. Flow field velocity and pattern have an important effect on the dispersion behaviour and uniformity, the volumetric mass transfer coefficient, rate of mass transfer, mean drop size and the minimum agitation velocity to get a complete dispersion. These parameters desire an intensive study and investigation.

Experimental approaches are insufficient for the insight of liquid-liquid dispersion in stirred vessels and for designing and scaling-up purposes. The numerical method by using the developed computational fluid dynamics (CFD) is adopted to simulate the single and multiphase flow in stirred vessels [12]. CFD simulation of the hydrodynamics in stirred vessels is very difficult, because the flow field in the vessel is complex and highly unsteady due to the interaction of the rotating impeller with multiphase dispersion. Very few investigations are done by CFD simulations. Most of the literature is limited to single phase and solid or gas-liquid flows [6]. Three dimensional flow patterns inside the vessel are important to get a better understanding of the fluids flow and of the mechanisms responsible for homogenization and transport processes. The inertial forces due to the movement of the stirrer as well as the hydrodynamic conditions affect the flow field and velocity distribution in the vessel. It is necessary to get more insight about the detailed picture of the flow to determine the ways in which the mixing process can be improved. The mathematical treatment of multiphase system is complicated compared with the single phase. The progress in the work on the simulation of multiphase flow in stirred vessels is much less than that in the chemical reactors like bubble and extraction columns, spray towers and fluidization beds. This is due to the complex interaction of the rotating impeller with stationary walls of the stirred vessel. The difficulties in the simulating multiphase stirred vessels are the accurate representation of the impeller action and the appropriate model of interphase interaction and the flow turbulence [12][15].

The aim of this study is to understand the physical and interfacial phenomena which involve the dispersion behaviour of cyclohexane in water experimentally and with CFD simulation. Mixing of immiscible liquids will be carried out in a non-baffled batch vessel stirred with anchor, rushton turbine, pitched blade and propeller impellers. Steady and transient 3D CFD simulations will be done along with Eulerian-Eulerian multi fluid model for the anchor and RTI impellers. The numerical simulation will be accomplished with the help of ANSYS CFX-11 and ICEM CFD software. The experimental data will be predicted from CFD to verify the computational approach.

This study includes the following investigations:

1. The flow field pattern and dispersion behaviour of cyclohexane in water will be investigated by using the visualization method with a red colour and solid particles tracers. The velocity distribution of the particles will be measured in the axial and radial distances by using the light cut method and Mathcad 14 software.
2. The shape and size distribution of cyclohexane droplets will be measured at the steady state when the equilibrium conditions are achieved. Sauter mean droplet diameter will be calculated. The effect of stirrer type, RTI clearance and the initial percentage volume of cyclohexane on the mean droplet diameter will be investigated.
3. The volume fraction of the cyclohexane in the axial and radial positions in the vessel will be measured. The effect of stirrer type and velocity on the axial and radial profiles of cyclohexane will be studied. The minimum stirrer velocity required for a complete and uniform dispersion of cyclohexane in water will be determined.
4. The effect of different grid sizes and different interphase momentum transfer models on the calculated volumetric fractions of cyclohexane will be predicted in the case of stirred vessel with RTI.
5. The mass transfer rate, mass transfer coefficient, interfacial area and volumetric mass transfer coefficient (kc A) of the benzoic acid (solute) from water to cyclohexane will be studied. They will be used as a criterion for the efficiency of this mixing process. The effects of dispersion time, stirrer type and velocity on these parameters will be investigated.
6. The axial and radial velocity fields and profiles will be calculated by using CFD for anchor and RTI at different velocities. The circulations and eddies formed in the vessel will be analyzed.
7. The results of 1-6 will be compared for optimization and design purposes.

2. THEORY AND IMPORTANT ASPECTS

2.1 Scope of mixing

Mixing is an operation used to change a non-uniform system into a uniform one. It can be classified according to various combinations between the gas, liquid, and solid phases. The aim of the mixing is to reduce the inhomogeneity in different parameters like the concentration, phase and temperature, also to increase the mass transfer, reaction rate and to improve product properties. Laboratory experiments and computational fluid dynamics (CFD) are used to investigate mixing phenomena and evaluate mixing equipment which goes beyond mechanical and costing considerations [9]. Qualitative and quantitative observations, experimental data, and flow region identifications are needed and should be emphasized in any experimental studies in mixing.

Mixing in vessels is an important area when considering the physical or transport process during the mixing process. Mixing efficiency in a stirred vessel is affected by baffles, impeller velocity, impeller type, clearance, vessel geometry and position of the impeller [16]. Liquid-liquid mixing is concerned with the mixing of two miscible or immiscible liquids. It is one of the most difficult and least understood mixing problems. Liquid-liquid mixing depends on the shape of the tank bottom, the geometry of the impeller, the relative size of the vessel to the impeller and power draw on the impeller geometry. Mixing, mass and heat transfer between phases can be accomplished by stirring; its intensity plays a controlling role in the liquid-liquid systems. It controls the breakup of drops (dispersion), the combining of drops (coalescence) and the suspension of drops within the system. The magnitude and direction of convective flows produced by the stirrer affect the distribution and uniformity throughout the vessel as well as the kinetics of dispersion. The intense turbulence and high shear forces near the impeller lead to drop dispersion, not coalescence, so that drops have a good chance of breaking up. Whereas lower turbulence shear stresses that found elsewhere in the vessel promotes coalescence by enabling drops to remain in contact long enough for them to coalesce. Drops may also be divided by physical contact with the stirrer. Laminar shear also leads to drop dispersion. If a drop is stretched beyond the point of critical elongation, it breaks. Otherwise, it returns to its prestressed state. The mixing system and duration of mixing have an important effect on drop size distribution, drop breakup and coalescence [9].

2.2 Mixing procedure

Liquid mixing in a stirred vessel depends on the conditions in the vessel and the properties of the mixed liquids. The dispersed liquid may pass through several four zones: the stirrer region, the free surface, the bottom of the vessel and the bulk. In each zone there is a chance that the liquid drops will be divided into smaller drops or mixed into the bulk liquid. In each zone the liquid drops have a chance to move to another zone. The impeller's energy input is divided between large scale flow and turbulence, depending on the type of the stirrer. The distribution of the flow types over the regions in the vessel are determined by the stirrer. Thus, each region makes its own characteristic contribution to the process of mixing, depending on the type of impeller and the flow conditions in the vessel [17].

2.3 Miscible and immiscible liquids

The term miscible refers to the property of liquids that allows them to be mixed together and form a single homogeneous phase [18]. The purpose for mixing of miscible liquids is to adjust the pH in fermentation and viscosity in diluting or thickening and temperature in sterilization, promote reactions in polymerization and to avoid stratification in storage vessels [19]. The molecular diffusion contributes to the maximum homogeneity in the mixing of miscible liquids [20]. Two things are required for miscible liquids mixing: The mixed liquids must be completely soluble, and there must be no resistance to dissolution at the fluid interface [9]. As soon as the two miscible liquids come into contact, diffusion will produce a region of intermediate viscosity between the bulk liquids.

The term immiscible liquid-liquid system refers to two or more insoluble liquids present as separate phases such as oil/water system. These phases are referred to as the dispersed or drop phase and the continuous phase. The dispersed phase is usually smaller in volume than the continuous phase. In dispersion, a two-phase system in which one phase is broken into discrete particles which are completely surrounded by the second phase. Particles may be solid, liquid or gas. For mixing purposes, the second phase is generally a liquid [9][21].

2.4 Fundamentals and Phenomena in immiscible liquid-liquid systems

Immiscible liquid-liquid systems involve many simultaneous, interdependent phenomena such as dispersion, coalescence, suspension, heat and mass transfer and chemical reaction. Flow patterns and turbulence in stirred vessels are complex phenomena which can be investigated by using a computational fluid dynamics (CFD).Turbulence consists of high energy eddies near the impeller, and lower energy eddies are located farther away from the impeller.

When two immiscible liquids are brought into contact in stirred vessel, dispersion is formed as a result of two processes: The rate at which the bulk liquid of the dispersed phase breaks up to produce fine drops and the droplet coalescence rate. If stirring continues over a sufficient long time, a local dynamic equilibrium is obtained between the break up and coalescence. The equilibrium drop size distribution in a batch mixing process will depend on relative magnitude of theses two processes. The breakage and coalescence rate depend on the geometry of the vessel, the energy input per unit mass, dispersed phase fraction and the physical properties of the two phases. The breakage rate dominates the coalescence rate during the initial period of a batch mixing process until the equilibrium drop size distribution is obtained.

The drop size and the interfacial area between the phases depend on the flow dependent dispersion and coalescence phenomena. When a drop is contained in a large eddy, it rotates within this eddy and does not break up. For a smaller eddy, a drop can be deformed and dispersed [9].

2.4.1 Drop dispersion and breakup

Liquid–liquid dispersion is a complex mixing operation. Dispersions are regarded as a mixture of two immiscible fluids with one fluid dispersed as drops in a second fluid which forms a continuous phase [3]. It is impossible to make dispersion of uniform drop size because of the wide range of properties and flow conditions. Drop dispersion results from shear forces created by the rotating impeller. Dispersion includes drop deformation which is caused by the mechanical forces induced by the surrounding fluid and the impact collisions with vessel walls and impeller blades and the breakage which occurs when the fluid forces exceed the surface and internal viscous resistance forces. The shear forces of the fluid and pressure fluctuation controls the drop deformation in stirred vessel. There are different types of drop deformation depending on the affected forces [9]:

1. Collision forces leads to lenticular deformation.
2. Uniform shear leads to cigar-shaped deformation.
3. Turbulent conditions lead to bulgy deformation.

Laminar shear or flow velocity produces orderly dispersion, whereas turbulent flows produce random break up for the drops with time. Newton’s law of viscosity can be used to describe the forces acting on the drop in laminar flow. A breakage of the drop occurs when a critical deformation is reached during stretching of the drop. Breakage results when the disruptive forces in the surrounding fluid exceed the cohesive forces due to interfacial tension and drop viscosity [22]. The factors affecting on dispersion are viscosity, density, stirrer velocity, initial conditions for dispersion and material of construction of the mixing equipment [23]. For low viscosity dispersed phase, the viscous stress is negligible and only the surface stresses (surface force per unit area) contributes to the cohesive forces. The forces causing drop dispersion in stirred vessels are non uniform. The flow velocity and deformation rate are highest near the impeller and diminish rapidly with the distance away from the impeller. There are no data for dispersions in stirred vessels under laminar flow conditions. Turbulent flows contain eddies of different size and intensity, each eddy creates forces that lead to drop deformation. Elongation can be occurred by counter rotating eddies. The forces in turbulent stirred vessels arise from the velocity fluctuations which appear from the interacting turbulent eddies. Large eddies carry the drops whereas small eddies deform the drops. A high dispersed phase volume fraction affects small scale turbulent eddies by reducing their intensity and making them less able to disperse drops. For dispersion in turbulent flow coalescence in dilute systems can be neglected.

2.4.2 Drop coalescence

Coalescence is the process of combining two or more drops to form one or more larger drops. It occurs when drops are suspended in a moving fluid or collide with one another or with impeller blades or vessel walls and when drops rise or settle due to gravity [9]. Coalescence is undesirable in some processes like suspension polymerization because it leads to buildup of polymer on the vessel walls and the impeller. The mass transfer processes such as extraction depend on coalescence to achieve the desirable rate of operation. Coalescence depends on the collision rate which increases the dispersed phase concentration. The collision depends on the stirring rate and the drop size. As the drops approach each other, a film of continuous phase fluid keeps them apart. When this film reaches to a critical thin thickness that allows damaging of the film, then coalescence and internal drop mixing occurs. The forces needed to damage the film of the continuous phase between the contact drops can be hydrodynamic which are formed by shear forces in laminar or turbulent flow, or hydrostatic forces due to gravity depending on the density differences between the drops and the continuous phase. The drops collect and coalescence on blade surfaces to form a condensed film. As this film grows in thickness it flows under centrifugal forces to the impeller tips and disperses into tiny drops. Gentle stirring enhance coalescence because it provides longer contact time between drops leading to damaging the formed film of the continuous phase between the drops. Coalescence rate increases with increasing the volume fraction of the dispersed phase due to an increase in the collision frequency and due to rheological changes that enable longer contact time intervals to be obtained [10].

2.4.3 Drop size

Drop size average and distribution are two important properties of dispersions because of their strong influence on the morphology of the products which affect their stability and rheology. Also they control the rates of heat and mass transfer [3][24]. Drop sizes depend on many factors such as breakage or coalescence of the drops [25][26]. They are not uniform and the maximum drop size is controlled by the impeller intensity.

Drop size distribution of the liquid–liquid dispersions during mixing can be measured by using the direct photographic technique [7]. This method is the most accurate, but the measuring procedure requires many pictures and long time for analysis. There are many investigations employed this method for drop size measurement in liquid-liquid dispersions. Skelland et al. [7] determined the drop size distribution by using the optical probes. There are also indirect methods to measure the drop size distribution like light transmittance [27][28], light scattering [29], Coulter counter [30] and the chemical method by measuring the interfacial area [31]. Bouyatiotis et al. [32] measured the droplet size by using the photographic probe, and the holdup of different organics as a dispersed phase in water as a continuous phase in a continuously flow stirred vessel. The measurements were done when a uniform dispersion was obtained. They found that when the holdup increases, the mean droplet size also increases. Whereas Lovick et al. [33] found that the dispersed phase volume fraction has no significant effect on the drop size. They used an endoscope attached to a video camera and light scattering techniques to measure the drop size distribution DSD. Drop size can be defined by using Sauter mean diameter d_{32} which is the ratio of the third to second moments of the DSD:

$$d_{32} = \frac{\sum_{i=1}^{i=m} n_i d_i^3}{\sum_{i=1}^{i=m} n_i d_i^2}. \tag{2. 1}$$

Where m is the number of size classes describing the DSD, n_i is the number of drops and d_i is the diameter of drops in size class i. The mean diameter d_{32} is directly proportional to the volume fraction of the dispersed phase ϕ and inversely proportional to the interfacial area per unit volume of the mixed phases a. The interfacial area can be found from DSD:

$$d_{32} = \frac{6\phi}{a}. \tag{2. 2}$$

The drop size of immiscible liquid–liquid mixing in stirred vessels is assumed to be greater than 3.0 μm and it is observed that a coalescence and phase separation occurs when stirring stops. Thus the drop size affects the phase separation after the completion of the multiphase process [33]. There are many correlations available in different literature to calculate the drop diameter in liquid–liquid stirred vessels depending on the following properties:

1. Physical properties of the dispersed and continuous phases such as the interfacial tension between the two phases, density and viscosity.

2. Operating conditions such as the impeller velocity and volume fraction of the dispersed phase and geometric parameters such as the impeller and tank diameters.

3. Type of the impeller and measurement techniques of the drop diameter.

Correlations for the transient drop size in a batch stirred liquid–liquid systems in the presence of mass transfer have not been established [7][34]. The drop size distribution in stirred liquid–liquid dispersions in the absence of mass transfer is investigated by using the drop population balances [35].

2.4.4 Dispersion time

The dispersion time is defined as the time at which the final drop size or the interfacial area does not change. The dispersion time is shorter than process time. During dispersion process, the drop size decreases rapidly and approaches the minimum size at times are often short compared to the process time. The decay to the equilibrium size is quite slow. For coalescing system, a small vessel reaches the equilibrium drop size in a shorter time than the larger one. When the equilibrium drop size is obtained, there will be no further decrease of the drop size with the dispersion time [9].

2.4.5 Holdup of the dispersed phase

The holdup is a measure of the local or global volume fraction of the dispersed phase incorporated in the continuous phase. Measurement of the holdup distribution of the dispersed phase is used to follow the progress of the dispersion process as a function of stirrer velocity and for a range of stirrer geometries and types [36]. The knowledge of the holdup distribution in the vessel axial and radial is very important to know the type of flow and the minimum velocity required to get complete or uniform dispersion of the dispersed phase. The dispersed phase holdup reaches the volume fraction of the dispersed phase presents initially at $t = 0$ when increasing the stirrer velocity or the impeller power to a certain level [32][24].

The detailed experimental measurements of hydrodynamics of liquid-liquid dispersion in stirred vessel are difficult and the report of the holdup distribution in the whole vessel is rare. Costas Tsouris et al. [37] used ultrasonic probe to measure the dispersed phase transient local volume fraction in stirred vessels. These measurements can be done at different positions in the vessel. It was found that the local variations in the holdup exist due to the density differences of the two phases. The measurements were obtained also during the phase inversion where the continuous phase becomes dispersed and the dispersed becomes continuous. Armenante et al. [38] presented experimental data on the dispersed phase holdup by using the sample withdrawal technique. This method is also used by Skelland et al. [39] and Okafi et al. [40]. The conductivity probe or ultrasonic method is also used to measure the holdup of liquid-liquid dispersion system.

Gosman et al. [41] used a computational procedure for the prediction of dispersed solid-liquid and gas-liquid two phase turbulent flows in baffled stirred vessel. A two flow Eulerian and k-ε turbulent models are employed. They calculated the phase fraction, particle size, phase density ratios and phase velocities. They found that two vortices are formed above and below the radial impeller. The maximum solids fraction is predicted near the bottom of the vessel. A sharp increase in the phase velocity is found below the impeller due to the gas introduction there in the case of gas-liquid dispersion. Comparison of the experimental data with the predictions results in a moderate quantitative agreement.

2.4.6 Complete and uniform dispersion velocity

The knowledge of the impeller velocity at which a complete dispersion and uniform dispersion of one liquid in the other is of great interest to enable efficient design of the mixer [42][43]. The minimum stirring velocity for complete liquid-liquid dispersion is defined as the velocity at which the thickness of the pure dispersed phase layer visually reaches around zero and becomes completely incorporated into the bulk of the fluid [5]. This velocity provides a realistic estimate of practical operating conditions. Increasing the impeller velocity above the minimum increases the cost of the power requirement, also more very small droplets which are formed resulting in separation and other problems [36]. The minimum velocity can be determined by visual observations. The homogeneous dispersion may occur at a velocity higher than the minimum mixing velocity [44].

Skelland et al. [4] found a correlation for the minimum impeller velocity that is needed for complete immiscible liquid-liquid dispersion in baffled vessel.

They calculated the degree of mixing for number of samples from different positions in the vessel by dividing the volume of the dispersed phase by the total volume of the sample. The averaging of the percentage mixing values gives the mixing index. A complete dispersion is obtained when the rotational velocity of the impeller eliminates the separate liquid layers. The nearly uniform mixing is obtained when the rotational velocity gives a mixing index of 98 %. They described the effects of the liquid properties, impeller velocity, size and location on the degree of mixing and mixing index [42].

Piero et al. [5] developed an experimental method to determine the minimum stirring velocity for complete dispersion of two immiscible liquids in stirred baffled vessel with pitched blade turbine. This method is based on the collection of samples from three different positions in the bulk of the mixture at different stirring velocities. The minimum stirring velocity is determined when no further increase of the volume fraction of the dispersed phase is obtained. They found that their method can be used in large scale industrial reactors where the visual method can not be used.

The effect of the physical properties of the continuous and dispersed phases on the minimum velocity was studied by Bushra et al. [45] in unbaffled vessel by using a four-bladed fat blade turbine.

2.5 Interphase mass transfer

The mixing of immiscible liquids includes mass and heat transfer in many applications such as extraction in which the solute distributes according to its solubility between the dispersed and continuous phases. Extraction rate of the solute is influenced by the breakage and coalescence of the drops, microscopic interfacial transport and macroscopic hydrodynamics in the vessel [35]. Mass transfer can be efficient in stirred heterogeneous vessels. It is caused by diffusion of a dissolved species across a phase boundary. Transport rates depend on the slip velocity between the phases. The mass transfer rate $\dot{m}_A$ of species A into or out of a drop depends on the interfacial area a (π d^2) per unit volume of the liquid in the vessel, the concentration driving force Δ C_A -which is the difference in concentration of species A inside and out side the drop- and the mass transfer coefficient k as shown by equation (2.3):

$$\dot{m}_A = k\,\pi\, d^2\, \Delta C_A. \tag{2.3}$$

Increasing the stirring intensity increases mass transfer. Since drop size decreases, the interfacial area is increased. Also eddy motion increases, causing an increase in the slip velocity and redispersion which are very important in liquid–liquid extraction. Transfer mechanism of the solute may be due to the film theory, penetration theory and surface renewal method (recommended).

Film theory assumes the mass transfer occurs by molecular diffusion in a film next to the interface, but it is negligible in the bulk liquid compared to the turbulent diffusion [46][47], the mass transfer coefficient is proportional to the diffusivity and film thickness.

Penetration theory assumes that the liquid surface consists of small fluid elements that contact the interface for an average time, after which they penetrate into the bulk of the liquid, each element is then replaced by another element from the bulk liquid. Hines et al. [48] suggested this theory for interfacial mass transfer. The mass transfer coefficient is proportional to the 0.5 power of the diffusivity.

Surface renewal of the dispersed phase occurs due to the coalescence, dispersion of the drops and diffusion. It is an extension to the penetration theory and assumes the time of contact is not constant, thus the interface is independent on the contact time [48]. The rate of mass transfer in liquid-liquid extraction depends on surface renewal by diffusion and turbulence in the continuous phase and diffusion, coalescence and breakup in the dispersed phase [49].

2.5.1 Solute concentration

Lower rate of mass transfer of the solute is desirable to be able to measure the concentration of the solute. This can be done by lowering the driving force. So it is better that the solute has low concentration in the continuous phase and large equilibrium solubility in the dispersed phase [49].

The solute concentration in the continuous phase can be measured physically by using the electrical conductivity of the continuous phase, and then the changes in the concentration in the dispersed phase can be calculated by material balance. The presence of the organic dispersed phase leads to two difficulties in the conductivity measurements. First the dispersed phase drops tend to stick to the electrodes and decreases the electrode area. Second the presence of the organic drops in the continuous phase passing between the electrodes leads to a decrease in the specific conductance readings which are dependent on the chemical and physical properties of the dispersed and continuous phases [49]. The chemical analysis method can be used also to measure the solute concentration whereas a sample is drawn out through a tube and analyzed by titration method.

2.5.2 Mass transfer coefficient

There are few studies on mass transfer coefficients for liquid-liquid systems in stirred vessels. Continuous phase mass transfer coefficient was studied by Shindler et al. [50] and Keey et al. [51] for continuous flow stirred vessel, and by Skelland et al. [52] and Mok et al. [53] for batch vessel. Treybal et al. [54] and Hiraoka et al. [55] studied the mass transfer in gas-liquid and solid-liquid systems. They found the mass transfer behaviour of tiny droplets was very similar to that of solid sphere. They found the mass transfer coefficient for tiny droplets satisfied the correlations for solid spheres. Thus the correlations developed for solid-liquid systems can be used for determining the mass transfer coefficients in stirred liquid-liquid systems.

Most of the work in the literature on liquid-liquid mass transfer is for steady state conditions in extraction columns and spray towers [56][57]. They correlated the volumetric mass transfer coefficient with the flow rates of the continuous and dispersed phases [58]. Two phase liquid-liquid mass transfer operations are affected by the equipment size which influence on the fluid motion conditions and the physical properties of the fluids [49]. Rushton et al. [49], Boyadzhiev et al. [59] and Nagata et al. [60] measured the mass transfer rates between two liquid phases in turbulent flow condition in a mixing vessel. They studied the effect of size and velocity of the impeller and the physical properties of the immiscible liquids on the mass transfer rate and the interfacial area between the two phases. They found that the interfacial area decreases to a certain extent by using a small ratio of organic to water phase. The low concentration of the solute in the continuous phase gives low driving forces and high equilibrium solubility which allows transfer of measurable amounts of solute. They found that the volumetric mass transfer coefficient (kA) decreases when the viscosity of either phase is increased and it directly proportional to the square of the impeller velocity. Nagata et al. [60] shown that the variation of the volumetric mass transfer coefficient with stirrer velocity corresponding to the variation of the interfacial area with the stirrer velocity.

Byoung et al. [61] and Rushton et al. [49] studied the mass transfer between two immiscible liquid phases in a stirred tank extractor. The motion of the drops is visualized by using a camera. They predicted the mass transfer resistance of the two phases by using different correlations adopted by previous investigators. They found also that the extraction efficiency increases when the stirrer velocity increases. Several correlations were found to calculate the mass transfer coefficients, but they were limited to the used systems. Comprehensive correlations over a range of physical properties can not be established.

2.5.3 Interfacial area

The interfacial area and the mass transfer rate are affected by the operating variables such as the velocity and size of the mixing impeller and the physical properties of the solute, the dispersing and continuous phases [25][62][63].

When masses of drops are present, there is a coalescence and breakup of them leading to the formation of new surface area as well as redistribution of the solute in the dispersed phase [49].

A correlation for the specific area (a) as a function of seven variables in liquid-liquid system is given by Eckert et al. [8]. The interfacial area is calculated based on mass transfer of the solute A between the continuous and the dispersed phases. The material balance on the solute A is:

$$V_c dC_A = k_c A\,(C_{eq.} - C_A)\,dt. \tag{2.4}$$

Where, k_c is the mass transfer coefficient for the continuous phase, A is the interfacial area in a two phase mixture varying with time, V_c is the volume of the continuous phase in the vessel, $C_{eq.}$ and C_A is the concentration of solute A at equilibrium and at time t, respectively.

Assuming V_c and C_{A0} are constant and integrating Eq. 2.4 from t_0 to t and from C_{A0} to C_A to get:

$$\ln \frac{C_{eq.} - C_A}{C_{eq.} - C_{A0}} = -\frac{k_c A}{V_c}(t - t_0). \tag{2.5}$$

Where, C_{A0} is the solute concentration at t_0 when the mixing starts. Plotting $\ln \frac{C_{eq.} - C_A}{C_{eq.} - C_{A0}}$ vs $(t - t_0)$ gives a straight line with a slope of $-\frac{k_c A}{V_c}$, consequently the overall volumetric mass transfer coefficient $k_c A$ can be obtained from the slope. If k_c is given, then the interfacial area A between the two phases can be determined. Also, the total interfacial area A can be calculated from the given values for droplet diameter of the dispersed phase d_{32}, volume fraction of the dispersed phase ϕ and the total volume of the mixed phases V as following in Eq. 2.6 [7][49]:

$$A = aV = \frac{6\phi}{d_{32}} V. \tag{2.6}$$

The interfacial area was measured indirectly in gas-liquid and liquid-liquid stirred dispersion in baffled cylindrical tank by means of a light transmission technique [64][65]. Coulter counter and photography technique are used also to measure the specific area [8]. Most of the previous experimental methods measure the specific area based on the local values of the holdup. But to obtain a true average specific area for the vessel as a whole would require complete exploration of the vessel volume with light transmittance device. For that CFD solves this problem by calculating the average volume fraction of the dispersed phase in the continuous phase [66][67][61].

Nagata et al. [60] studied the rates of mass transfer for liquid-liquid extraction in mixing vessel. He used a chemical reaction to measure the mass transfer rates. He worked with a 0.65 % dispersion of the organic phase with a small density difference between the dispersed organic drops and the continuous aqueous phase. He found that the rate of mass transfer is proportional to the interfacial area between the two phases and it is affected by the volume fraction of the dispersed phase. While Rushton et al. [49] used 8.2 % dispersion of organic phase in a flat bottomed baffled glass vessel stirred with a six flat blade turbine in a turbulent flow condition. They measured the mass transfer coefficient between the two liquid phases which have different physical properties like viscosity. They found that the size and velocity of the stirrer and the physical properties of the liquids affect the fluid flow conditions and the mass transfer rate of the solute between the two liquid phases. Electrical conductivity method is used to measure the solute concentrations. The overall mass transfer coefficient is calculated from the concentration change of the solute and material balance and plotted as a function of stirrer velocity and the viscosity of the continuous or the dispersed phase. They found that the volumetric mass transfer coefficient decreases when the viscosity of either phase is increased and the coefficient increases approximately as the square of the impeller velocity.

2.6 Types of agitators

Agitator is a device consisting of at least a power package, a shaft and an impeller to provide agitation of the contents of a vessel [21]. The basic types of agitators are shown in Fig. 2.1 [68]. It is an important to study how the dispersed phase distribution gradually becomes more uniform with increasing impeller velocity. It is of interest to identify the most energy efficient impeller, since the low input energy reduces the capital and operating costs [69].

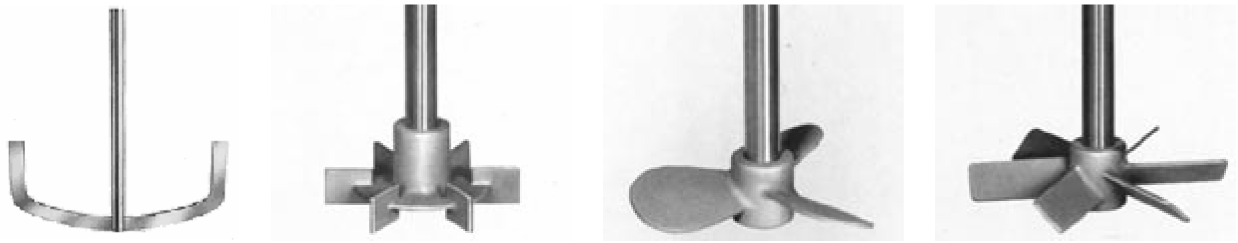

Anchor Impeller Rushton Turbine Propeller Pitched Blade Turbine

Figure 2.1: Agitator types [68].

2.7 Impeller selection for immiscible liquid-liquid system

The mixing of immiscible liquids is affected by impeller type and geometry, number of required impellers, impeller to vessel diameters ratio and the location of the impeller in the vessel. The impellers commonly used for immiscible liquid-liquid systems include disk turbines, pitched blade turbine and propellers. The best impeller is that creates the maximum interfacial area and uniformly sized drops. The choice of the impeller depends on the application. For high interfacial area (small drop diameters), rushton turbine impeller is a good choice. The loop impeller is used when larger drops of a narrow size distribution are required. Disk turbines are used in extraction and they are operated at moderately low speed to avoid over dispersing [9].The coaxial flow combination of helical ribbon impeller with the propeller impeller is recommended for the dispersion of solid/liquid system for laminar high viscosity or turbulent low viscosity systems [70].

2.8 Flow patterns

Mixing by stirring of liquids involves the transfer of momentum from the moved stirrers to the liquid by shearing stress perpendicular to the direction of flow such as the rotating disc or by normal stress in the direction of flow such as the propeller [20]. The discharge characteristics of an impeller determine the recirculation pattern of the fluid. Flow patterns are influenced by the type of impeller. They are sensitive to impeller geometry, the number of impellers and the impeller position in the vessel. The propeller and pitched blade turbine create an axial flow through the impeller and the central axial flow may be upwards or downwards depending upon the direction of the rotation. They are used in blending and solid suspension applications where the axial flow of the impeller sweeps the solid off the tank bottom [71]. Since axial flow impeller produce only one loop right and left to the shaft as shown in Fig. 2.2, fluids are mixed faster and mixing time is reduced compared to radial flow impellers with two loops. The power consumption of these flow impellers is less than that of radial flow impellers at the same stirrer velocity and diameter [16][20][21].

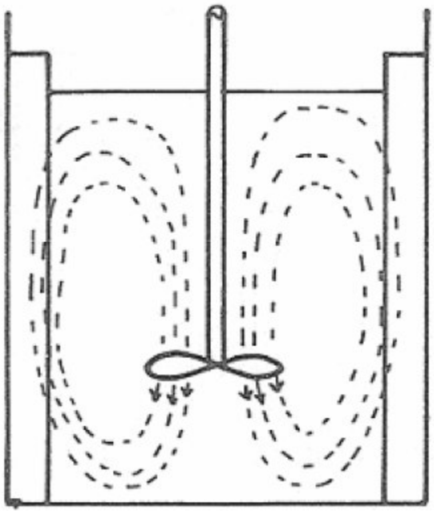

Figure 2.2: Axial flow pattern [21].

The flat blade turbine produces a strong radial flow outwards from the impeller, creating a circulation zones in the top and bottom of the vessel [72]. Rushton turbine impeller provides radial flow and generates significant shear. These impellers are employed in dispersing immiscible fluid phases (gas/liquid and liquid/liquid) typically for interphase mass transfer [73]. The radial flow will split into two streams upon collision with tank wall. Each flow loop will continue along the wall and then return to impeller as shown in Fig. 2.3. The movement of a fluid is generally from the centre of the vessel to the wall. Radial flow is found with a turbine type or a paddle stirrer [16][20][21].

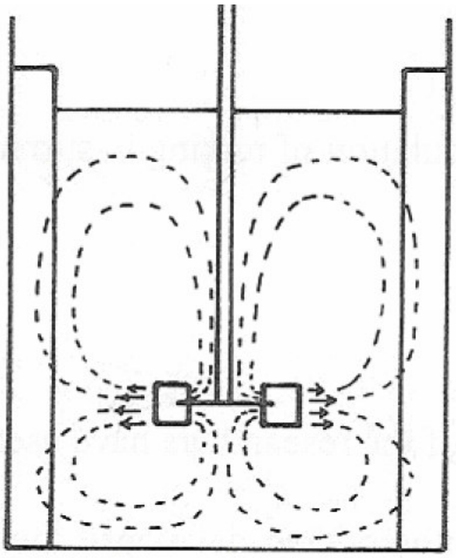

Figure 2.3: Radial flow pattern [21].

The anchor impeller produces tangential flow; it does not contribute to the mixing in a vertical direction. It is always converted into radial flow by the centrifugal force. In the unbaffled vessel with the impeller rotating in the centre, centrifugal force acting on the fluid raises the fluid level near the wall and lowers the level at the shaft. This flow is shown in Fig. 2.4 [16][20]. Anchor impeller act directly on large proportion of the fluid and do not rely on induced motion to bring about mixing action [74].

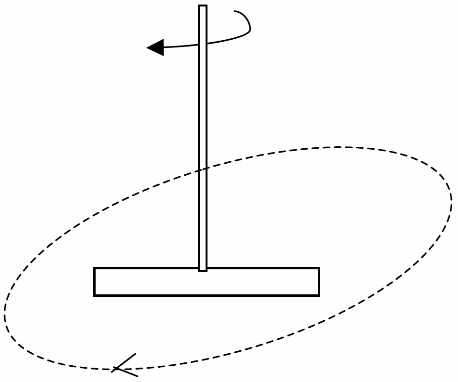

Figure 2.4: Tangential flow pattern [16].

Due to the primary rotational flow (Fig. 2.5-left), a centrifugal force results and produces the secondary flow. This force drives the liquid outwards in a radial direction. The liquid flows at the vessel wall either upwards or downwards forming vortex rings (Fig. 2.5-right). A vortex is produced due to the centrifugal force acting on the rotating liquid. The depth and the shape of the vortex depend on impeller and vessel dimensions as well as on stirrer velocity. The secondary flow consists of radial and axial velocity components which are required in the mixing process. Primary fluid flow may be considered as an energy reservoir for the secondary flow [16][75].

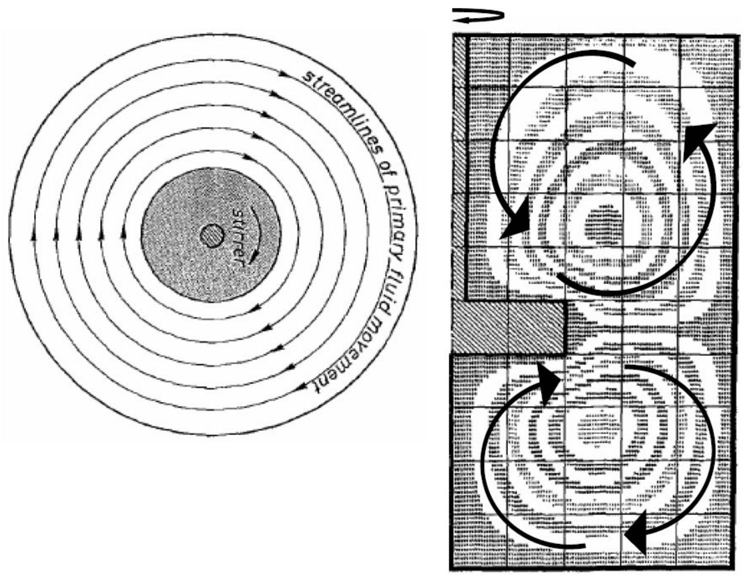

Figure 2.5: Primary flow (left) and secondary flow (right) by anchor impeller.

For small clearance impellers when using laser beam, no experimental data can be measured and consequently it is impossible to obtain the velocity profile at whole stage during a cycle (a cycle is the required time for impeller to rotate one revolution), this can be done by CFD. Ohta et al. [76] proposed the numerical study for a Newtonian fluid mixing in stirred vessel with anchor impeller. They studied a two dimensional model for secondary flow to express the flow field in a vertical plane. The effect of the wall clearance and the anchor speed on the flow field was studied. They found that two vortices are formed in the upper and lower region of the vessel. The number and flow rate of axial circulations become greater with an increase of the anchor velocity. The impeller rotation velocity has a greater effect on the secondary axial flow than on the primary tangential flow. Peixoto et al. [77] studied the behavior of the stirred vessels with anchor impellers using a computational fluid dynamics. CFX-4.2 software was used to calculate the flow generated by the anchor impeller using three dimensional and finite volume methods. A single axial recirculation zone centered near the curve separating bottom and vessel walls, a little bit above the curve of the anchor blade. As the velocity of the impeller increases, the fluid circulation increases and the low velocity region near the free surface is eliminated.

A detailed characterization of the three dimensional flow pattern inside the vessel is important to get a better understanding of the flow state of the fluids and of the mechanisms responsible for homogenization and transport processes [78]. A three dimensional model applied by Abid et al. [79] to the flows generated in a stirred vessel with anchor stirrers in a laminar flow region. Long anchor stirrer without horizontal shaft and short anchor stirrer with horizontal shaft are used for comparison of the mixing efficiency. The effects of wall clearance or the ratio of clearance between blades and wall to the vessel diameter, the height of the vertical blades or the ratio of the height of the blades to the level of the liquid on the flow field and mixing were studied. They found that the horizontal blades enhance the axial circulation and the vertical blades are more efficient if their tips are slightly below the liquid level. Secondary flows are created between the blades and the central shaft when short anchor stirrer with horizontal shaft is used, this enhance the mixing in the vessel by producing new axial circulations. Velocity of the stirrer influence the appearance of more or less recirculation loops behind the blades, but does not change the flow structures. A large upward axial flow is generated, and the radial movement increases, compared with the long anchor for the same liquid level in the vessel. Primary tangential flow is created by the rotation of the horizontal blade. They found that short anchor with the horizontal blade is the best to use because it requires lower power consumption and produces axial circulations.

Flow patterns in a stirred vessel are not depending only on the type of the impeller but also on the characteristics of the fluid, size and vessel geometry. Variation in the ratio of the diameter of the impeller to that of vessel results in changes to flow pattern. Small ratio generates intense agitation in the impeller region and a large, less intense recirculation patterns. An increase in the ratio results in a more intense recirculation flow in the vessel [80]. Espinosa et al. [81] studied the effect of wall and bottom clearance on power consumption for anchors by considering the variations in the flow patterns. They found that it the bottom clearance to the vessel diameter ratio increases, and then the power input decreases. Changing the bottom clearance produces axial flows which affect the primary flow patterns and thus the power consumption.

The Laser Doppler Anemometry LDA is used by Fredrik et al. [2] to measure the velocity field of the continuous phase in liquid-liquid stirred vessel showing that the turbulence is damped by the presence of the dispersed phase. From these measurements it can be seen how the macroscale structure and the turbulence are influenced in a stirred vessel when using different percentage of the dispersed phase. Fredrik et al. [2] also studied the effect of the volume percentage of the dispersed phase on the measured velocity vector fields by using the LDA in stirred vessel with rushton impeller. They found that the vortex below the impeller is stretched with increasing the dispersed phase content and the turbulent is damped. Ljungqvist et al. [82] compared the measured solid-liquid two phase flow field data by the phase-Doppler anemometry with that predicted in axially stirred vessel by using CFX-4. The results of the velocity components (axial, radial and tangential) and the turbulent kinetic energy showed a qualitative agreement. It is found that the solid particles move faster downwards and more slowly upwards than the fluid phase.

2.9 Batch and continuous modes for immiscible liquids

Most industrial mixers have three modes: batch, semibatch and continuous. Batch mixing experiments of the immiscible liquids, enable to follow quantitatively the droplet breakage and mass transfer with time by measurement of the mass transfer coefficient, drop size and surface area of the dispersed phase. In contrast, experiments with continuous flow give only average transfer conditions corresponding to many different elements of the dispersed phase which enter the vessel at different times and in different stages of mass transfer and drop break up at any given instant. The time history of a given element of the dispersed phase in the vessel can not be followed to model the process. Many correlations for mass transfer in a batch system can be found [7].

A batch type experiment minimizes the bulk of the equipment and material to be handled. It provides a sufficient accuracy so that the data may be translated to the performance of a continuous flow operation. Large size batch experiment can be made at less cost than for large scale continuous operation [49].

The study of the interfacial area, drop size and the holdup of liquid-liquid dispersion in stirred vessels have been limited to baffled vessels, with few exception to batch operation unbaffled vessels. Unbaffled vessels operate more efficiently with less power consumption than do the baffled vessels [83]. Batch mixing is the simplest mode of operation. The industrial mixer is filled with media and product mixing is allowed to proceed. When mixing is complete, the vessel’s contents are emptied for downstream processing. The industrial mixer is then cleaned and refilled for mixing another batch. Batch mixing process requires a large amount of time and energy to achieve good end product quality [84]. The batch reactor is very useful to investigate a wide variety of chemical reactions. The batch process shows high flexibility towards different operation procedures and the possibility to reach high conversions. Continuous mixers are suitable for production applications, because they can run for long periods of time without being shutdown [85].

2.10 Computational fluid dynamics (CFD) for multiphase flow

CFD is a computer based tool for simulating the behavior of systems involving fluid flow, heat transfer, and other related physical processes. Fluid flows are governed by partial differential equations PDE (Navier-Stokes equations) which represent conservation laws for the mass, momentum, and energy. CFD is the method of replacing such PDE systems by a set of algebraic equations which can be solved using digital computers. These equations are solved over a region of interest, with specified conditions on the boundary of that region [86].

There are two approaches for analyzing multiphase flow: the Euler- Lagrange approach in which the prime phase fluid is treated as a continuum and solved by solving Navier Stokes equations, while the dispersed phase fluid is solved by tracking the individual particles. Hartmann et al. [87] and Khopkar et al. [88] found that the volume fraction of dispersed phase should be less than 10 vol% in Euler-Lagrange approach which is not suitable for high volume fraction of the dispersed phase. The Euler-Euler two fluid approach is more complex, but can simulate the flows with wide range of volume fraction of the dispersed phase. In this approach, the different phases are treated as interpenetrating continua and interacting with each other in the whole domain [89]. Conservation equations for each phase are derived to obtain a set of equations with regard to momentum, continuity and energy [90]. In a complex turbulently stirred multiphase flows, the turbulent model should be properly chosen to close the Reynolds average Navier Stokes (RANS) equations. 3D calculations with application to mixing vessel were done on the gas-liquid [41] and solid-liquid [91] flows. There are quite limited investigations regarding multiphase mixing process. Vikhansky et al. [92] performed the Eulerian-Lagrangian approach to model the liquid-liquid two phase flow in a rotating disk contractor, whereas an algebraic slip mixture model was adopted to simulate the liquid-liquid Taylor Couette-Poiseulle flow by Zhu et al. [93]. With the Euler-Lagrange approach, Jaworski et al. [94] [95] [96] developed a two phase, both laminar and turbulent flow of two liquids like water (continuous phase) and silicon oil (dispersed phase) in static mixers. The velocity field was computed by using the Eulerian approach, but the residence time and drop path was computed by the Lagrangian approach.

CFD methods are applied to predict the hydrodynamics characteristics of single phase and two phase flows, such as solid-liquid [41][97][98] and gas-liquid [99][100] system in stirred vessels [1]. It helps to understand the flow and dispersion behaviour of liquid-liquid two phase systems in stirred vessels, but the progress on liquid-liquid systems is little as reviewed by Kuipers et al. [101]. In regards to the stirred vessel, only a few studies were on the numerical simulation of complex 3D turbulent liquid-liquid two phase flow in a stirred vessel [102] [1] [103].

The fluids in a multiphase flow are assumed to be mixed at macroscopic length scales, much larger than molecular. Different velocity fields are solved for each fluid which interacts with each other by means of interfacial forces and mass transfer across the phase interfaces. The relative movement of the rotating impeller to static vessel is encountered through the improved inner-outer iterative algorithm [104]. Wang et al. [13] simulated the gas-liquid stirred tank with a Rushton turbine impeller by using this procedure. The gas-liquid flow and gas holdup distribution in the impeller and bulk flow of a stirred tank were presented and compared with the experimental data. It was found a reasonable agreement between the predicted results and the experimental data. They used the two-fluid and k-ϵ two equation models to simulate the two phase turbulent flow in a stirred vessel. Calabrese et al. [105] employed the sliding mesh and RANS simulation for rotor-stator mixer, the predicted mixing behavior is validate with the flow measurements with the Laser Doppler Anemometry (LDA) and Particle Image Velocimetry (PIV). Deen et al. [106] also employed this method to simulate the interaction between the impeller and baffles in gas-liquid system.

Haiyan et al. [107] studied the distribution of the gas hold up in surface aerated baffled stirred vessels experimentally and numerically with CFD. They measured the gas hold up by using a conductance probe at different operating conditions. They found that the gas hold up distribution in this vessel is non uniform and the baffles improve the aeration rate particularly at higher stirrer velocity. The two-fluid with k-ϵ turbulent models predicted reasonably the gas hold up distribution in the upper region of the vessel.

Han et al. [108] predicted the gas holdup distribution in a rushton stirred tank by using Lagrangian method (discrete particle method), whereas Wang et al. [109] used the Eulerian-Eulerian method with k-ϵ model for the turbulent flow. They found that the gas holdup in the impeller discharge stream is under predicted, but in the bulk region, the results of the simulation are in good agreement with the experimental data. Yanhong et al. [104] used the Eulerian-Eulerian method with k-ϵ and large eddy simulation (LES) models for comparison to predict the velocity flow field for gas-liquid system in a stirred vessel with rushton impeller. They found many small vortexes in the gas and liquid flow fields and the flow pattern change with time.

The solid particles are tracked numerically in the Eulerian flow field by Hartmann et al. [110] through solving the dynamic equations of linear and rotational motion of the particles. They concluded that the k-ε model was able to provide an accurate representation of the flow field in a stirred vessel after assessing LES and RANS simulations in comparison with that measured by means of LDA. The numerical study of solid-liquid dispersion is also done by Wang et al. [6][111]. They predicted the flow field of the solid phase and the critical stirrer velocity for complete dispersion of the solid particles in a baffled stirred vessel with rushton impeller. They calculated the solid concentration profiles at a specific monitor point at different stirrer velocities. They suggested that the minimum stirrer velocity is that at which a sudden change in the slope of the profile occurs. They calculated the axial velocity of solid phase in the tank bottom at the location where the solid particles are difficult to suspend at different stirrer velocities. They found that the positive numerical value of simulated axial velocity of solid phase at that location shows the minimum stirrer velocity for complete dispersion.

2.11 CFD developments and applications

Computers have been used to solve fluid flow problems for many years. Different programs have been written to solve different problems. For that purpose, CFD solvers were developed. They required powerful computers as well as knowledge of the fluid dynamics, and large amounts of time to set up simulations.

Development of the computing power with powerful graphics and interactive three dimensions manipulation of models made the process of creating a CFD model and analyzing results much less labor intensive and reducing time and cost. Advanced solvers contain algorithms which enable accurate solution of the flow field in a reasonable time [86].

CFD provides a qualitative prediction of fluid flows by means of mathematical modelling (partial differential equations), numerical methods (discretization and solution techniques) and software tools (solvers, pre and post processing utilities). It enables to perform numerical experiments (computer simulations) in a real experiment. CFD simulation is able to model physical fluid phenomena that cannot be easily measured with the experiment [112].

2.11.1 Mathematical and discretisation methods

The set of partial differential equations which describe the processes of momentum, heat and mass transfer are known as the Navier Stokes equations. These equations can be discretised and solved numerically. Equations describing other processes such as turbulence can also be solved in conjunction with the Navier Stokes equations. The discretization of these equations is performed on a staggered grid. A suitable discretization method of approximating the differential equations by a system of algebraic equations should be chosen for the variables at some set of discrete locations in space and time. There are many approaches such as finite difference (FD), finite element (FE) and finite volume (FV) method, the one on which CFX is based [113]. In this technique, the region of interest is divided into small sub-regions, called control volumes. The equations are discretised and solved iteratively for each control volume. As a result, an approximation of the value of each variable at specific points throughout the domain can be obtained, thus the behavior of the flow can be derived [86].

2.11.1.1 Finite difference method

It is used for simple geometries. FD method can be applied to any grid type, but it has been applied mostly to structured grids. At each grid point, the differential conservation equation is approximated by replacing the partial derivatives by approximations in terms of the nodal values of the functions. The result is one algebraic equation per grid node, in which the variable value at this node and a certain number of neighbour nodes appear as unknowns. Taylor series expansion or polynomial fitting is used to obtain approximations to the first and second derivatives of the variables with respect to the coordinates [113].

2.11.1.2 Finite element method

The FE method is similar to the FV method in many ways. The domain is broken into a set of discrete volumes or finite unstructured elements, they are triangles or quadrilaterals in two dimensions, while tetrahedral or hexahedra are often used in three dimensions. The equations in FE method are multiplied by a weight function before they are integrated over the entire domain. The solution is approximated by a linear shape function within each element in a way that guarantees continuity of the solution across element boundaries. Such a function can be constructed from its values at the corners of the elements. The weight function is usually of the same form. This approximation is then substituted into the weighted integral of the conservation equations [113]. The derivative of the integral with respect to each nodal value is set to be zero. The result is a set of non-linear algebraic equations.

2.11.1.3 Finite volume method

The FV method uses the integral form of the conservation equations as its starting point. The solution domain is subdivided into a finite number of continuous control volumes, and the conservation equations are applied to each control volume. At the centroid of each control volume lies a computational node at which the variable values are to be calculated. Interpolation is used to express variable values at the control volume surface in terms of the nodal values. Surface and volume integrals are approximated using suitable quadrate formula. The FV approach requires interpolation and integration approximations. As a result, an algebraic equation is obtained for each control volume, in which number of neighbour nodal values appears. The value of a variable at each cell centred node is connected to its nearest neighbours by algebraic relations. The FV method is suitable for complex geometries [113][20]. Chap.2.13.3 shows how this method is applied in Ansys CFX-11.

2.11.2 Iterative solution strategy

The coupled nonlinear algebraic equations must be solved iteratively by updating the coefficients of the discrete problem by using the solution values from the previous iteration to get rid of the nonlinearities. The resulting sequence of linear sub problems is solved by an iterative method because direct solvers like Gaussian elimination are expensive. The iterations convergence is verified by checking and monitoring the residuals, relative changes of integral quantities and checking if the prescribed tolerance is attained [114].

2.11.3 Validation

The goal of validation is to check if the model itself is suitable for practical purposes and to ensure that the CFD code produces reasonable results for a certain range of flow problems. This can be done by comparing the results with available experimental data to check if the reality is represented accurately enough when using different models, geometry, and initial/boundary conditions.

2.12 Calculation methods of the flow patterns by CFD

The following CFD methods are used to calculate the flow pattern around the impeller blades without describing any experimental data in stirred vessels.

2.12.1 Sliding mesh

The sliding mesh method is dealing with the impeller interaction. The main advantage of the sliding mesh method is that no experimentally obtained boundary conditions are needed, as the flow field around the impeller blades is being calculated in detail. This allows modelling of the impeller and vessel for which experimental data is difficult to obtain. With the sliding mesh method the vessel is divided in two regions that are treated separately: the impeller region and the vessel region that includes the bulk of the liquid, the cylindrical wall and the vessel bottom. The grid in the impeller region rotates with the impeller. The grid in the vessel remains stationary. The two grids slide past each other at a cylindrical interface. In the vessel region the conservation equations for mass and momentum are solved. In the rotating impeller region, a modified set of balance equations is solved [115].

A disadvantage of this method is the long calculation time. An important application for the sliding mesh method is the development of new optimized impeller designs for specific industrial applications and the prediction of flow patterns in multiple impeller systems, where there is significant interaction between the impellers and to predict time dependent flow patterns. The predicted laminar flow patterns of different impellers in a baffled vessel by using sliding mesh method were validated by Bakker et al. [115], and compared with that obtained from the Laser-Doppler Velocimetry (LDV). They found that this method is suitable and a good agreement with the experimental data was found. The flow patterns were shown by means of velocity vectors. Two circulations are formed above and below the impeller. The length of the vectors is proportional to the magnitude of the liquid velocity. They found also as Reynolds number increases, the flow changes from the radial to the axial [115].

2.12.2 Rotating frame

The rotating frame model solves the momentum equations for the entire domain in a rotating frame. Problems solved in a rotating frame use the angular velocity of the primary rotating component as the angular velocity of the frame. In stirred vessels, the frame is assumed to rotate with the impeller. The vessel rotates in the opposite direction must have a rotational boundary condition of negative angular velocity value. This approach is useful for unbaffled vessels with smooth tank walls that are geometrically equivalent to a perfect surface of revolution [9].

2.12.3 Multiple reference frames

More than one rotating or non rotating reference frame can be used in a simulation with the multiple reference frames (MRF) model. This steady state approach allows for the modelling of baffled and unbaffled stirred vessels. A rotating frame is used for the region containing the rotating components while a stationary frame is used for regions that are stationary. In the rotating frame containing an impeller, the impeller is at rest. In the stationary frame containing the tank walls and baffles, the walls and baffles are at rest [9].

2.13 Features of ANSYS CFX-11 software

CFX-11 is a computational fluid dynamics (CFD) code, combining an advanced solver with powerful pre and post processing capabilities. It consists of five software modules which are linked by the flow of information required to perform a CFD analysis in Fig. 2.6 [86]:

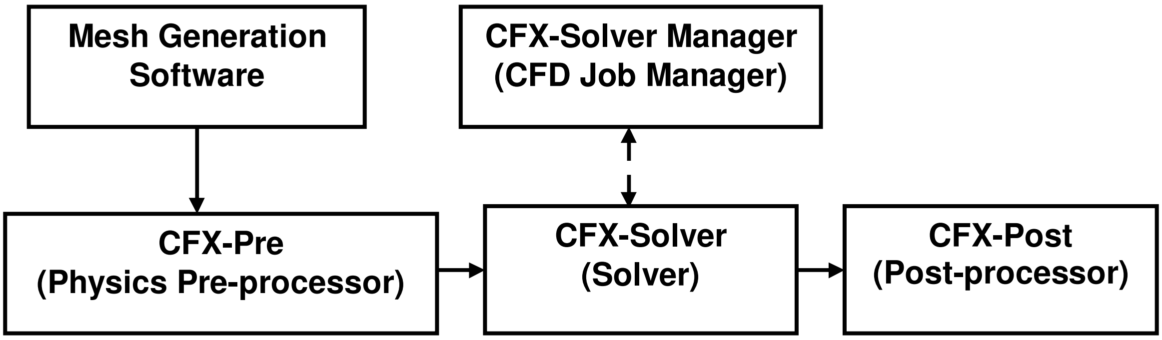

Figure 2.6: The procedure for simulation a problem with CFD.

2.13.1 Geometry and mesh generation

ICEM CFD is used to generate a closed geometric solid and the corresponding mesh. Different types of grids can be generated [116]:

1. Structured grid (uniform grid) where all the nodes have the same number of elements around it, thus the matrix of algebraic equations system has a regular structure. It is used for simple geometries.
2. Unstructured grid (non uniform grid) which is used for very complex geometries. The grids are made of triangles or quadrilaterals in two dimensions and tetrahedral or hexahedra in three dimensions. The solvers for the algebraic equation system for unstructured grids are usually slower than those for structured grids [78].
3. Block-structured grid which is a structured grid inside each block, the order of blocks is irregular.

2.13.1.1 Cell types

There are four types of cells, which are identified by the number of nodes: Tetrahedrons (4 nodes), pyramids (5 nodes), wedges or prisms (6 nodes) and hexahedrons (8 nodes). The vertex ordering for the elements follows Patron Neutral File element conventions, and is shown in Fig. 2.7 [117].

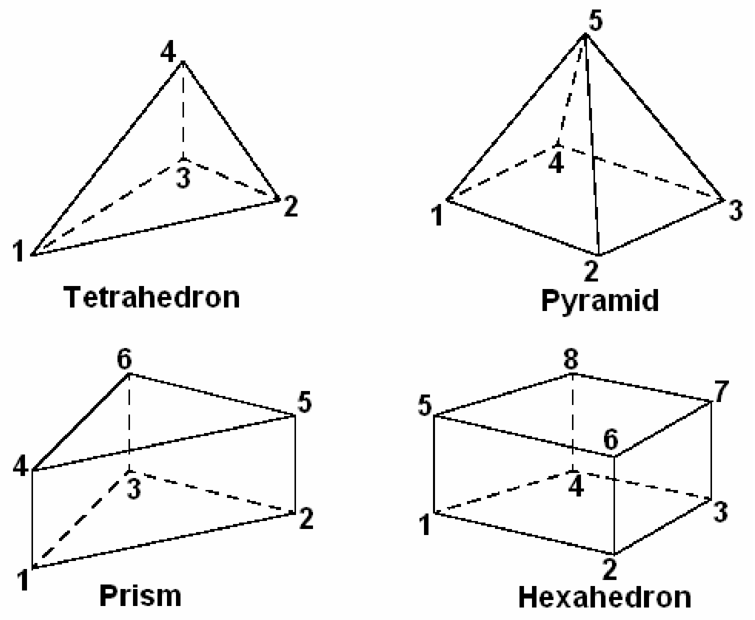

Figure 2.7: Cell types and vertex ordering.

2.13.2 Physics definition pre-processor

CFX-pre is used to import meshes that produced in ICEM CFD and to apply the suitable physical models that describe the problem. Flow physics, fluid properties, initial values and solver parameters are specified in CFX-pre. A full range of boundary conditions including inlets, outlets and openings, together with boundary conditions for heat transfer models and periodicity are all available in CFX-pre [86].

2.13.3 Numerical methodology by CFX solver

CFX-solver produces the required results in a non-interactive batch process. The CFD problem is solved by integrating the partial differential equations, which obtained from applying mass and momentum conservation law, to each control volume over all the control volumes, that obtained by using a finite volume method as described in chap. 2.11.1.3, in the region of interest. These integral equations are converted to a system of algebraic equations by generating a set of approximations for the terms in the integral equations. Many discrete approximations developed for CFD are based on series expansion approximations of continuous functions such as the Taylor series. The resulted algebraic equations are finally solved iteratively.

An iterative approach is required because of the non-linear nature of the algebraic equations and the solution is converged when it approaches the exact solution. For each iteration, an error or residual is reported as a measure of the overall conservation of the flow properties. How close the final solution is to the exact solution depends on a number of factors, including the size and shape of the control volumes and the size of the final residuals. Resolution of the algebraic equations is carried out by using high resolution advection and second order backward Euler schemes. Fig. 2.15 shows a typical mesh in two-dimension on which one surface of the finite volume is represented by the shaded area, each node is surrounded by a set of surfaces which contain the finite volume. All the solution variables and fluid properties are stored at the element nodes [118].

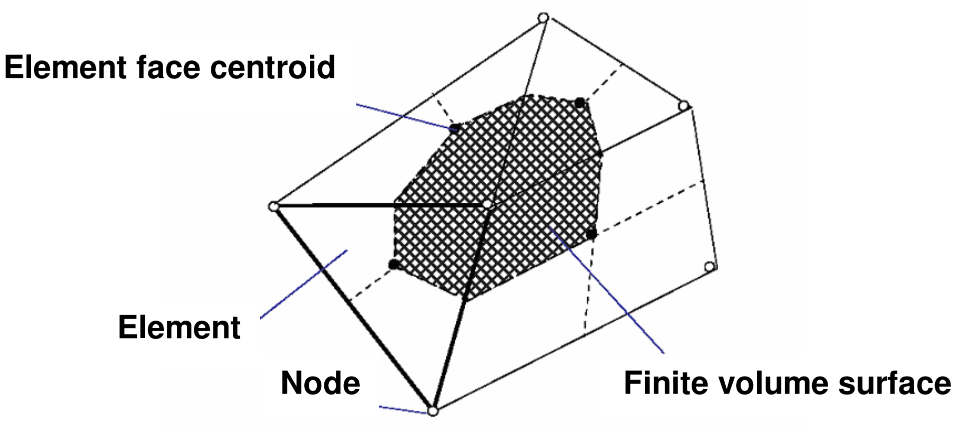

Figure 2.8: Finite volume surface.

2.13.3.1 Coupled solver

It is an important feature of CFX-11 in which all the hydrodynamic equations are solved as a single system simultaneously. The coupled solver is faster than the segregated solver and less iteration are required to obtain a converged flow solution [86]. This solution approach uses a fully implicit discretisation of the equations at any given time step.

The linear sets of equations that arise by applying the finite volume method to all elements in the domain are discrete conservation equations. The system of equations can be written in the form:

$$\sum_{nb_i} a_i^{nb} \phi_i = b_i \, . \tag{2-16}$$

Where ϕ_i is the variable vector, b here is the solution, a is the coefficient matrix of the equation, i here is the identifying number of the finite volume or node in question, and nb is the central coefficient multiplying the solution at the ith location. This method is applicable to both structured and unstructured meshes. The set of these equations for all finite volumes constitutes the whole linear equation system. For the coupled, three dimensions mass-momentum equation set, they can be expressed as (4 x 4) matrix and (4 x 1) vector as in the following:

$$a_i^{nb} = \begin{bmatrix} a_{uu} & a_{uv} & a_{uw} & a_{up} \\ a_{vu} & a_{vv} & a_{vw} & a_{vp} \\ a_{wu} & a_{wv} & a_{ww} & a_{wp} \\ a_{pu} & a_{pv} & a_{pw} & a_{pp} \end{bmatrix}_i^{nb} \quad \text{and} \quad \phi_i = \begin{bmatrix} u \\ v \\ w \\ p \end{bmatrix}_i , \quad b_i = \begin{bmatrix} b_u \\ b_v \\ b_w \\ b_p \end{bmatrix}_i$$

The advantages of such a coupled treatment over a non-coupled or segregated approach are efficiency, generality and simplicity, but it requires high memory. These advantages all combine to make the coupled solver an extremely powerful feature of any CFD code.

2.13.3.2 Solver manager

The CFX-solver manager provides greater control to manage the CFD task, it is a graphical user interface that allows setting attributes for the CFD calculation, controlling the CFX-solver interactively and viewing information about the emerging solution. It also specifies the input files to the CFX-solver, monitors the progress of the solution, sets up the CFX-solver for a parallel calculation (using the cluster) and starts/stops the CFX-solver [86][119].

2.13.4 Post-processing

CFX-post is a post-processor graphics tools for CFX-11. It allows easy visualization of the geometry and the variables in magnitude and/or direction, analyzing, presenting and quantitative post-processing the results of CFD simulation by using 3D isovolumes, 2D contours, vector and graphical plots [86] [120].

3. EXPERIMENTS

Dispersion of cyclohexane/water is carried out in a non-baffled batch vessel, stirred with anchor, pitched blade turbine, propeller and rushton turbine impellers. The batch mixing is used to minimize the used bulk of the equipment and material, and to provide sufficient accuracy. The dispersion behaviour is visualized as a function of stirrer velocity and time by using a video camera and red dye tracer, see chapter 3.3.1. The droplet size of cyclohexane is measured by using a particle vision microscope PVM V819 system. The volumetric mass transfer coefficient of the solute (benzoic acid) from the continuous phase (water) to the dispersed phase (cyclohexane) is determined from the measurements of its concentration in the continuous phase by using the chemical titration method. The volume fraction distribution of the dispersed phase in the axial and radial distances is measured by using withdrawal technique. The velocity flow field of the cyclohexane/water system is measured by using the photographic light cut method, and analyzed by using the Mathcad 14 program. All these experiments are done under different operating conditions such as: Stirrer type and velocity, bottom clearance of the stirrer and percentage volume of the dispersed phase.

3.1 Liquid-Liquid multiphase components

Cyclohexane is used as the dispersed phase. It is colorless liquid and has low viscosity, a greasy or petroleum smell. It is a non polar solvent, useful for the chemical industry and as a raw material for the industrial production of adipic acid. It is used as a standard and in the laboratory analysis. It is immiscible in water and is produced by reacting benzene with hydrogen.

Benzoic acid is used as the solute in this work. It is a colorless crystalline solid and aromatic carboxylic acid. It has a density of 1320 kg/m^3. Its solubility in water is 3.4 g/L at 25 °C [49]. This solute has low rates of transfer, so that the concentration changes of the benzoic acid with time can be measured accurately. Its concentration can be measured by chemical and physical methods accurately.

This weak organic acid is used as a food preservative and in synthesis of many organic substances. Benzoic acid inhibits the growth of yeast and bacteria.

Water (distilled) is used as the continuous phase in this work. It is a polar and immiscible in cyclohexane. It has low viscosity. The continuous phase is chosen based on that; the solute is able to be ionized in the aqueous phase.

Sodium hydroxide is used for the acid-base titration method to measure the concentration of benzoic acid in water (continuous phase).

Phenolphthalein is used as an indicator for the acid-base titration method.

Table 3.1: Some physical properties of the immiscible liquids [47].

	$\rho_{25\,°C}$ [kg/m^3]	$\mu_{25\,°C}$ [Pa s]	σ [N/m]
Cyclohexane (C_6H_{12})	779.000	0.001020	0.05
Water (H_2O)	997.130	0.000891	

3.2 Experimental setup

A cylindrical glass vessel with a rounded bottom is used for mixing. Different types of stirrers, which produce different flow patterns, such as anchor, six bladed rushton turbine, three bladed propeller and four bladed pitched blade turbine impellers are used in the mixing processes as shown in Fig. 3.1.

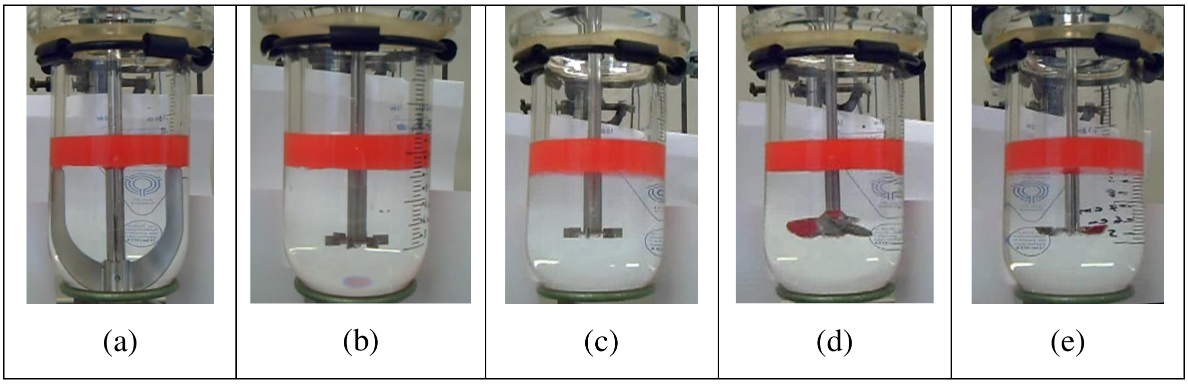
(a) (b) (c) (d) (e)

Figure 3.1: Stirred vessel with different types of stirrers: (a) anchor stirrer (b) rushton turbine at clearance of 3.2 cm, (c) rushton turbine at clearance of 4.1 cm, (d) propeller at clearance of 4.1 cm and (e) pitched blade turbine at clearance of 4.1 cm.

The dimensions of vessel, anchor and rushton turbine impellers are illustrated in Figs. 3.2 and 3.3. Pitched blade turbine has a diameter of D = 4.3 cm and D/d_v = 0.52. Propeller impeller diameter to the vessel diameter ratio is

D/d_v = 4.5 cm /8.2 cm = 0.54. All the ratios of the stirrer diameter to the vessel diameter are according to the standard design of the mixing vessel and stirrer [70]. The stirrer is connected to a variable speed motor (Euro-ST P DV) with a maximum speed of 2000 rpm which is measured by using a velocity control box as can be seen in Fig. 3.4.

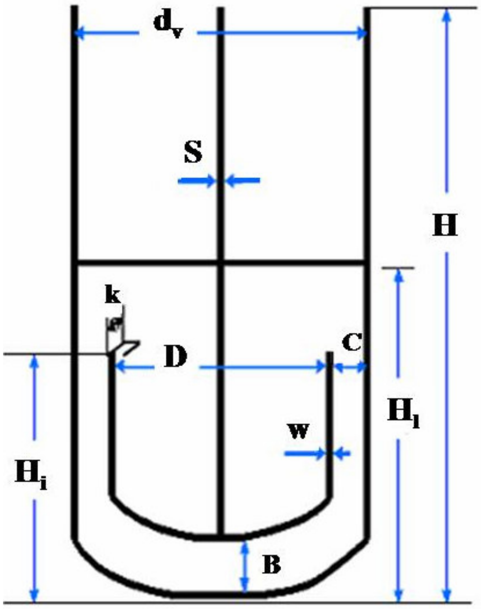

Vessel diameter	d_v	0.082 m
Vessel height	H	0.160 m
Total liquid height	H_l	0.110 m
Stirrer diameter	D	0.075 m
Impeller height	H_i	0.085 m
Blade width	w	0.01 m
Blade thickness	K	0.002 m
Shaft diameter	S	0.010 m
Bottom clearance	B	0.005 m
Wall clearance	C	0.004 m

Figure 3.2: The geometric sizes of the vessel and the anchor impeller with the ratios of the vessel to the anchor impeller sizes.

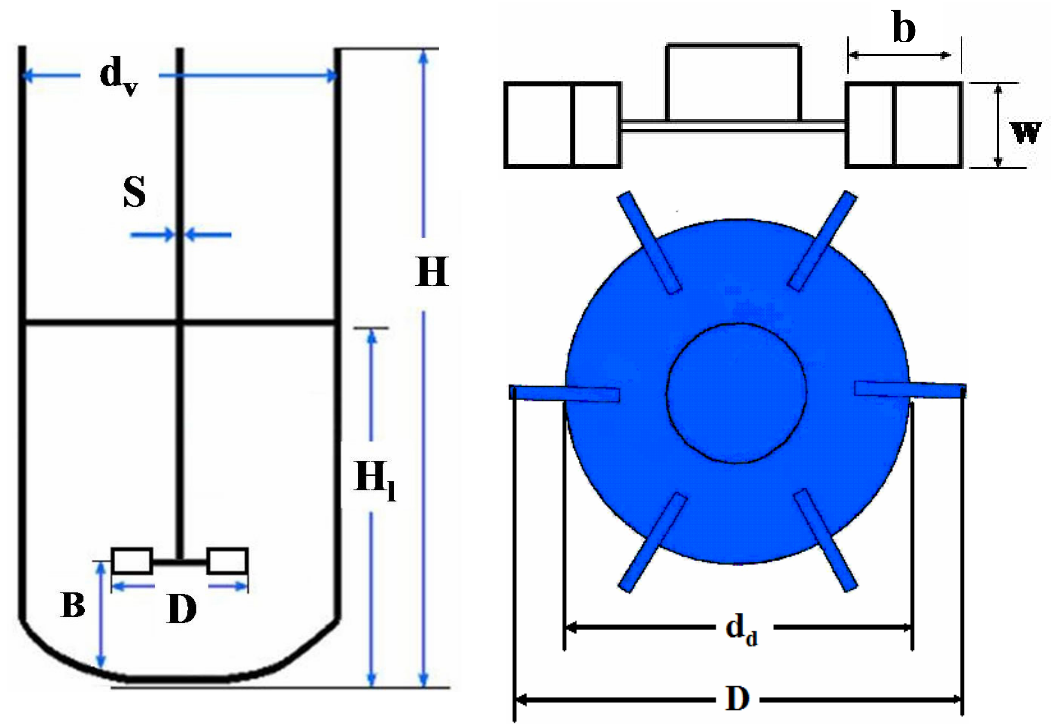

Figure 3.3: The geometric sizes of the vessel and the RTI with D = 3.3 cm, stirrer diameter to the vessel diameter D/d_v = 0.41, disk diameter to the stirrer diameter d_d/D = 0.75, blade width b = 0.25D = 0.825 cm and blade thickness W = 0.2D = 0.66 cm.

Figure 3.4: Schematic experimental setup.

3.3 Measuring methods

3.3.1 Visualization method

The turbulent flow effect on the dispersion behaviour of cyclohexane/water system and flow field patterns is visualized by using a video camera and a red organic colour tracer. This dye is soluble in the organic cyclohexane phase. It is mixed with 100 mL cyclohexane well by using a magnetic stirrer, until a homogeneous red coloured mixture is obtained. The vessel is filled with 400 mL water, the coloured cyclohexane is added slowly above the water phase forming the top red layer at t = 0 as can be seen in Fig. 3.5 for the stirred vessel with anchor impeller. The video camera starts recording the dispersion process when the stirrer starts rotation.

The velocity of the stirrer is varied from 150 to 450 rpm in case of the anchor impeller, whereas for the other stirrers, it varies from 300 to 750 rpm. This is done to determine and recognize the minimum stirrer velocity for complete and uniform dispersions for each stirrer, depending on the red colour distribution. The disappearance of the red cyclohexane layer at the top layer and its spread in the whole vessel will be followed. The visualization experiments are done in case of RTI for two bottom clearances of 3.2 cm and 4.1 cm.

A schematic experimental setup for the visualization experiments is shown in Fig. 3.5. The shaft of the anchor impeller is connected to the electrical motor which is connected with the velocity control box. A light source is fitted behind the vessel whereas the video camera is placed in front of the vessel. A white screen behind the light source was necessary to see clearly the dispersion of cyclohexane in water and the droplets of cyclohexane.

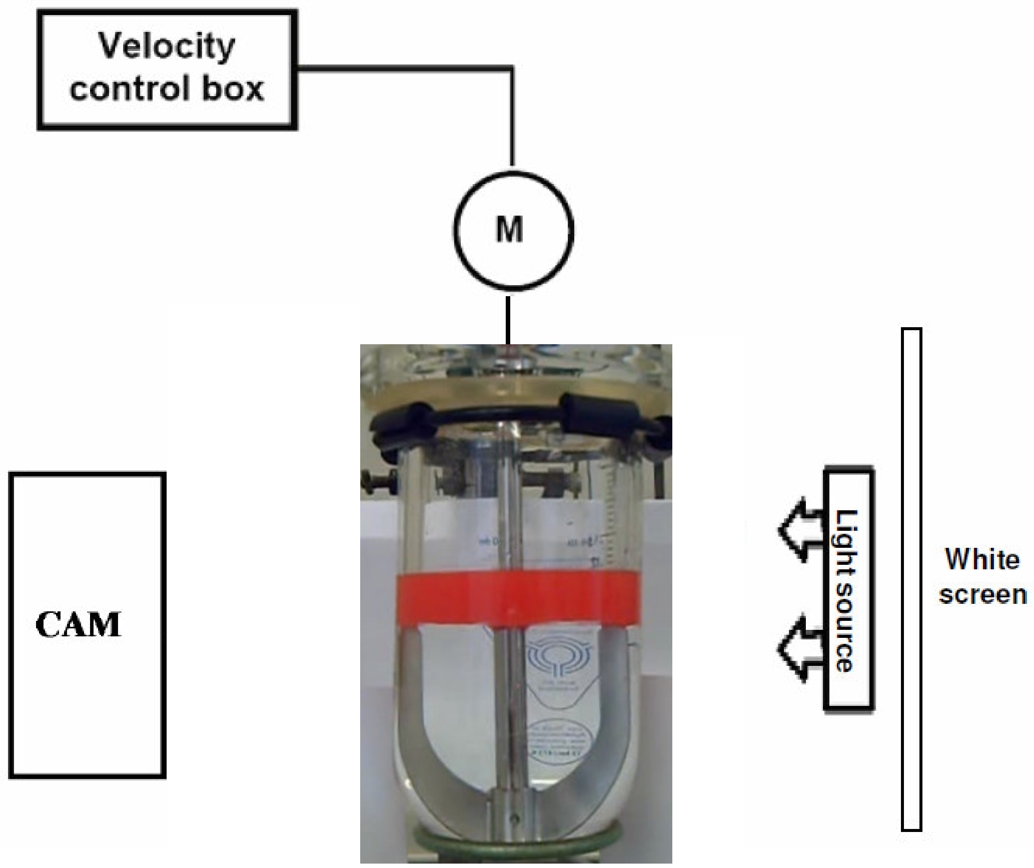

Figure 3.5: The experimental setup for the visualisation of the dispersion behaviour of cyclohexane/water in a batch stirred vessel with anchor impeller for $H_l = 0.11$ m.

3.3.2 Particle Vision Microscope (PVM)

This method is used to measure the droplet size and shape of cyclohexane. The PVM V819 system in Fig. 3.6 provides real-time and in process images of particle and droplet systems. The PVM technology uses a high resolution CCD (charge-coupled device) camera and internal laser illumination to obtain high quality images. This system consists of V819 probe, which is inserted in the vessel containing the liquid-liquid dispersions at an angle between 30-60°for best image resolution, in the middle between the shaft and the cylindrical wall at a height of about 1.0 cm above the impeller level, to begin the image acquisition at the probe tip which contains six lenses. The probe conduit connects to the electronics unit that contains laser light sources. The unit connects to the computer with an Ethernet CAT 6 cable. PVM software version 8.3 is used to display, save and analyze the captured images. The experimental setup of the PVM V819 system is shown in Fig. 3.7. The lenses at the probe tip (probe window) focus laser illumination on the measurement zone. The probe micrometer is used to adjust the focal plane to get a sharp image. A CCD camera inside the probe acquires the images which are displayed on the computer screen. The probe dimensions and components are shown in Figs. 3.8 and 3.9.

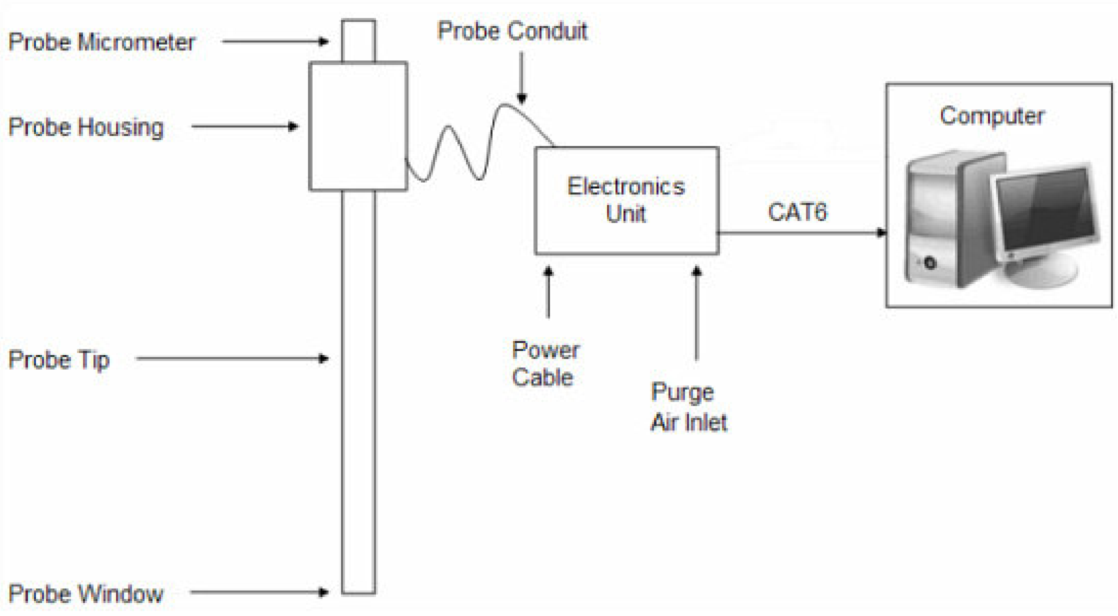

Figure 3.6: PVM V819 system setup.

Figure 3.7: Experimental setup with the PVM V819 system.

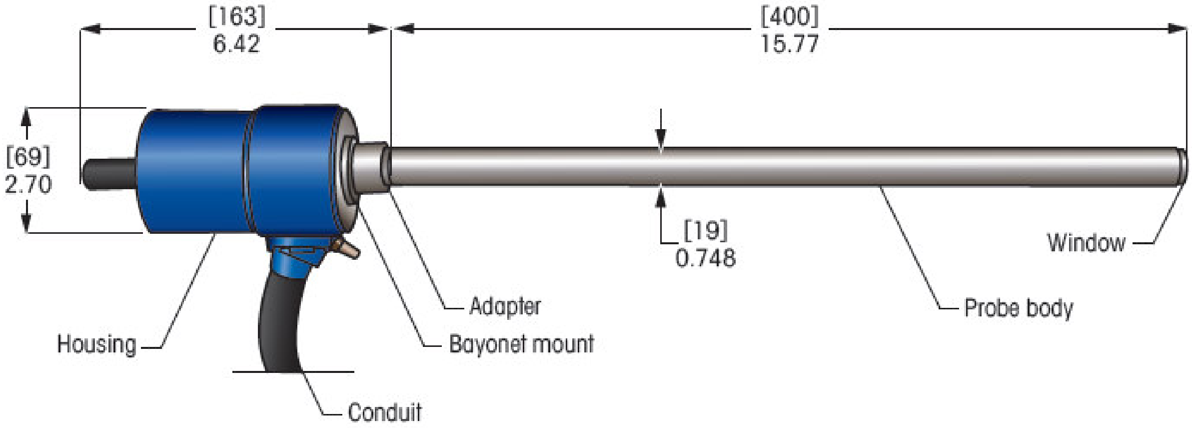

Figure 3.8: PVM V819 Probe dimensions and components.

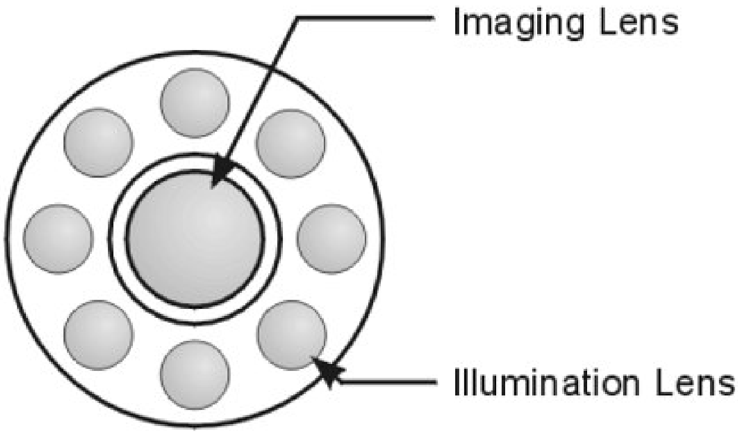

Figure 3.9: Probe window.

3.3.2.1 Image analysis procedure

The dispersion of cyclohexane/water is done under the following operating conditions:

1. Dispersion of 20 vol% cyclohexane/water by using RTI at velocity of 700 rpm and bottom clearance of 3.2 cm and 4.1 cm.
2. Dispersion of 10 vol% cyclohexane/water by using RTI at velocity of 700 rpm and bottom clearance of 3.2 cm.
3. Dispersion of 20 vol% cyclohexane/water by using propeller and PBT impellers at velocity of 700 rpm and bottom clearance of 4.1 cm as well as anchor impeller at a velocity of 350 rpm.

The acquired images for each operating condition are collected after 20 min of agitation to attain the equilibrium conditions and steady state. The dispersions are allowed at the velocity of 700 rpm where a complete and nearly uniform dispersion of the two phases is achieved. So the dispersion below the probe window is well mixed and representative of the droplet populations.

The images are saved by using the PVM software and at least 1000 images are captured. The rate of images acquitting is set to $\Delta t = 0.1$ s (10 images per sec). The size and number of the cyclohexane droplets in the acquired images are measured. By using the mean statistics, it is possible to calculate the Sauter mean diameter from the size and the number of droplets corresponding to this size for each condition (see equation 2.1). The droplet size distribution and the number frequency of the droplet size of cyclohexane are also calculated.

3.3.3 Sampling withdrawal method

This method is used for measuring the holdup of the dispersed phase (cyclohexane) with the help of the vacuum pump, to collect different samples of the cyclohexane/water dispersions in the radial and axial distances, and to measure the volume fraction of the dispersed phase (cyclohexane). The experimental setup for measuring the volume fraction of cyclohexane in water in the stirred vessel is shown in Fig 3.10. The sampling apparatus consists of a vertical stainless steel tube, 1 mm internal diameter, placed between the shaft of the stirrer and the cylindrical wall of the vessel. The distance of the sampling point could be varied in the radial direction from the shaft of the stirrer and also in the axial direction from the bottom of the vessel. The sampling tube is connected to triple valve to change the direction of the sampling, one is connected to the reservoir to ensure that the material initially contained in the sampling tube would not be included in the real sample. The second is connected to the collector which is then discharged to the graduated cylinder to measure the volume fraction of cyclohexane. The collector and reservoir are connected to a vacuum system through the valves, and a bottle is used to protect the vacuum system from accidentally receiving some liquid.

3.3.3.1 Measuring procedure for the cyclohexane volume fraction

The stirred vessel is charged with 400 mL (80 vol%) distilled water, as the continuous phase which has the higher density, and 100 mL (20 vol%) of cyclohexane is added slowly to the vessel, forming the top lighter layer which has the lower density. The total height of the liquid phases is 11 cm. A sampling tube made of stainless steel with a diameter of 1.0 mm is fixed in the axial or radial position. The motor is started with the stirring velocity of 350 rpm. After an equilibration period varying between 10 and 15 min is reached, the vacuum pump system is activated. Then the triple valve will be opened to permit the liquid flow from the vessel through the sampling tube into the reservoir to collect a volume of 10 mL. After that this valve is closed and will be opened in a direction to permit the liquid flow from the vessel into the collector to collect a sample of about 10 mL. This sample is discharged into a graduated cylinder and is allowed to separate into two phases to determine the volume fraction of the dispersed phase in the sample. All the liquids will be returned to the vessel to ensure the sampling system delivers the representative samples on holdup. The same procedure is repeated at different radial and axial sampling points and at different stirrer velocities to cover the range from the incipient dispersion to the nearly uniform dispersion. Different stirrers are used and different bottom clearances for RTI of 3.2, 4.1 and 5.5 cm are used in this experimental method.

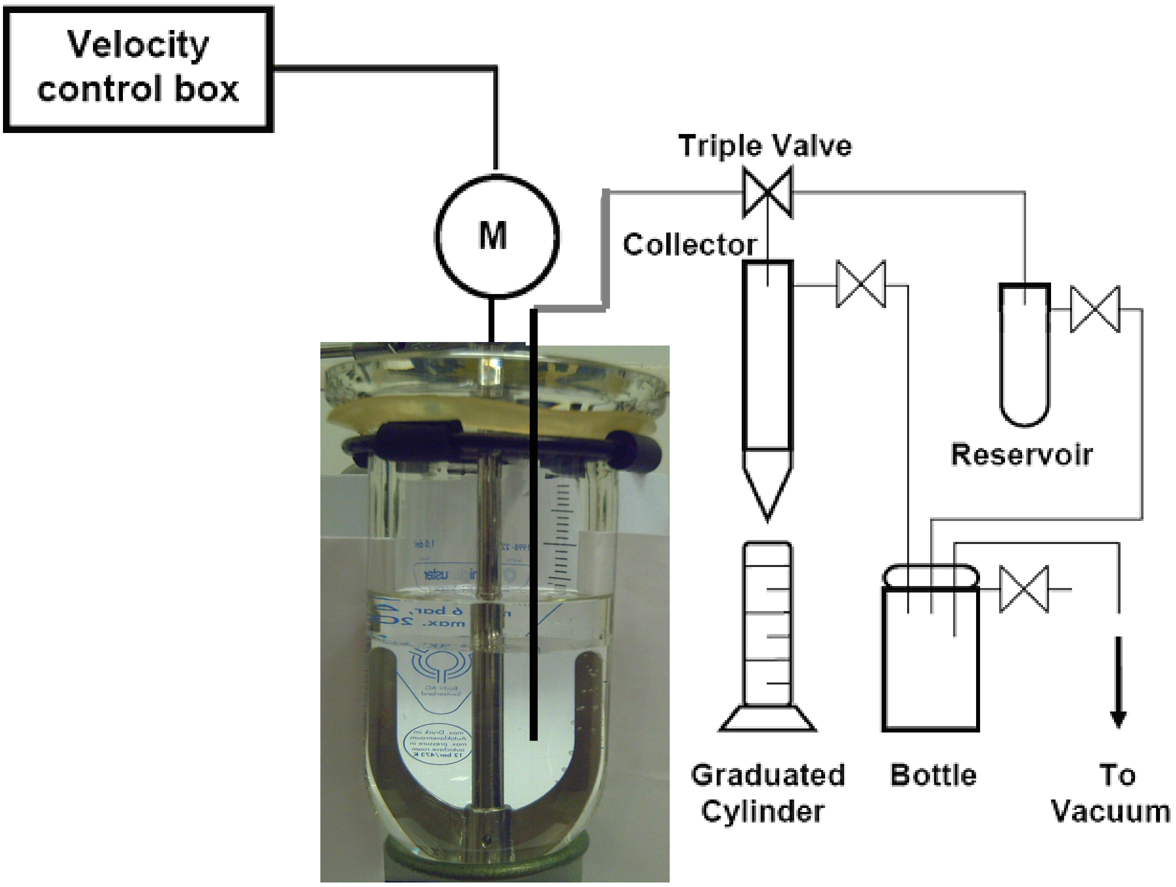

Figure 3.10: Experimental setup for volume fraction measurement with anchor impeller.

3.3.4 Chemical analysis method

This method is used to measure the solute (benzoic acid) concentration in the continuous phase (water) and to calculate mass transfer of benzoic acid from water to the cyclohexane. A saturated aqueous solution of benzoic acid is prepared by dissolving excess mass of benzoic acid of about 21 g in 5 L distilled water. The initial concentration of benzoic acid in water is measured by taking 10 mL sample of benzoic acid/water solution by using pipette tube. One drop of the phenolphthalein indicator is added to the sample to determine the end point. A colourless solution is obtained. A dilute solution of sodium hydroxide is used as titrate for the acid/base titration reaction. It is added slowly to the sample until a pink colour appears (end point). The required volume of sodium hydroxide V_{SH} [mL] to react with all benzoic acid in the sample is determined. The molar concentration of benzoic acid C_{BA} in the sample is calculated based on the fact that, 1 mL of sodium hydroxide reacts with 4.7812 mg of benzoic acid. The mass of the benzoic acid M_{BA} [g] in the sample can be calculated by using Eq. 3.1.

$$M_{BA} = 4.7812 \bullet 10^{-3}\, V_{SH}. \qquad (3.1)$$

The molar concentration of benzoic acid C_{BA} [mol/L] in the sample of V_s = 10 mL can be calculated by using Eq. 3.2.

$$C_{BA} = M_{BA} / (M_w\, V_s \bullet 10^{-3}). \qquad (3.2)$$

Where, M_w = 122.12 g/mol, is the molar mass of benzoic acid.

The stirrer velocity is adjusted to the target one; the vessel is filled with 400 mL (80 vol%) of the benzoic acid/water solution, and 100 mL (20 vol%) of cyclohexane is added slowly near the interface of the aqueous solution. Two layers of the immiscible liquid phases are obtained. The concentrations of the benzoic acid are measured after dispersing cyclohexane in water at different dispersion times between 15 to 3600 s. To measure the equilibrium concentration of benzoic acid, maximum dispersion time of 1 hr is allowed to attain the equilibrium. New liquids should be used for each dispersion time measurement. After reaching the desired dispersion time, a sample of 10 mL benzoic acid/water solution is taken from the bottom of the vessel and titrated with sodium hydroxide as illustrated before. Thus the molar concentration of benzoic acid in the continuous phase is calculated after each dispersion time.

This experiment is repeated for different types of stirrers at different velocities. Stirrer velocity is varied between 150 to 450 rpm in case of anchor impeller, and between 350 to 650 rpm in case of the propeller, RTI and PBT impellers. For each stirrer velocity, different dispersion times are used. The molar concentration of benzoic acid in cyclohexane is calculated from the mass balance on the benzoic acid.

The concentration values of benzoic acid are used to calculate the volumetric mass transfer coefficient and the interfacial area between cyclohexane/water-benzoic acid solution phases (see section 2.5.3).

3.3.5 Photographic – light-cut method

The velocity and flow fields of the liquid in a batch stirred vessel can be tracked by using solid tracer particles with the help of a light and CCD camera. Tracer particles of Redoxharz II with size of 90 µm are mixed with distilled water to track the flow field generated in the vessel by using propeller and RTI at stirrer velocity varies from 400 rpm to 800 rpm. The radial and axial movement of particles is investigated by using photographic images and MathCAD software. The digital camera takes pictures with a shutter speed of (1 / 30) second. The particles can be seen as points in the images. The travelled distances by the particles in a certain time and the flow velocities of particles are determined. The velocity of the particles can be calculated from the travelled distance divided by the shutter speed. The images show the distribution of particles in the vessel. Thus the photographic method allows the detection of the flow fields and to calculate the velocity of particles in the vessel.

3.3.5.1 Schematic setup

The experiments are done in a rounded bottom vessel with a diameter of 0.12 m filled with distilled water to a level of 0.185 m, 4 baffles made of stainless steel with a width of 0.012 m (1 / 10 of the inside diameter of the vessel) are used to eliminate the air vortex around the shaft of the stirrer. The vessel is placed in a container filled with water to get a better light cut. A lamp at a distance of 0.230 m from the vessel is used to produce the light. A black cover is used to get a narrow beam of light. A CCD camera (Canon EOS 20D) is used to visualize the flow field of the particles. The propeller and RTI are used for this experiment. The experimental setup is shown in Fig. 3.11.

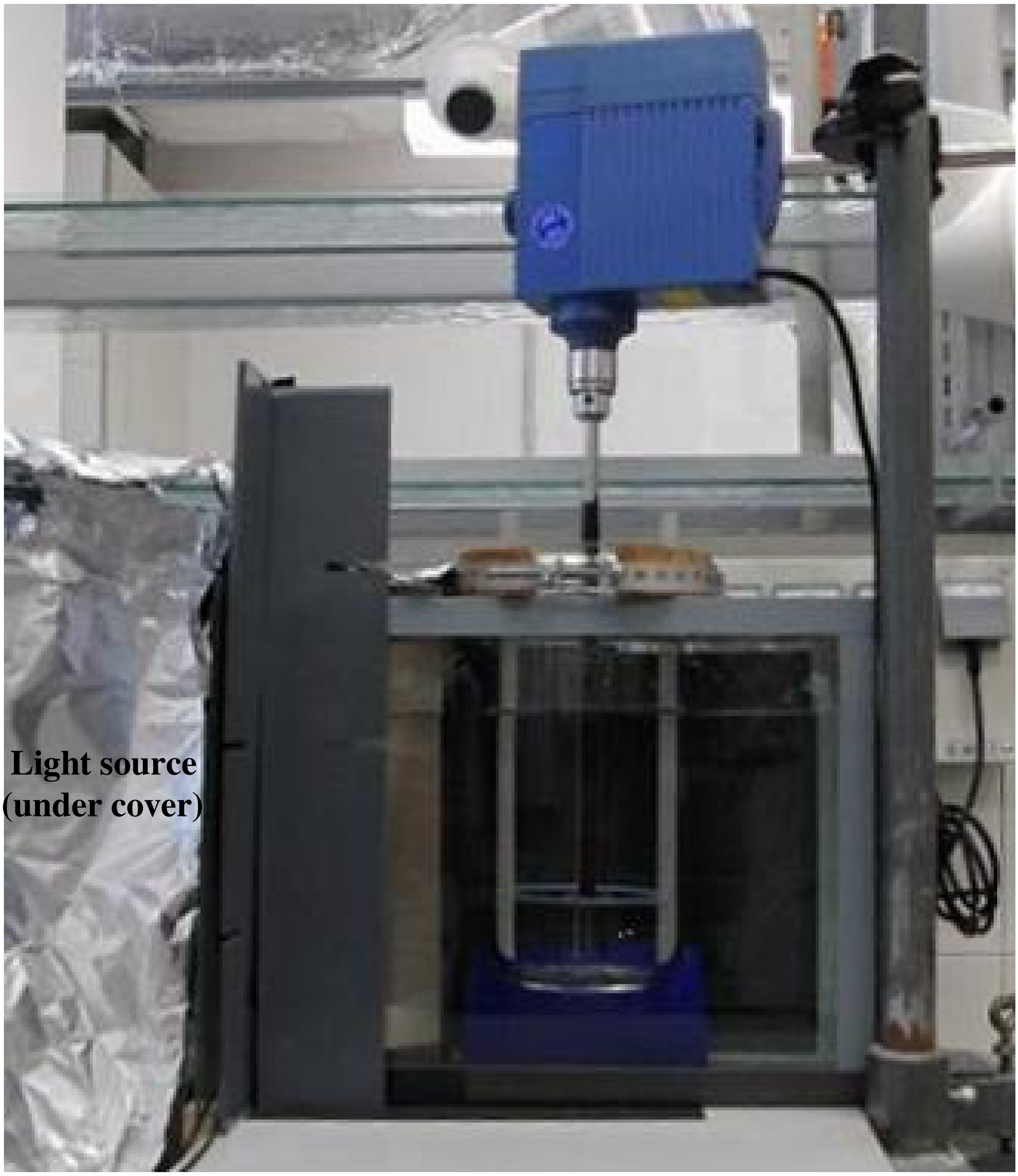

Figure 3.11: Experimental setup of the light cut method.

3.3.5.2 Measuring procedure of the tracer particles

The vessel is filled with distilled water. The propeller or RTI is installed in the middle of the vessel. The velocity of the stirrer should be slowly increased until the desired number of revolutions is obtained. The light source should be installed behind the stirred vessel. A small gap of about 1 mm in width is built between the illuminating lamp and the vessel to create a visual thin lighted wall in the vessel which is called light-cut. The light beam must be perpendicular through the centre of vessel. The light source (HJR 400/140-6985) in this experiment is about 0.23 m from the vessel. Through this illumination it is possible to see the flow field and the moved particles. Finally Redoxharz II white spherical particles are added to the water. The stirrer starts to rotate at the desired velocity. The camera is placed on a tripod, approximately 1 m in front of the stirred vessel. The exposure time of 1 / 30 second must be set manually. The measurement starts with a low velocity of 400 rpm after 3-5 minutes of the rotation to ensure that the particles reached the steady state. For each stirrer velocity, three photos are taken. The procedure is then repeated with the second stirrer at different velocities. All photographs are stored and transferred to the computer for further processing.

3.3.5.3 Analysis procedure for tracer particles velocity

Analysis of the captured images by the camera is done by using the Mathcad 14, Paint and Picture Manager Programs. It is possible to measure the distance that travelled by the particles and the direction of the motion. The images are recorded with the resolution of 3504 x 2336 pixels. The position of the particles in terms of pixels in the images is determined by using Mathcad 14. It assigns the luminous dots of the particles on the photographs pixel coordinates x, y (radial and axial). The start and end points for the motion of a particle can thus be determined, and their values are presented in columns and rows. The distances travelled by the particles through the exposure time of (1 / 30) second are calculated. Euclidean distance equation is used to convert the unit of the distance from pixel to mm. From the number of pixels and the length of one pixel in mm, it is possible to calculate the distance between two coordinates in mm. The velocity of each particle in (mm/s) can be calculated then by dividing the distance in mm over the exposure time of (1 / 30) second.

4. CFD SIMULATION AND SUBMODELS

This work presents a detailed CFD approach to predict the dispersion behaviour of cyclohexane/water in stirred vessel with anchor and rushton turbine impellers. The numerical simulations are done by using ANSYS CFX-11 and ICEM CFD tools. Eulerian-Eulerian two fluid inhomogeneous multiphase models are employed. The gas phase (air) is involved in the simulations; the interaction between the gas/liquid phases is modelled by using the free surface model. The two equations turbulence k-ε model and other interphase momentum exchange models are used. The droplets of dispersed cyclohexane are treated as rigid sphere with a constant diameter. The effect of breakup and coalescence is ignored in this work. The simulation is aimed to predict the axial and radial volume fraction profiles of the dispersed phase, the density and holdup distribution of cyclohexane, the velocity flow fields, the axial and radial velocity profiles of cyclohexane/water and the interfacial area density between the two phases. These predictions are compared with the experimental measurements to validate the computational procedure. Half geometry stirred vessel with anchor impeller is used in the simulation to reduce the required time for numerical calculations. A full geometry stirred vessel with RTI is used to predict the real velocity flow field and eddies which are formed around the six bladed RTI.

4.1 Geometry and mesh generation

Rounded bottom cylindrical vessel equipped with anchor and rushton turbine impellers are generated in three dimensions. ANSYS ICEM CFD 5.1 is used to create 3D stirred vessel with the same dimensions as those used in the experiment as can be seen in Figs. 3.2 and 3.3. Unstructured tetrahedral cells are used for the created complex geometries. The meshing limitations are to optimize the time for numerical simulation and to get precise and accurate results. The total numbers of the unstructured tetrahedral cells for the stirred vessel with anchor impeller and RTI are 200586 and 1474979, respectively as shown in Fig. 4.1. The cell size for the stirred vessel with anchor and RTI are 0.003 m and 0.0005 m, respectively. Fine mesh with smaller cell size is required for a good matching between the RTI and the vessel, because the diameter and size of the RTI is small compared to that of the anchor impeller.

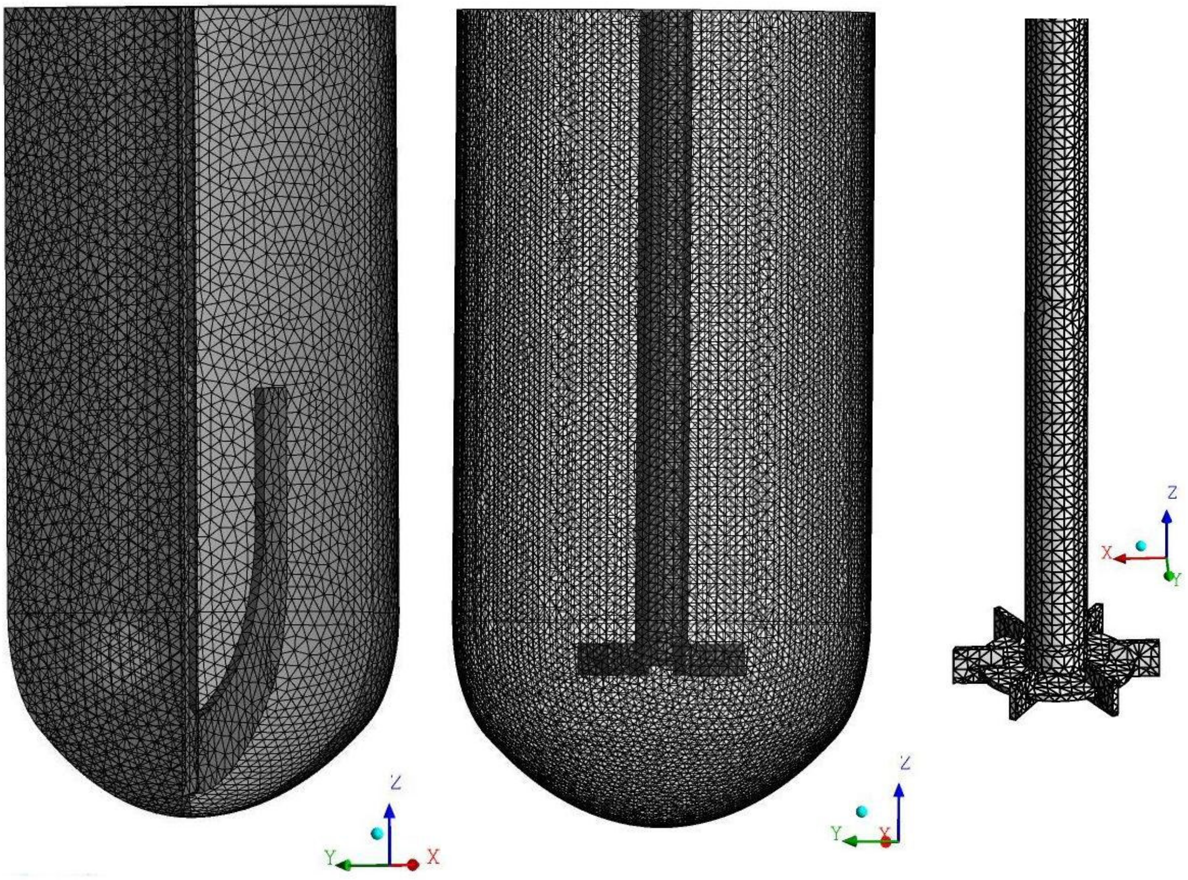

(a) (b) (c)

Figure 4.1: The grid of unstructured tetrahedral cell for the stirred vessel with (a) anchor impeller (b) RTI and (c) Six bladed RTI.

The effect of grid size is studied, for that a computational grid with cell size of 0.004 m is generated for the stirred vessel with RTI as can be seen in Fig. 4.2. The total number of unstructured tetrahedral cells is 167642.

For modelling the accurate interaction between the RTI and the vessel, it is important to create a rotating impeller region including the six blades RTI, and a stationary vessel region including the shaft and vessel walls. New interfaces are created between the stationary and rotating regions as shown in Fig. 4.3. The unstructured tetrahedral grids on both regions are generated with cell size of 0.001 m. Both grids coincide with each other on the surfaces at the interface only with generation of a very fine grid. The cells number for the rotating RTI part is 320352, whereas the cells number for the stationary part is 1009763. The total number of tetrahedrons for both parts is 1330115.

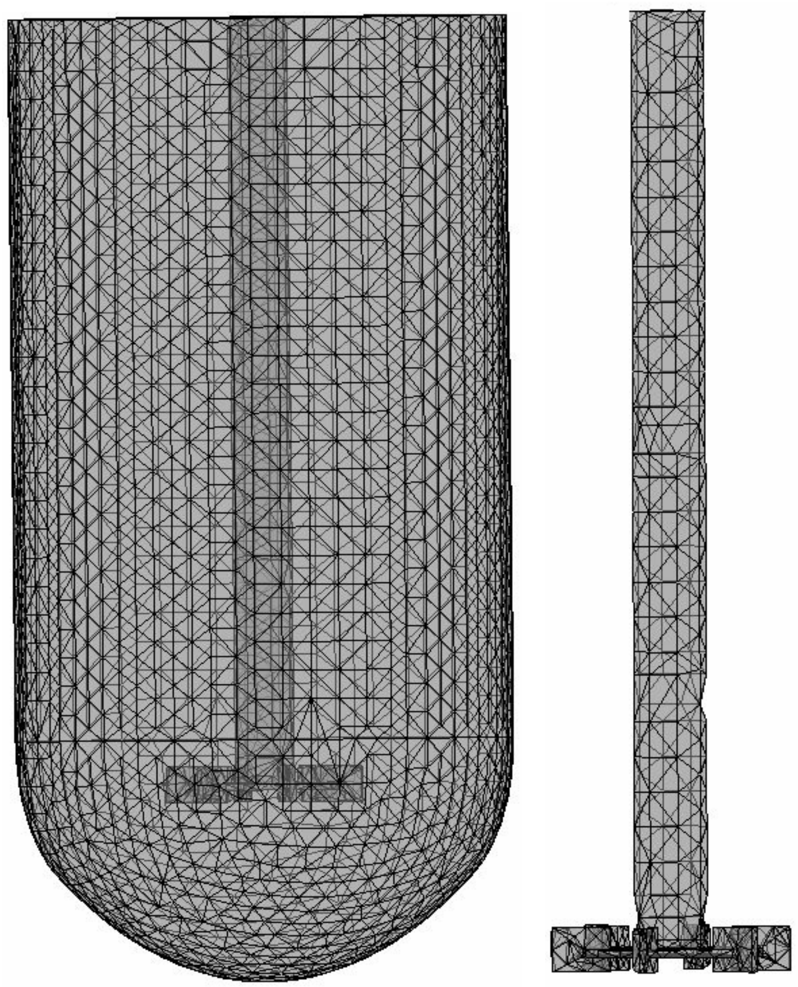

Figure 4.2: The grid of unstructured tetrahedral cell for the stirred vessel with RTI for cell size of 0.004 m.

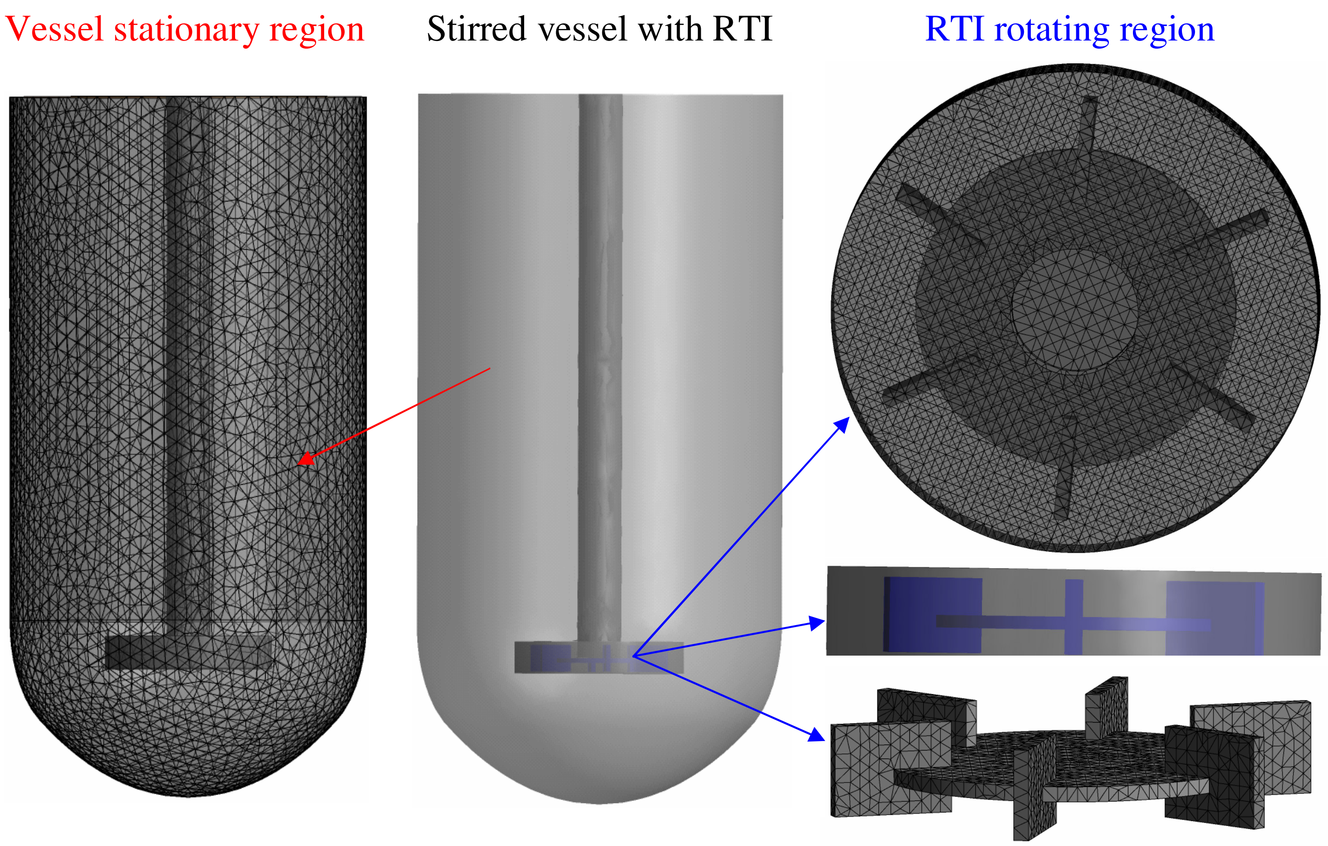

Figure 4.3: The grid of the stationary vessel (left) and rotating RTI (right) regions for the full geometry vessel (mid).

4.2 Type of simulation

Steady and transient 3D simulations are used to calculate the dynamic mixing behaviour with space and/or time, respectively by using finite volume method. For accurate and precise results, 10000 iterations are used for steady simulations. Time step of 0.01 s is used for transient simulations. Steady simulations are used because the experimental measurements are taken when the system reaches the steady state. The flow patterns around the impeller is calculated in this case by using the rotating reference frame, see section 2.12.2. Transient simulations are used to see the variation of the flow patterns with time which is calculated by using sliding mesh method as can be seen in sections 2.12.1 and 4.3.3.3.

4.3 Multiphase cyclohexane/water flow modelling

The two cyclohexane/water phases are mixed on a macroscopic scale, with a separate interface between them. Eulerian multiphase approach assumes the both phases coexist at every point in space in the form of interpenetrating continua with interaction [25][41]. It is used to calculate the velocity and pressure fields. The pressure field is assumed to be the same for both phases. This multiphase flow problem is complex because it includes fluid interfaces. It is assumed no mass or energy transfer between the two phases. The used models in the simulations will be described in the following sections.

4.3.1 Inhomogeneous model

The inhomogeneous model is used when the interface is not well defined because one phase is entrained in the other. The disadvantage of this model is that it requires large time and memory for numerical simulation [121][122]. With the interfluid transfer multiphase flow, separate velocity fields and other relevant fields are calculated for each phase. The pressure constraint assumes that the pressure field is shared by all phases [123][124][125]. In the inhomogeneous multiphase model, there is one solution field for each separate phase. Transported quantities for cyclohexane/water interact via interphase transfer terms which are calculated by using the inhomogeneous hydrodynamic equations [126][127][118]:

Continuity equation

$$\frac{\partial}{\partial t}\left(r_\alpha \rho_\alpha\right) + \nabla\left(r_\alpha \rho_\alpha U_\alpha\right) = S_{MS\alpha} + \sum_{\beta=1}^{N_P} \Gamma_{\alpha\beta} \,. \qquad (4\text{-}1)$$

There are no mass transfer sources $S_{MS\alpha}$ and there is no interphase mass transfer $\Gamma_{\alpha\beta}$.These terms are neglected.

Momentum equation:

$$\begin{aligned}&\frac{\partial}{\partial t}\left(r_\alpha \rho_\alpha U_\alpha\right)+\nabla\left(r_\alpha\left(\rho_\alpha U_\alpha \otimes U_\alpha\right)\right)\\&=-r_\alpha \nabla p_\alpha+\nabla\left(r_\alpha \mu_\alpha\left(\nabla U_\alpha+\left(U_\alpha\right)^T\right)\right)\\&+\sum_{\beta=1}^{N_P}\left(\Gamma_{\alpha\beta} U_\beta-\Gamma_{\beta\alpha} U_\alpha\right)+S_{MS\alpha}+M_\alpha .\end{aligned} \tag{4-2}$$

Where, M_α represents momentum transfer with other phases.

Volume fraction equation:

$$\sum_{\alpha=1}^{N_P} r_\alpha = 1 \ . \tag{4-3}$$

4.3.2 Free surface flow model

Free surface models refer to flows with a distinct interface between the gas and liquid phase with a large density difference. It is used to study the deformation of the liquid at the interface and to get a sharp interface between air and liquid phases [128]. Volume fractions between the air and the liquid phase can be calculated. The pressure field is assumed to be hydrostatic in the liquid phase and uniform in the air phase [129][130][131]. Interfacial area density $A_{\alpha\beta}$ is used to calculate this interface with equation (4-4) [132][118]. No mass transfer between gas/liquid phases is assumed.

$$A_{\alpha\beta} = \left|\nabla r_\alpha\right| \ . \tag{4-4}$$

The inertia of the gas is usually negligible due to its low density. The only influence of the gas is its pressure acting on the interface. The liquid can thus move freely, and the locations of the free surface can be determined by solving equation (4-4). Simulation of free surface flows requires defining boundary and initial conditions to set up appropriate pressure profile and volume fraction fields. This is done by using special expressions and functions for the pressure gradients to ensure that the flow remain sharp at the interface and using a suitable discretization scheme for the prediction of the phase volume fractions.

4.3.3 Submodels

4.3.3.1 Fluid buoyancy model

The density difference between air and a liquid mixture produces a buoyancy force in multiphase flows. Buoyancy is a natural and mixed convection flows in which gravity is important. Natural convection happens when the fluid is driven only by local density variations. Convection in the multiphase flow occurs when the fluid is driven by both a pressure gradient and buoyancy forces due to variations in the volume fraction of the dispersed phase which results in the density variations.

In the buoyancy calculations, the gravity vector components in x, y and z are set in the Cartesian coordinate. Buoyancy is simulated in this work by using the density difference buoyancy model. A buoyancy reference density as an approximate average value of the expected domain density is specified for the lower density phase. The volumetric buoyancy force F_α is modelled by considering the difference in density between phases with the equation:

$$F_\alpha = \left(\rho_\alpha - \rho_{ref}\right) g . \tag{4-5}$$

The hydrostatic pressure is responsible for driving the flow. It depends on the density of the liquid mixture and buoyancy forces. The drag and buoyancy axial forces act on the gas phase near the free surface. Initial and boundary conditions are defined in terms of this pressure gradient. The hydrostatic pressure is included.

4.3.3.2 Turbulent k-ε model

Turbulence consists of fluctuations in the velocity flow field in time and space. It is a complex process, mainly because it is three dimensional, unsteady and consists of many scales. The velocity fluctuation is affected by the dispersed phase, for that the fluctuating velocity and fluctuating holdup, $r_\alpha u'^{i}_{\alpha}$ appearing in both continuity and momentum conservation equations, that represent the transport of mass and momentum by dispersion. The following correlation is used to estimate the velocity and holdup fluctuations:

$$r_\alpha u'^{i}_{\alpha} = \frac{-\nu_{\alpha\tau}}{\sigma_\tau}\frac{\partial\left(r_\alpha\right)}{\partial x^i} \tag{4-6}$$

Where σ_τ is the turbulent Schmidt number for phase dispersion, which is set to 0.9 in the present work after preliminary numerical trials, $\nu_{\alpha\tau}$ is the turbulent kinematic viscosity of phase α.

These velocity and holdup fluctuations have a significant effect on the characteristics of the flow. Turbulence occurs when the inertia forces in the fluid become significant compared to viscous forces, and is characterized by a high Reynolds Number. Three dimensional turbulent two phase liquid/liquid flow is simulated by solving the Reynolds averaged Navier Stockes equations of two phases formulated by the two fluid Eulerian-Eulerian model. There are different turbulent models like shear stress turbulent SST and large eddy simulation LES. The turbulence effect is formulated in this work by using k-ε model by adding an extra source term generated from the presence of the dispersed phase in the turbulent kinetic energy transport equation of the continuous phase. The k-ε model is recommended for mixing processes by many authors and researchers, because it gives a good agreement between the measured and predicted values of the velocity profiles.

The k - ε model assumes that the turbulence viscosity μ_t in linked to the turbulence kinetic energy and dissipation via the relation:

$$\mu_t = C_\mu \rho \frac{k^2}{\varepsilon}. \tag{4-7}$$

Where C_μ = 0.09. The turbulence velocity scale is computed from the turbulent kinetic energy k which is provided from the solution of its differential transport equation 4.8. The dissipation rate of the turbulent kinetic energy ε is provided from the solution of its transport equation 4.9.

$$\frac{\partial(\rho k)}{\partial t} + \nabla(\rho U k) = \nabla\left[\left(\mu + \frac{\mu_t}{\sigma_k}\right)\nabla k\right] + P_k - \rho\varepsilon. \tag{4-8}$$

$$\frac{\partial(\rho\varepsilon)}{\partial t} + \nabla(\rho U \varepsilon) = \nabla\left[\left(\mu + \frac{\mu_t}{\sigma_\varepsilon}\right)\nabla \varepsilon\right] + \frac{\varepsilon}{k}\left(C_{g1}P_k - C_{g2}\rho\varepsilon\right). \tag{4-9}$$

Where ∇ is nabla operator for partial differentiation in x, y and z directions, $C_{\varepsilon 1}$= 1.44, $C_{\varepsilon 2}$= 1.92, σ_k= 1 and σ_ε= 1.3. P_k is the turbulence production due to viscous and buoyancy forces, which is modelled by using:

$$P_k = \mu_t \nabla U\left(\nabla U + U^{\mathrm{T}}\right) - \frac{2}{3}\nabla U\left(3\mu_t \nabla U + \rho k\right) + P_{kb}. \tag{4-10}$$

The production term is due to the dispersed phase, it depends on the drag force between the two phases which depends on the velocity difference between the two phases. For full buoyancy model, the buoyancy production term P_{kb} is modelled by:

$$P_{kb} = \frac{\mu_t}{\rho\sigma_\rho} g \nabla\rho. \tag{4-11}$$

The buoyancy turbulence is assumed to be due to the production and dissipation, for that the buoyancy dissipation $P_{\varepsilon b}$ is modelled in the ε equation by:

$$P_{\varepsilon b} = C_3 \max(0, P_{kb}). \tag{4-12}$$

Where $C_3 = 1$ and $\sigma_\rho = 1$.

4.3.3.3 Sliding mesh model

To apply this method, it is important to create two domains, one is for the rotating impeller and the second is for the stationary vessel that including the vessel walls. The same models and conditions should be applied to the both domains. During the solution, the grid surrounding the rotating components physically moves. The velocity of the impeller and shaft relative to the moving mesh region is zero. The motion of the impeller is realistically modeled, because the grid surrounding the impeller moves as well as accurate simulation of the impeller-wall interaction as shown in Fig. 4.3. The relative movement of the rotating impeller to the static vessel is considered through the inner-outer iterative algorithm. The set of conservation equations is solved in an iterative process until convergence is reached. The grid moves again, and convergence is once again obtained from an iterative calculation. During each of these quasi-steady calculations, information (the calculated variables) is passed through the interfaces from the rotating to the stationary regions and back again. In order to rotate one mesh relative to another, the boundary between the meshes needs to be a surface of revolution. The grid on this boundary must have two surfaces. One remains with the rotating mesh region, and the other remains with the stationary mesh region. When information is passed between the rotating and stationary grid regions, interpolation is required to match each cell with its neighbors across the interface [115][9].

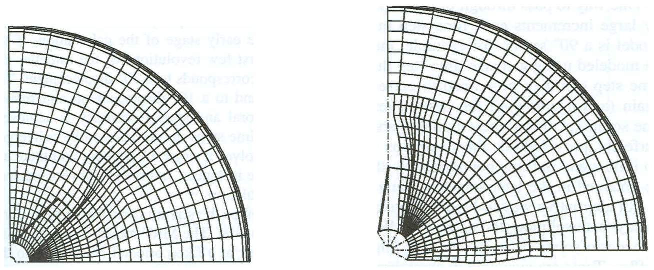

Figure 4.3: Sliding mesh in two orientations shown in 2D.

4.3.3.4 Interphase momentum transfer models

These models are used to calculate the most important interphase transfer terms. The interphase momentum transfer between the two phases $M_{\alpha\beta}$ is calculated from the interfacial area between the two phases by using the particle model, and from the interphase drag force that depends on the drag coefficient by using Ishii-Zuber model in case of the anchor impeller and the algebraic slip model ASM in case of the RTI.

4.3.3.4.1 Interphase transfer Particle model

This model is inhomogeneous multiphase model used to calculate the interphase transfer terms. It can model the interfacial area density. It can be used when one of the phases is continuous (phase α) and the other is dispersed (phase β). It is suitable for modeling the dispersion of liquid droplets in immiscible liquids. The surface area per unit volume is then calculated by assuming that phase β is present as spherical particles of mean diameter d_β. The interphase contact area $A_{\alpha\beta}$ is calculated by:

$$A_{\alpha\beta} = \frac{6\, r_\beta}{d_\beta}. \tag{4-13}$$

4.3.3.4.2 Interphase drag force model

It is the most important transfer interphase term which can be defined as the force exerted on an immersed body (dispersed phase) by a moving fluid (continuous phase). The interphase drag arises from two mechanisms:

1. Skin friction which is due to the viscous surface shear stress.
2. Drag which is due to the pressure distribution around the immersed body (dispersed phase).

The forces between the phases are equal and opposite, see equation 4-14. The total interfacial force between the two phases arises from different independent physical effects: drag forces $\mathrm{M}_{\alpha\beta}^{D}$ and non drag forces like the lift forces $\mathrm{M}_{\alpha\beta}^{L}$, wall lubrication force $\mathrm{M}_{\alpha\beta}^{LUB}$, mass force $\mathrm{M}_{\alpha\beta}^{VM}$ and turbulent disperse force $\mathrm{M}_{\alpha\beta}^{TD}$ as can be seen in equation 4-15.

$$\mathrm{M}_{\alpha\beta} = -\mathrm{M}_{\alpha\beta}. \tag{4-14}$$

$$\mathrm{M}_{\alpha\beta} = \mathrm{M}_{\alpha\beta}^{D} + \mathrm{M}_{\alpha\beta}^{L} + \mathrm{M}_{\alpha\beta}^{LUB} + \mathrm{M}_{\alpha\beta}^{VM} + \mathrm{M}_{\alpha\beta}^{TD} + \ldots.. \tag{4-15}$$

Mainly the interphase exchange term is due to the drag forces. The other non drag forces are neglected because they have negligible effect compared to the drag force; this is verified by Wang et al. [12], Gosman et al. [41] and Khopkar et al. [133].

The total drag force is expressed in terms of the dimensionless drag coefficient C_{D}. For the dispersed droplets, the interphase drag can be calculated by using Ishii-Zuber drag model which needs to define the buoyant and the surface tension coefficient between cyclohexane/water which is equal to 0.05 N/m, and the ASM which uses the closed relationship for the slip velocity in the drag force balance.

4.3.3.4.2.1 Ishii-Zuber drag model

The interphase drag force $\mathrm{D}_{\alpha\beta}$ acting on the continuous phase α due to the dispersed phase β is calculated by using the following equation:

$$\mathrm{D}_{\alpha\beta} = c_{\alpha\beta}^{(d)} \left(U_\beta - U_\alpha \right). \tag{4-16}$$

Where $c_{\alpha\beta}^{(d)}$ is a coefficient that can be calculated from the dimensionless drag coefficient models. For a particle model, this coefficient is derived as follows:

The drag force exerted by a single droplet on the continuous phase is:

$$\mathrm{D}_p = \frac{1}{2} C_D \rho_\alpha A_p \left| U_\beta - U_\alpha \right| \left(U_\beta - U_\alpha \right). \tag{4-17}$$

The total drag force exerted by a number of droplets on the continuous phase is:

$$\mathrm{D}_{\alpha\beta} = n_p \mathrm{D}_p = \frac{3}{4} \frac{C_D}{d} r_\beta \rho_\alpha \left| U_\beta - U_\alpha \right| \left(U_\beta - U_\alpha \right). \tag{4-18}$$

Where n_p is the number of particles per unit volume, d is the mean diameter.

$$n_p = \frac{r_\beta}{V_p} = \frac{6 r_\beta}{\pi d^3}. \tag{4-19}$$

The volume of single particle V_p is given by:

$$V_p = \frac{\pi d^3}{6}. \tag{4-20}$$

The area of the single particles projected in the flow direction A_p is:

$$A_p = \frac{\pi d^2}{4}. \tag{4-21}$$

By substituting equations (4-19), (4-20) and (4-21) in equation (4-18) and comparing the resultant equation with equation (4-16), the $c_{\alpha\beta}^{(d)}$ will be obtained as:

$$c_{\alpha\beta}^{(d)} = \frac{3}{4}\frac{C_D}{d} r_\beta \rho_\alpha \left| U_\beta - U_\alpha \right|. \tag{4-22}$$

This can be written as:

$$c_{\alpha\beta}^{(d)} = \frac{C_D}{8} A_{\alpha\beta} \rho_\alpha \left| U_\beta - U_\alpha \right|. \tag{4-23}$$

The drag coefficient will be calculated from Ishii-Zuber model. It is used in case of large droplet Reynolds numbers and when the inertial or distorted droplets exist. Thus the surface tension between the phases is important and should be considered in the calculation of the drag coefficient. It is found that the droplets become at first ellipsoidal in shape and finally they become spherical cap shaped. In the distorted particle regime, the drag coefficient is approximately constant, independent on Reynolds number, but dependent on particle shape through the dimensionless group known as Eotvos number (Eo), which measures the ratio between the gravitational and the surface tension forces.

$$\mathrm{Eo} = \frac{\mathrm{g}\Delta\rho \mathrm{d}^2}{\sigma}. \tag{4-24}$$

Where, $\Delta\rho$ is the density difference between the phases, g is the gravitational acceleration and σ is the surface tension coefficient.

For ellipsoidal shaped particles, the drag coefficient is calculated as:

$$C_D(\text{ellipse}) = \frac{2}{3}\text{Eo}^{1/2}. \tag{4-25}$$

For spherical cap shaped particles:

$$C_D(\text{cap}) = \frac{8}{3}(1 - \text{r}_\text{d})^2. \tag{4-26}$$

The droplets are assumed spherical for small Reynolds numbers, and thus the drag coefficient can be calculated as:

$$C_D(\text{sphere}) = \frac{24}{\text{Re}}(1 + 0.15\text{Re}^{0.687}). \tag{4-27}$$

The shape of the particles is taken into account according to the following limitations:

$C_D = C_D$ (sphere). If C_D (sphere) $\geq C_D$ (ellipse)

$C_D = \min$ (C_D (ellipse), C_D (cap)). If C_D (sphere) $< C_D$ (ellipse)

4.3.3.4.2.2 Algebraic slip model

Algebraic slip model (ASM) along with the Eulerian multiphase model is used for two interpenetrating fluids such as cyclohexane/water system. The basic limitation of ASM is its application to two phases and no mass transfer modelling is allowed [134]. A full set of Navier Stokes equations is solved for the primary fluid (continuous phase). An algebraic equation for the slip velocity between the fluids is solved. The slip velocity is derived from the fluid properties and local flow conditions. It is used to compute the velocity of the secondary phase (dispersed phase). The ASM needs to define a variable composition mixture containing the fluids, when setting the thermodynamic state of the mixture. The continuous phase should be set to constraint. Transport equations and algebraic slip components can be combined, that means a mixture of components may be present in the continuous phase. The algebraic slip model is chosen for the dispersed phase. The drag force balance uses the closed relationship for the slip velocity. The dispersion behaviour of cyclohexane/ water is modelled by using the following equations:

(1) *Phase equations*:

Each phase has its own velocity field. The continuity equation for phase α is calculated from equation (4-28) and the momentum equation (4-29).

Continuity mass conservation:

$$\frac{\partial(\rho_\alpha r_\alpha)}{\partial t}+\frac{\partial(\rho_\alpha r_\alpha u^i{}_\alpha)}{\partial x^i}=0. \tag{4-28}$$

Momentum conservation:

$$\rho_\alpha r_\alpha \frac{\partial u^i_\alpha}{\partial t}+\rho_\alpha r_\alpha u^j_\alpha \frac{\partial u^i_\alpha}{\partial x^j}=-r_\alpha \frac{\partial p}{\partial x^i}+\frac{\partial\left(r_\alpha \tau^{ji}_\alpha\right)}{\partial x^j}+r_\alpha \rho_\alpha g^i+M^i_\alpha. \tag{4-29}$$

(2) *Bulk equations*:

A bulk continuity equation is derived by summing equation (4-28) over all phases resulting in equation (4-30). And a bulk momentum equation by summing equation (4-29) over all phases gives equation (4-31).

Bulk continuity equation:

$$\frac{\partial \rho_m}{\partial t}+\frac{\partial(\rho_m u^i_m)}{\partial x^i}=0. \tag{4-30}$$

Where:

$$\rho_m=\sum_\alpha r_\alpha \rho_\alpha \qquad \text{and} \qquad \rho_m u^i_m=\sum_\alpha r_\alpha \rho_\alpha u^i_\alpha .$$

Bulk momentum equation:

$$\frac{\partial\left(\rho_m u_m^i\right)}{\partial t}+\frac{\partial\left(\rho_m u_m^j u_m^i\right)}{\partial x^j}=-\frac{\partial p}{\partial x^i}+\frac{\partial\left(\tau_m^{ji}+\tau_D^{ji}\right)}{\partial x^j}+\rho_m g^i \,. \qquad (4\text{-}31)$$

Where:

$p_\alpha = p$ for all $\alpha = 1,\ldots,N_P$, $\tau_m^{ji} = \sum_\alpha r_\alpha \tau_\alpha^{ji}$ and

$$\tau_D^{ji} = -\sum_\alpha r_\alpha \rho_\alpha \left(u_\alpha^i - u_m^i\right).$$

The effect of τ_D^{ji} in the bulk momentum equation is neglected in this work. Thus the viscous stresses and apparent diffusion stresses are neglected. The momentum equation becomes:

$$\underbrace{\frac{\partial\left(\rho_m u_m^i\right)}{\partial t}}_{\text{Accumulation}}+\underbrace{\frac{\partial\left(\rho_m u_m^j u_m^i\right)}{\partial x^j}}_{\text{Convection}}=\underbrace{-\frac{\partial p}{\partial x^i}}_{\text{Pressure gradient}}+\underbrace{\frac{\partial \tau_m^{ji}}{\partial x^j}}_{\text{Shear stress gradient}}+\underbrace{\rho_m g^i}_{\text{Buoyancy}} \,. \qquad (4\text{-}32)$$

(3) *Drift and slip relations:*

The slip velocity is the phase velocity relative to the continuous phase:

$$u_{S\alpha}^i = u_\alpha^i - u_C^i . \qquad (4\text{-}33)$$

And the drift velocity is the phase velocity relative to the liquid mixture velocity in the bulk as:

$$u_{D\alpha}^i = u_\alpha^i - u_m^i . \qquad (4\text{-}34)$$

The slip and drift velocities are related by the following equation:

$$u_{D\alpha}^i = u_{S\alpha}^i - \sum_\alpha r_\alpha u_{S\alpha}^i . \qquad (4\text{-}35)$$

With these relationships, the phase continuity equation is written in terms of volume fraction and drift velocity as:

$$\frac{\partial(\rho_\alpha r_\alpha)}{\partial t}+\frac{\partial\left(\rho_\alpha r_\alpha\left(u_m^i+u_{D\alpha}^i\right)\right)}{\partial x^i}=0. \tag{4-36}$$

(4) *Derivation of the algebraic slip equation*:

The phase and bulk momentum equations are first transformed to non conservative form by combining them to eliminate the pressure gradient term, yielding:

$$\begin{aligned} M_\alpha^i = r_\alpha&\left(\rho_\alpha\frac{\partial u_{D\alpha}^i}{\partial t}+(\rho_\alpha-\rho_m)\frac{\partial u_m^i}{\partial t}\right)\\ &+r_\alpha\left(\rho_\alpha u_\alpha^j\frac{\partial u_\alpha^i}{\partial x^j}-\rho_m u_m^j\frac{\partial u_m^i}{\partial x^j}\right)\\ &-\frac{\partial\left(r_\alpha\tau_\alpha^{ji}\right)}{\partial x^j}+r_\alpha\frac{\partial\left(\tau_m^{ji}+\tau_D^{ji}\right)}{\partial x^j}\\ &-r_\alpha(\rho_\alpha-\rho_m)g^i. \end{aligned} \tag{4-37}$$

Several assumptions are made:

(1) The dispersed phase is assumed to immediately reach its final velocity, so the transient term on the drift velocity can be neglected.

(2) The approximation is made that:

$$u_\alpha^j\frac{\partial u_\alpha^i}{\partial x^j}\approx u_m^j\frac{\partial u_m^i}{\partial x^j}\ . \tag{4-38}$$

(3) The viscous stresses and apparent diffusion stresses are neglected.

With these approximations, the equation (4-37) simplifies to:

$$M_\alpha^i=r_\alpha(\rho_\alpha-\rho_m)\left(\frac{\partial u_m^i}{\partial t}+u_m^j\frac{\partial u_m^i}{\partial x^j}-g^i\right). \tag{4-39}$$

Also, it is assumed that the interphase momentum transfer is due only to drag forces and the particles are spherical:

$$M_{\alpha}^{i} = -\frac{3}{4}\frac{r_{\alpha}\rho_{i}}{\mathrm{d_P}} C_D \left|u_{S\alpha}\right| u_{S\alpha}^{i} \,. \tag{4-40}$$

Equating equations 4-39 and 4-40 leads to the following closed relationship for the slip velocity:

$$\left|u_{S\alpha}\right| u_{S\alpha}^{i} = -\frac{4}{3}\frac{\mathrm{d}}{\rho_{i}\, C_D}\left(\rho_{\alpha} - \rho_{m}\right)\left(\frac{\partial u_{m}^{i}}{\partial t} + u_{m}^{j}\frac{\partial u_{m}^{i}}{\partial x^{j}} - g^{i}\right). \tag{4-41}$$

Where the subscript *m* refers to bulk quantities, α refers to dispersed phase quantities and ρ_i refers to the density of component. The drag coefficient is a function of the Reynolds number in a laminar flow, but it is found that the drag coefficient is constant for turbulent flow with Reynolds number greater than 1000. The drag coefficient C_D is specified as a constant value of 0.44; the mean droplet diameter d is assumed to be a constant value of 399 μm which is obtained from the measurements with the PVM method as can be seen in chapter 5.2. Models for algebraic slip were introduced by Ishii [135], Manninen and Taivassalo [136] to provide a more general formulation.

In the steady state simulations with ASM, a standard set of the continuity and momentum equations is solved for the whole two phase mixture, treated as a continuum, and additionally the continuity equation for the dispersed phase is included. Depending on the space fraction occupied by the continuous phase or the dispersed phase, the volume fractions can take any value from 0 to 1 range. The model offers computations of the local volume fraction and velocity of the two flowing phases.

(5) *Volume fraction constraint equation*

The flow of a continuous phase (water) is modelled using a constraint equation, its volume fraction is calculated to ensure that all phases volume fractions sum to unity. The CFX-11 solver solves $N_\mathrm{p} - 1$ volume fraction equations for all phases except one. The remaining phase is known as the constraint phase because its volume fraction is determined by the constraint equation:

$$\sum_{\alpha=1}^{N_P} r_\alpha = 1 \ . \tag{4-42}$$

4.4 Domain conditions

4.4.1 General conditions

The domain of the liquid phases with stirred vessel is rotating at a required stirrer velocity between ω = 150 rpm and 400 rpm for anchor and between 350 rpm and 750 rpm for RTI around the z coordinate clockwise. The reference pressure is p_{ref} = 1.013 Pa. A rotating reference frame is used to perform the simulation. The equivalent heights for 400 mL water and 100 mL cyclohexane in the vessel are z = 0.09 m and 0.02 m, respectively. The total liquid height is z = 0.11 m, which corresponds to the total liquid volume of V = 500 mL.

For the multiphase buoyancy model, the density of the light fluid (air) is used as the reference density. This simplifies the definition of pressure gradient, and hence the specification of pressure initial and boundary conditions in the hydrostatic limit:

$$\frac{\partial p}{\partial z} = -(\rho - \rho_{ref})g \ . \tag{4-43}$$

4.4.2 Initial conditions

Cyclohexane is set on the top part of the vessel with 20 vol% of the total liquid volume. The initial conditions for the pressure field and volume fraction at t = 0 are defined by using command expression language (CEL) and the time step functions which describe the free surface shape between the air and the liquid phase. The initial volume fractions of air/liquid phases and cyclohexane/water phases are defined as following:

(1) The initial volume fraction field of air/liquid phases at t = 0 are defined. The volume of water fills the vessel to a height of 0.09 m and the volume of cyclohexane fills the vessel for a height from 0.09 m to 0.11 m above water. The air phase is included in the simulation to study the deformation at the interface between the air and the multifluid liquid phases. An initial volume fraction field is calculated where the volume fraction above the free surface is 1 for air and 0 for the liquid phases and below the free surface is 0 for air and 1 for the liquid phases. Air is set to be above the total liquid height of 0.11 m. CEL step functions are set to define this situation:

$$\mathrm{InitAir} = \mathrm{step}((z - 0.11[m])/1[m]). \tag{4-44}$$

$$\mathrm{InitMix} = \mathrm{step}((0.11[m] - z)/1[m]). \tag{4-45}$$

Where InitAir is the initial volume fraction of the air phase and InitMix is the initial volume fraction of the multifluid liquid phase. The step function is 0 for negative value of this function, 1 for positive value and 0.5 for zero value. The value of this function must be dimensionless. This condition is used for air/liquid phases.

(2) The initial volume fractions of water/cyclohexane in the liquid phase are defined relative to their heights in the vessel. Two distinct layers are formed between the two immiscible liquids. These layers are defined in the program by using the following step functions:

$$\mathrm{InWater} = \mathrm{step}((z/1.0[m] - 0.09). \tag{4-46}$$

$$\mathrm{InTotal} = \mathrm{step}((z/1.0[m] - 0.11). \tag{4-47}$$

$$\mathrm{InCH} = \mathrm{InWater} - \mathrm{InTotal} \tag{4-48}$$

Where InWater is the initial volume fraction of the water and InCH is the initial volume fraction of the cyclohexane in the multifluid liquid phase.

4.4.3 Boundary conditions

4.4.3.1 Wall top

Using an opening boundary condition for the wall top of the domain helps to constrain the flow and improve convergence. As the liquid mixture level increases, air tries to flow through the opening to maintain conservation of mass. The opening allows only the air to flow through but not the liquid phase. This does not influence the flow or mixing process of the immiscible liquid phases, but changes the air flow above the two liquid phases.

4.4.3.2 Bottom and cylindrical walls

The boundary conditions at the bottom and vessel walls are those derived assuming no-slip condition and counter rotating walls (stationary walls).

No-slip means that the velocity of the fluid at the wall boundary is set to zero regarding to Dirichlet condition, so the boundary condition for the velocity becomes:

$$U_{Wall} = 0 \text{ at } \mathrm{r} = \frac{\mathrm{d_V}}{2}. \qquad \Rightarrow \qquad u_x = u_y = u_z = 0$$

Where r is the vessel radius, $\mathrm{d_V}$ is the vessel diameter and $u_{x,y,z}$ is the velocity of the liquid in the coordinate directions x, y and z.

4.4.3.3 Shaft and impeller

No-slip boundary conditions are used at the anchor impeller and the shaft.

$$\text{At } \mathrm{r} = 0 \qquad \Rightarrow \qquad u_x = u_y = 0 \qquad \Rightarrow \qquad \frac{\partial u}{\partial z} = 0$$

4.4.3.4 Periodic interface boundary

For the half geometry it is necessary to define the periodic interface boundary in which B1 = B2, where B is the transport property.

4.4.3.5 General grid interface (GGI)

It is used to make connection between two created grids, to model frame change between domains and to create periodic regions between domains. The rotating domain includes only the RTI as a boundary. The domain motion is set to be rotating clockwise as in the experiment at the required angular velocity. The stationary domain includes the rest parts of the geometry like the vessel cylindrical and bottom walls, wall top and the shaft as shown in Fig. 4.3.

GGI is a physically based intersection algorithm to provide the complete freedom to change the grid topology and physical distribution across the interfaces. A control surface approach is used to perform the connection across a GGI. This connection was done by creation different domain interfaces.

4.4.3.6 Fluid-fluid interfaces

The calculated variables are transferred from the interface of the RTI to the corresponding interface of the vessel. This was done by creating three domain interfaces:

1- Wall top interface.
2- Wall bottom interface.
3- Cylindrical wall interface.

For example, the calculated variables are transferred from the top interface of the stirrer to the top interface of the vessel. The surface fluxes along each side of the interface are discretized in terms of nodal dependent variables, and in terms of control surface equations and variables.

4.4.3.7 Rotor-stator

It is a GGI frame change connection. It is used to calculate the velocity transfer from the rotating domain to the stationary domain. This model is important to account for transient interaction effects at a sliding (frame change) interface. It predicts the true transient interaction of the flow between the stator and rotor passage. The transient relative motion between the components on each side of the GGI connection is simulated. It accounts for all interaction effects between components that are in relative motion to each other. The interface position is updated each timestep, as the relative position of the grids on each side of the interface changes [20].

4.5 Solution algorithm

Transport equations for mass and momentum are formulated for each phase in volume averaged form. These equations with turbulence transport equations are solved by a finite volume method; the discretization of the differential equations is affected by volume integration over each volume by using a staggered arrangement of variables as illustrated in chapters 2.11.1.3 and 2.13.3.

The phase momentum equations are coupled through the shared pressure field and the interphase momentum exchange terms (the drag forces). This coupling is handled by means of the implicit iterative algorithm, which allows the calculation of the mean phase velocities, volume fraction and mean slip velocity. The iteration is completed by solving turbulence quantities of k and ε. The solution is considered converged when the residuals in the solved equations become smaller than the prescribed tolerance. The maximum allowed residual is 0.0001. The minimum number of coefficient loops to get converged results is 7 in transient simulations, whereas 10000 iterations are used for steady simulations.

A pressure equation is derived by combining the density weighted overall continuity equation and the phase momentum equations. The resulting pressure field drives the phase velocities in the direction satisfying continuity. The volume fraction of the continuous phase is obtained by solving its continuity equation, and the volume fraction of the dispersed phase can be calculated from the volume fraction constraint equation. The momentum and turbulent equations are solved by using high resolution advection and 2nd order Eulerian schemes.

5. RESULTS AND DISCUSSION

5.1 Flow field visualisation of cyclohexane /water dispersion

5.1.1 Anchor impeller

The dispersion behaviour of cyclohexane (20 vol%) in water at anchor velocities of 150, 200, 250, 300, 350, 400 and 450 rpm is visualized by a video camera and a red tracer as can be seen in Fig. 5.1-a and b. Two distinct layers are formed at t = 0 when there is no rotation of the stirrer (Fig. 5.1-a). The above red layer is the light cyclohexane phase with lower density, and the lower colourless layer is the heavy water phase. For low anchor velocity of 150 rpm, the nearest layers of cyclohexane to the tip of the anchor impeller is transported by the effect of its shear forces from the walls of the vessel near the tip of the impeller towards the shaft leading to a symmetrically wide vortex around the shaft of the impeller. The interface between the two liquid phases is renewed continuously without any disrupting. The free surface shape between air and liquid phases is flat. The dispersed droplets of cyclohexane start to appear below the interface between the two phases at anchor velocity of 200 rpm (see Fig. 5.1-b). The cyclohexane layer will be broken into small droplets due to the high shear forces near the tip of the anchor impeller. These droplets spread into water in the upper region between the two vertical arms of the anchor impeller. The free surface is still flat at anchor velocity of 200 rpm and the red cyclohexane layer is partially dispersed in the continuous phase.

With further increase of the anchor velocity up to 450 rpm, large eddies are formed and transported with a high velocity from the top near the wall in a conical form toward the bottom of the shaft of the impeller leading to several eddies. The formed drops near the tip of the impeller rotate within the eddy and not break more. The interaction between the cyclohexane eddies and water phase leading to several collisions, breakage and coalescence at the interface, resulting in a surface renewal between the two phases. The axial flow results by the anchor impeller in a low viscosity liquid as found by Al-Qaessi [14][137].

High pressure forces and high interfacial tension between cyclohexane/water of 0.05 N/m as well as eddies make the centrifugal forces dominant, and push the water phase outside towards the walls of the vessel upward. The centrifugal forces effect appears at anchor velocity of 250 rpm and the level of water phase becomes higher than that of cyclohexane. The continuous water phase occupies the place of the dispersed cyclohexane phase in the top at anchor velocity of 400 rpm. The symmetrical vortex around the shaft fills the entire field between the blades of the anchor impeller at a minimum anchor velocity of 400 rpm (Fig. 5.1-b). Thus the level of water near the walls of the vessel increased.

The absence of the radial flow which can be formed by the horizontal arm of the anchor impeller, results in no dispersion of cyclohexane towards the walls of the vessel in the radial direction. Thus cyclohexane is concentrated around the shaft of the impeller. The cyclohexane is completely incorporated in the water phase at a minimum anchor velocity of 350 rpm because the initial thickness of cyclohexane layer has reached zero. With the anchor impeller it is not possible to get a uniform or a homogeneous distribution of cyclohexane in the whole vessel due to the formed cyclohexane eddy inside the larger water eddy.

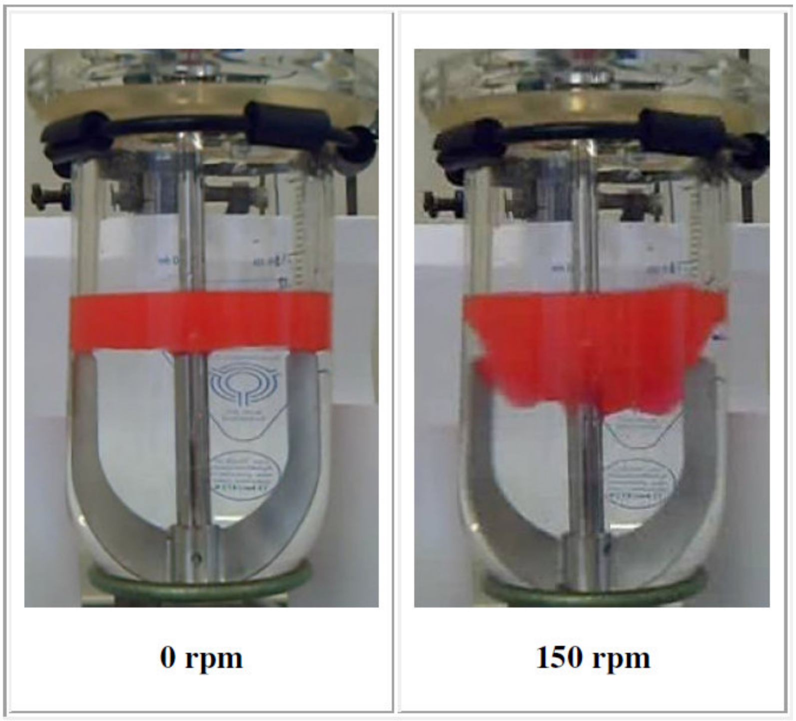
0 rpm

150 rpm

Figure 5.1-a: Dispersion behaviour of cyclohexane/water as a function of anchor velocity of 0 and 150 rpm.

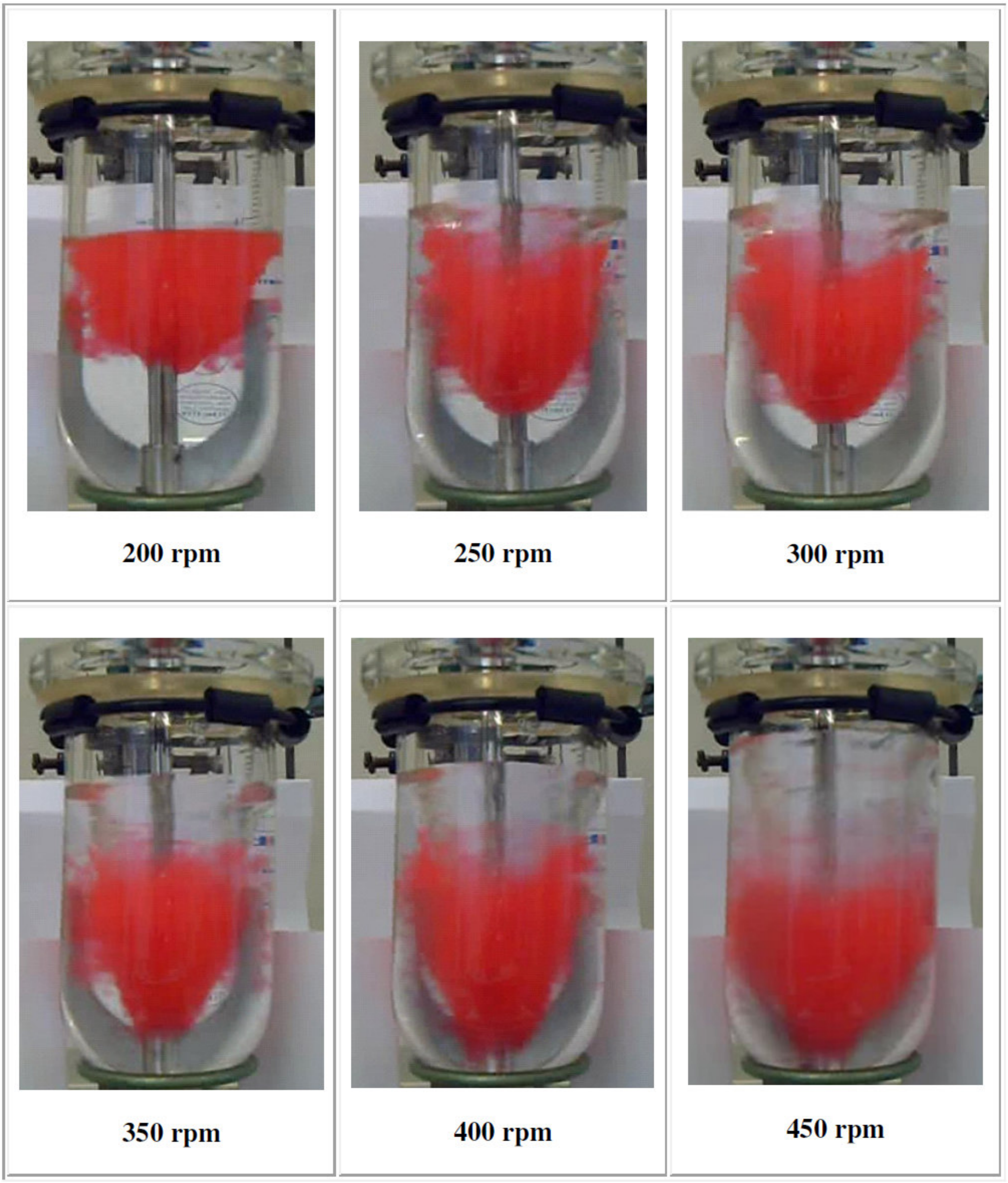

200 rpm

250 rpm

300 rpm

350 rpm

400 rpm

450 rpm

Figure 5.1-b: Dispersion behaviour of cyclohexane/water as a function of anchor velocity from 200 to 450 rpm.

5.1.2 Rushton turbine impeller (RTI)

The flow pattern and dispersion behavior of cyclohexane/water system at different RTI velocities from 150 rpm to 700 rpm and bottom clearances of 3.2 and 4.1 cm is shown in Figs. 5.2-a,b and 5.3-a,b, respectively. RTI is a small impeller gives low discharge radial stream and high turbulence, for that it requires higher velocities than those in case of anchor impeller to achieve the dispersion. The top red layer of cyclohexane starts the dispersion into water phase at a minimum velocity of 200 rpm as can be seen in Fig. 5.2-a at RTI clearance of 3.2 cm. When the RTI velocity increased to 350 rpm, cyclohexane is pulled down from the middle of the lower layer of cyclohexane along the shaft towards the bottom of the shaft, forming a symmetrical vortex around the shaft. A small decease in the thickness of the top red layer of cyclohexane is obtained.

When the cyclohexane layers reach the blades of the RTI at a velocity of 400 rpm (Fig. 5.2- b), they are deformed and broken into small droplets that spread in the radial direction towards the cylindrical walls of the vessel, the large part of these droplets rise upward because they are lighter in density forming the first vortex above the impeller and a small part goes downward forming the second vortex below the RTI impeller as can be seen at the high velocities of 500 and 550 rpm. This occurs due to the large interaction between the liquids and the blade of the impeller as well as the walls of the vessel, leading to higher velocity fluctuation, turbulence and energy dissipation in the region of the RTI. The small vortices above and below the RTI make it easy for drops to deform and breakup due to the large numbers of the recirculation loops that caused by the accumulation of the dispersed phase around the impeller. The thickness of the red cyclohexane layer at the top decrease significantly and starts to disappear at a minimum RTI velocity of 600 rpm where the symmetric vortex is broken.

Further increase of the RTI velocity to 650 rpm improves the homogeneity of the dispersion; most of cyclohexane is dispersed uniformly in the upper side of the vessel above the RTI, and starts the dispersion towards the lower side of the vessel below the RTI. A complete dispersion of cyclohexane with a nearly uniform distribution can be obtained at a minimum RTI velocity of 700 rpm where the red color is distributed uniformly in the whole vessel.

The total level of the liquid phases remains approximately constant, because the droplets of cyclohexane and the formed small eddies will not form high pressure forces on water phase, thus no significant effect of the centrifugal forces appears. This complex flow pattern is important to investigate because of its great effect in case of the mass transfer of a solute between the two phases as can be seen in chapter 5.5.

5.1.2.1 Effect of RTI bottom clearance

The dispersion behaviour of cyclohexane/water with RTI clearances of 4.1 and 3.2 cm is similar as can be seen in Fig. 5.3-a,b. The improvement of the dispersion of the cyclohexane in the upper region above the RTI is faster in case of the RTI clearance of 4.1 cm, due to the smaller distance between the cyclohexane layer at the top and the impeller. This leads to a wider symmetric vortex around the shaft at RTI velocity of 350 and 400 rpm and touch the blades of the impeller faster than that in the case of RTI clearance of 3.2 cm.

Further increase of the RTI velocity above 400 rpm makes the dispersion above the impeller more uniform in case of RTI clearance of 4.1 cm. But the dispersion of cyclohexane in the lower part below the impeller is more uniform in case of the RTI clearance of 3.2 cm at a high velocity of 700 rpm, because of a lower distance between the impeller and the vessel bottom (Figs. 5.2-b and 5.3-b).

The complete dispersion velocity can be obtained at RTI velocity of 600 and 550 rpm with RTI clearances of 3.2 and 4.1 cm, respectively, because the zero thickness of cyclohexane layer is approached faster due to the larger clearance. The minimum velocity to get a uniform dispersion in case of RTI clearance of 4.1 cm should be 750 rpm to improve the homogeneity below the impeller.

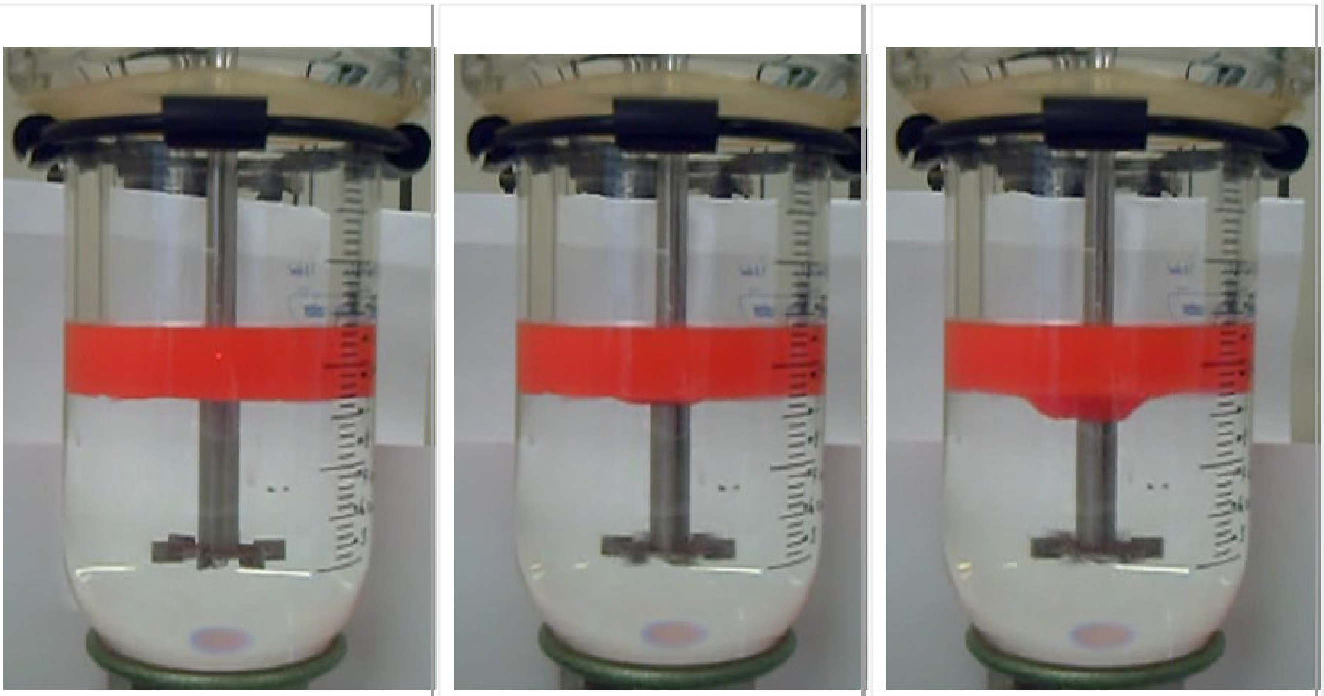

0 rpm **150 rpm** **200 rpm**

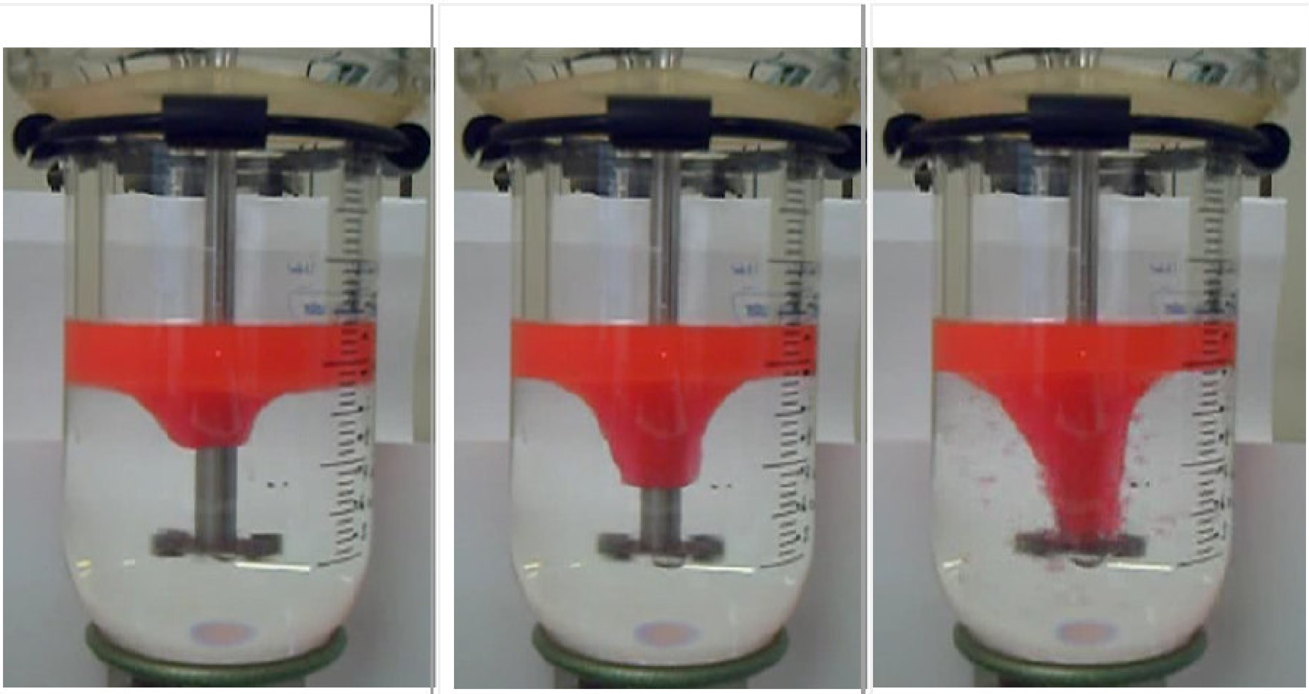

250 rpm **300 rpm** **350 rpm**

Figure 5.2-a: Dispersion behavior of cyclohexane/water as a function of RTI velocity from 0 to 350 rpm at clearance of 3.2 cm.

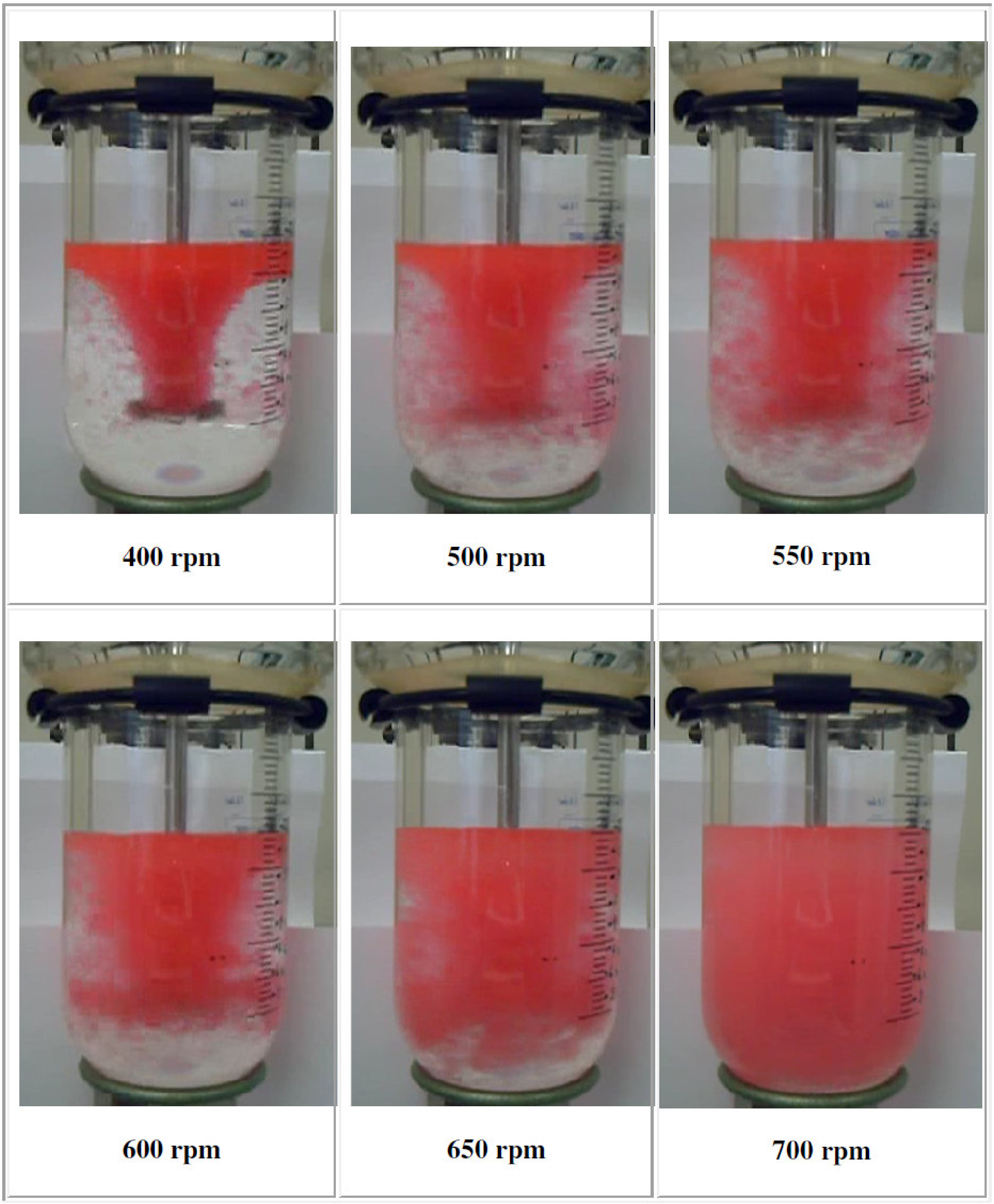

400 rpm

500 rpm

550 rpm

600 rpm

650 rpm

700 rpm

Figure 5.2-b: Dispersion behavior of cyclohexane/water as a function of RTI velocity from 400 to 700 rpm at clearance of 3.2 cm.

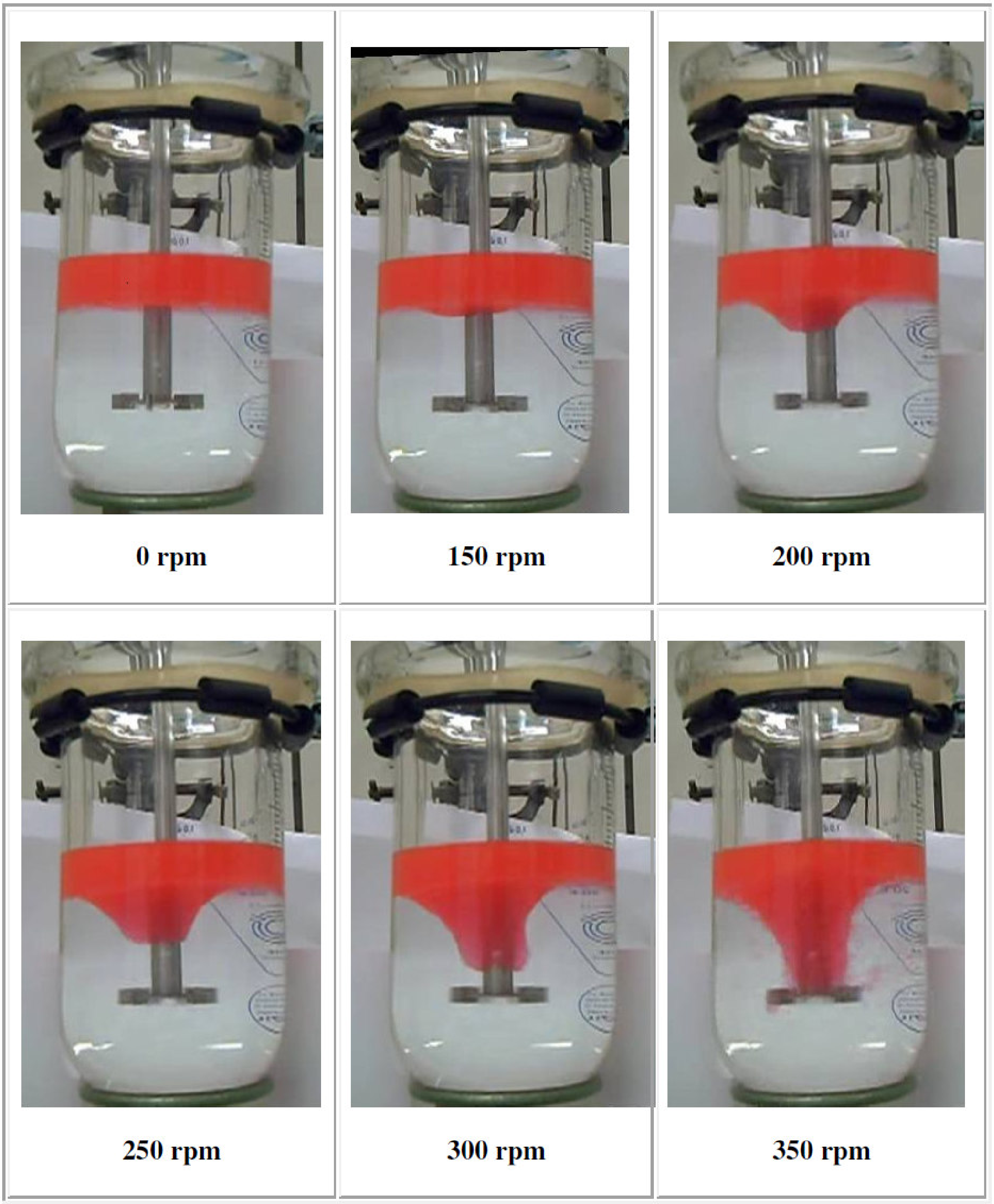

0 rpm 150 rpm 200 rpm

250 rpm 300 rpm 350 rpm

Figure 5.3-a: Dispersion behavior of cyclohexane/water as a function of RTI velocity from 0 to 350 rpm at clearance of 4.1 cm.

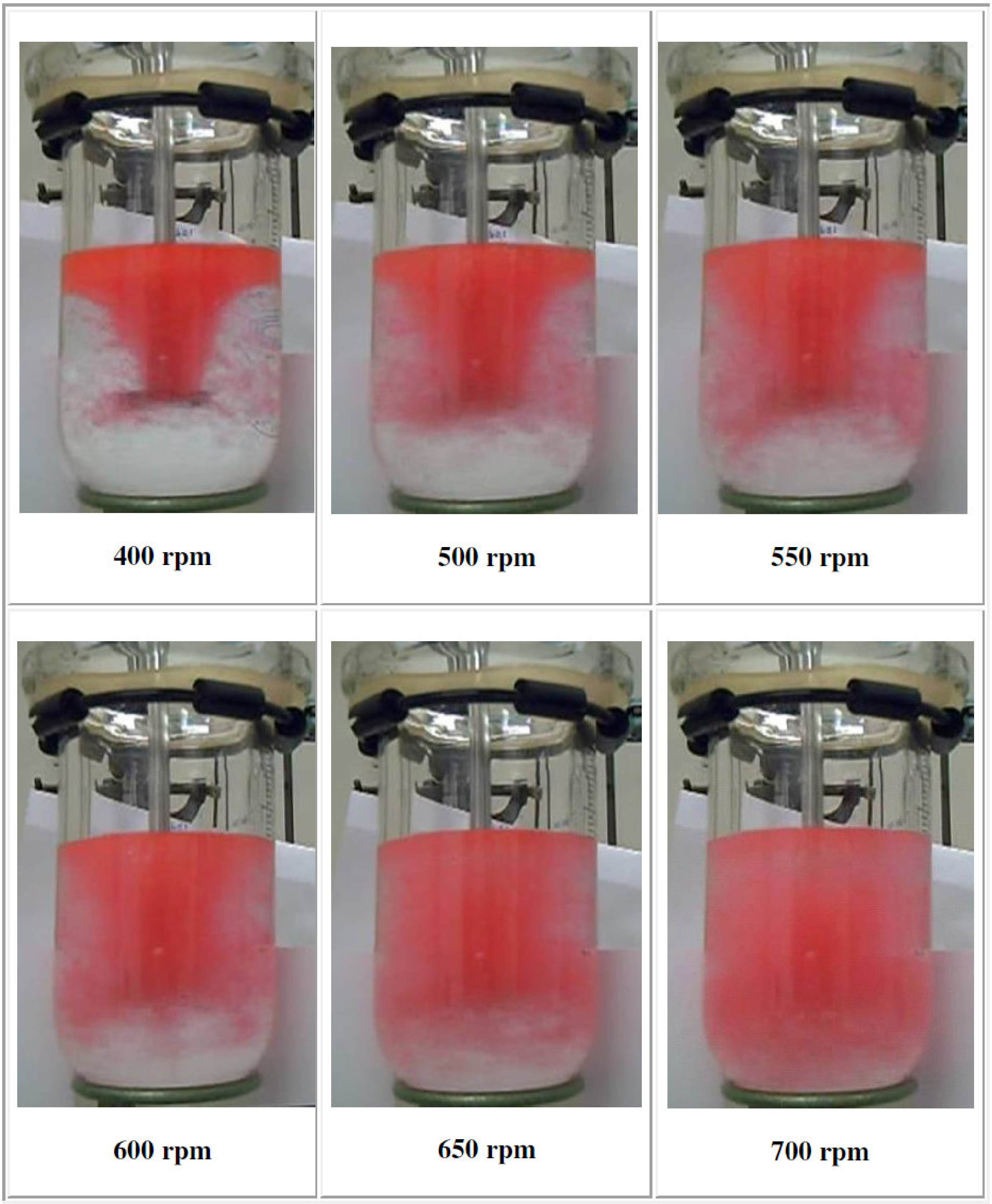

400 rpm

500 rpm

550 rpm

600 rpm

650 rpm

700 rpm

Figure 5.3-b: Dispersion behavior of cyclohexane/water as a function of RTI velocity from 400 to 700 rpm at clearance of 4.1 cm.

5.1.3 Propeller impeller

The dynamic dispersion of cyclohexane/water system at propeller velocities from 150 to 650 rpm and clearance of 4.1 cm can be seen in Figs. 5.4-a and b. The way of the dispersion of cyclohexane in water is similar to that with RTI from the mid of the lower layer of cyclohexane towards the bottom of the propeller shaft forming a symmetrical vortex around the shaft. The volume and size of this vortex is larger, wider and reach to the blades of the propeller at lower velocity of 250 rpm than that obtained with RTI. The droplets are formed at a propeller velocity of 300 rpm and moved towards the upper side of the vessel above the propeller at a velocity of 350 rpm (see Fig. 5.4-a).

The dispersion towards the lower side of the vessel below the impeller starts at propeller velocity of about 450 rpm where a complete dispersion of cyclohexane is found. This can be seen in Fig. 5.4-b where the cyclohexane layer at the top of the vessel approximately disappeared. The quick development of the dispersion below the impeller is found at a velocity of about 550 rpm, whereas the minimum velocity to get a nearly homogeneous distribution is 650 rpm (Fig. 5.4-b). From these observations, propeller impeller gives higher dissipation energy and turbulence than that given by the RTI. For that it needs lower velocity to get a complete dispersion of cyclohexane in the whole vessel. Thus larger numbers with smaller sizes of cyclohexane droplets are expected to be produced by the propeller impeller, which leads to higher interfacial area and thus higher volumetric mass transfer coefficients in case of mass transfer of a solute between the two phases as can be seen in chapter 5.5.

Propeller impeller produces large turbulent axial flow, which leads to withdrawing the cyclohexane layers together as a body towards the shaft of the impeller, and then they spread axially from the impeller to the upper part of the vessel and then back to the lower part of the vessel, results in a complete dispersion of the total volume of cyclohexane in the vessel at a velocity lower than that for the RTI. But it can be seen that the distribution of cyclohexane in the whole vessel may be not uniform, due to the variation of the brightness appearance of the red colour tracer. This can be verified from the holdup distribution of cyclohexane by using sample withdrawal method in chapter 5.3.

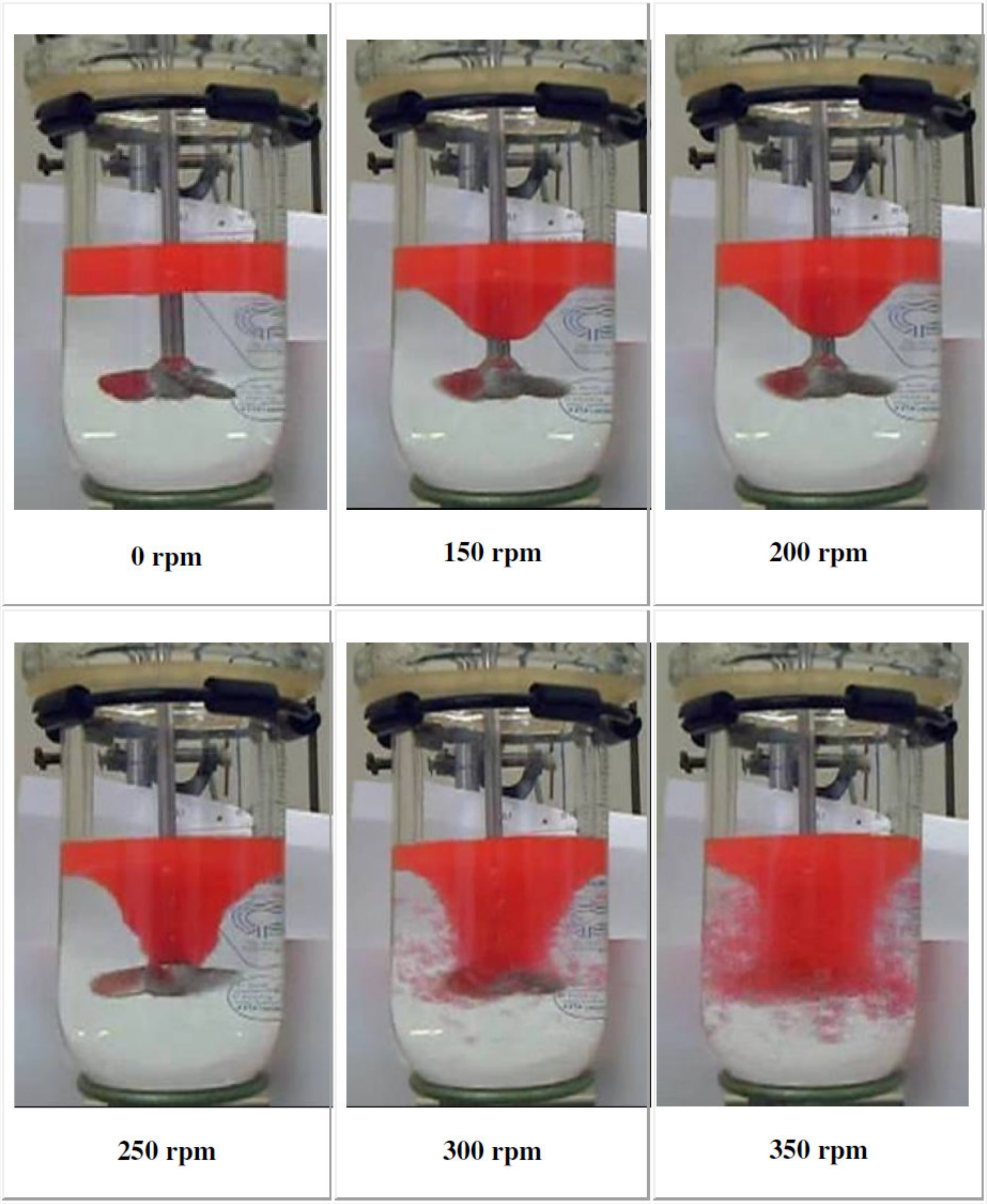

0 rpm

150 rpm

200 rpm

250 rpm

300 rpm

350 rpm

Figure 5.4-a: Dispersion behavior of cyclohexane/water as a function of propeller velocity from 0 to 350 rpm at clearance of 4.1 cm.

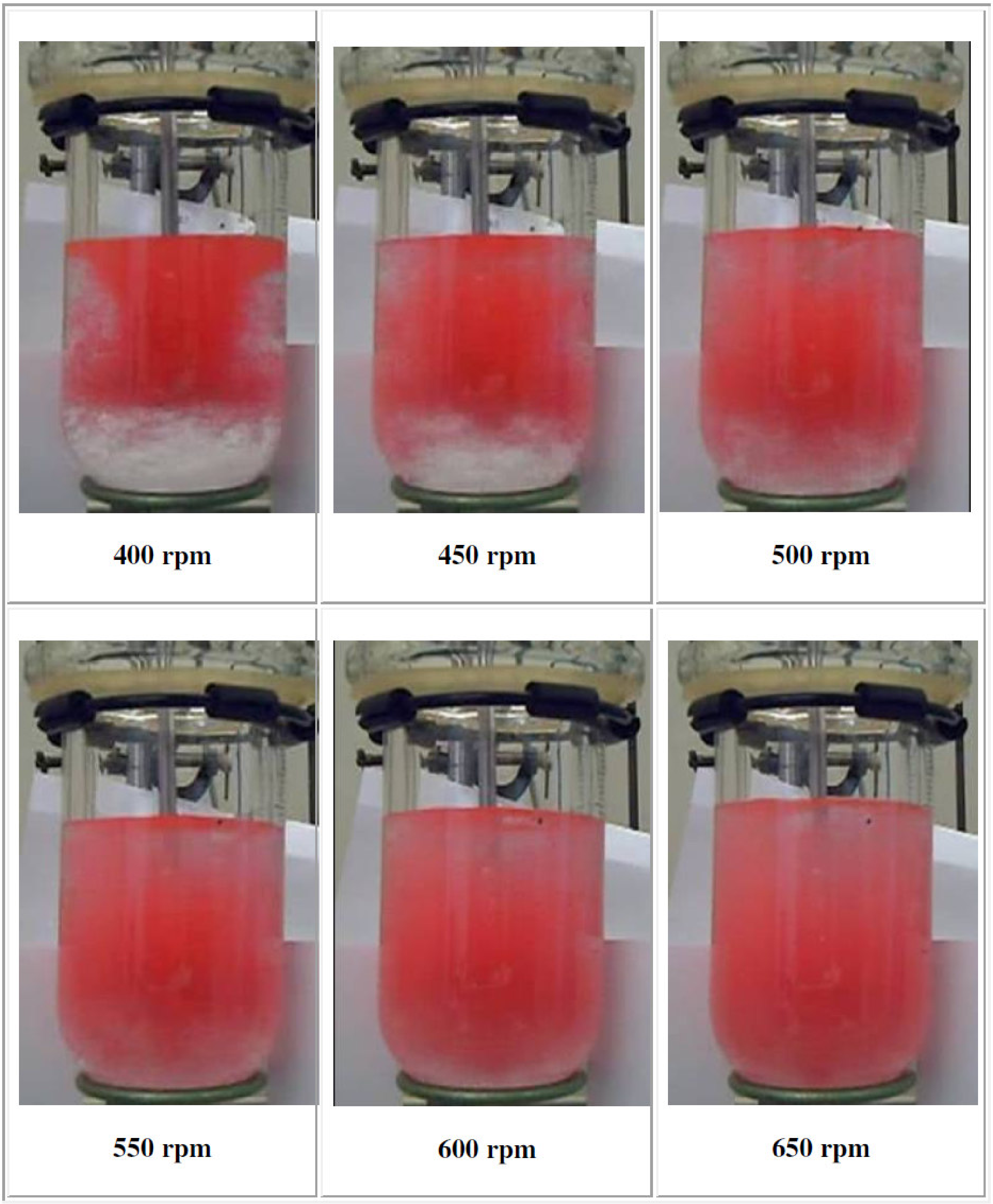

400 rpm

450 rpm

500 rpm

550 rpm

600 rpm

650 rpm

Figure 5.4-b: Dispersion behavior of cyclohexane/water as a function of propeller velocity from 400 to 650 rpm at clearance of 4.1 cm.

5.1.4 Pitched blade turbine impeller (PBT)

The development of the dispersion behavior of cyclohexane/water with increasing the PBT velocity from 150 to 550 rpm, and at bottom clearance of 4.1 cm is closer to that obtained with the RTI more than that obtained by the propeller impeller, regarding to the shape and size of the vortex around the shaft (Fig. 5.5-a and b). The flow pattern produced by PBT is radial combined with axial flow. Cyclohexane red layer is dispersed gradually as a function of PBT velocity in the same way as described in case of RTI, until a uniform distribution is achieved at PBT velocity of 550 rpm.

The vortex reaches the blades of the PBT impeller at a velocity of 350 rpm (Fig. 5.5-a) like that with the RTI. The symmetric vortex is broken at a velocity of 500 rpm, so a complete incorporation of the cyclohexane into water is nearly achieved. At this velocity it can be noticed a dense dispersion is formed above the impeller, and mostly clear water below the impeller is remarked with a small dispersion of cyclohexane starts below the PBT impeller.

A small increase of the PBT impeller velocity from 500 to 550 rpm caused a sudden and fast development of the dispersion as can be seen in Fig. 5.5-b, where a uniform distribution is obtained as can be seen from the colour distribution in the whole vessel, in contrary with that in the case of the propeller impeller where the colour is not uniform.

This phenomenon may be due to the combined axial and radial flow effect which shows different behaviour of cyclohexane dispersion in comparison with the axial propeller and the radial RTI. Thus the PBT impeller requires lower velocity (550 rpm) than that is required by the propeller (650 rpm) and RTI (750 rpm) to get a nearly uniform dispersion of cyclohexane into water.

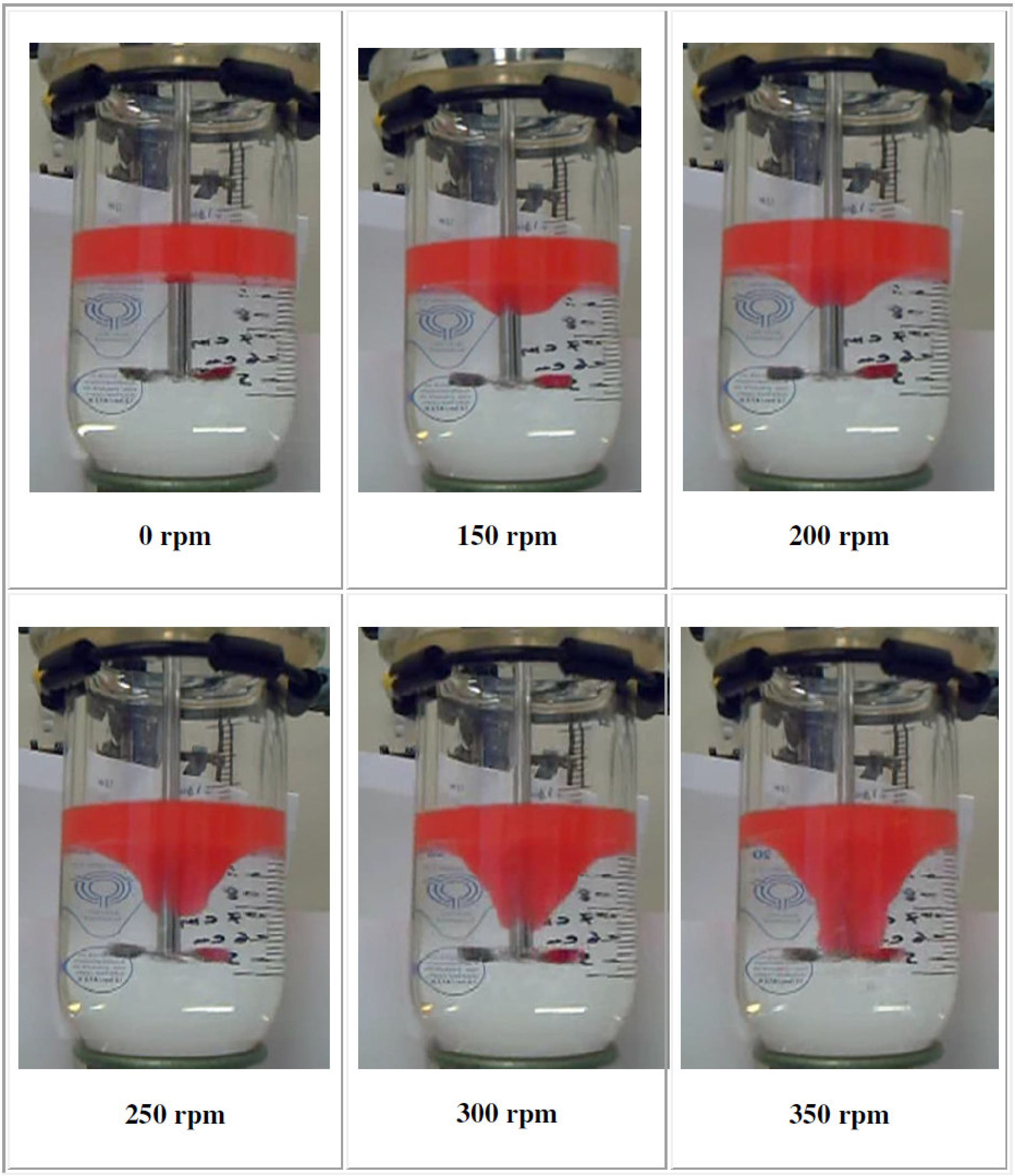

0 rpm

150 rpm

200 rpm

250 rpm

300 rpm

350 rpm

Figure 5.5-a: Dispersion behavior of cyclohexane/water as a function of PBT velocity from 0 to 350 rpm at clearance of 4.1 cm.

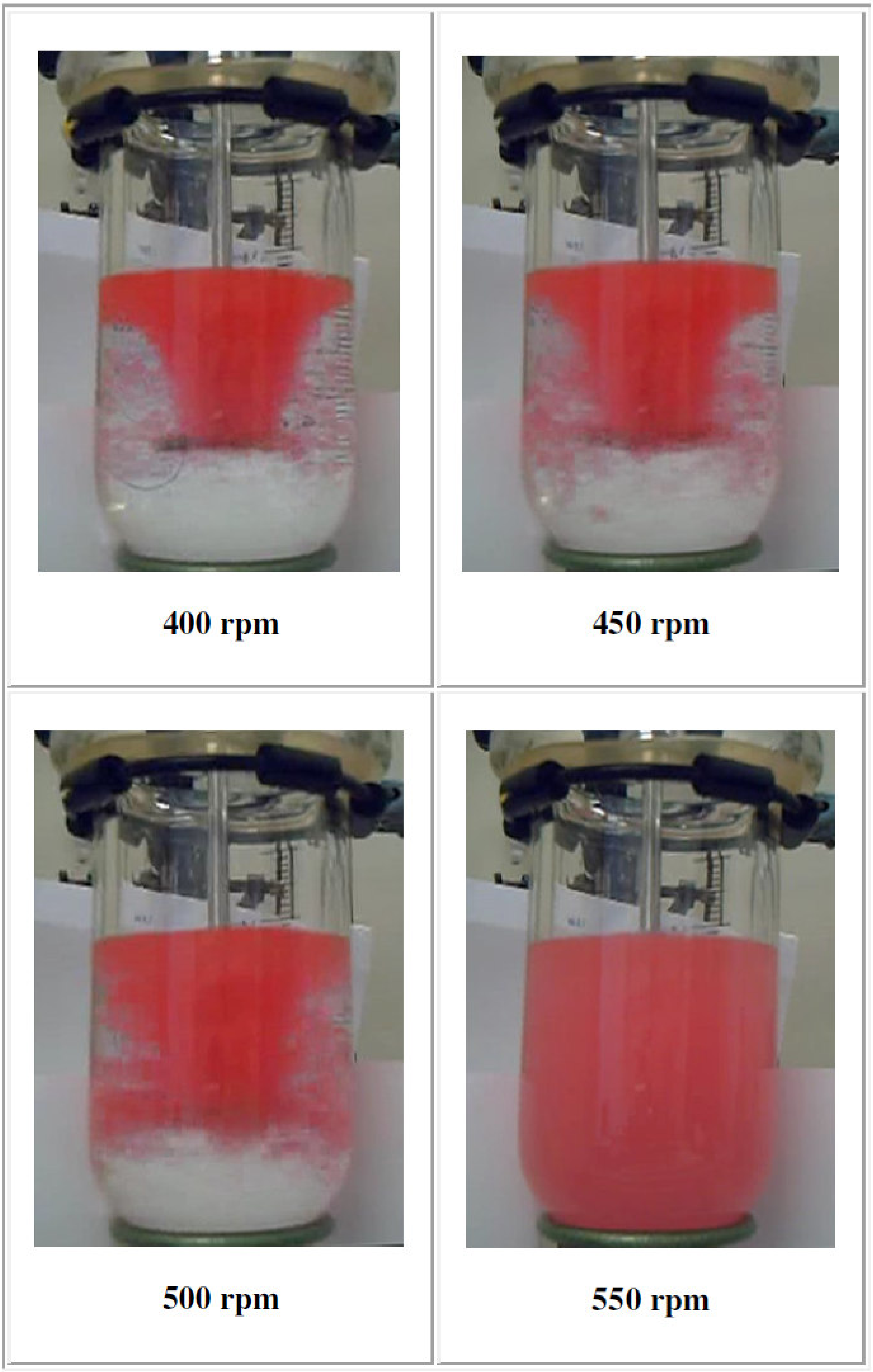

400 rpm

450 rpm

500 rpm

550 rpm

Figure 5.5-b: Dispersion behavior of cyclohexane/water as a function of PBT velocity from 400 to 550 rpm at clearance of 4.1 cm.

5.2 Dispersed droplets – shape and size distribution

The equilibrium droplet size is measured when the rate of coalescence equal the rate of breakup. For that the equilibrium size is measured after allowing the dispersion for 20 minutes. The shape of the cyclohexane dispersed droplets is found to be spherical under the influence of different operating conditions like the RTI impeller clearance, the percentage of the dispersed phase and the stirrer type as shown in Figs. 5.13 to 5.18. Various droplet sizes are found in the dispersions. Sauter mean droplet diameter is calculated from the number of droplets and the corresponding sizes (equation. 2.1). The drop size distribution is fitted by the normal number frequency and the cumulative number distribution for better understanding of the cyclohexane/water dispersions. The size of drops in the stirred vessel is the result of two processes: drop breakup and coalescence. When stirring starts, the bulk of the dispersed phase is pulled down into the continuous phase and is broken into small drops. The rate of drop breakup in this stage is larger than the rate of drop coalescence and it decreases continuously during the stirring process until reaching the steady state, and thus the drop size remains constant [33][32]. Also the rates of drop breakup and coalescence are balanced. Drop breakup and coalescence rates may be different in different zones of the vessel because they depend on the local values of energy production and dissipation that depends on the turbulence intensity. Drop breakup dominates near the impeller where the local rate of energy dissipation is high [3].

5.2.1 Influence of the RTI clearance

The drop size of cyclohexane is measured and analyzed by using the PVM software as described in the chap. 3.3.2. The drop sizes for more than 1000 drops of cyclohexane are measured in the impeller region at RTI velocity of 700 rpm and clearance of 3.2 cm and 4.1 cm as illustrated in Figs. 5.14 (a, b) and 5.15 (a, b), respectively in the left side. The right side of these figures shows the spherical shape of the drops. The coalescence does not appear clearly in the pictures, may be due to the intensive turbulence results in re-dispersion of the possibly coalescent droplets through the recirculations that occurs below and above the RTI. For both clearances of RTI, the sizes of the droplets are analyzed by calculating and drawing the number frequency and the cumulative number as a function of droplet diameter as can be seen in Figs. 5.6 and 5.7. The drop distributions are found to be uni-modal normal distribution. It is characterized by the height and width of the distribution. The number frequency distribution varies as a polynomial function from the fourth degree of the drop diameter for both RTI clearances. It is shifted slightly to the right towards the higher drop sizes in the range between 300-600 µm, with a lager number frequency in case of RTI clearance of 3.2 cm as can be seen in Fig. 5.6. From the histogram, it can be seen that RTI clearance of 4.1 cm gives higher number frequency of small drop sizes in the range between 0-100 and 200-300 µm.

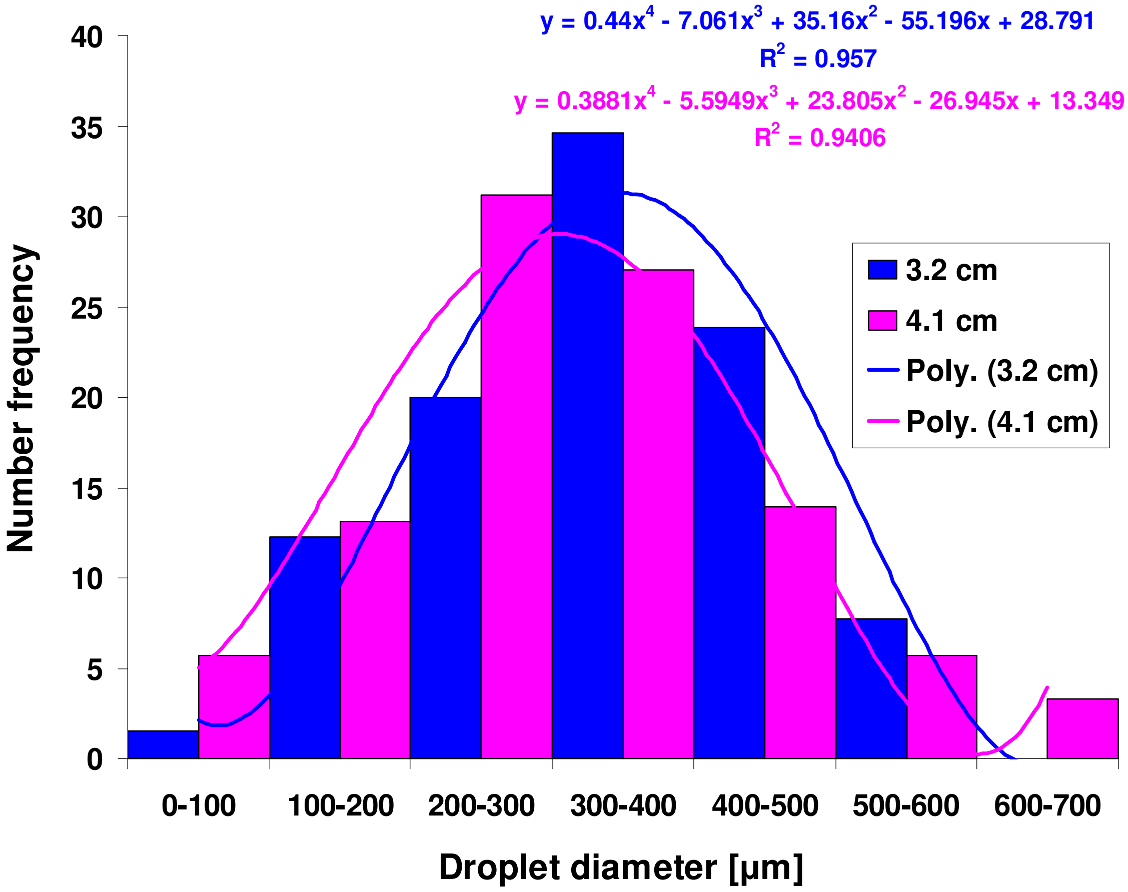

Figure 5.6: Number frequency drop size distribution for RTI velocity of 700 rpm and clearance of 3.2 cm and 4.1 cm.

The calculated Sauter mean droplet diameters of cyclohexane for the dispersions with RTI clearance of 3.2 cm and 4.1 cm are 399 µm and 409 µm, respectively, they are very close. The drop size distribution is more representative than the Sauter mean droplet diameter. The cumulative drop size distribution of cyclohexane is also similar for the dispersions with both RTI clearances with very small differences as shown in Fig. 5.7. That means, the impeller clearance has a slight effect on the mean droplet size and the drop size distribution.

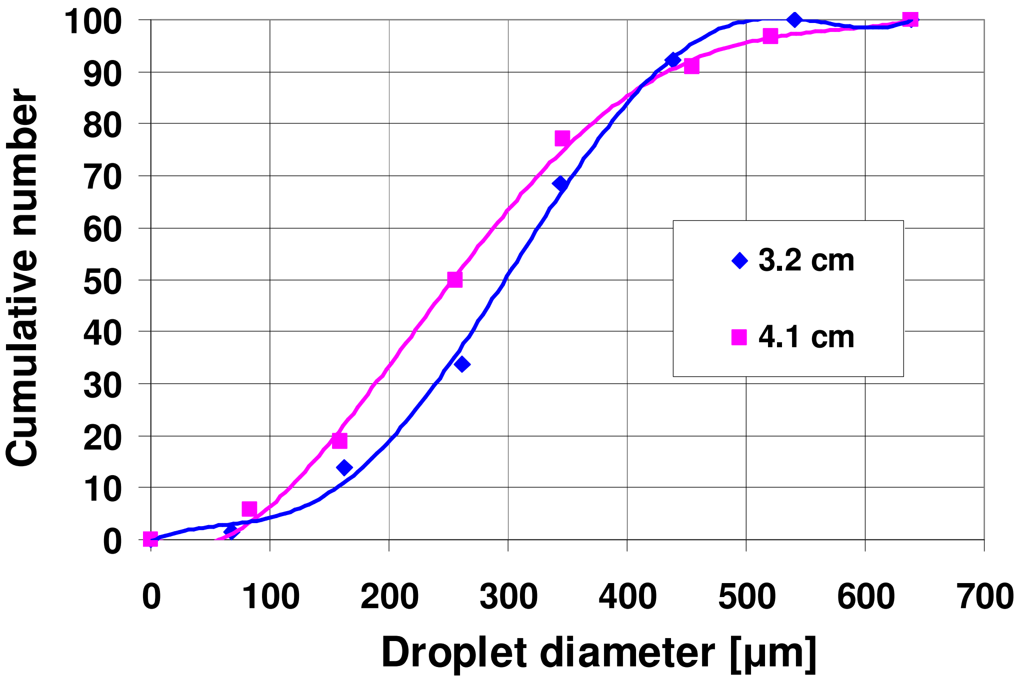

Figure 5.7: Cumulative number drop size distribution for RTI velocity of 700 rpm and clearance of 3.2 cm and 4.1 cm.

5.2.2 Influence of the percentage of the dispersed phase

The volume fraction of the dispersed phase in the continuous phase has a great effect on the mean droplet size and drop size distribution. Uni-modal number frequency drop size distribution can be seen in Fig. 5.8. When the volume fraction of cyclohexane increases from 10 vol% to 20 vol%, the calculated Sauter mean droplet diameter increases from 348 µm to 399 µm, respectively, because the probability of droplet collision followed by subsequent coalescence of droplets increases, and thus the turbulence decreases. The number frequency distribution varies as a polynomial function from the sixth and fourth degree of the drop diameter for 10 vol% and 20 vol% cyclohexane, respectively, and it is clearly shifted to the right towards the higher drop sizes in case of 20 vol% cyclohexane. It can be seen from the histogram in Fig. 5.8 that the number frequency of the droplets with small drop sizes from 0 to 300 μm are higher in case of 10 vol% cyclohexane, whereas the number frequency of the droplets with large drop sizes from 300 to 700 μm are higher in case of 20 vol% cyclohexane. That means, the larger percentage of the dispersed phase gives different behaviour of the droplets during the dispersion process.

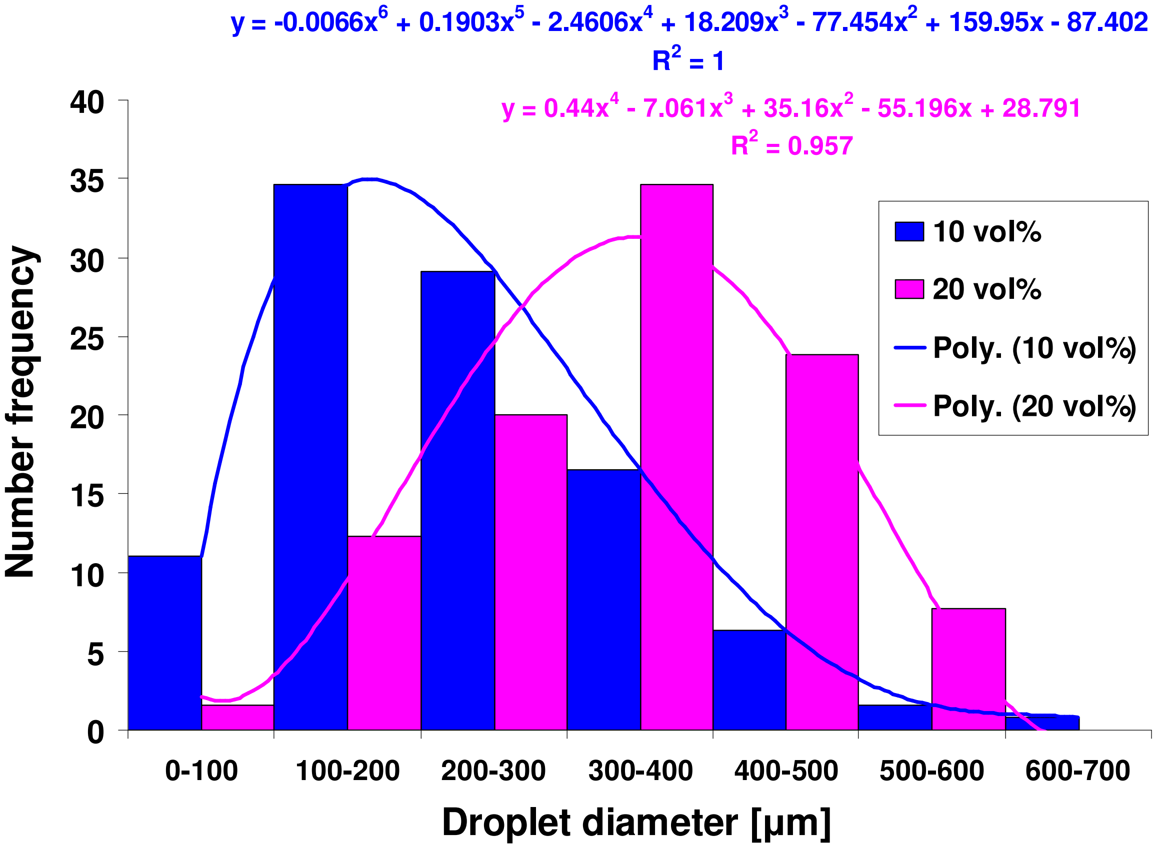

Figure 5.8: Number frequency drop size distribution for 10 vol% and 20 vol% cyclohexane at RTI velocity of 700 rpm and clearance of 4.1 cm.

The cumulative number drop size distribution for 10 vol% cyclohexane is higher than that for 20 vol%, for drop sizes up to 450 μm as can be seen in Fig. 5.9. The maximum cumulative number (100) for 10 vol% and 20 vol% cyclohexane is obtained at drop sizes of 350 and 450 μm, respectively.

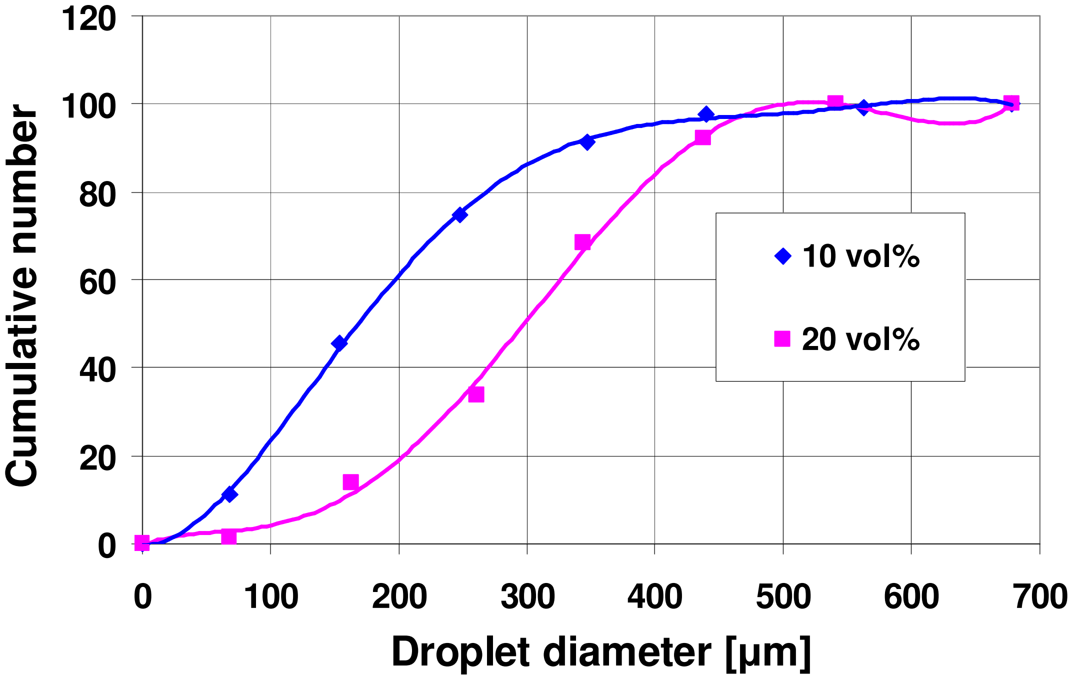

Figure 5.9: Cumulative drop size distribution for 10 vol% and 20 vol% cyclohexane at RTI velocity of 700 rpm and clearance of 4.1 cm.

5.2.3 Influence of the stirrer type

The effect of stirrer type such as anchor, RTI, propeller and PBT on the number frequency drop size distribution is illustrated in Fig. 5. 10. It is found that the propeller and PBT impellers have similar normal uni-modal distribution for drop sizes less than 100 µm and greater than 200 µm, whereas propeller impeller gives higher number frequency for drop sizes between 100-200 µm. This may be due to the higher energy dissipation around the propeller impeller. RTI gives a wider normal drop size distribution shifted to the high drop size region in comparison with the other stirrers. The number frequency obtained by RTI at low drop sizes between 0-200 µm is lower than that obtained by the other stirrers, whereas higher number frequency is obtained for drop sizes between 200-600 µm. That may results from the higher rates of droplets breakup and energy dissipation in case the axial flow propeller and the combined (axial and radial) flow PBT impellers, whereas the radial flow RTI may causes higher rates of collisions and thus coalescence of the droplets, leading to higher droplet size. The number frequency for the anchor impeller which gives mainly axial flow shows a bi-modal drop size distribution: a narrow distribution for drop sizes between 0-300 μm with a higher number frequency than that for propeller, PBT and RTI, and a wide distribution for drop sizes between 300-600 μm with a lower number frequency than that for RTI. This behavior may be due to the fact that the rates of drop breakup and energy dissipation are very high near the tip of the anchor impeller due to the high shear forces there, and thus very small droplet sizes with narrow distribution are formed. These droplets are pulled into the bulk of the liquid and rotate within the large eddy around the shaft and not break more. The accumulation of cyclohexane around the shaft increases the possibility for droplets coalescence, and produces larger droplets. For that a second drop size distribution shifted to the high drop sizes is obtained. The number frequency is a polynomial function of the drop diameter with a power of 6 for anchor impeller, 5 for propeller and PBT impellers and 4 for RTI. The cumulative drop size distribution in Fig. 5.11 shows similar distribution for propeller and PBT with a maximum drop size of about 350 μm, as well as for anchor impeller with two maximum drop sizes of 150 and 450 μm resulted from the bi-modal distribution. The cumulative drop size distribution for RTI is lower than that for the other stirrers with a maximum drop size of about 450 μm.

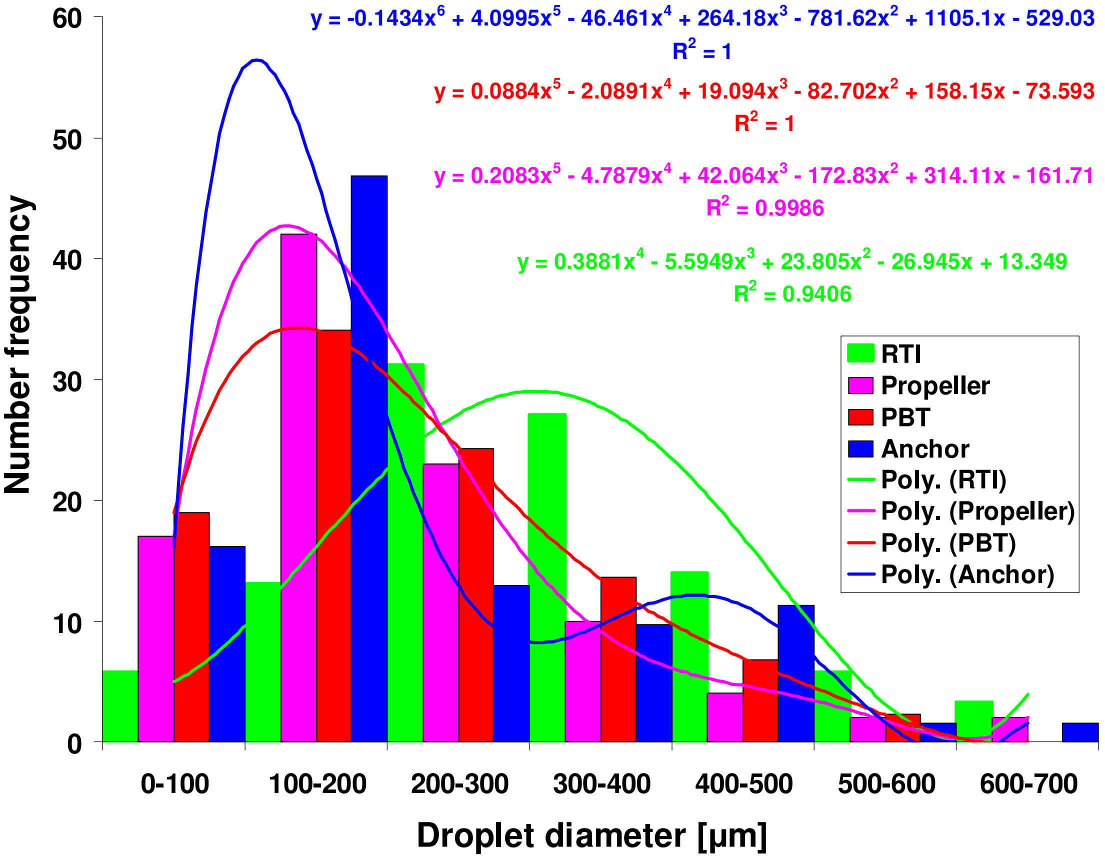

Figure 5.10: Number frequency drop size distribution for RTI, propeller and PBT at a velocity of 700 rpm and clearance of 4.1 cm, also for anchor impeller at a velocity of 350 rpm.

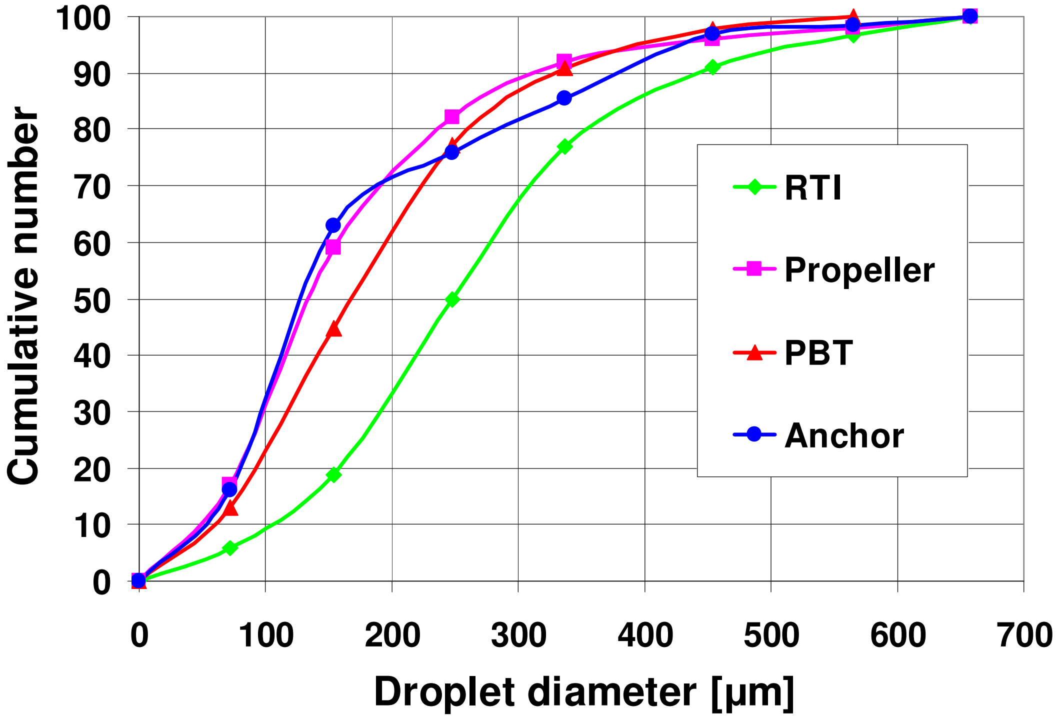

Figure 5.11: Cumulative drop size distribution for RTI, propeller and PBT at a velocity of 700 rpm and clearance of 4.1 cm, also for anchor impeller at a velocity of 350 rpm.

5.2.4 Sauter mean droplet diameter

All the images of cyclohexane droplets are analyzed statistically. Sauter mean droplet size is computed from the equation 2.1. The effect of RTI bottom clearance, the percentage volume of cyclohexane and stirrer type on the Sauter mean droplet diameter (d_{32}) are investigated and represented by the histogram diagram in Fig. 5.12. It is found that:

1. d_{32} for RTI at clearance of 4.1 cm and 20 vol% cyclohexane (409 μm) > d_{32} for RTI at clearance of 3.2 cm and 20 vol% cyclohexane with very small difference (399 μm).

2. d_{32} for RTI at clearance of 3.2 cm and 20 vol% cyclohexane (399 μm) > d_{32} for RTI at clearance of 3.2 cm and 10 vol% cyclohexane (348 μm).

3. d_{32} for RTI at clearance of 4.1 cm and 20 vol% cyclohexane (409 μm) > d_{32} for anchor impeller with 20 vol% cyclohexane (388 μm) > d_{32} for propeller impeller at clearance of 4.1 cm with 20 vol% cyclohexane (376 μm) > d_{32} for PBT impeller at clearance of 4.1 cm with 20 vol% cyclohexane (343 μm).

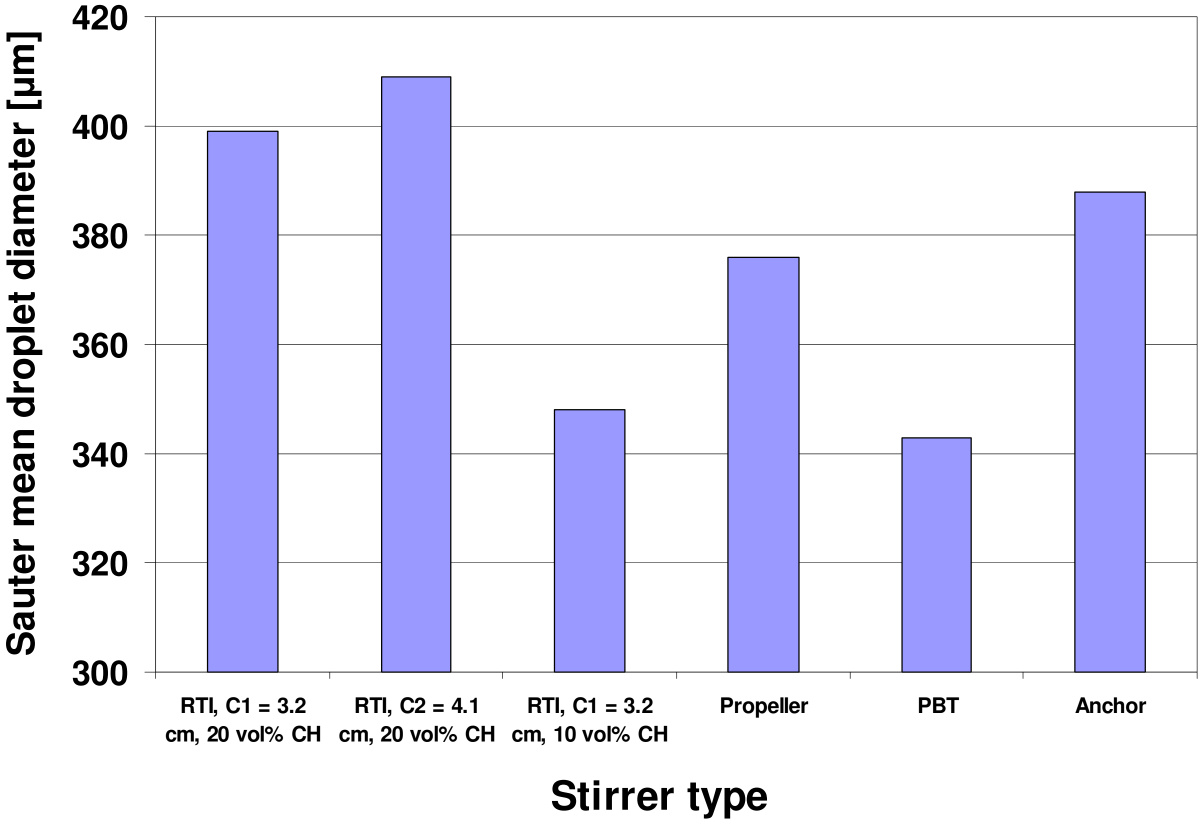

Figure 5.12: Sauter mean droplet diameter of cyclohexane for RTI at clearance of 3.2 and 4.1 cm, RTI with 10 and 20 vol% cyclohexane, propeller, PBT and anchor impellers.

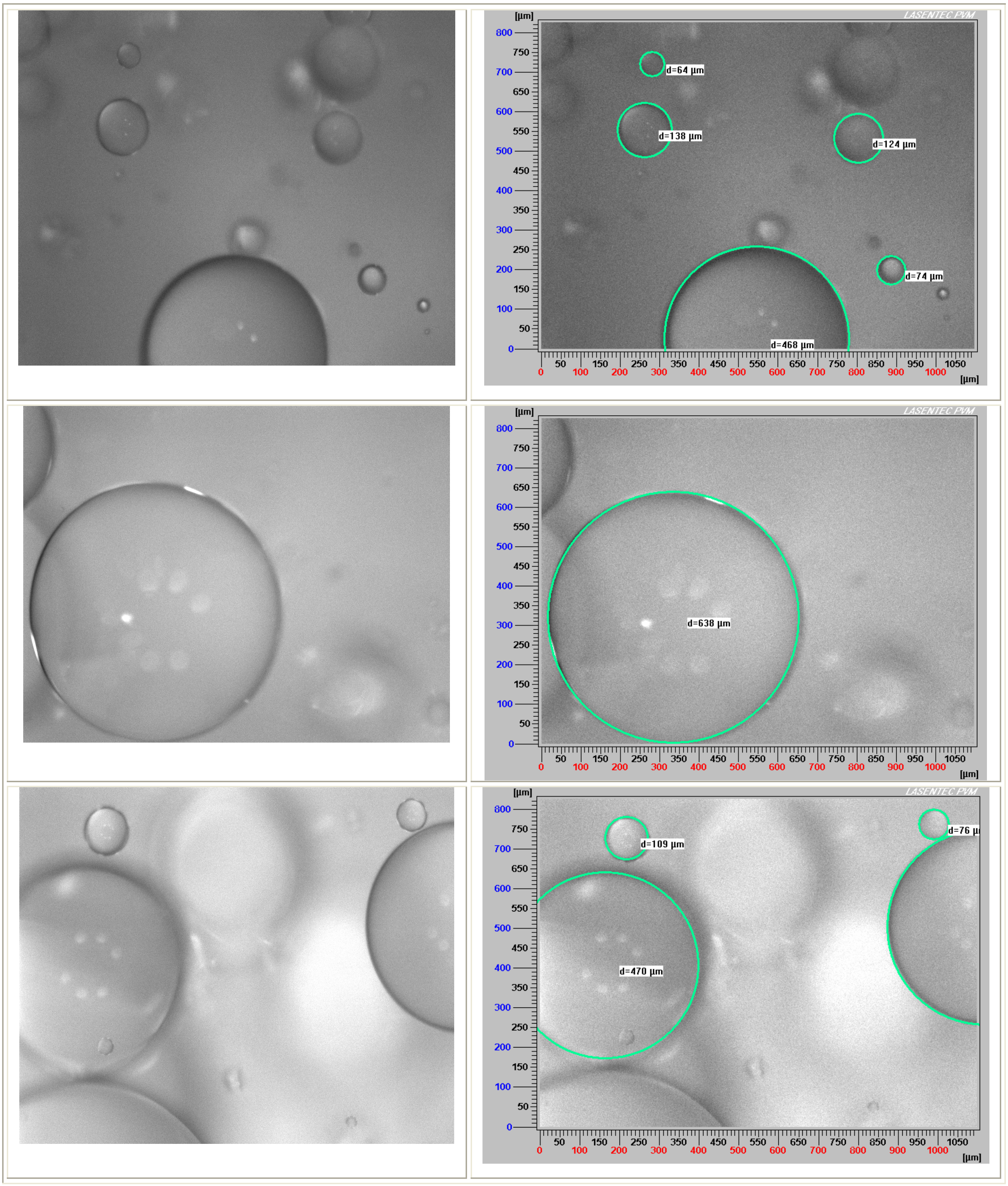

Figure 5.13-a: Images for 20 vol% cyclohexane in water dispersion (left) and droplets size analysis (right) with anchor impeller at a velocity of 350 rpm, Δt = 0.1 s.

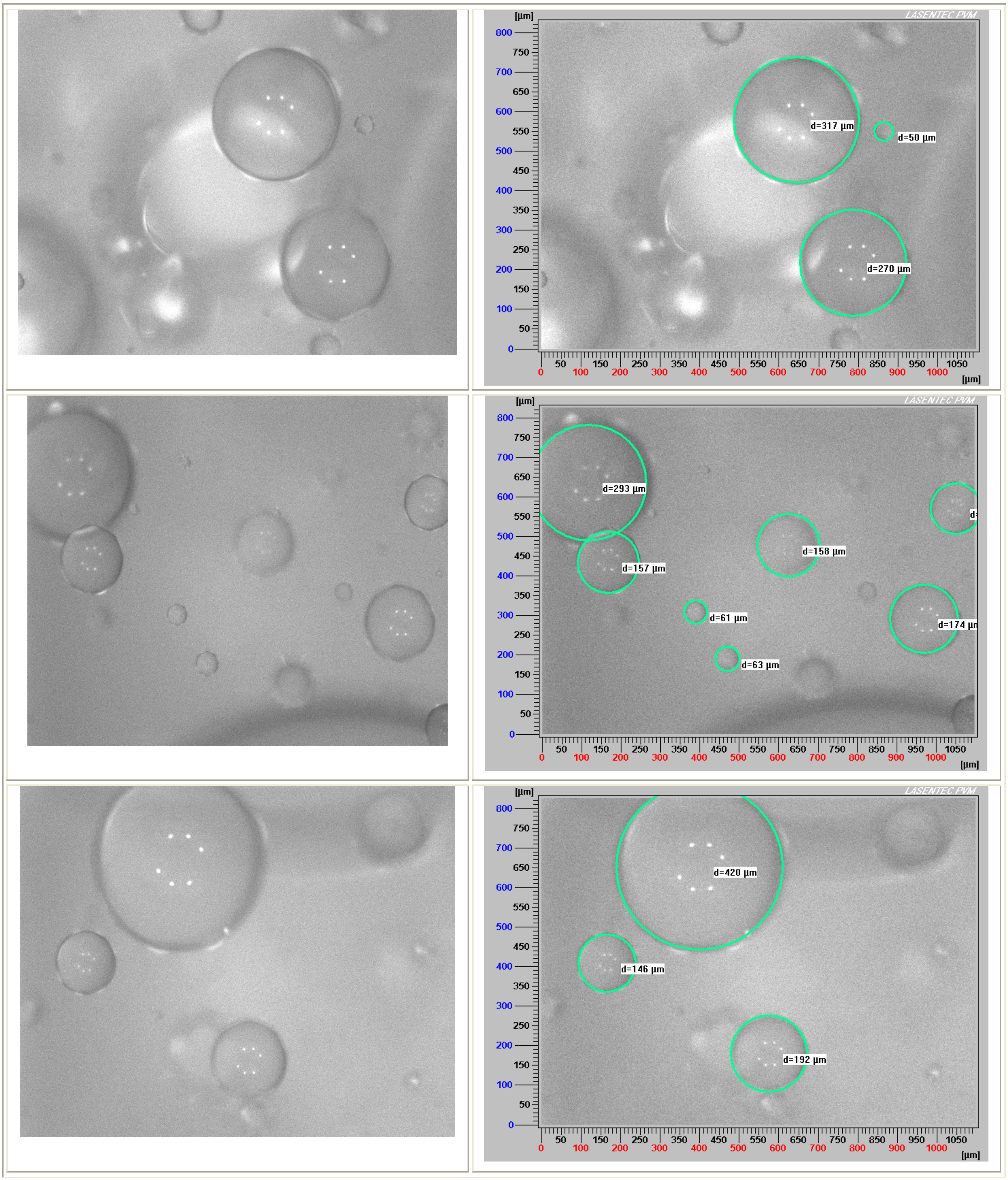

Figure 5.13-b: Images for 20 vol% cyclohexane in water dispersion (left) and droplets size analysis (right) with anchor impeller at a velocity of 350 rpm, Δt = 0.1 s.

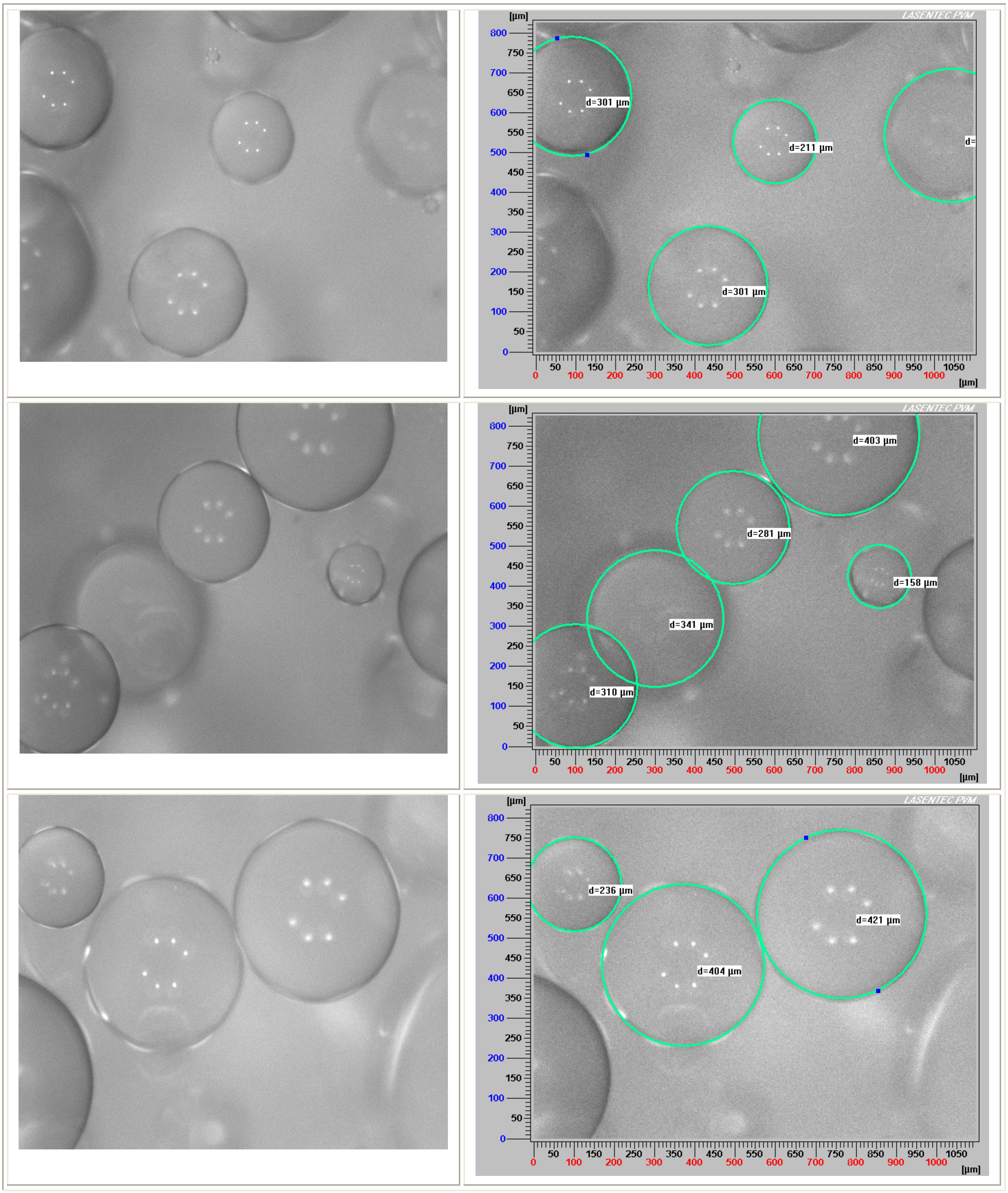

Figure 5.14-a: : Images for 20 vol% cyclohexane in water dispersion (left) and droplets size analysis (right) with RTI at a velocity of 700 rpm and bottom clearance of 3.2 cm, Δt = 0.1 s.

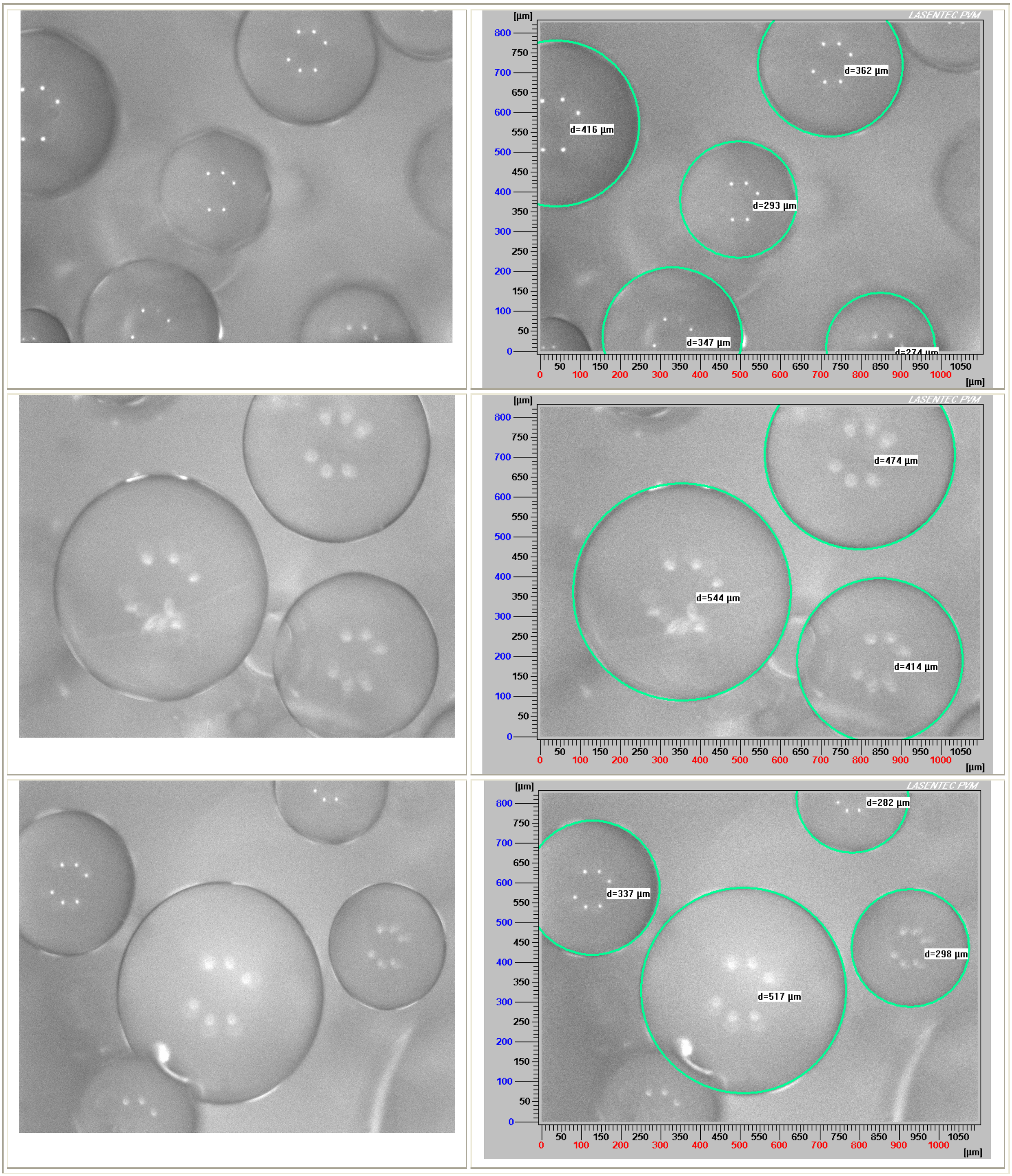

Figure 5.14-b: Images for 20 vol% cyclohexane in water dispersion (left) and droplets size analysis (right) with RTI at a velocity of 700 rpm and bottom clearance of 3.2 cm, Δt = 0.1 s.

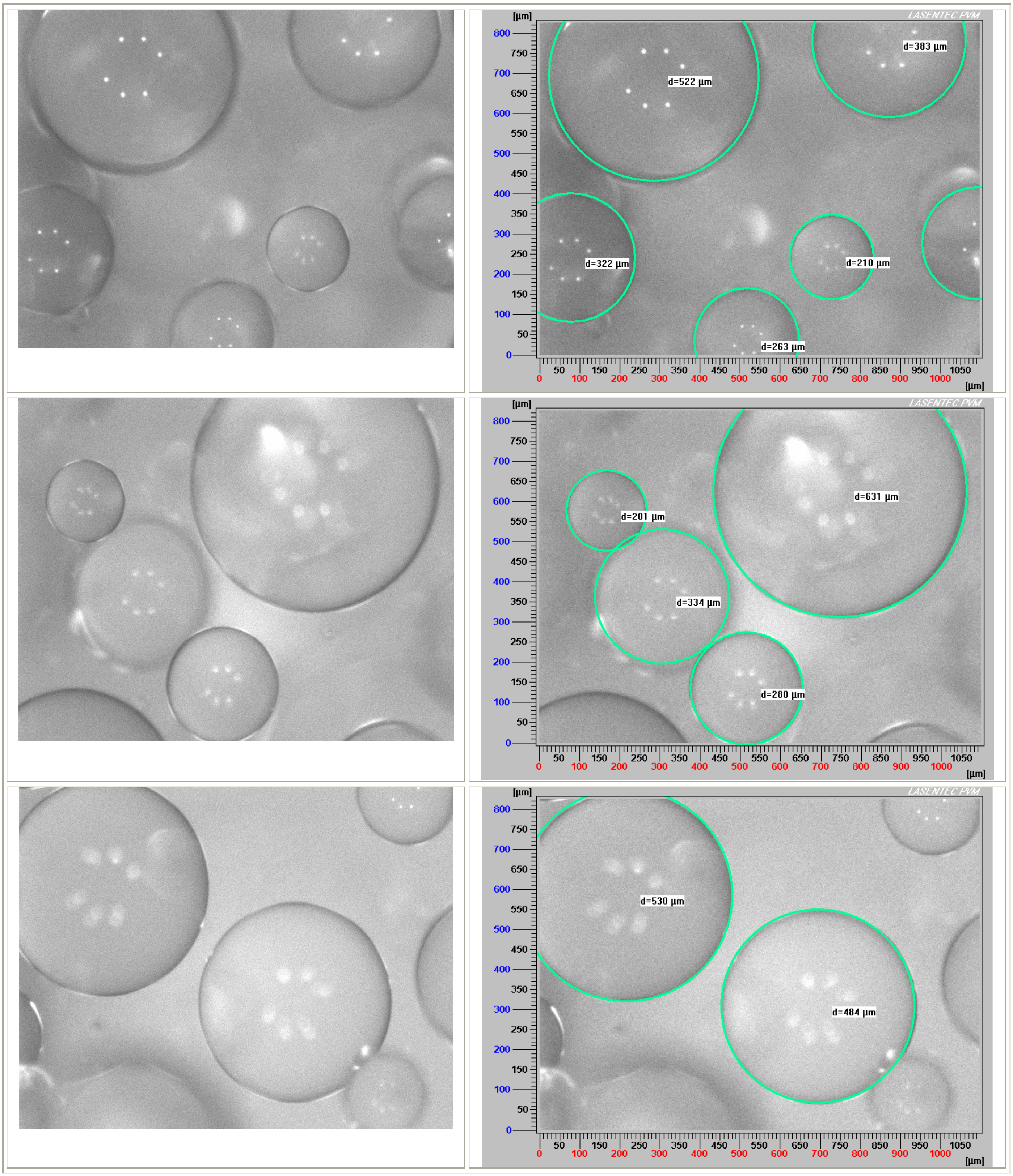

Figure 5.15-a: Images for 20 vol% cyclohexane in water dispersion (left) and droplets size analysis (right) with RTI at a velocity of 700 rpm and bottom clearance of 4.1 cm, Δt = 0.1 s.

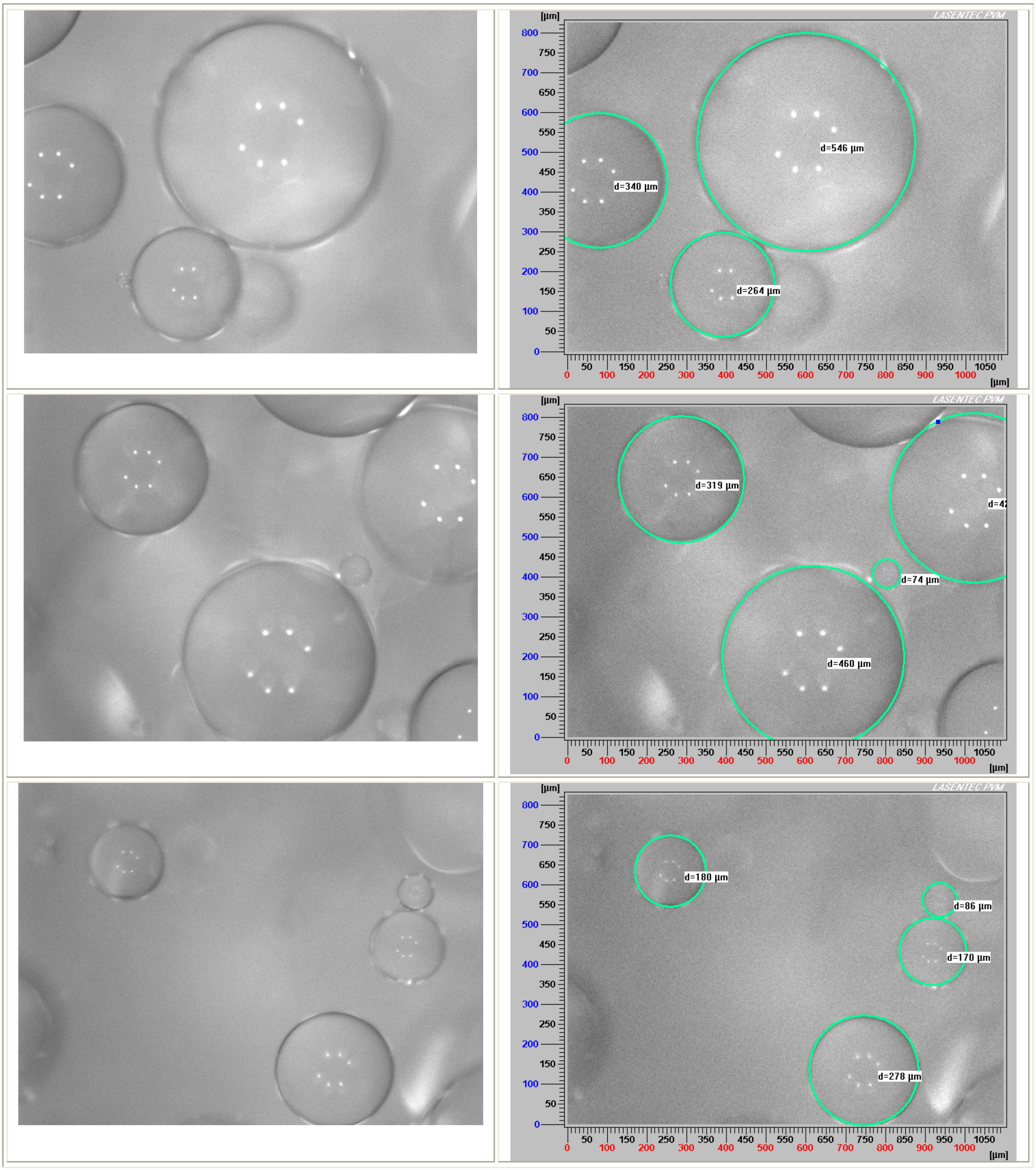

Figure 5.15-b: Images for 20 vol% cyclohexane in water dispersion (left) and droplets size analysis (right) with RTI at a velocity of 700 rpm and bottom clearance of 4.1 cm, Δt = 0.1 s.

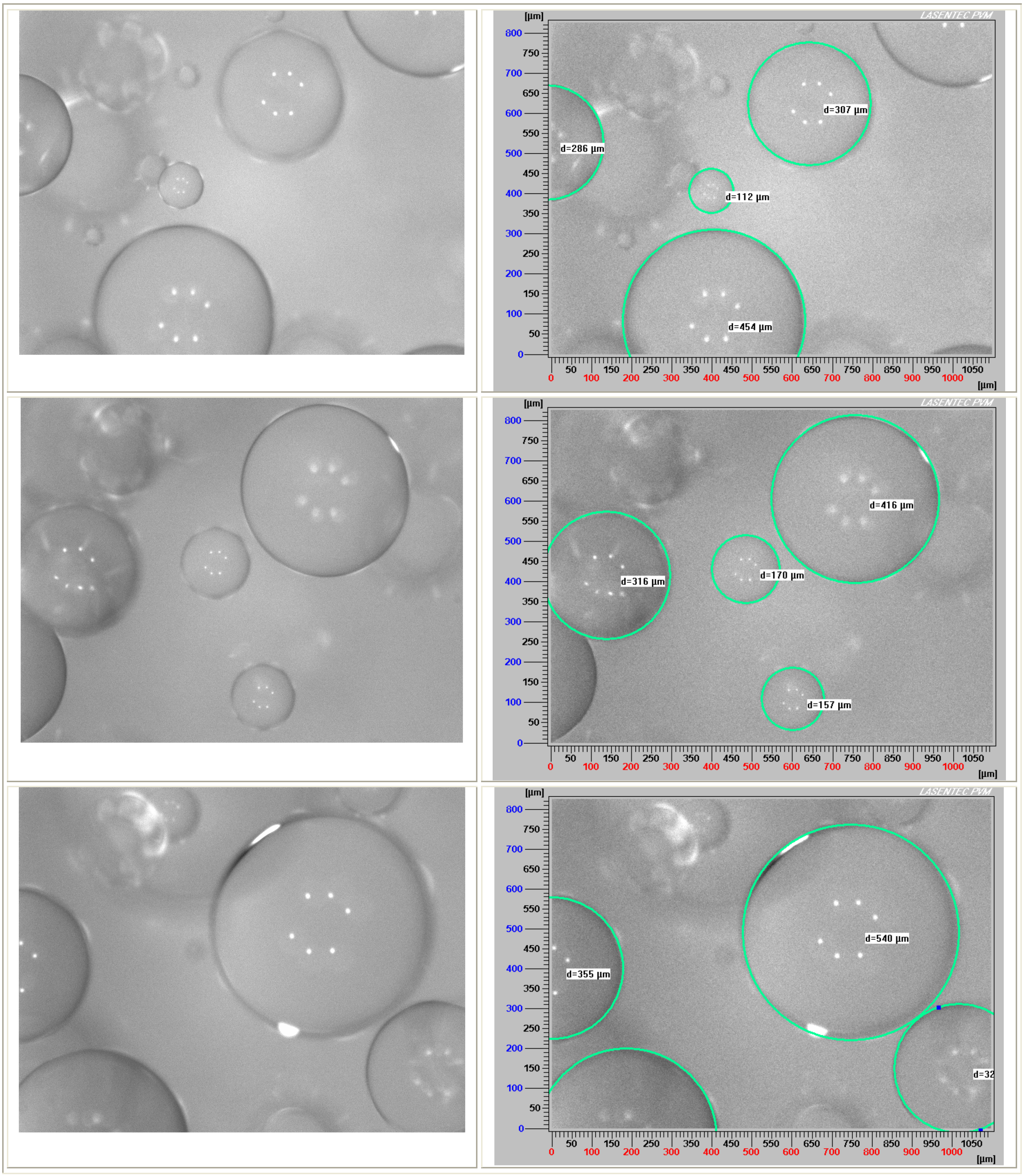

Figure 5.16-a: Images for 10 vol% cyclohexane in water dispersion (right) and droplets size analysis (left) with RTI at a velocity of 700 rpm and bottom clearance of 3.2 cm, Δt = 0.1 s.

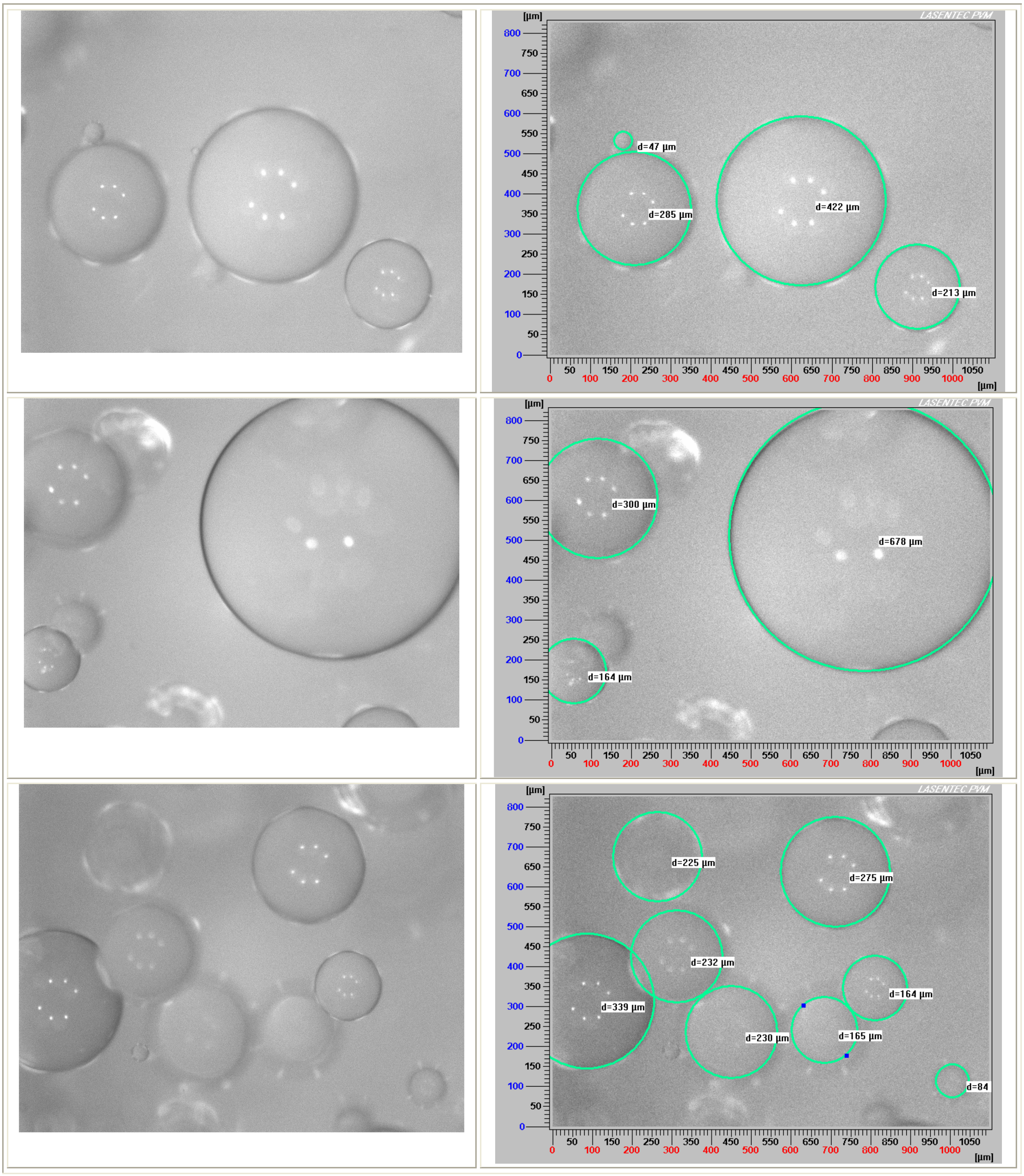

Figure 5.16-b: Images for 10 vol% cyclohexane in water dispersion (right) and droplets size analysis (left) with RTI at a velocity of 700 rpm and bottom clearance of 3.2 cm, Δt = 0.1 s.

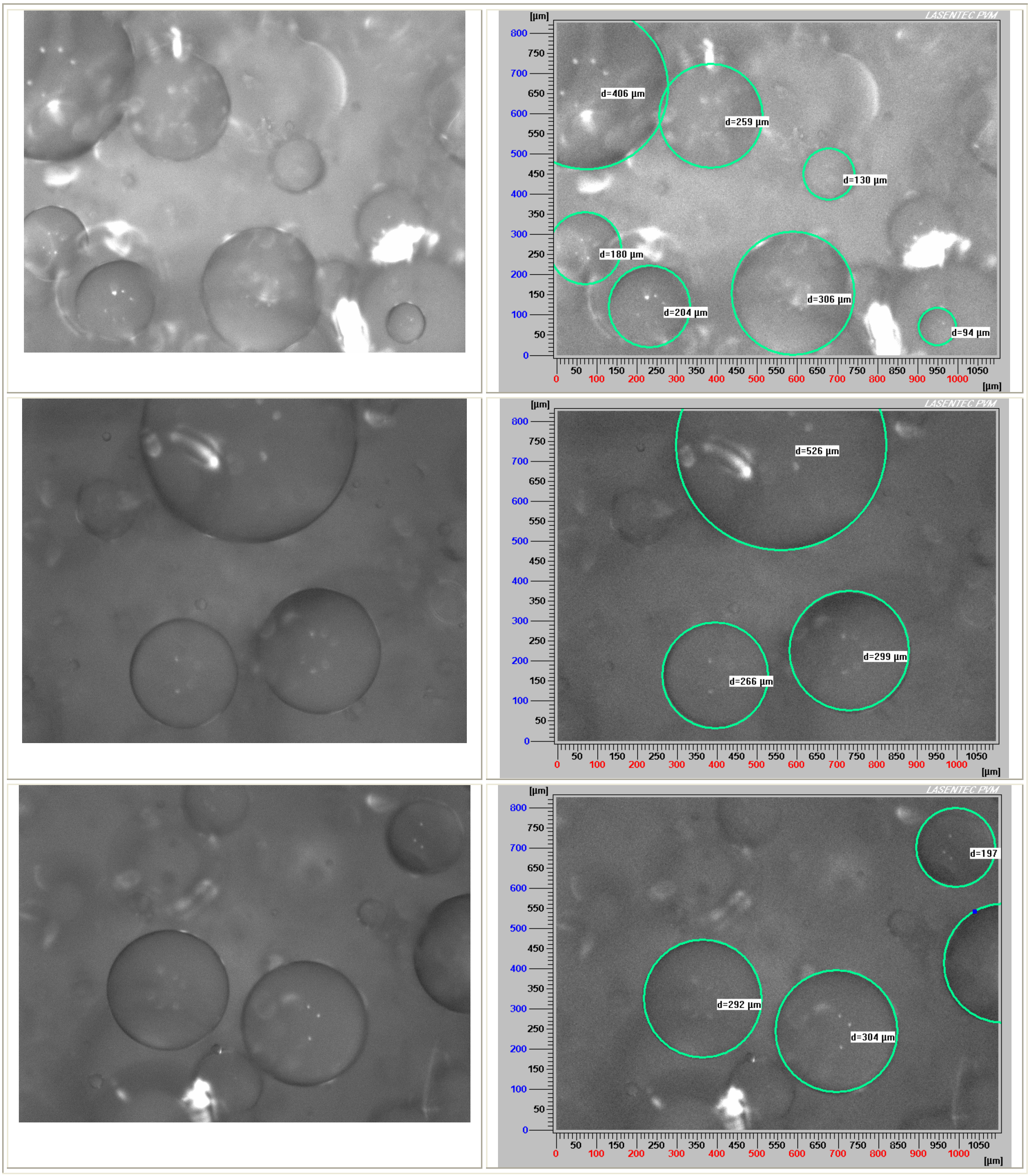

Figure 5.17-a: Images for 20 vol% cyclohexane in water dispersion (left) and droplets size analysis (right) with propeller impeller at a velocity of 700 rpm, $\Delta t = 0.1$ s.

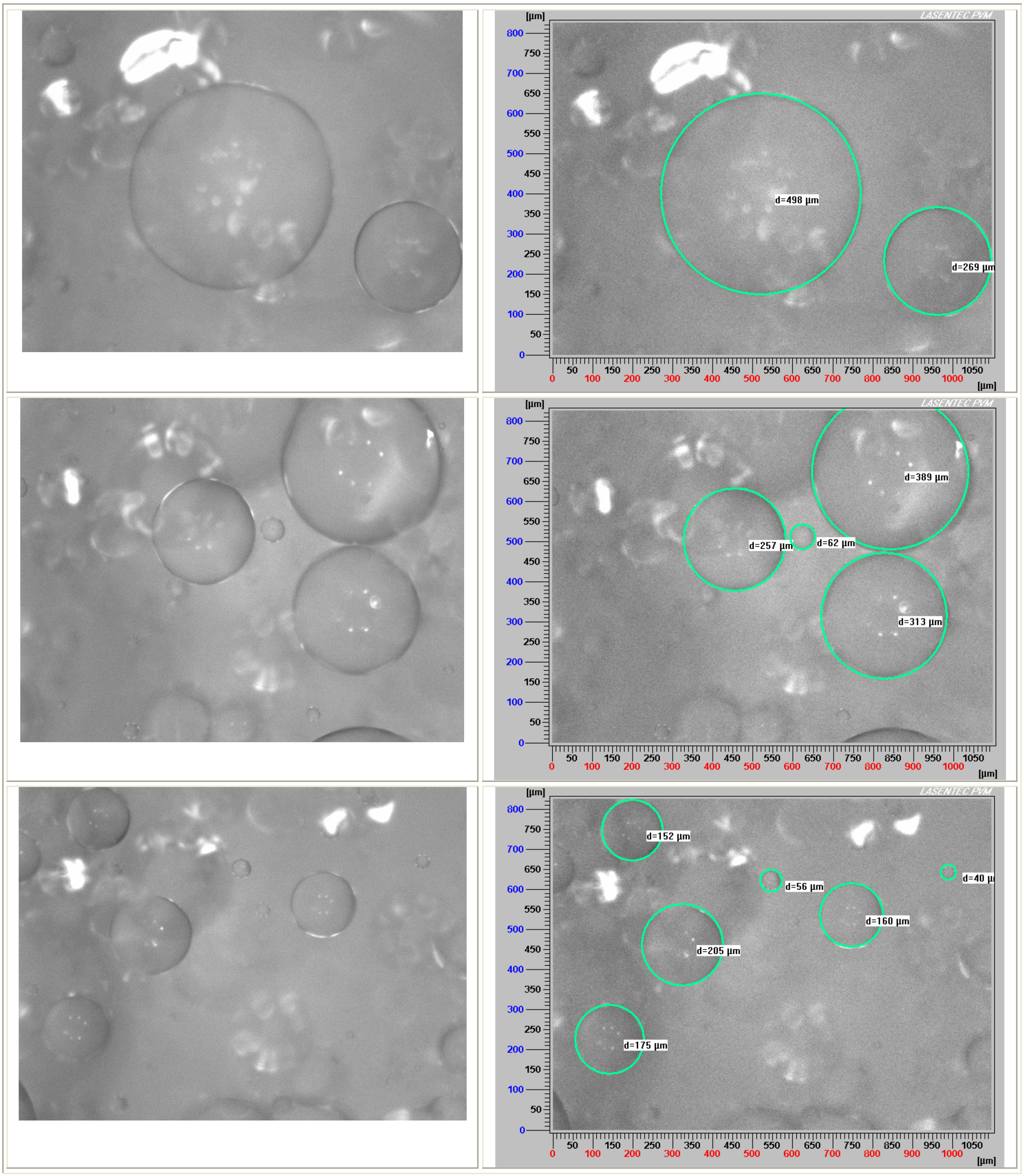

Figure 5.17-b: Images for 20 vol% cyclohexane in water dispersion (left) and droplets size analysis (right) with propeller impeller at a velocity of 700 rpm, Δt = 0.1 s.

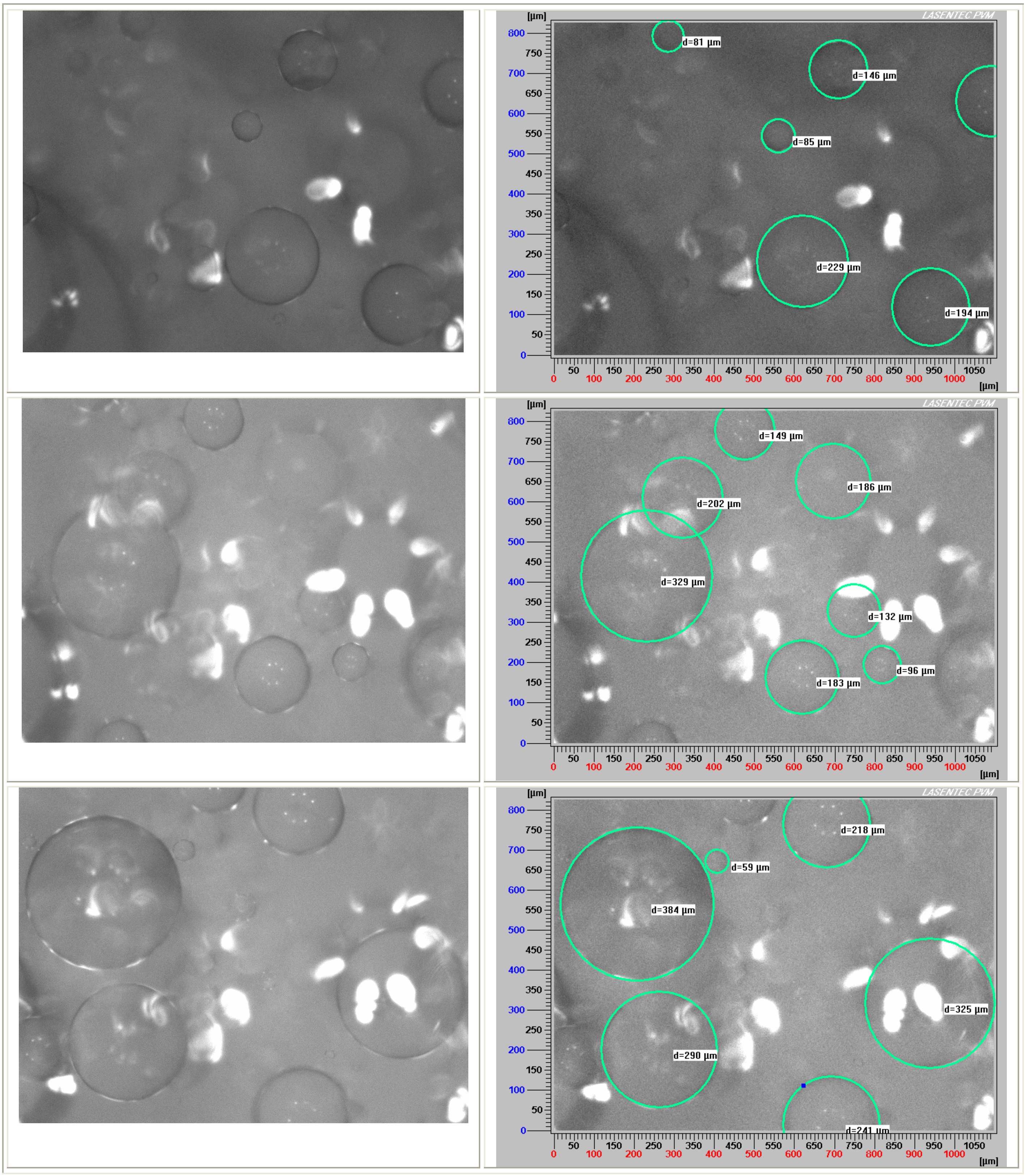

Figure 5.18-a: Images for 20 vol% cyclohexane in water dispersion (left) and droplets size analysis (right) with PBT at a velocity of 700 rpm, Δt = 0.1 s.

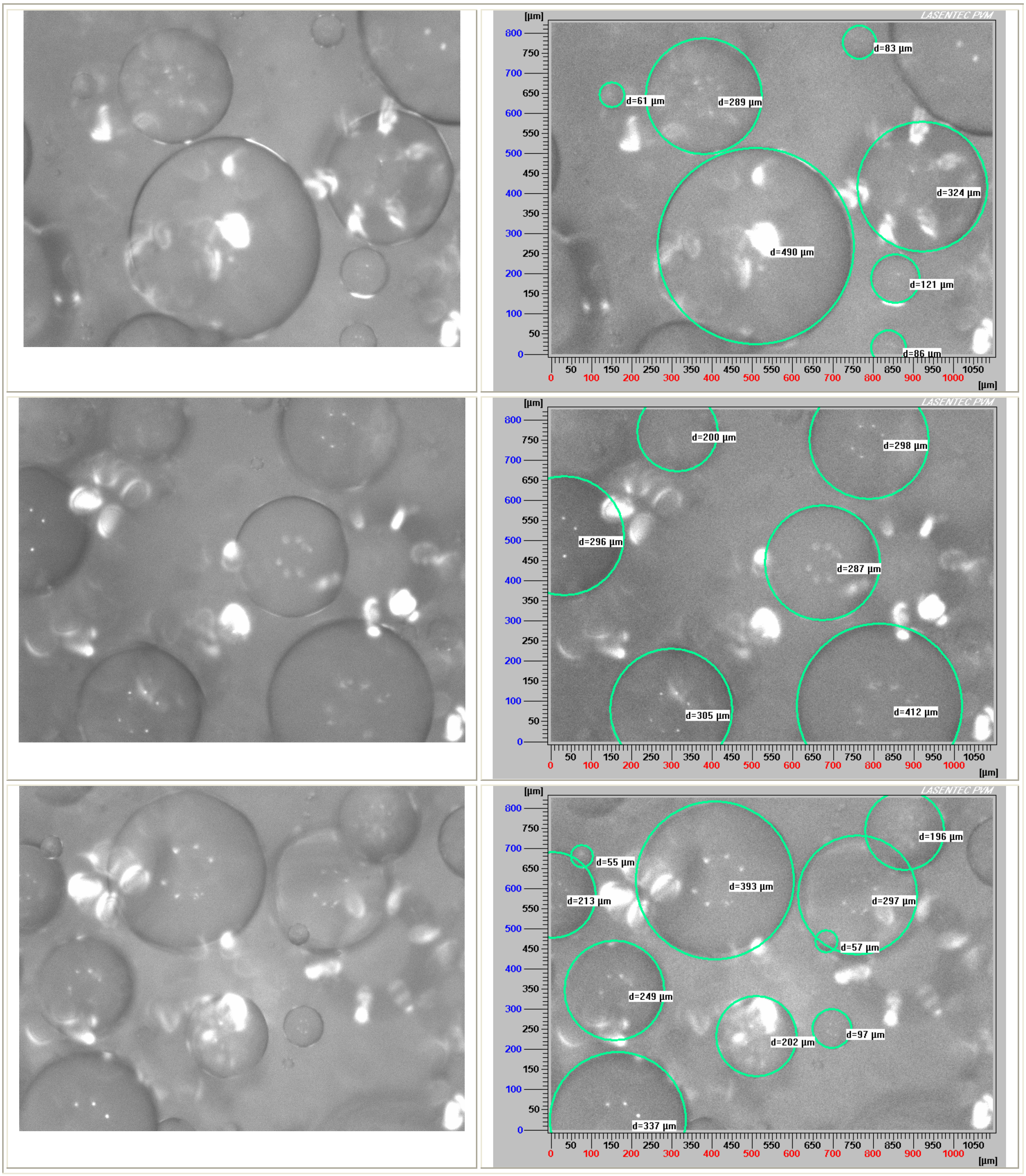

Figure 5.18-b: Images for 20 vol% cyclohexane in water dispersion (left) and droplets size analysis (right) with PBT at a velocity of 700 rpm, Δt = 0.1 s.

5.3 Experiment and CFD simulation for holdup (volumetric fraction) profiles of cyclohexane

The volume fraction of cyclohexane in water is measured in a stirred vessel with anchor impeller, RTI at bottom clearances of 3.2, 4.1 and 5.5 cm, propeller and PBT impellers at clearance of 4.1 cm. It is only predicted by using CFD in the stirred vessel with the anchor impeller and RTI at bottom clearance of 3.2 cm. The stirrer velocity is monitored by following the axial and radial distribution profiles of cyclohexane volume fraction, which represent the development of the dispersion as a function of stirrer velocity. The minimum velocity to get complete and uniform dispersion is determined. The effects of ASM and Ishii-Zuber momentum transfer models and the grid cell size on the calculated hlodup profiles of cyclohexane are investigated.

5.3.1 Cyclohexane dispersion with anchor impeller

5.3.1.1 Axial profile

The measured and predicted local volume fractions of cyclohexane CHVF are plotted in Fig. 5.19 as a function of the axial distances z, from the impeller level to the top near the free surface, at a radial distance of r = 2 cm from the centre of the shaft, and at anchor velocities of 150 and 350 rpm, they show very good agreement. Ishii-Zuber momentum transfer model is used to predict the volume fractions of cyclohexane at different positions in the vessel. The high pressure gradient at the interface between the two phases produces the inertial forces due to the centrifugal forces. This phenomenon occurs due to the dominant effect of the surface tension between cyclohexane/water, which prevents the interpenetration between the two phases and leads to the formation of distorted droplets. These droplets become at first ellipsoidal in shape, and finally they become spherical cap shaped. Based on these criteria, Ishii-Zuber model is suitable because it considers the drag coefficient nearly constant and independent on Reynolds number in a turbulent flow, but dependent on the droplet shape through the dimensionless group known as the Eotvos number (equation 4.24 in section. 4.3.3.4.2.1). At low anchor velocity of 150 rpm, cyclohexane is pulled down gradually into water to reach the minimum axial height of about 6.5 cm. The volume fraction of cyclohexane decreases from 1.0 to 0, when it disperses into water through the axial heights from z = 10 cm to z = 6 cm, respectively. A layer of pure cyclohexane with a thickness of about 1.0 cm is found at the top of the liquid phases with a volume fraction of 1.0. The trend of the axial profile of CHVF is different when the anchor velocity increases to 350 rpm. All the layer of cyclohexane is pulled down and dispersed into water to reach minimum height of 1.0 cm near the lowest point of the shaft of the anchor impeller. The volume fraction of cyclohexane increases from 0.2 at z = 4.0 cm to reach the maximum of 0.5 at z = 6.0 cm, then it decreases to reach the minimum at z = 10 cm, where the top layer of cyclohexane disappeared.

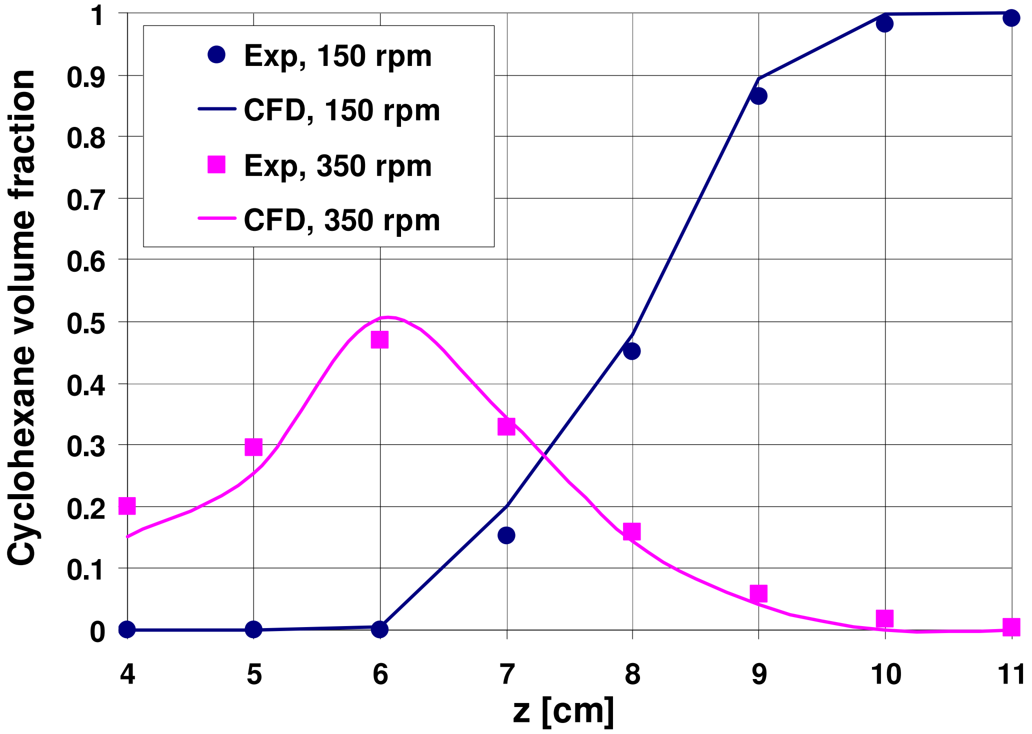

Figure 5.19: The axial profile of cyclohexane volume fraction at r = 2.0 cm for anchor velocity of 150 rpm and 350 rpm, experimentally and with CFD simulations.

The complete dispersion of cyclohexane is obtained at anchor velocity of 350 rpm, but not uniform because all the layers of cyclohexane are accumulated around the shaft of the impeller forming a symmetrical vortex around the shaft with little dispersion in the radial distance. Thus the CHVF values are different.

The layers at the interface with water consist of distorted droplets of cyclohexane, which disperse into water to fill the space between the vertical arms of the anchor impeller near the tip.

5.3.1.2 Radial profile

The experimental and predicted radial profiles of cyclohexane volume fraction at the axial position of z = 7 cm in Fig. 5.20 show good agreement for both anchor velocities of 150 and 350 rpm. The laminar flow at 150 rpm gives different trend for the CHVF distribution than that obtained in the turbulent flow at 350 rpm. For the anchor velocity of 350 rpm, the CHVF are high near the shaft and decreases gradually from 1.0 at r = 1 cm to 0.2 at r = 2.5 cm. Whereas at anchor velocity of 150 rpm, the dispersion with water is very weak between the shaft and r = 1.4 cm, and between r = 2.2 cm and the anchor impeller. The sudden dispersion of cyclohexane into water occurs in the radial position between r = 1.5 and 2 cm may be due to the high intensity of turbulence there.

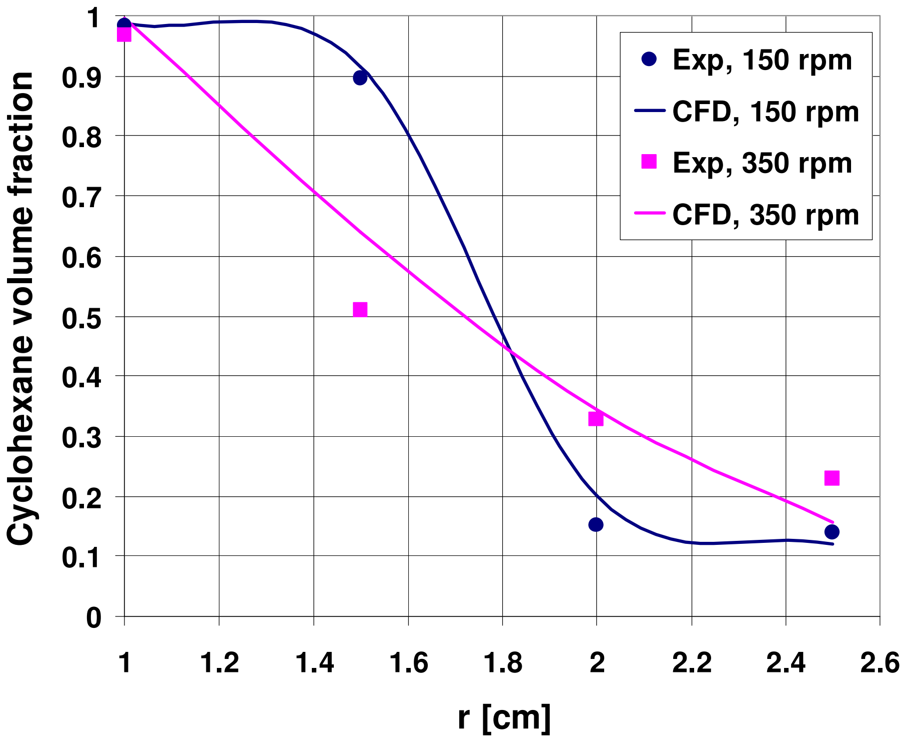

Figure 5.20: The radial profile of cyclohexane volume fraction at z = 7 cm for anchor velocity of 150 rpm and 350 rpm, experimentally and with CFD simulations.

Because of the high relative velocity between the two phases and high pressure fluctuations, there will be no uniform distribution of cyclohexane in the radial distances because the CHVF values are not similar.

5.3.1.3 Anchor velocity for complete and uniform dispersion

The measured and predicted local volumetric fractions of cyclohexane as a function of anchor velocity at z = 7 cm and r = 2.5 cm show a good agreement as can be seen in Fig. 5.21. When the anchor velocity increases, the holdup of cyclohexane at this position increases to reach the maximum at anchor velocity of 250 rpm, and then decreases at higher velocities to reach the minimum volume fraction of 0.21 at anchor velocity of 350 rpm. The dispersed phase holdup reaches the volume fraction of the dispersed phase presents initially at t = 0 at the top above water phase, when increasing the anchor velocity and impeller power. There will be no significant change on the holdup of cyclohexane with further increase of the anchor velocity to 400 rpm, because the system reaches the steady state. For that the minimum anchor velocity for complete dispersion of cyclohexane is approximately 350 rpm, but there is no uniform distribution of cyclohexane in the axial and radial distances as can be seen in Figs. 5.19 and 5.20.

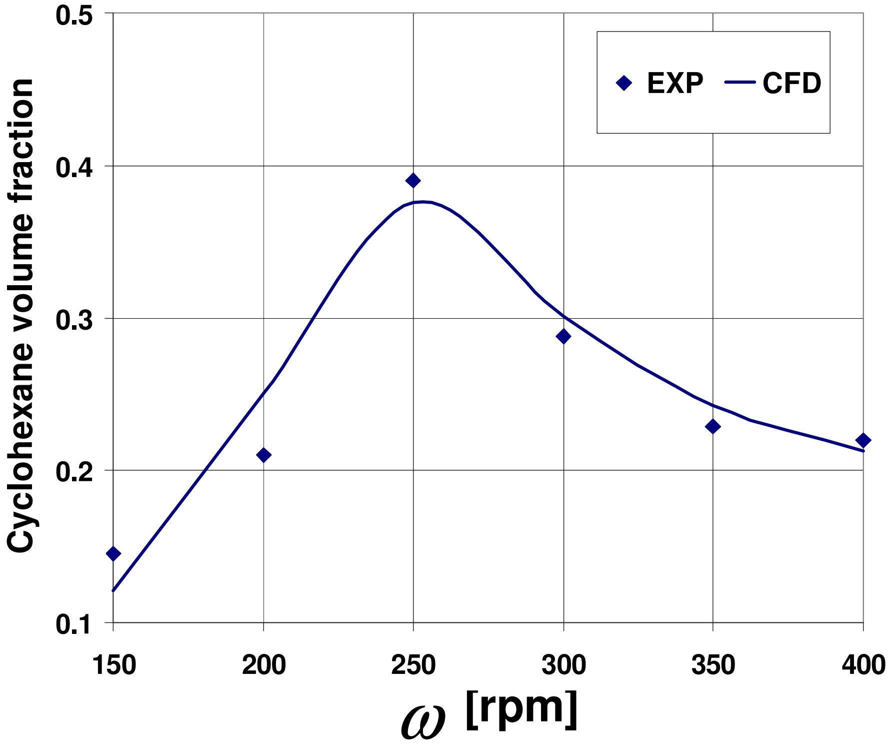

Figure 5.21: Measured and calculated cyclohexane volume fractions as a function of anchor velocity at z = 7 cm and r = 2.5 cm.

The averaged volume fraction of cyclohexane is calculated by using CFD over the total volume of the continuous phase, and drawn as a function of anchor velocity in Fig. 5.22. It is clear that the holdup of cyclohexane increases gradually when the anchor velocity increases to reach a constant and maximum value of about 0.19 at anchor velocity of 350 rpm, which is a confirmation for the minimum anchor velocity to get a complete dispersion of cyclohexane that obtained from Fig. 5.21 at a local position in the vessel. The predicted averaged volumetric fractions of cyclohexane can not be measured experimentally.

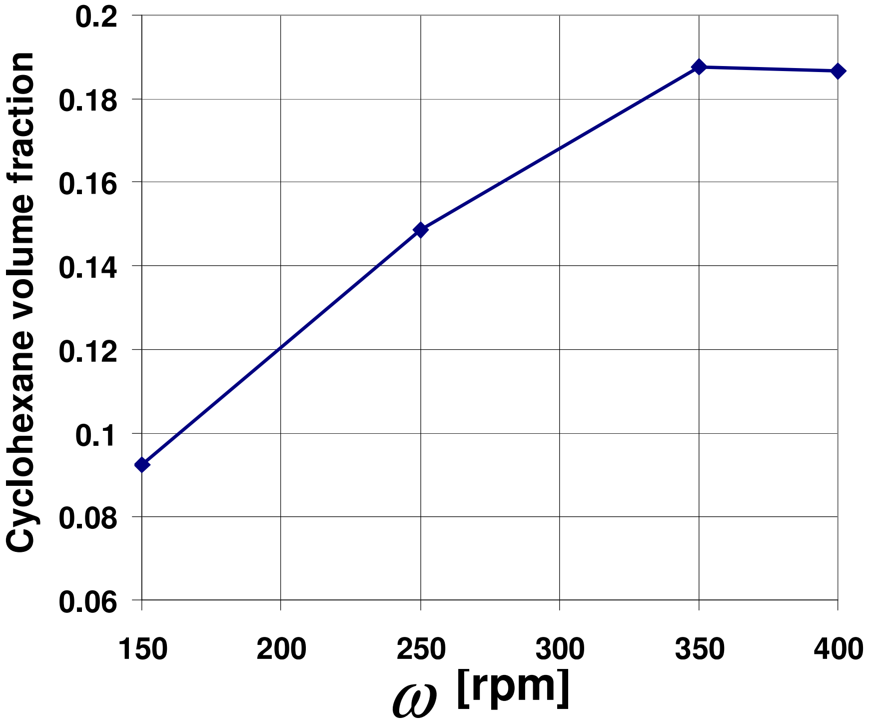

Figure 5.22: The calculated averaged cyclohexane volume fraction as a function of anchor velocity by using CFD over the total volume of the continuous phase (water).

5.3.2 Cyclohexane dispersion with rushton turbine impeller

5.3.2.1 Axial profile

The volumetric fractions of cyclohexane in the axial distances are taken in a stirred vessel with RTI at clearance of 3.2 cm and velocities from 350 to 750 rpm, higher than that for the anchor impeller because RTI size is small and requires higher input energy to drawn cyclohexane into water as shown in Fig. 5.23. The measured and calculated CHVF profiles are presented at different radial distances from the shaft to the cylindrical wall of the vessel (from r = 0.5 cm to r = 4 cm) and show a good agreement.

When the RTI rotates at a velocity of 350 rpm, cyclohexane is pulled down into water towards the impeller around the shaft, so the concentration of cyclohexane is high (unmixed) at the top, about 3 cm below the free surface between z = 8 to 11 cm, and low near the impeller level. This result coincides with the visualised dispersion behaviour of cyclohexane in section 5.1.2 in Fig. 5.23-a. The thickness of the cyclohexane layer decreases as the RTI velocity increases, it disappears at a velocity > 550 rpm, where all of the cyclohexane is incorporated in the water phase (Fig. 5.23-a). The cyclohexane is highly concentrated near the shaft at r = 0.5 cm and it requires a velocity > 750 rpm to be spread in the radial direction towards the walls of the vessel until reaching the initial volume fraction of cyclohexane of about 0.2 at t = 0 . The minimum uniform CHVF of about 0.45 is obtained at RTI velocity of 750 rpm. The minimum RTI velocity to get a uniform distribution of cyclohexane in the axial distances between 4 cm < z < 9 cm is 650 rpm, where CHVF values are constant and close. A small air vortex is formed around the shaft with depth of 2 cm from the free surface (z = 9 cm) at a velocity of 650 rpm and 3 cm (z = 8 cm) at a velocity of 750 rpm. The dispersion efficiency is improved, when the velocity of RTI increases, thus the CHVF increases at z = 4 cm near the impeller and decreases in the top layer of cyclohexane at z = 9 cm, the CHVF becomes more uniform and reach the initial value of nearly 0.2.

When the RTI velocity increases a way from the shaft at r = 1.5 cm, the holdup of cyclohexane increases in the axial distances from z = 4 to 8 cm and decreases from z = 10 to 8 cm as can be seen in Fig. 5.23-b. The uniform axial distribution of cyclohexane at r = 1.5 cm (radius of the RTI) is obtained at RTI velocity of 650 rpm. The liquid in this radial distance is highly affected by the turbulence and dissipation energy that formed in the region of the impeller.

The number of cyclohexane droplets increases due to the increased rate of collision with the impeller, bulk liquid and the cylindrical walls, resulting in the upper and lower circulations which improve and enhance the dispersion through the periodic flow. The trend of the axial cyclohexane volume fraction profiles is nearly similar at $r \geq 1.5$ cm and 4 cm $\leq z \leq$ 8 cm. The high RTI velocity increases the intensity of the radial flow and the turbulent velocity of the dispersion. It is found that, the CHVF at low RTI velocity of 350 and 450 rpm is lower (mixed region) than that near the shaft in the radial distances between $r = 2$ and 3 cm, near the free surface at $z = 9$ and 10 cm as can be seen in Fig. 5.23-c to f. At a minimum RTI velocity of 550 rpm, 50 vol% of cyclohexane at the interface between the two phases is mixed with water at $r = 2$ cm (Fig. 5.23-c). The cyclohexane layer is pulled down towards the shaft of the impeller from the radial position at $r = 2.5$ cm and $z = 9$ cm at the interface between the two phases, see Fig. 5.23-d and e.

Near the walls of the vessel at $r = 3.5$ and 4 cm (Fig. 5.23-f and g), cyclohexane is incorporated into water in the axial distances up to $z = 9$ cm for all RTI velocities. Unmixed cyclohexane (CHVF nearly 1) exists between 9 cm $< z <$ 10 cm at RTI velocities less than 550 rpm. The uniform dispersion of cyclohexane in the axial distances for a given radial position is obtained at RTI velocity of 650 rpm. The complete dispersion of cyclohexane into water is obtained from the axial profiles at RTI velocity of 550 rpm.

The uniform distribution is achieved when the slip velocity of the droplets relative to the bulk becomes zero. The level of the total liquid phases remains constant and it is not increased at high RTI velocities, due to the absence of the centrifugal force effect. The results of the dispersion behaviour of cyclohexane/water from the visualisation coincides with the results of the cyclohexane volume fractions profiles in the whole vessel.

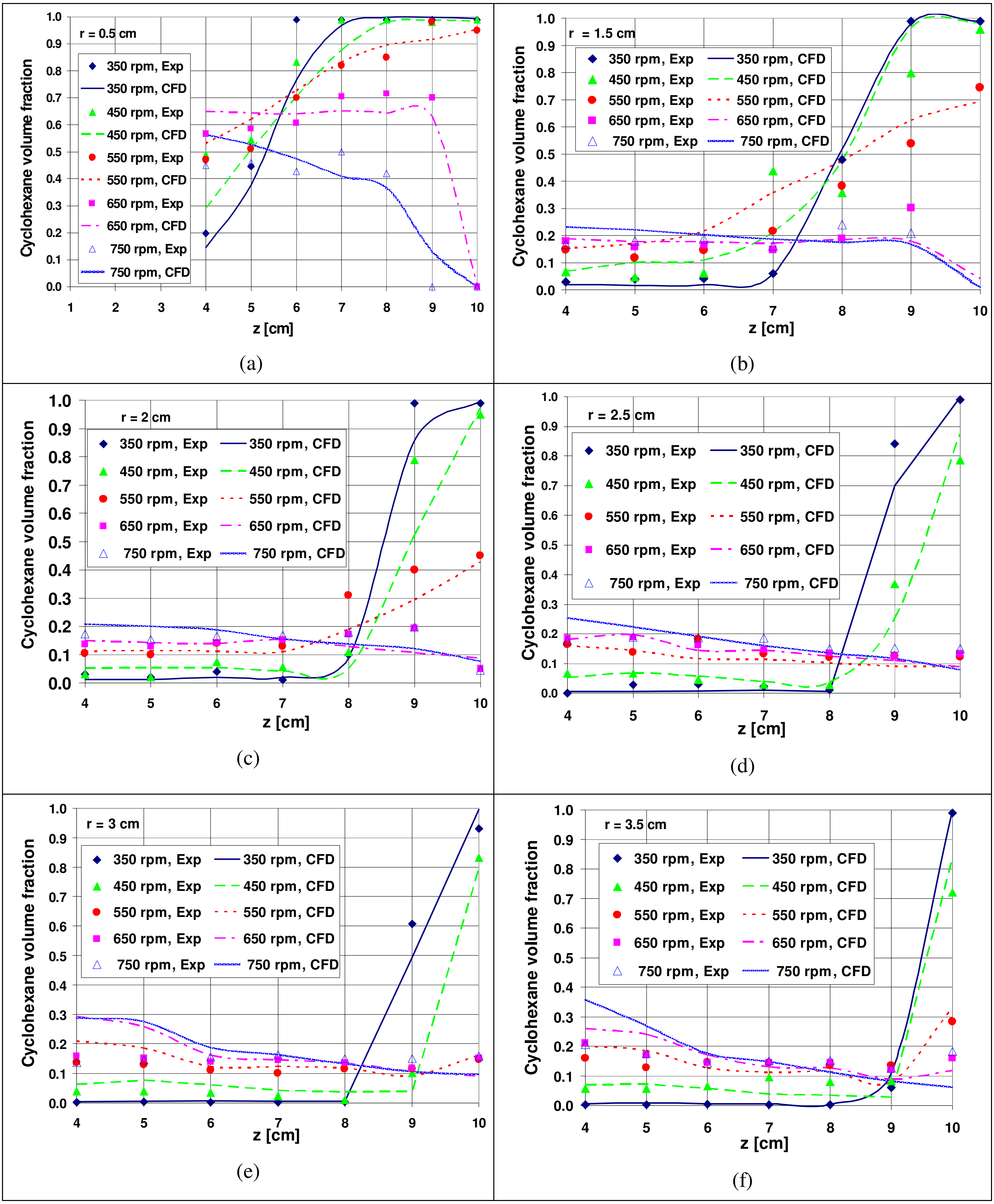

(a) (b) (c) (d) (e) (f)

Figure 5.23: Measured and predicted axial profiles of cyclohexane volume fraction at different RTI velocities and radial positions at r = 0.5, 1.5, 2, 2.5, 3 and 3.5 cm.

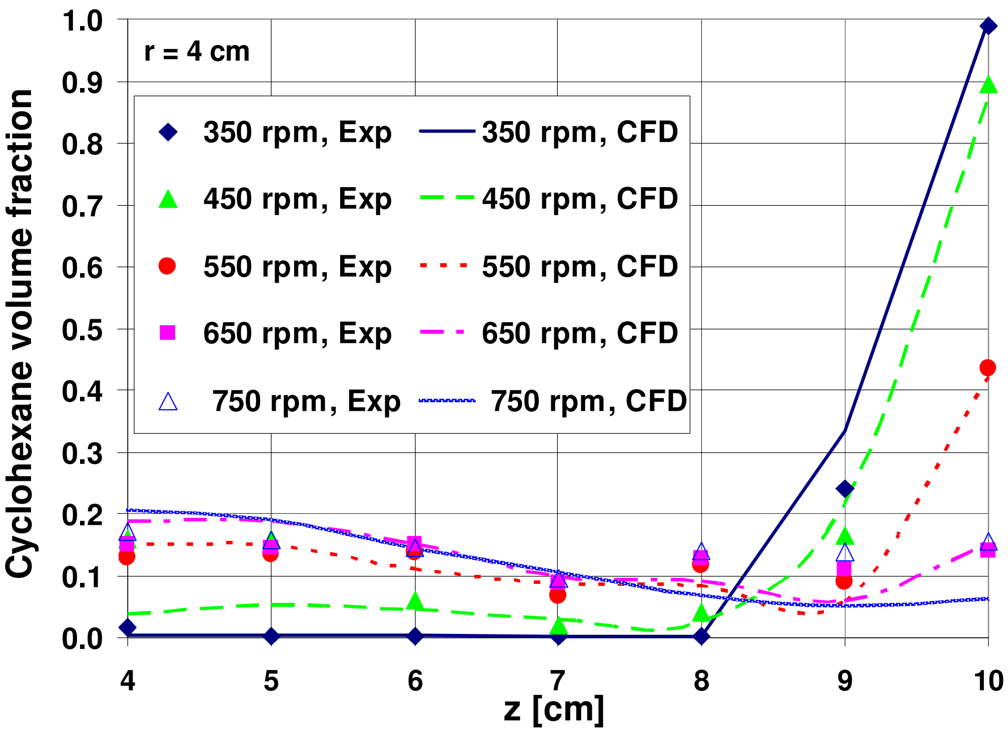

Figure 5.23-g: Measured and predicted axial profiles of cyclohexane volume fraction at different RTI velocities and radial position at r = 4 cm.

5.3.2.2 Radial profile

The radial cyclohexane volume fraction profiles at different axial distances from z = 4 cm to z = 10 cm and RTI velocities from 350 to 750 rpm can be seen in Fig. 5.24. The trend of the radial holdup profiles of cyclohexane is similar for 4 cm < z < 8 cm, especially for r ≥ 2 cm as can be seen in Fig. 5.24-a to e, where the highly turbulent recirculation exists as found from the visualization method. The cyclohexane volume fractions there increase when the RTI velocity increases, the uniform volume fraction of cyclohexane of about 0.2 is obtained at the minimum RTI velocity of 550 rpm.

The holdup of cyclohexane in the region between the shaft and the cylindrical walls 0.5 cm < r < 4 cm at 4 cm < z < 5 cm increases when the RTI velocity increases, the maximum CHVF near the shaft of about 0.6 is obtained at RTI velocity of 650 rpm, but it decreases to 0.4 at velocity of 750 rpm, see Fig. 5.24-a and b. Whereas the CHVF (about 1) decreases near the shaft at r = 0.5 cm in the region between 6 cm < z < 8 cm, when the RTI velocity increases to reach the minimum of about 0.4 at RTI velocity of 750 rpm as can be seen in Fig. 5.24-c, d and e. For a given RTI velocity, the CHVF decreases gradually in the radial distances towards the walls of the vessel, where the intensity of energy dissipation and kinetic energy increases. Unmixed cyclohexane (pure) exists at z = 9 cm between the shaft and r = 2 and 1.5 cm at RTI velocity of 350 rpm and 450 rpm, respectively (Fig. 5.24-f). Cyclohexane is dispersed into water with different degrees at r > 2 cm due to the variable intensity of turbulence and dissipation energy. Cyclohexane starts to disperse into water from the interface between the two phases at 2.5 cm < r < 3.5 cm towards the shaft of the RTI, for that a large volume percentage of cyclohexane is mixed with water results in the lowest volume fraction of cyclohexane of about 0.2 at these positions (Fig. 5.24-f). At RTI velocity of 550 rpm, the upper layer of cyclohexane at this height is completely dispersed into water, but high concentration of cyclohexane exists near the shaft at r = 0.5 cm. Further increase of the RTI velocity reduces the volume fraction of cyclohexane to reach the minimum of about 0.2 at RTI velocity of 750 rpm. The homogeneous dispersion of cyclohexane at z = 9 cm is found at r > 1.5 cm at a minimum RTI velocity of 650 rpm, see Fig. 5.24-f. The unmixed cyclohexane layer exists at all radial positions at z = 10 cm and low RTI velocity of 350 rpm, and between the shaft and r = 2 cm at RTI velocity of 450 rpm, but it is mixed with water at different percentages at RTI velocity of 550 rpm as illustrated in Fig. 5.83-g. Cyclohexane near the walls at r > 2.5 cm is firstly dispersed into water towards the shaft, second comes the cyclohexane between the shaft and r = 2.5 cm as can be seen clearly at RTI velocity of 550 rpm at z = 10 cm in Fig. 5.24-g. Air vortex near the shaft is formed at a minimum RTI velocity of 650 rpm between the shaft and r = 1.5 cm. The initial total liquid height is about 0.11 cm. The depth of the vortex is about 1 cm. The constant and steady volume fraction of cyclohexane is obtained at RTI velocity of 650 rpm at z = 10 cm (Fig. 5.24-g). The axial and radial distribution profiles of CHVF confirm the distribution and flow field of cyclohexane obtained from the visualization with the red tracer.

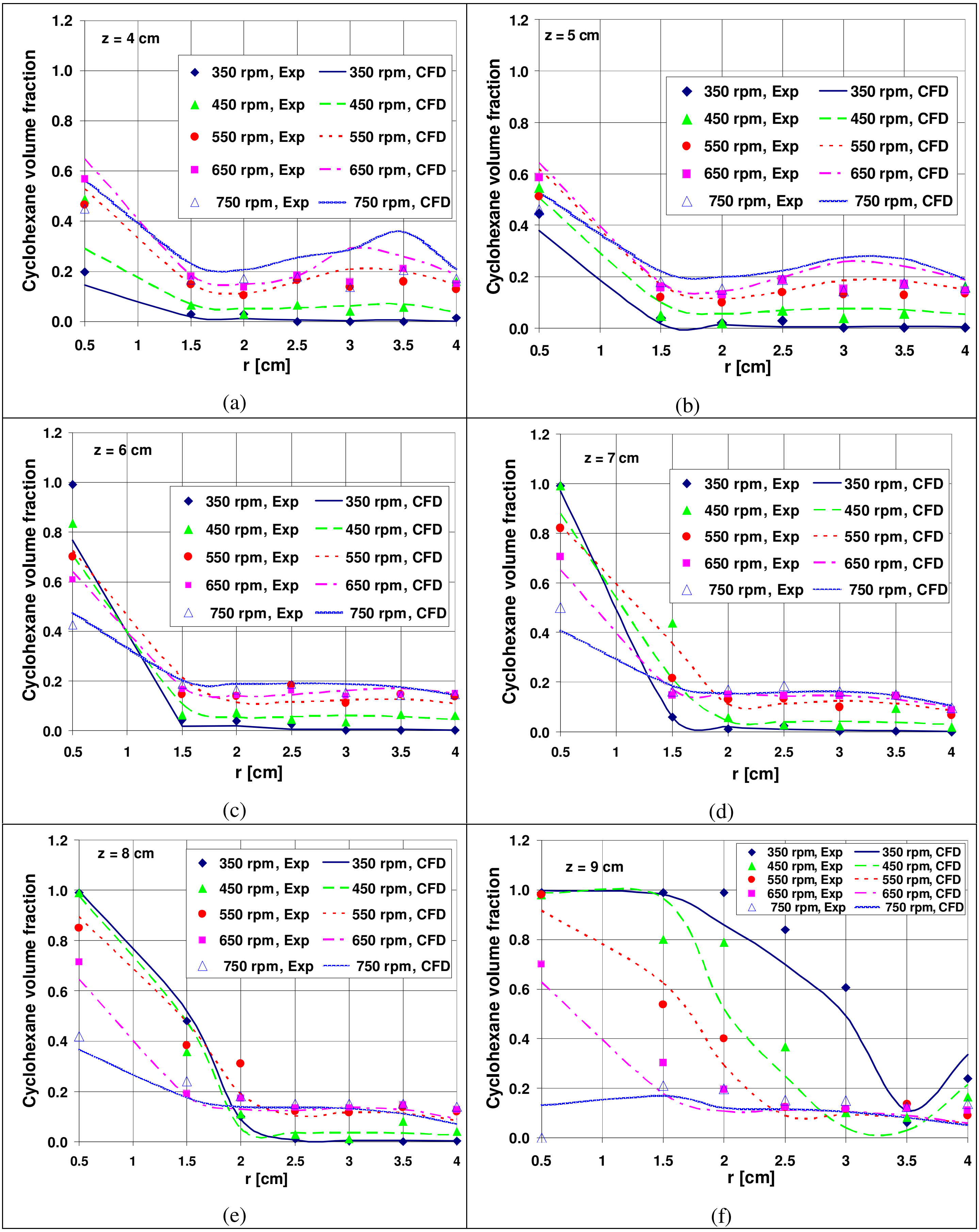

(a) (b) (c) (d) (e) (f)

Figure 5.24: Measured and predicted radial cyclohexane volume fraction profiles at different RTI velocities and axial positions at z = 4 cm, 5 cm, 6 cm, 7 cm, 8 cm and 9 cm.

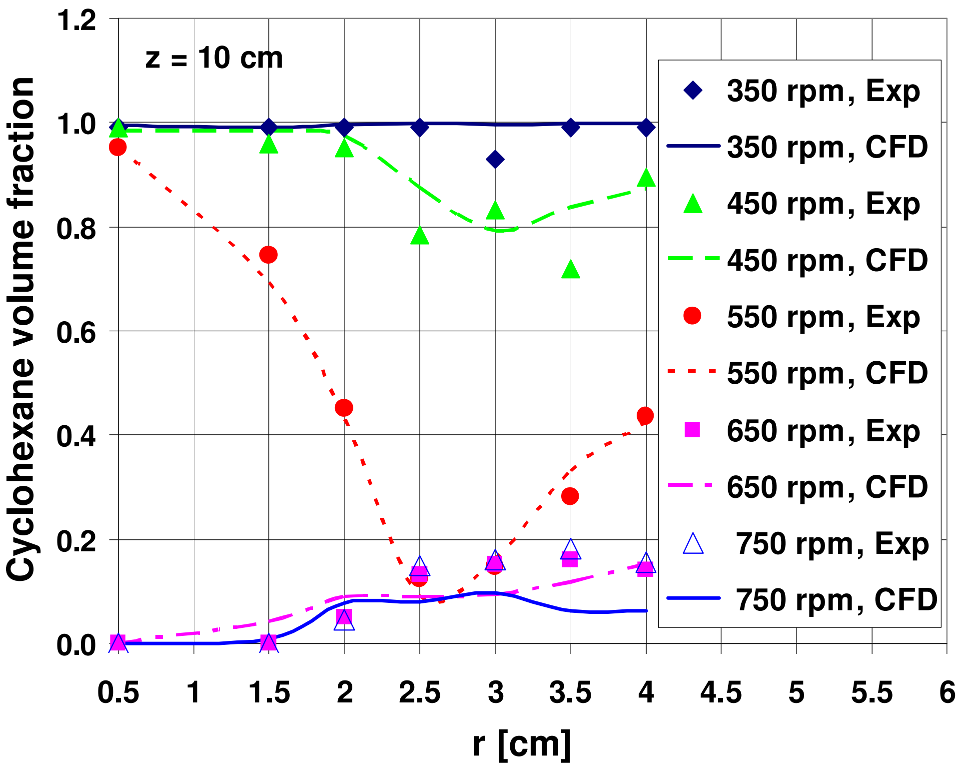

Figure 5.24-g: Measured and predicted radial cyclohexane volume fraction profiles at different RTI velocities and z = 10 cm.

5.3.2.3 RTI velocity for complete and uniform dispersion

The minimum velocity for complete dispersion is determined when there is no pure cyclohexane at the top near the free surface, whereas the minimum velocity to get a uniform dispersion is obtained when the volumetric fractions of cyclohexane have approximately similar values in the axial and radial positions in the vessel. For that the CHVF values are plotted as a function of RTI velocity for radial positions from r = 0.5 to 4 cm in Figs. 5.25- a to f and axial positions from z = 4 to 10 cm in Fig. 5.26- a to f. The minimum velocity to get a complete dispersion is found to be dependent on the sampling position, it is 550 rpm at r = 0.5 cm, 450 rpm at r = 1.5, 2 cm and 400 rpm at r = 2.5, 3 and 4 cm. The minimum velocity to get a uniform dispersion is 750 rpm at r = 0.5 cm near the shaft, 650 rpm at r = 1.5 and 2 cm, 550 rpm at r = 2.5 and 3 cm and 650 rpm at r = 4 cm near the wall. The uniform cyclohexane volume fraction near the shaft is about 0.45 and about 0.2 in the vicinity of the vessel. For that the minimum velocity to get a complete dispersion at the radial positions in the vessel is

550 rpm and to get a nearly uniform dispersion is 750 rpm. Thus the RTI velocity should be little bit greater than 750 rpm to get a homogeneous distribution in the whole vessel. The effect of the RTI velocity on the axial and radial distribution profiles of cyclohexane is illustrated in the previous sections and can be also confirmed from the illustrations in Figs. 5.25 and 5.26.

Cyclohexane holdup approaches the volume fraction of the dispersed phase initially of 0.2 at a minimum RTI velocity of 550 rpm when $r \geq 1.5$ cm (between the impeller blades and the cylindrical walls) and 4 cm $\leq z \leq$ 6 cm (Fig. 5.26-a,b and c), the highly dispersed turbulence region that affected by the strong radial flow of the impeller, and 650 rpm when 8 cm $\leq z \leq$ 10 cm (the upper region of the dispersion which possesses lower intensity of energy dissipation and turbulence) as can be seen in Fig. 5.26-d,e and f. The minimum velocity to get a complete dispersion is determined by following the CHVF profile at 8 cm $\leq z \leq$ 10 cm, when the unmixed pure layer of cyclohexane at the top disappears and incorporated into water phase. It is found to be 450 rpm for $r \geq 1.5$ cm and 550 rpm for 0.5 cm $\leq r \leq$ 4 cm. A nearly constant CHVF of about 0.45 is approached near the shaft in the axial distances at RTI velocity of 750 rpm. For that the minimum velocity to get a complete dispersion is 550 rpm and to get a uniform dispersion is 750 rpm in the whole axial positions in the vessel. The maximum intensity of the dissipation energy and liquid velocity is found near the blades of the impeller, for that it requires lower stirrer velocity to reach the uniform dispersion there. Whereas it requires higher velocities near the shaft and in the upper level of the dispersion at $z \geq 8$ cm. The maximum height of the upper circulation is about 6 cm from the bottom of the vessel, and about 2.8 cm above the RTI.

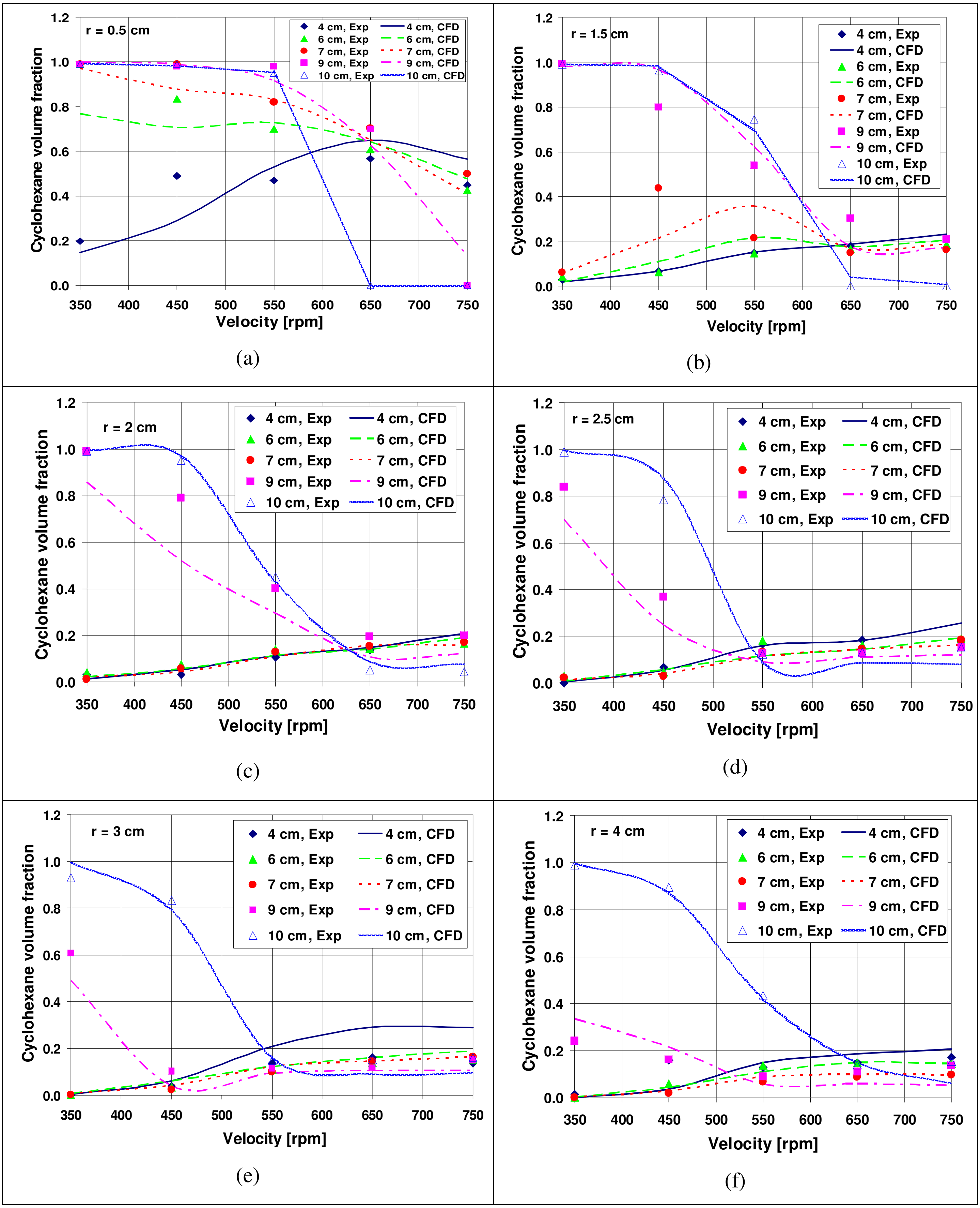

Figure 5.25: Measured and predicted cyclohexane volume fraction profiles at different RTI velocities and radial coordinates of 0.5 cm, 1.5 cm, 2 cm, 2.5 cm, 3 cm and 4 cm.

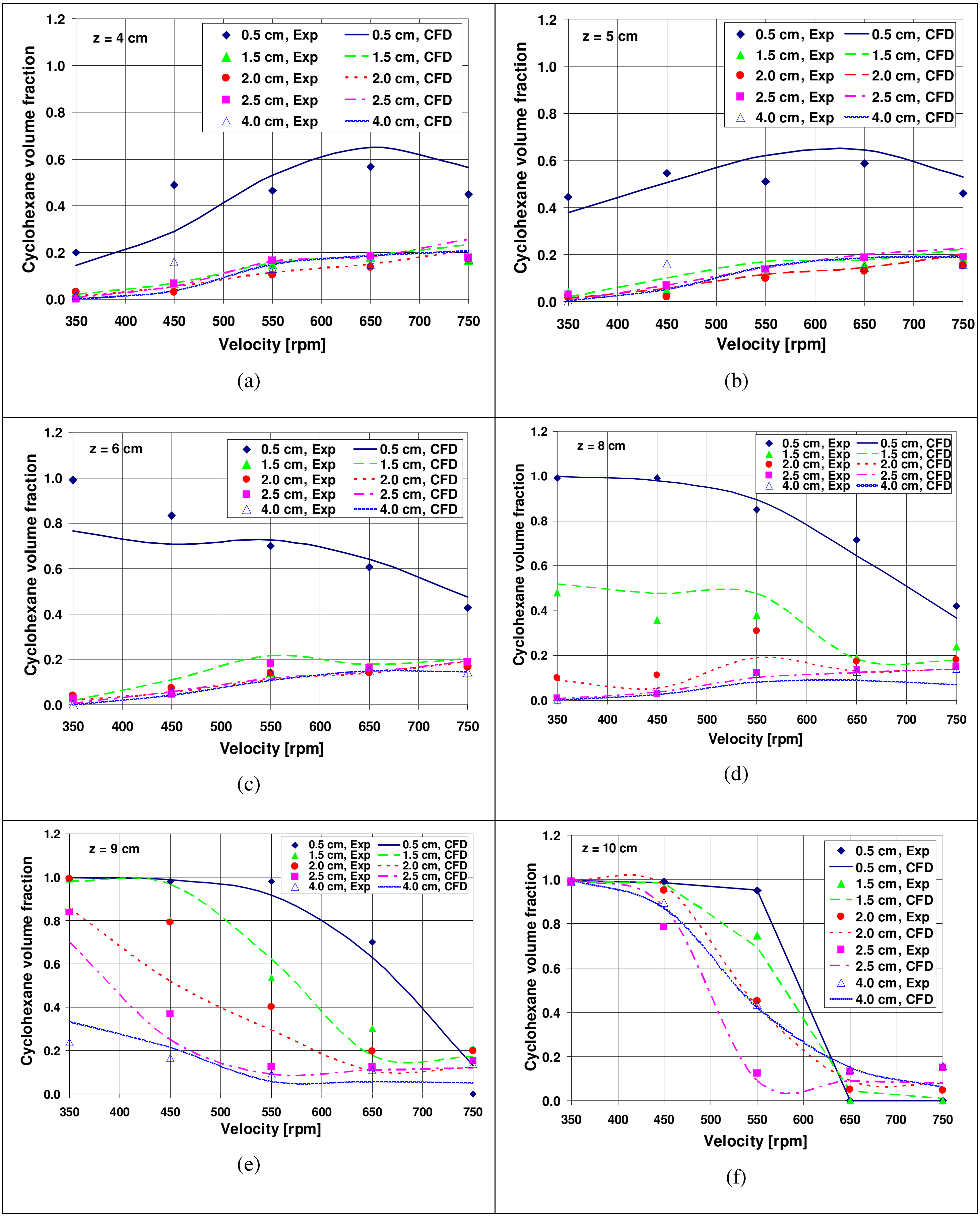

(a) (b) (c) (d) (e) (f)

Figure 5.26: Measured and predicted profiles of cyclohexane volume fraction at different RTI velocities and axial coordinates of 4 cm, 5 cm, 6 cm, 8 cm, 9 cm and 10 cm.

5.3.2.4 Effect of RTI clearance

When the RTI bottom clearance increases from 3.2 (near the bottom of the vessel) to 5.5 cm (nearly the mid of the total dispersion height) at a low velocity of 350 rpm, the thickness of the unmixed cyclohexane layer at r = 0.5 cm (near the shaft) decreases from 4 to 2 cm, respectively suggesting incomplete dispersion of cyclohexane as illustrated in Fig. 5.27-a.

Further increase of the RTI velocity to 550 rpm, reduces the thickness of the unmixed cyclohexane layer to 1 cm below the free surface at RTI clearance of 3.2 cm. Whereas a complete dispersion of cyclohexane is obtained at clearances of 4.1 and 5.5 cm, because the small distance between the impeller and the upper cyclohexane phase enhance the transport of the turbulence and impeller velocity to that region, thus the holdup of cyclohexane into water is improved when RTI bottom clearance increases. An air vortex is formed around the shaft with depth of 1 cm and 2 cm below the free surface at clearances of 4.1 and 5.5 cm, respectively.

The dispersion will be much faster and uniform above the impeller, but it is expected to be smaller and less uniform below the RTI impeller when the clearance increases, because the dispersion flow is radial towards the walls of the vessel then upwards above the impeller, caused by the dominant buoyancy effect where the gravitational force effect is smaller.

Increasing the RTI velocity to 750 rpm for RTI clearance of 5.5 cm increases the depth of the air vortex to a level close to the impeller, whereas a uniform dispersion of cyclohexane is obtained at 4 cm < z < 8 cm for RTI clearances of 3.2 and 4.1 cm, see Fig. 5.27-a. The trend of the axial profile of cyclohexane volume fraction and the dispersion behaviour near the shaft and in the region of the impeller for RTI clearances of 4.1 and 5.5 cm are similar to that described in case of RTI clearance of 3.2 cm (section 5.3.2.1).

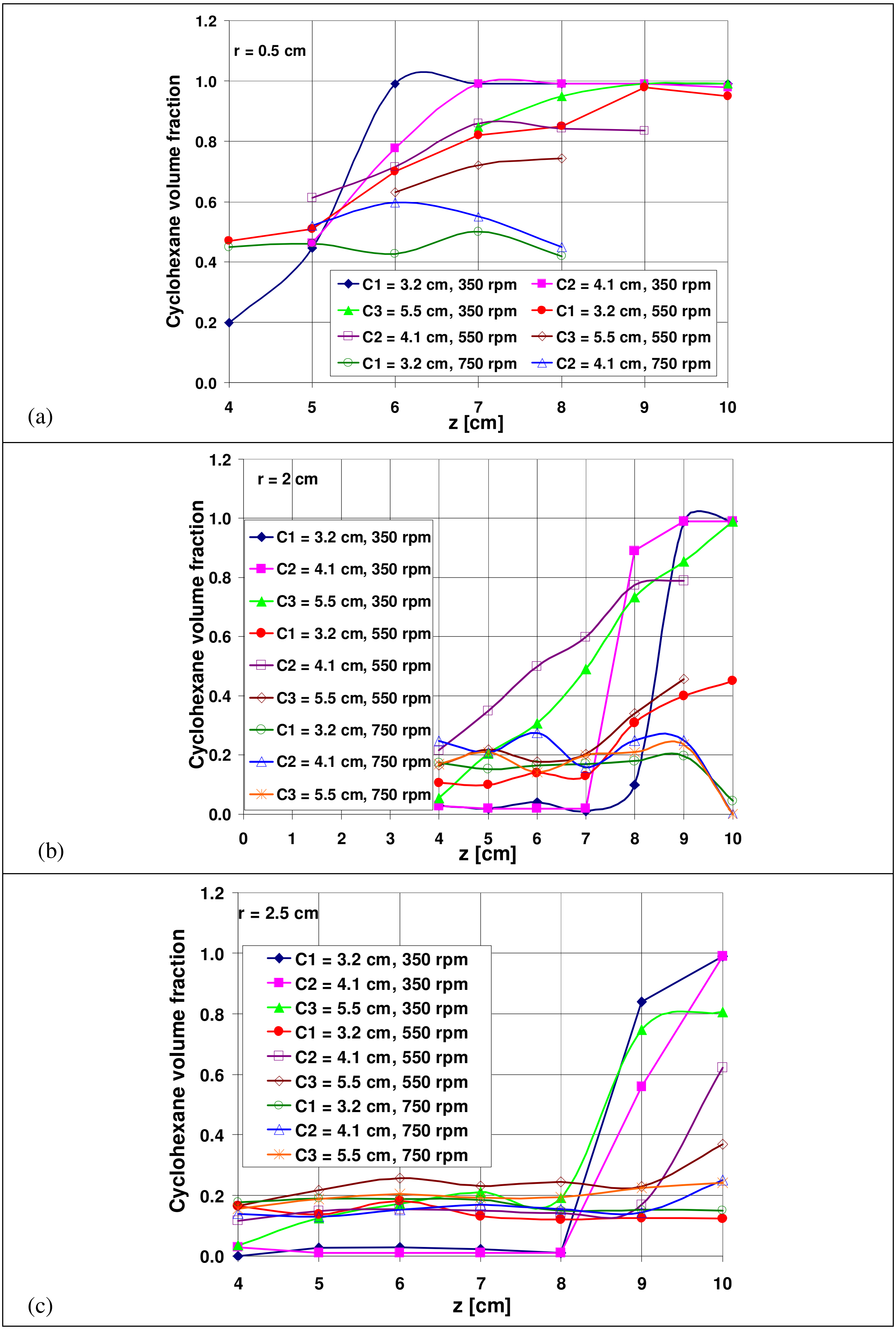

Figure 5.27: Axial profiles of cyclohexane volume fraction at r = 0.5, 2 and 2.5 cm for RTI velocity of 350, 550 and 750 rpm at clearances of 3.2, 4.1 and 5.5 cm, experimentally.

At low RTI velocity of 350 rpm, the axial holdup of cyclohexane between 4 cm < z < 8 cm (high energy dissipation and re-circulated vortices region) at RTI clearance of 3.2 cm is lower than that at 4.1 cm, but it shows the highest values at RTI clearance of 5.5 cm, due to the short distance between the impeller and the top layer of cyclohexane, that helps to transport the energy of the stirrer faster, and moves larger volume of cyclohexane towards the blades of the impeller, resulting in higher dispersion efficiency and collisions rates in the radial direction towards the cylindrical wall of the vessel, see Fig. 5.27-b.

At RTI velocity > 550 rpm, both clearances of 3.2 and 5.5 cm give similar holdup profiles of cyclohexane with very small difference in the all axial and radial positions, especially at r ≥ 2.5 cm as can be seen in Fig. 5.27-c and d.

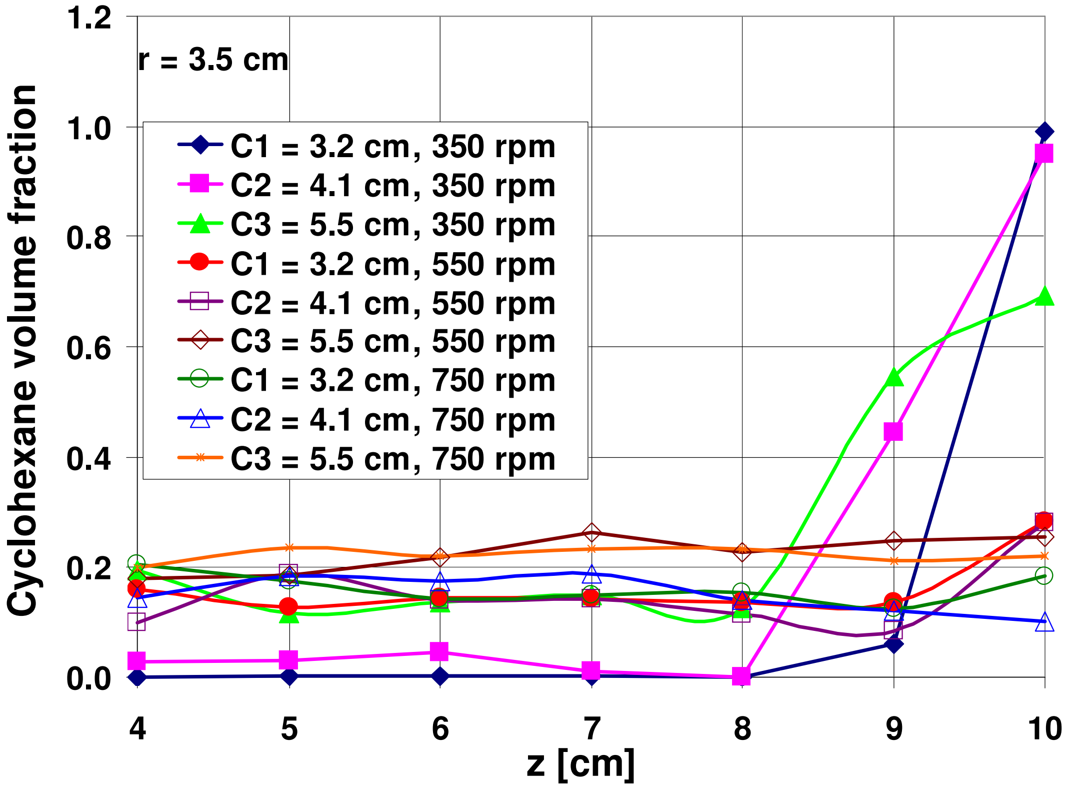

Figure 5.27-d: Axial profiles of cyclohexane volume fraction at r = 3.5 cm for RTI velocity of 350, 550 and 750 rpm at clearances of 3.2, 4.1 and 5.5 cm, experimentally.

The minimum RTI velocity to get a uniform dispersion of cyclohexane is 750 rpm for the three clearances, which means it is independent on the impeller clearance. The complete dispersion velocity for the RTI clearance of 5.5 cm is (400 rpm) < 4.1 cm (500 rpm) < 3.2 cm (550 rpm).

The effect of RTI clearance on the radial profiles of cyclohexane volume fractions is shown in Fig. 5.28-a to c. When the RTI clearance increases to 5.5 cm, the holdup of cyclohexane at $z = 5$ cm (near the blades of the impeller) will be higher than that at clearances of 3.2 and 4.1 cm at all RTI velocities, but with very small difference at high RTI velocity of 750 rpm, see Fig. 5.28-a.

At $z = 7$ cm, the cyclohexane is concentrated around the shaft at low RTI velocity of 350 rpm, and then it spreads outside towards the walls of the vessel, thus the volumetric fractions decreases around the shaft and increases in the vicinity of the vessel around the impeller.

At RTI velocity of 750 rpm, it is possible to get a uniform and constant values of cyclohexane volume fraction in all of the axial positions at a given radial position, but this situation can be obtained only at $r \geq 1.5$ cm in the radial positions at a given axial position, because the dispersion around the shaft is most difficult where high volume fractions of cyclohexane exist.

The air vortex is formed at RTI velocity of 550 rpm for RTI clearance of 5.5 cm at $z = 9$ cm with width of about 2 cm as can be seen in Fig. 5.28-c, whereas it is formed at RTI velocity of 750 rpm for RTI clearance of 4.1 cm, and no air vortex is formed at 3.2 cm clearance.

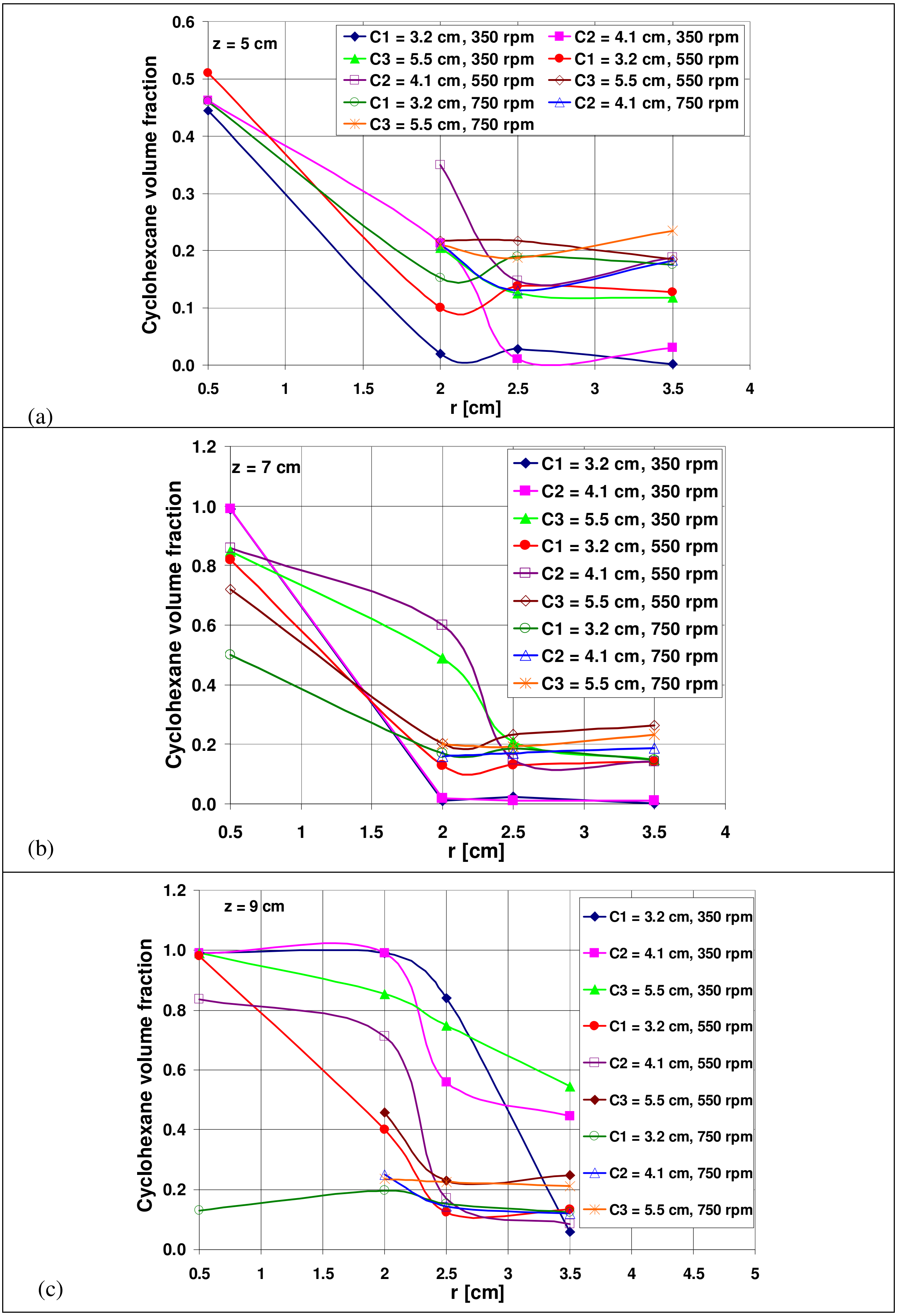

Figure 5.28: Radial profiles of cyclohexane volume fraction at z = 5, 7 and 9 cm for RTI velocity of 350, 550 and 750 rpm at clearances of 3.2, 4.1 and 5.5 cm, experimentally.

5.3.3 Cyclohexane dispersion with propeller impeller

5.3.3.1 Axial profile

The axial profiles of cyclohexane volume fraction at r = 2 cm in the middle between the shaft of the propeller and the walls of the vessel is shown in Fig. 5.29 at propeller velocity from 300 to 650 rpm and bottom clearance of 4.1 cm. Similar trend is found for all propeller velocities.

The axial profile of CHVF is divided into three regions because the intensity of the dissipation energy varies with the position in the vessel regarding to the impeller location: the highly efficient dispersion impeller region between 5 cm $\leq$ z $\leq$ 7 cm which possesses large input energy and turbulence, the intermediate dispersion efficiency between 7 cm < z < 9 cm and the weak dispersion region between 9 cm $\leq$ z $\leq$ 10 cm which shows a small dispersion of cyclohexane into water (high volume fractions) because the minimum dissipation energy and turbulence exist there. The strong axial circulations produced by the propeller impeller are responsible for this distribution of cyclohexane in the axial distances. Increased propeller velocity improves the dispersion in the axial direction, more significantly near the impeller between 5 cm $\leq$ z $\leq$ 7 cm. When the propeller velocity increases, the volume fractions of cyclohexane near the impeller increase, and they decrease at the top near the free surface. Air-liquid interface is affected by the axial and radial flow impellers. An air vortex with a depth of about 1 cm and width of about 2 cm is formed at a propeller velocity of 550 rpm (Fig. 5.29).

A uniform and a homogeneous dispersion with a nearly constant value of CHVF (about 0.2, the initial volume fraction of cyclohexane) between 5 cm $\leq$ z $\leq$ 8 cm is obtained at a minimum propeller velocity of about 400 rpm, whereas cyclohexane is dispersed into water with different volume percentage between 8 cm < z < 10 cm. The dispersion behaviour and the minimum velocity for complete and uniform distribution obtained from the CHVF distribution profiles are very similar to that obtained from visualization.

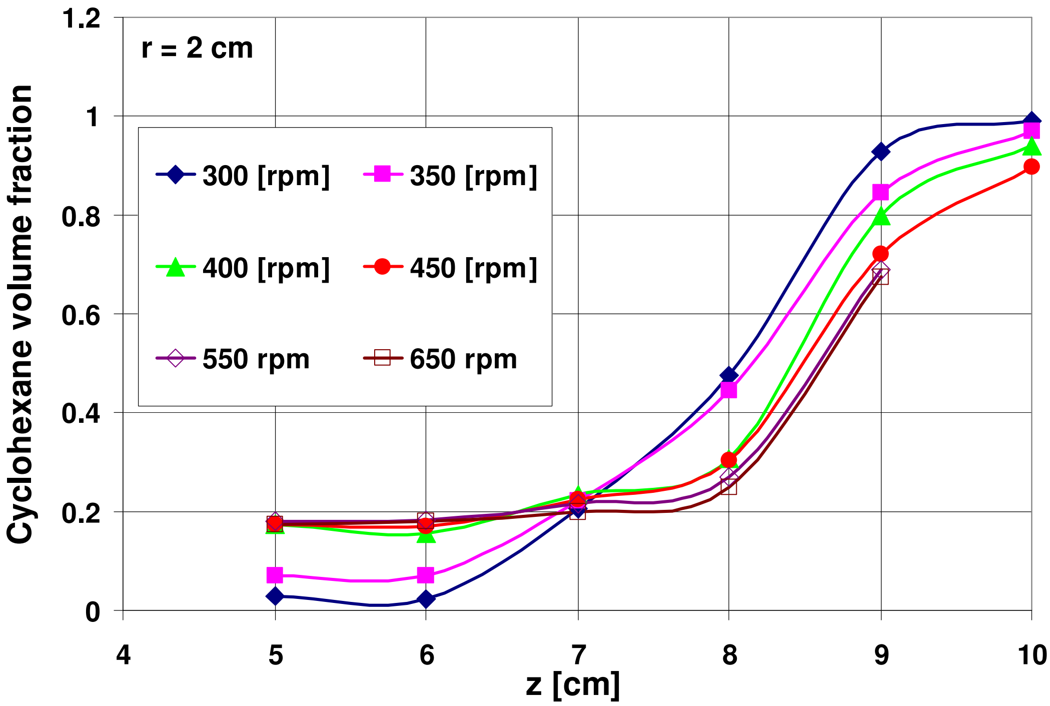

Figure 5.29: The axial profile of cyclohexane volume fraction at r = 2.0 cm for different propeller velocities at clearances of 4.1 cm, experimentally.

5.3.3.2 Radial profile

The radial profile of cyclohexane volume fractions at a given axial position z = 7 cm and propeller velocity from 350 to 650 rpm is shown in Fig. 5.30. High volume fractions of cyclohexane between 0.8 and 0.95 at all propeller velocities are found near the shaft, suggesting very poor dispersion there. For r > 2 cm and z = 7 cm, a nearly uniform dispersion of cyclohexane is obtained at a minimum propeller velocity of about 450 rpm. There can be seen a sudden change of the CHVF between 1.5 cm < r < 2 cm. Increasing propeller velocity has no effect on the holdup of cyclohexane between 1.5 cm < r < 2.5 cm, suggesting formation of dead zone there. When the propeller velocity increases, the volume fraction of cyclohexane decreases slightly at r < 1.5 cm near the shaft, and increases at r > 2.5 cm near the cylindrical walls. This distribution of cyclohexane into water emphasize the formation of the axial circulation between 1.5 cm < r < 2.5 cm by the propeller impeller. There is no significant effect of the propeller velocity inside the axial circulation. It can be remarked from the axial profile of CHVF in Fig. 5.29 that the axial circulation may exists between 7 cm ≤ z ≤ 9 cm.

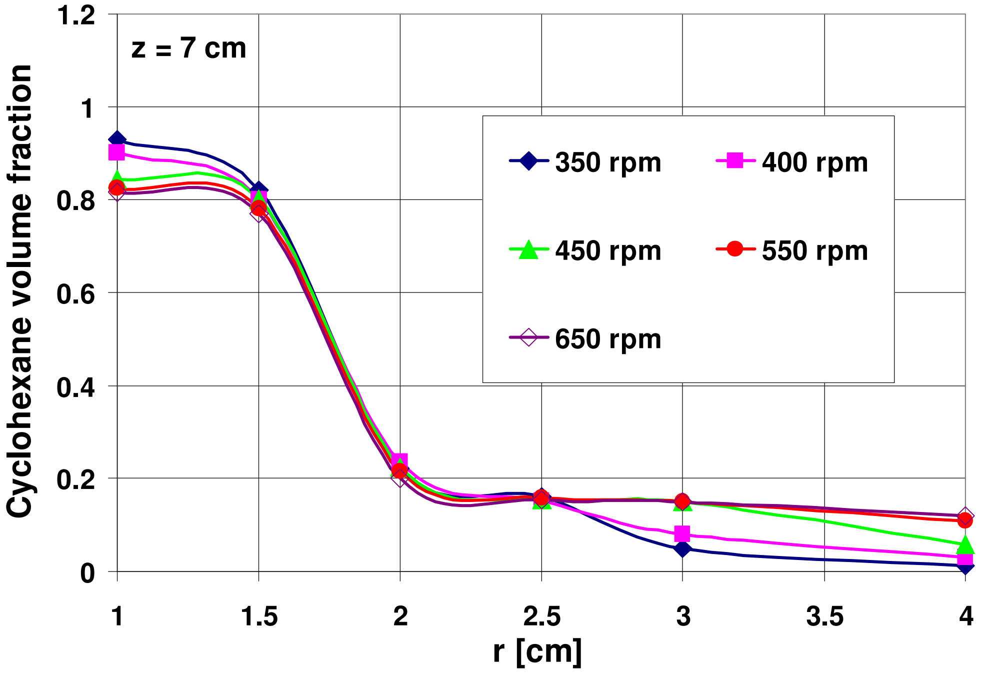

Figure 5.30: The Radial profile of cyclohexane volume fraction at z = 7.0 cm for different propeller velocities at clearances of 4.1 cm, experimentally.

5.3.3.3 Propeller velocity for complete and uniform dispersion

Cyclohexane volume fraction is plotted as a function of the propeller velocity at r = 2 cm at different axial positions as illustrated in Fig. 5.31. The minimum propeller velocity to get a complete dispersion of cyclohexane into water is between 350 and 400 rpm as can be seen at z = 10 cm (near the free surface), where there is no pure cyclohexane at that level near the free surface. It is possible to get a uniform dispersion of cyclohexane (CHVF reaches approximately the initial volume fraction of 0.2 at t = 0) into water in the axial position between 5 cm ≤ z ≤ 8 cm at a minimum velocity of 450 rpm (Fig. 5.31) and in the radial positions between 2 cm ≤ r ≤ 4 cm at a higher RTI velocity of 550 rpm (Fig. 5.32), because the dispersion in the axial distances is caused by the axial flow of the propeller. The energy and efficiency of the downward stream in the axial vortex affect the dispersion velocity in the radial distances. Weak dispersion of cyclohexane is found near the shaft at r = 1 and 1.5 cm, where the volume fractions of cyclohexane are high and they become nearly constant at a minimum velocity of 450 and 400, respectively as can be seen in Fig. 5.32. A minimum velocity of 350 rpm is enough to get a uniform dispersion at r = 2 and 2.5 cm (near the blades of the propeller), may be it is the starting point for the upward stream in the axial circulation, whereas the minimum velocity at r = 3 and 4 cm (near the cylindrical walls of the vessel), may be pass through the downward stream in the axial circulation, are 450 and 550 rpm, respectively, see Fig. 5.32.

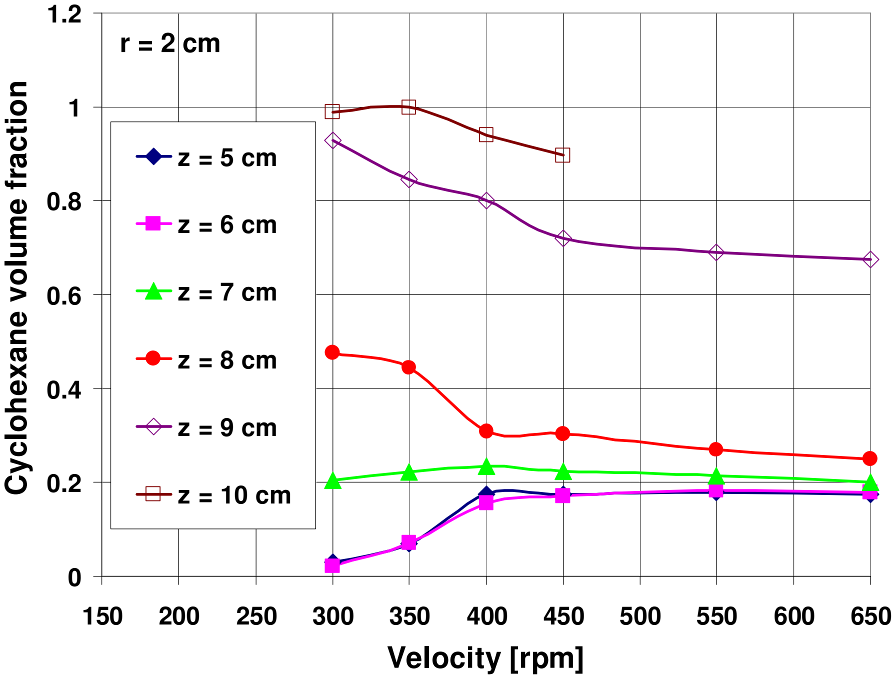

Figure 5.31: Axial profile of cyclohexane volume fraction at r = 2.0 cm as a function of propeller velocity at different axial positions and clearances of 4.1 cm, experimentally.

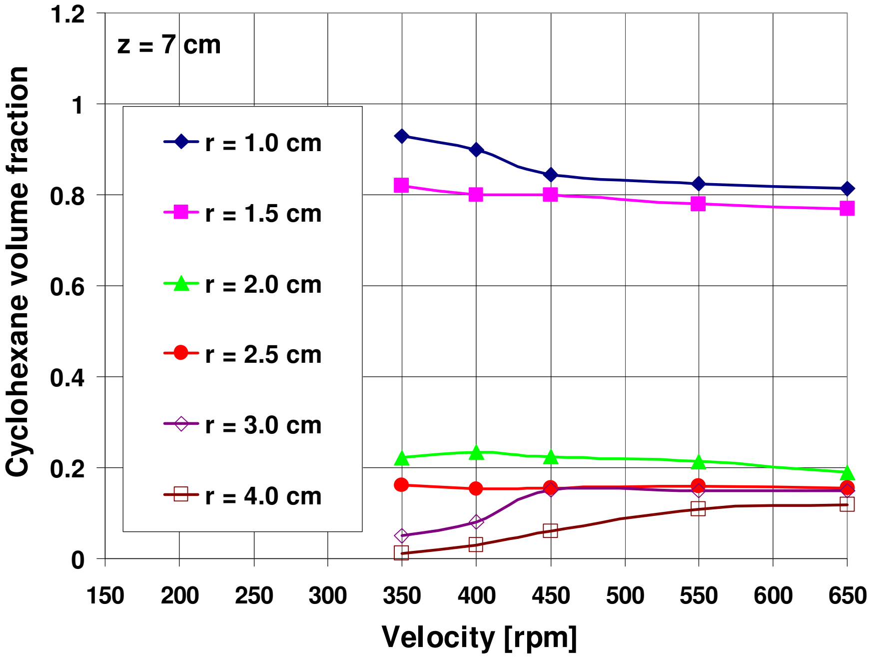

Figure 5.32: Radial profile of cyclohexane volume fraction at z = 8.0 cm as a function of propeller velocity at different radial positions and clearances of 4.1 cm, experimentally.

5.3.4 Cyclohexane dispersion with pitched blade turbine impeller

5.3.4.1 Axial profile

The axial profile of cyclohexane volume fraction at $r = 2$ cm and pitched blade turbine (PBT) velocity from 350 to 650 rpm can be seen in Fig. 5.33. The trend is similar to that found when RTI is used, because it produces a combined radial and axial flow, but mainly radial. The volume fractions of cyclohexane increase in the axial positions between 4 cm $\leq z \leq$ 8 cm (the region of high intensity of dissipation energy and turbulence) when the PBT velocity increases to reach a constant value of 0.2 (the initial volume fraction of cyclohexane) at a minimum velocity of about 500 rpm.

The volume fractions of cyclohexane decrease in the axial distances at $z > 8$ cm when the PBT velocity increases until the uniform dispersion of cyclohexane is obtained at a minimum PBT velocity of 550 rpm, where cyclohexane volume fraction reaches a nearly constant value of 0.2. It can be seen from Fig. 5.33 that the air vortex does not exist at $r = 2$ cm and $z = 10$ cm, may be due to the small effect of the inertial forces (centrifugal forces).

The combined flow of the PBT helps to disperse the cyclohexane droplets in the radial direction towards the cylindrical walls, resulting in vortices above and below the impeller, in addition to the axial flow which increase the kinetic energy in the upper layers of cyclohexane phase, thus enhance the rate of collision and turbulence which reduce the relative velocity between the two phases at lower PBT velocity of 550 rpm in compared with the axial and radial stirrers.

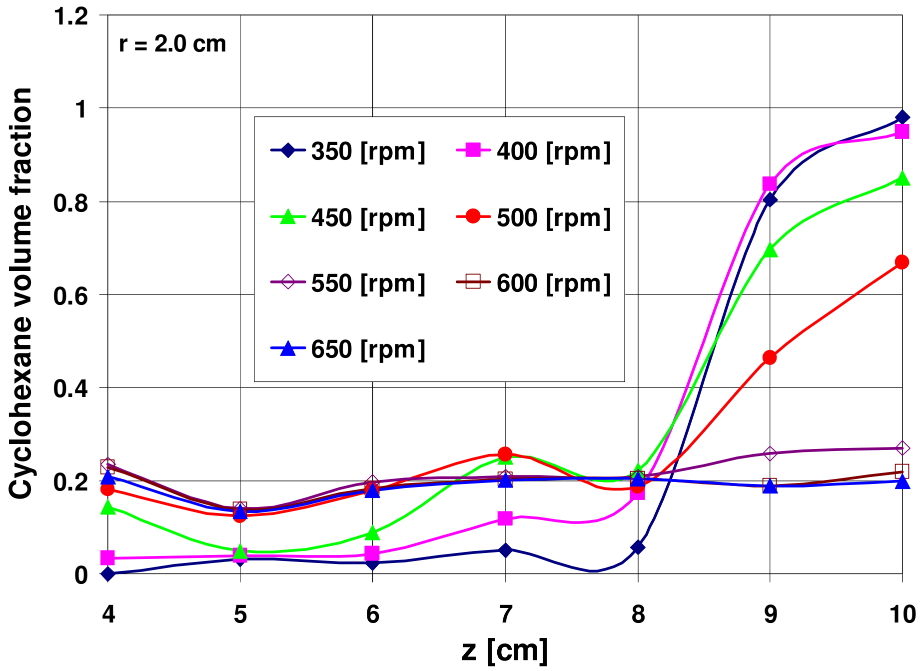

Figure 5.33: Axial profile of cyclohexane volume fraction for PBT impeller at different velocities and at r = 2.0 cm and clearance of 4.1 cm, experimentally.

5.3.4.2 PBT velocity for complete and uniform dispersion

The complete dispersion occurs at a minimum PBT velocity of 450 rpm as can be seen at z = 10 cm, and the uniform dispersion of cyclohexane occurs at a PBT velocity of 550 rpm where a similar value of CHVF of about 0.2 is obtained in all of the axial positions at r = 2 cm (Fig. 5.34) and radial positions at z = 7 cm (Fig. 5.35).

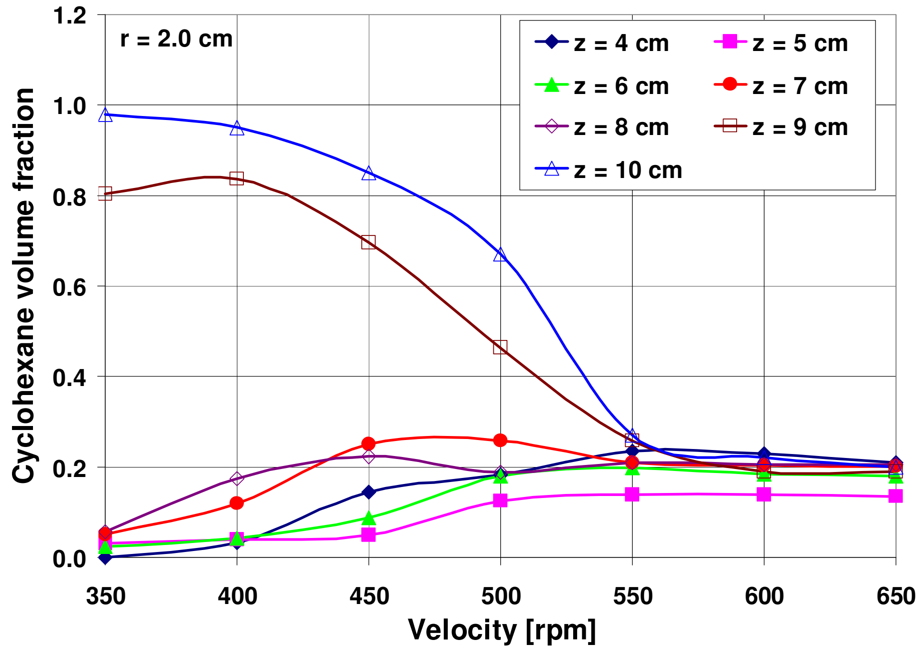

Figure 5.34: Axial profile of cyclohexane volume fraction for PBT impeller as a function of PBT velocity at r = 2.0 cm and clearance of 4.1 cm, experimentally.

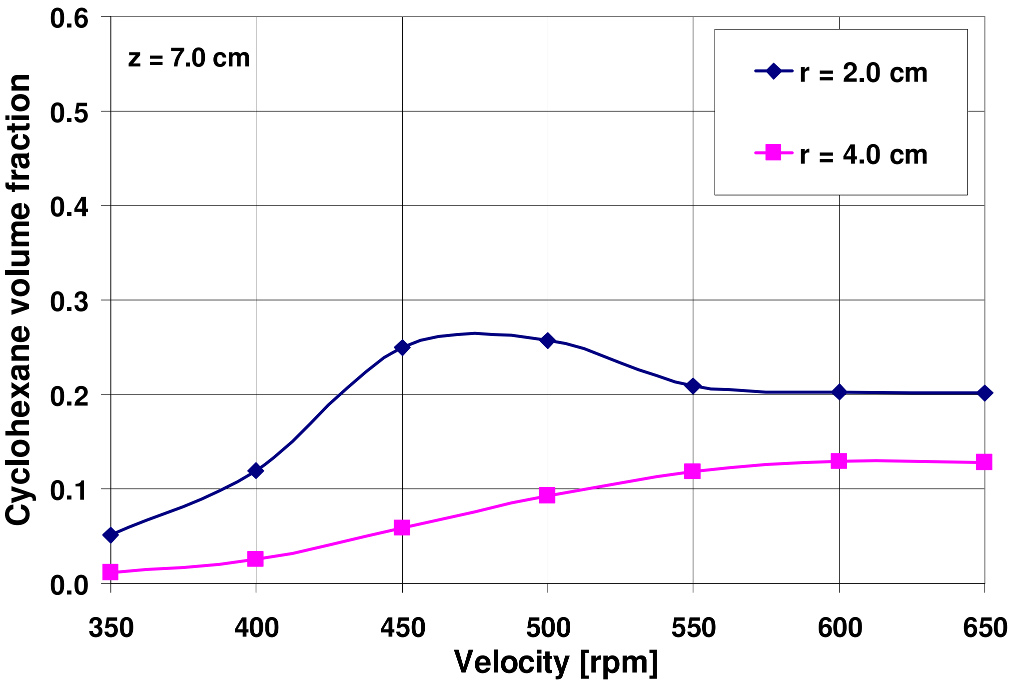

Figure 5.35: Radial profile of cyclohexane volume fraction for PBT impeller as a function of PBT velocity at z = 8.0 cm and clearance of 4.1 cm, experimentally.

5.3.5 Comparison the effect of stirrer type

The axial cyclohexane volume fraction profiles at r = 2 cm for anchor, RTI, propeller and PBT impellers at different stirrer velocities are illustrated in Fig. 5.36. Stirrer type has an effect on the interfacial tension between the two phases, which affects on the minimum velocity and power required for complete dispersion. The trend of the axial profile and the magnitudes of the cyclohexane volume fractions for anchor impeller at low velocity of 150 rpm is very close to that for the propeller at the minimum velocity of 350 rpm, but they are different in magnitude from the PBT and RTI, because the dispersion of cyclohexane at low stirrer velocity starts from the cylindrical walls towards the shaft of the impeller. The trend of the axial profile of CHVF at anchor velocity of 350 rpm is completely different from the other stirrers at a velocity ≥ 350 rpm. The cyclohexane is concentrated around the shaft of the anchor impeller due to the considerable effect of the surface tension between the two phases. In addition to the high centrifugal forces and velocity fluctuations between the two phases, this pushes the water phase outside to the walls of the vessel and upwards forming a large axial vortex in the water phase (see section 5.3.1). An air vortex is formed between the shaft and r = 2 cm and 9 cm < z < 10 cm for RTI and propeller impeller at a velocity of 550 rpm, but this vortex is not found at this position in the case of the PBT impeller. The holdup of cyclohexane in the case of PBT > propeller > RTI at stirrer velocity of 550 rpm (Fig. 5.36), because the PBT reduces the surface tension between the two phases strongly due to the high turbulence, dissipation energy and rate of collisions around the PBT, thus increasing the holdup of cyclohexane into water.

The complete dispersion of cyclohexane requires a velocity in the order of Anchor (350 rpm) < propeller (400 rpm) < PBT (450) < RTI (500 rpm). The dispersion of cyclohexane becomes uniform and homogeneous at PBT velocity of 550 rpm and at RTI velocity of 750 rpm.

With propeller impeller, uniform distribution is obtained at a minimum velocity of 550 rpm in the axial circulation between 4 cm ≤ z ≤ 8 cm. For z > 8 cm, there is no uniform distribution of cyclohexane.

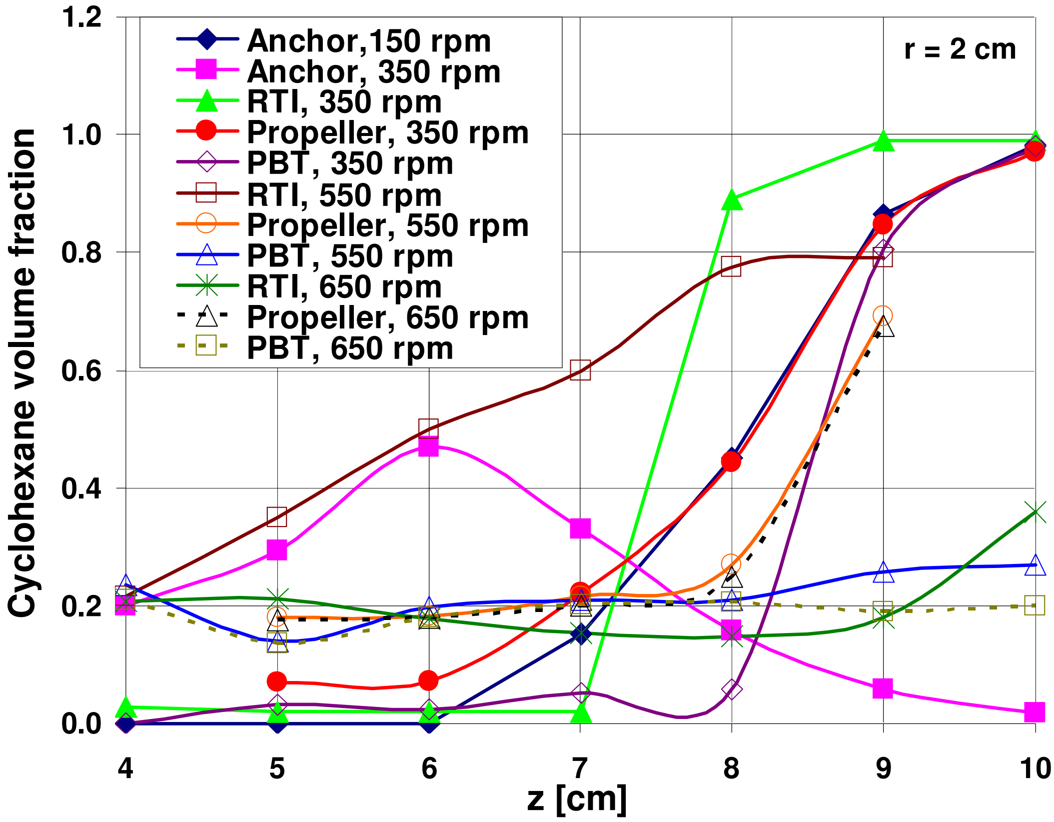

Figure 5.36: Axial cyclohexane volume fraction for Anchor, RTI, propeller and PBT for different velocities at r = 2.0 cm and clearance of 4.1 cm, experimentally.

The effect of the centrifugal forces and the relative velocity between the two phases are higher in case of the anchor impeller compared with that in the case of propeller. For that the level of the dispersion increases when the anchor velocity increases, but it remains nearly constant in the case of the propeller impeller. The large axial flow produced by both impellers is responsible for the absence of the homogeneity in the whole vessel.

Comparing the radial profiles of cyclohexane for the four stirrers at z = 7 cm as a function of stirrer velocity is illustrated in Fig. 5.37. The anchor at a velocity of 150 rpm shows similar radial profile like that obtained by the propeller impeller for velocities ≥ 350 rpm. Whereas in case of the RTI, when the velocity increases, the holdup of cyclohexane increases in the radial distances and then cyclohexane is distributed above and below the RTI impeller.

A nearly uniform dispersion of cyclohexane can be obtained with the RTI in the radial positions, but this can be for the propeller impeller only at r ≥ 2 cm near the blades of the propeller.

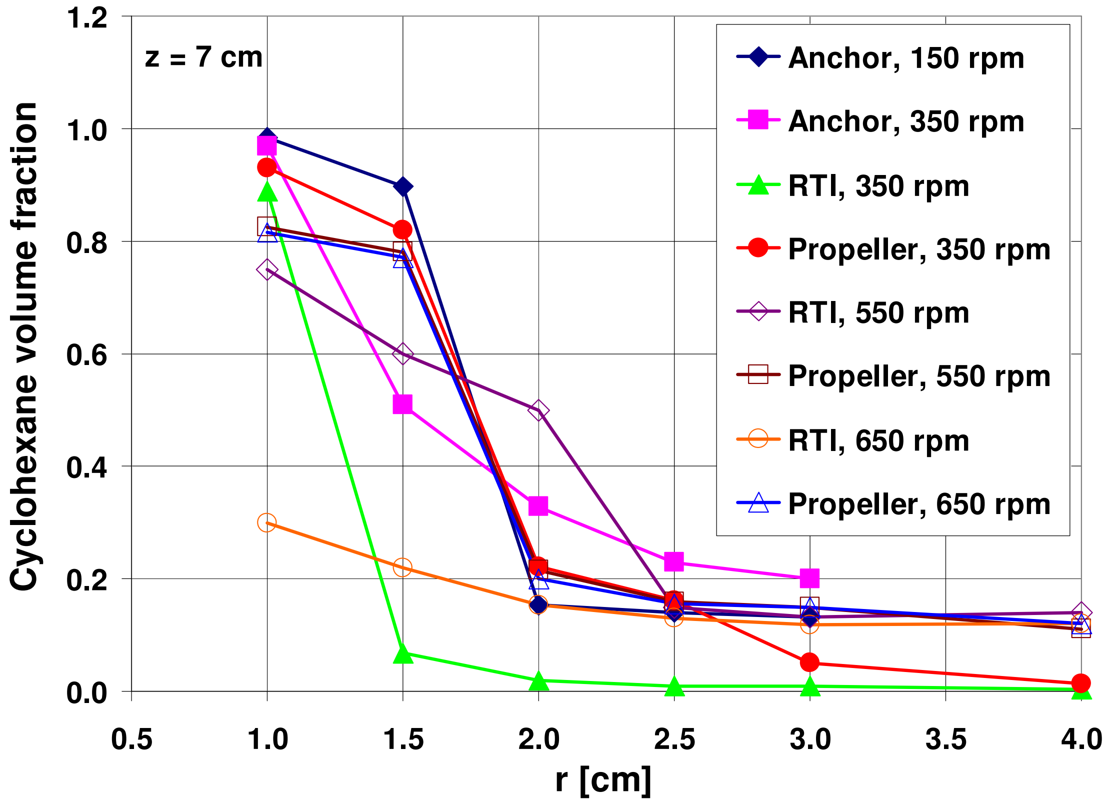

Figure 5.37: Radial cyclohexane volume fraction for Anchor, RTI, propeller and PBT for different velocities at z = 7.0 cm and clearance of 4.1 cm, experimentally.

5.3.6 Effect of the momentum transfer model

In the dispersion with the RTI, the surface tension effect is very small compared to the breakup rate of the cyclohexane droplets, due to the formation of small eddies above and below the RTI, thus the droplets have spherical shape (no distorted droplets). The flow produced by RTI is turbulent, for that the drag coefficient C_D is independent on neither Reynolds number nor the shape of the droplets, and thus it has a constant value of 0.44. For that ASM is used in this case, it considers the slip and drift velocities of the cyclohexane that included in the drag force balance and momentum equation. The relative velocity between the two phases becomes close when the stirrer velocity increases. Whereas the effect of the interfacial tension between the two phases is considered by Ishii-Zuber model as described in section 5.3.1.1.

The calculated axial cyclohexane volume fraction profile at RTI velocity of 550 rpm by using the ASM and Ishii-Zuber drag force models in the different radial positions are validated by the comparison with the experimental data in Fig. 5.38. The ASM gives a very good agreement with the experimental date rather than the Ishii-Zuber model. With the ASM the dispersion of cyclohexane into water is higher than that with Ishii-Zuber model, where all of the cyclohexane layers at the top of the liquid phase are completely dispersed into water to reach the lowest point in the stirrer and spread towards the walls in the radial direction. As a result of the collisions with the walls of the vessel and the bulk water phase, cyclohexane dispersion is improved at high stirrer velocity of 550 rpm.

With the Ishii-Zuber model, very thin layer of cyclohexane can be found at the top of the liquid phases at $z = 10$ cm and $r \geq 1.5$ cm. Most of the cyclohexane is concentrated around the shaft of the RTI at $r = 0.5$ cm. Unmixed pure cyclohexane exists between 7 cm $< z <$ 10 cm and little bit between 5 cm $< z <$ 7 cm, with very few dispersion in the radial direction as can be seen clearly at r = 2.5 and 3.5 cm for the axial distances between 4 cm < z < 9 cm. A sharp increase of the cyclohexane holdup is found at z > 9 cm.

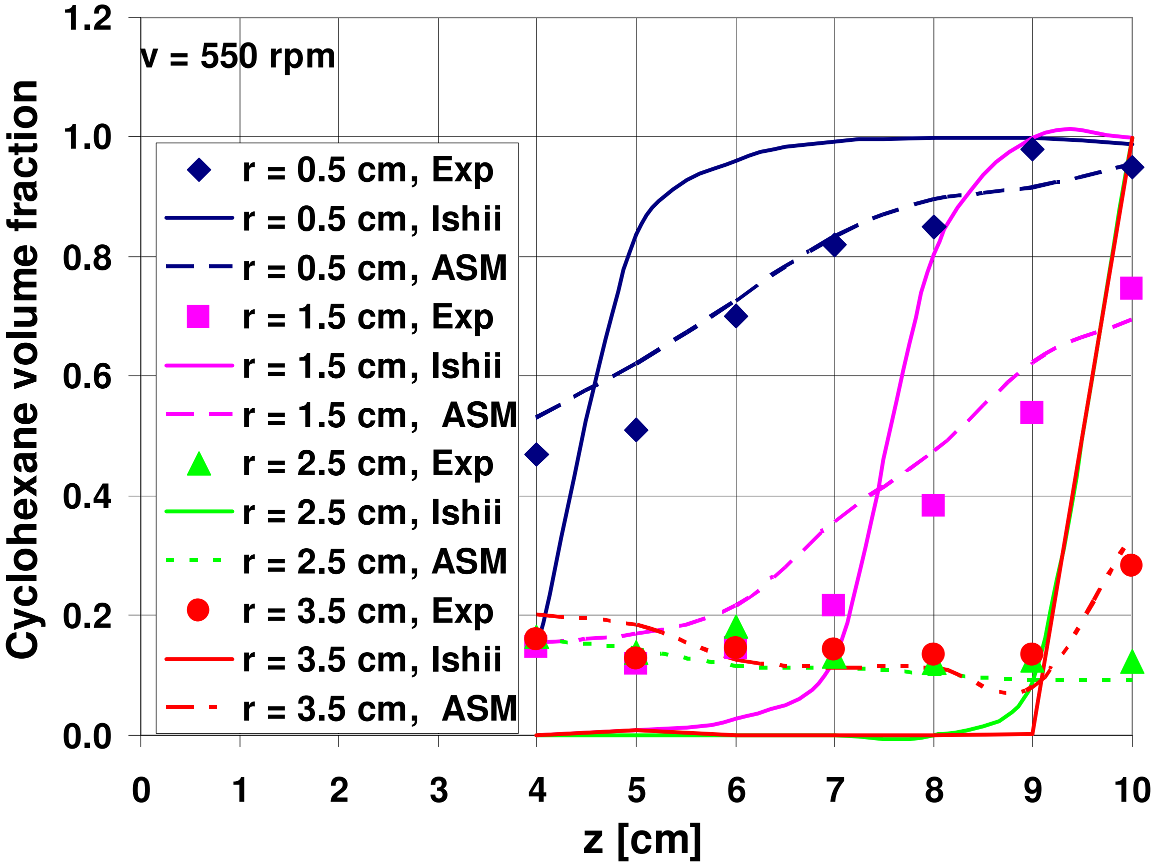

Figure 5.38: Cyclohexane volume fraction profile at different axial and radial positions for RTI velocity of 550 rpm, experimentally and with CFD simulation for ASM and Ishii-Zuber models for cell size of 0.001 m.

5.3.7 Effect of the grid cell size

The influence of the different grids on the flow field and distribution of the dispersed phase is investigated. The calculated axial profiles of cyclohexane volume fraction at RTI velocity of 550 rpm as a function of the grid cell size of 0.001 and 0.004 m in different radial positions by using Ishii-Zuber model are compared with the experimental data in Fig. 5.39. Unstructured fine grids allow much better cells around the blades resulting in higher radial dispersion of the cyclohexane and improve the dispersion around the impeller. The using of cell size of 0.001 m gives similar distribution of cyclohexane volume fractions that follow the trend of the measured data, because this very small cell size helps to transport the calculated variable from one cell to the neighbors more precise, based on the finite volume discretization method. The cell size of 0.004 m gives completely different distribution of cyclohexane volume fractions in the axial and radial distances, especially in the region of the impeller at r ≥ 1.5 cm, which are not consistent with the measured data.

In addition, fine mesh is very important in the case of RTI because there are two separate domains: the rotating small 6-blades RTI and the static vessel. If the mesh is not enough fine, there will be a gap between the small cells at the RTI and the large cells at the vessel (unmatched grid), so there will be missed data and inconsistency of the calculated variables in the two domains, resulting in a high numerical discretization error.

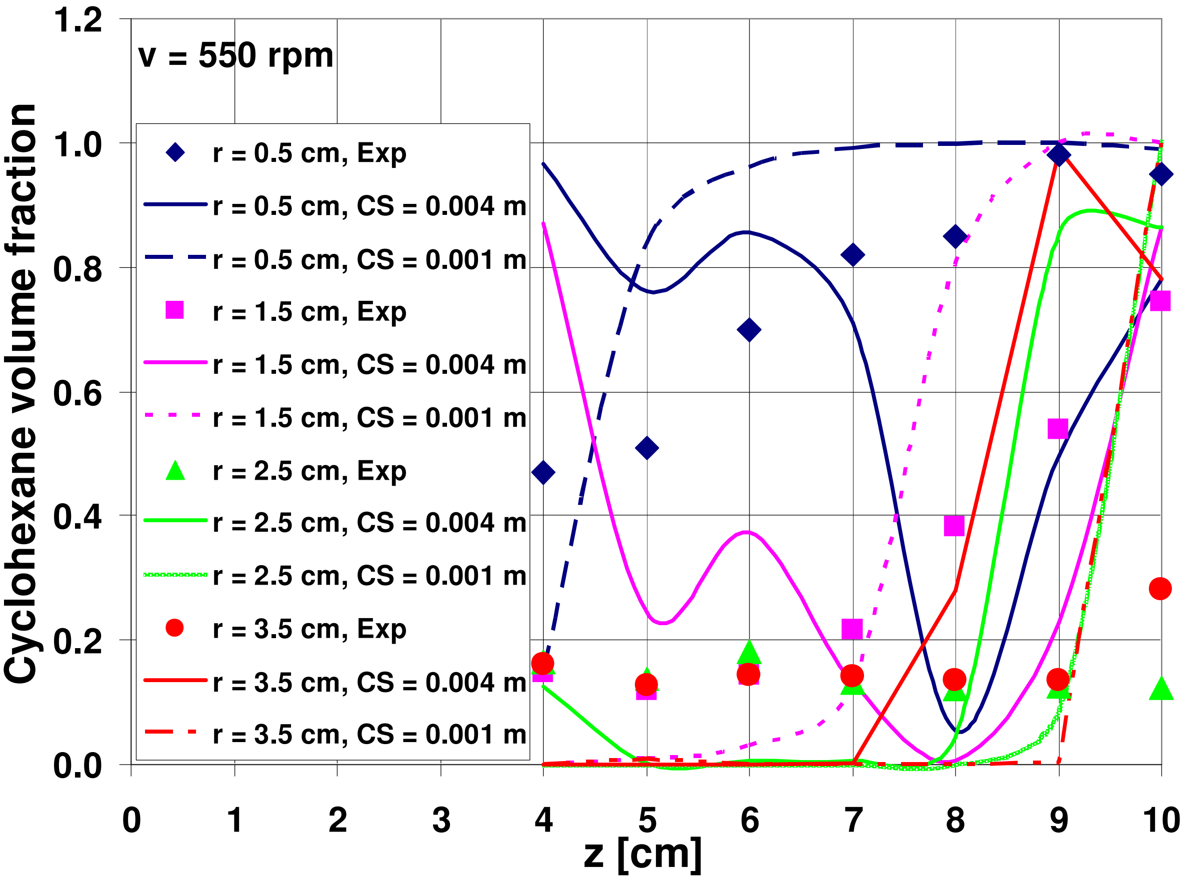

Figure 5.39: Cyclohexane volume fraction profile at different axial and radial positions for RTI velocity of 550 rpm, experimentally and with CFD simulation for cell size of 0.001 and 0.004 m by using Ishii-Zuber model.

5.4 Predicted and measured cyclohexane/water dispersion behaviour

The predicted cyclohexane/water dispersion behaviour from the CFD simulations is compared with the experimental data for validation of the used physical models.

5.4.1 Anchor impeller

5.4.1.1 Steady state dispersion behaviour

The predicted dispersion of cyclohexane in water is illustrated by using the isovolumes and contours for the density and cyclohexane volume fractions distribution in the vessel at different anchor velocities as can be seen in Fig. 5.40.

It is found that the multi-fluid and drag force Ishii-Zuber models are able to describe the dispersion and distribution of cyclohexane into water, which are very similar to that obtained from the visualisation method as well as the sampling method. The dispersion of cyclohexane starts from the walls of the vessel towards the shaft of the anchor, results in a wide symmetrical vortex that fills the distance between the vertical blades of the anchor impeller near the tip at a low velocity of 150 rpm, where a small volume of cyclohexane is dispersed into water. Increasing the velocity of the anchor impeller gradually from 150 rpm to 400 rpm increases the impeller power and energy dissipation which withdraws the cyclohexane into water towards the lower point in the shaft.

Dispersion occurs mainly at the interface between the two phases which consists of cyclohexane droplets as can be seen at high velocities of 350 and 400 rpm. The height of the cyclohexane vortex reaches the tip of the anchor impeller at a minimum velocity of 350 rpm, its width also fill the distance between the vertical arms of the anchor.

Due to the high centrifugal forces that dominate the shear forces of the anchor impeller, the water phase is pushed outside towards the walls of the vessel upwards, and cyclohexane phase downwards to the bottom of the vessel.

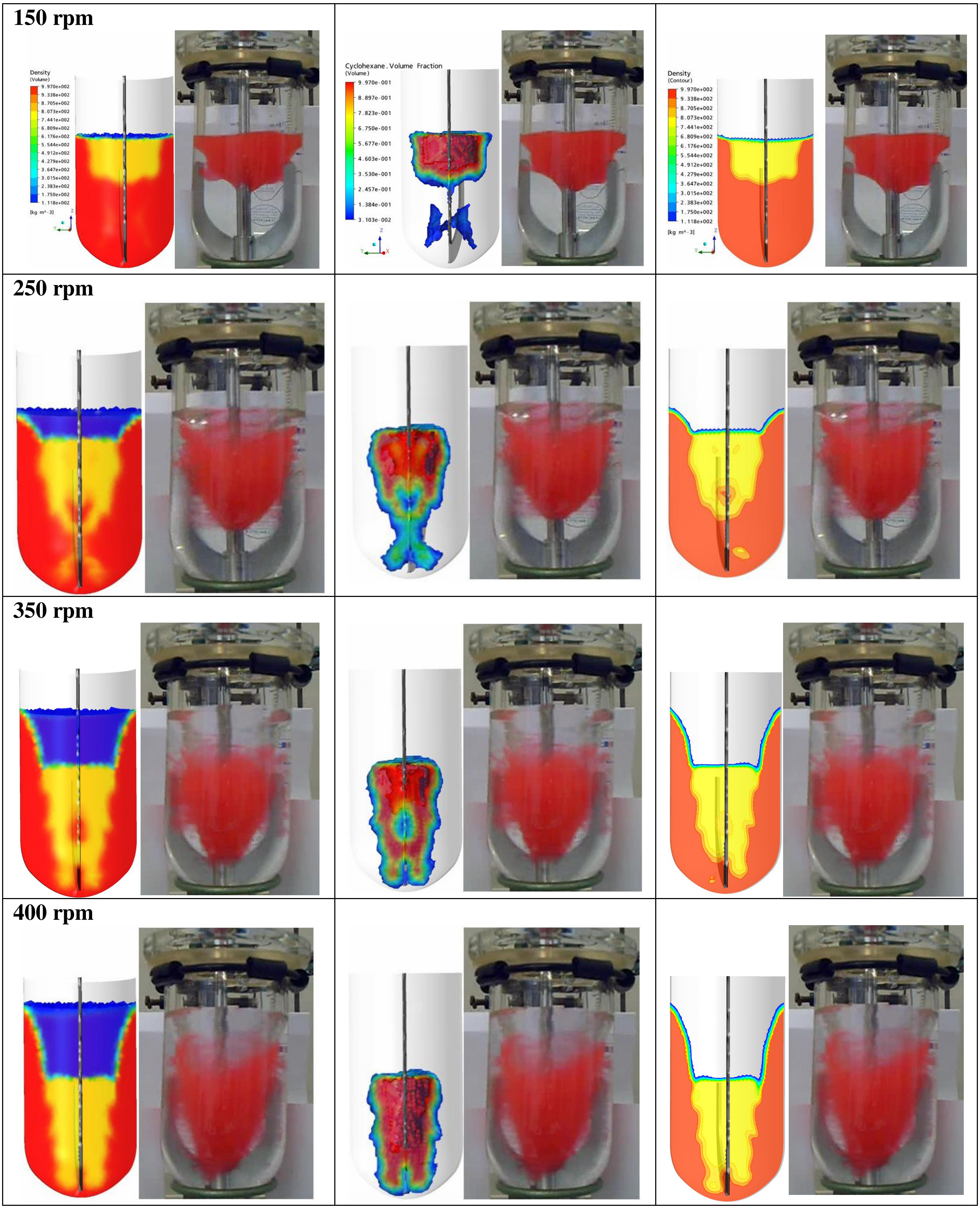

Figure 5.40: Dispersion behavior of cyclohexane in water, experimentally and with CFD simulations of the density distribution by using volume from surface (left) and contour (right), and volume fraction distribution by using isovolumes (middle) at different anchor velocities.

Small volume of water remains in the middle of the cyclohexane eddy at velocity of 250 and 350 rpm, see the cyclohexane volume fraction distribution in Fig. 5.40 (middle).

An air vortex is formed at the top leading to air/water and air/cyclohexane interfaces. The depth of the air vortex increases when the anchor velocity increases, caused by the high pressure forces exerted on the liquid phases by the anchor impeller, see Fig. 5.40 (left and right) for the density distribution in the vessel.

5.4.1.2 Transient predicted dispersion behaviour

The distribution of cyclohexane into water at anchor velocity of 150 rpm as a function of time is illustrated in Fig. 5.41 by using the contour plots of cyclohexane volume fraction. The development of the dispersion with time from the walls of the vessel towards the shaft is continued gradually until a steady flow is obtained and there is no further change in the flow pattern at t = 10 s.

The flow field results from transient calculations is very close to that obtained from the steady simulations (Fig. 5.40), but more precise predictions of CHVF at the interface between the two phases is found by using the transient simulations. So that very precise calculations between the impeller and the vessel are obtained, but they need very long time of calculations and large number of processors in parallel.

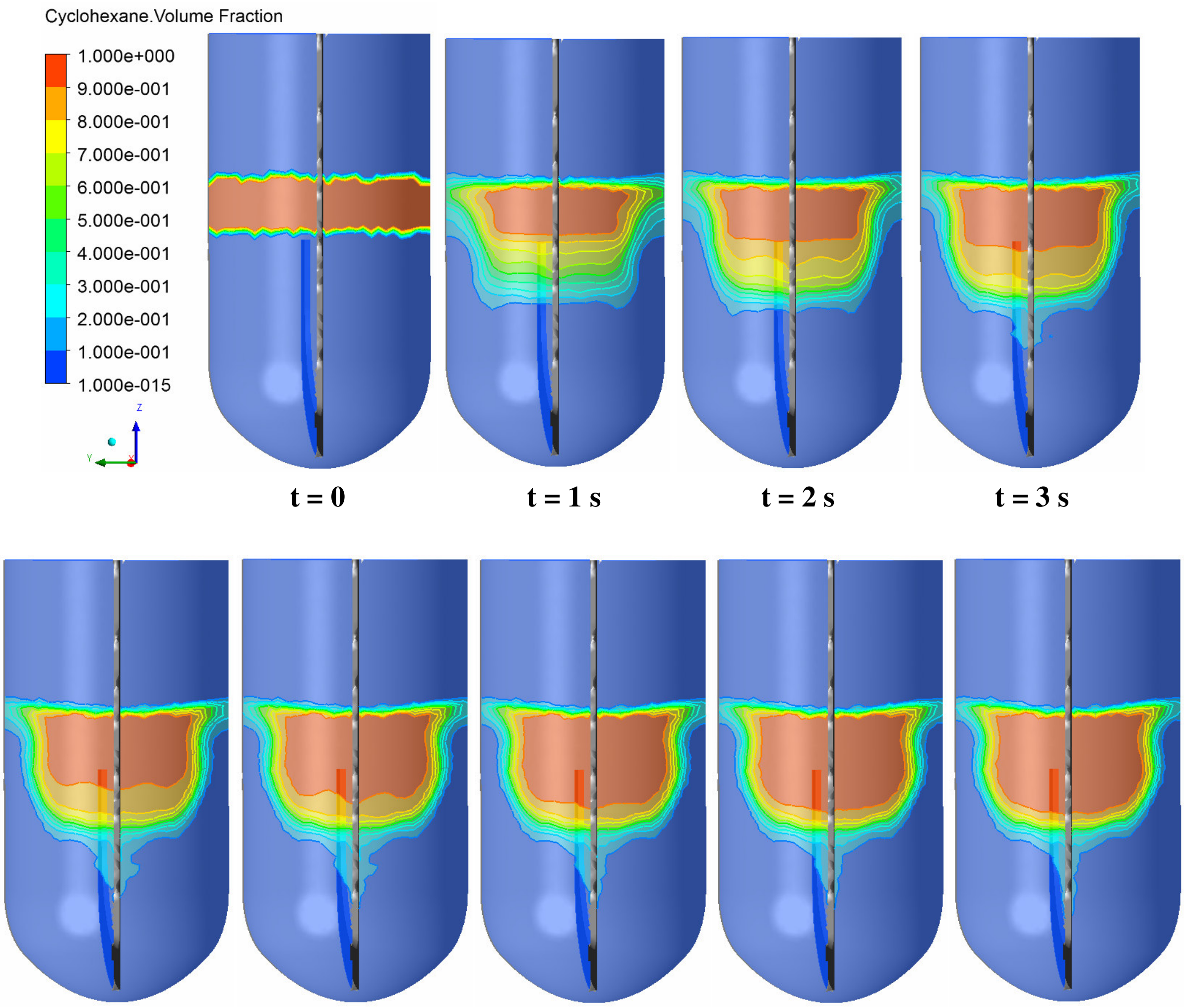

t = 0 t = 1 s t = 2 s t = 3 s

t = 4 s t = 5 s t = 6 s t = 7 s t = 10 s

Figure 5.41: Transient dispersion behaviour of cyclohexane/water system at anchor velocity of 150 rpm by using the contour plots of cyclohexane volume fraction.

When the anchor velocity increased to 350 rpm in Fig. 5.42, a sudden dispersion of the total body of cyclohexane at t = 1 s occurs, where it reaches quickly to the lower point in the shaft of the anchor impeller, forming a large eddy that fills the space between the blades of the anchor impeller (mainly the vertical arm) as explained in section 5.1.1. The flow pattern of cyclohexane distribution is close to that obtained from the steady state predictions with very small differences near the vertical blades. A proximately 60 s is the minimum dispersion time required to reach the steady flow field of cyclohexane.

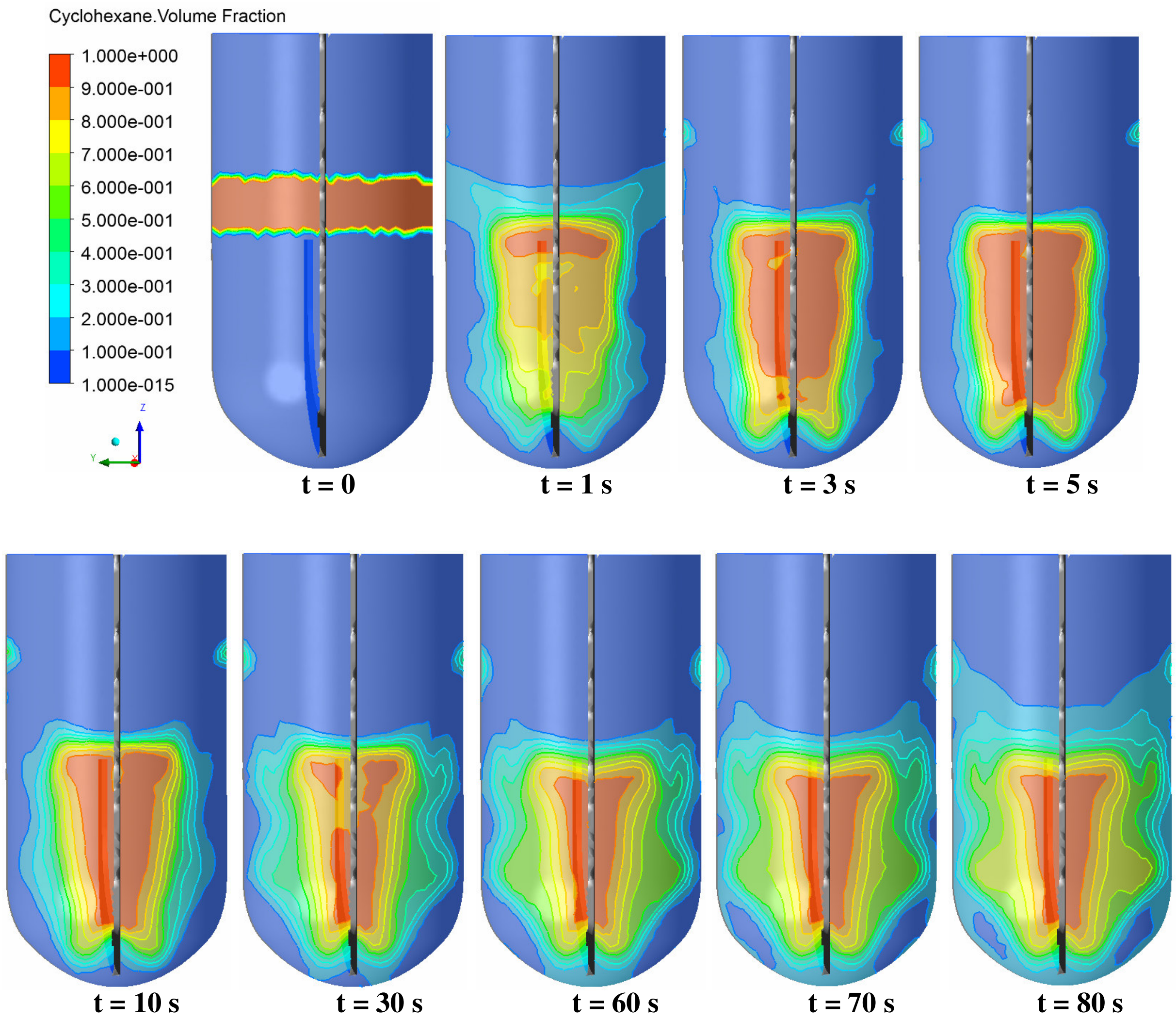

t = 0 t = 1 s t = 3 s t = 5 s

t = 10 s t = 30 s t = 60 s t = 70 s t = 80 s

Figure 5.42: Transient dispersion behaviour of cyclohexane/water system at anchor velocity of 350 rpm by using the contour plots of cyclohexane volume fraction.

5.4.2 Rushton turbine impeller

5.4.2.1 Steady state dispersion behaviour

The power of the impeller at low RTI velocity of 350 rpm (Fig. 5.43-a) is able to move the cyclohexane layer at the interface between the two phases towards the shaft of the impeller by diffusion. The volume of the red cyclohexane layer at the top of the liquid phases is still large.

Increasing the stirring intensity to 450 rpm increases the volume of the dispersed cyclohexane into water and decreases the volume of the layer at the top, so that the width of the vortex around the shaft increases. When the cyclohexane layer hits the impeller blades, it will breakup into small droplets that disperse into water towards the walls of the vessel in a radial flow. When these droplets collide the walls, they will be divided into two circulations as can be seen clearly at RTI velocity of 550 rpm from the density distribution contour plot in Fig. 5.43.b, the upwards one is the larger and the smaller one is formed downwards. Most of the droplets are dispersed in the upper part above the impeller because they are lighter than the water phase.

Similar results can be seen experimentally and with CFD simulations from the density and cyclohexane volume fraction distribution in Fig. 5.43-a and b. When the RTI velocity increases above 450 rpm (Fig. 5.43-b), the dispersion of cyclohexane droplets continues from that collected on the shaft and impeller blades and is distributed well, first in the upper side of the vessel. At a RTI velocity of 550 rpm the cyclohexane layer at the top nearly disappeared, suggesting that a complete dispersion of cyclohexane is obtained.

It can be seen that the weak dispersion areas are those found near the walls of the vessel near the free surface at the top and in the lower point in the bottom of the vessel due to the lower turbulent kinetic energy there.

The nearly uniform dispersion of cyclohexane into water can be obtained at RTI velocity of 750 rpm, where increasing the intensity of turbulence, number of recirculation and dissipation energy increase the dispersion of cyclohexane in the lower part below the impeller.

The uniform distribution of the red tracer in the vessel means that all cyclohexane is distributed uniformly in the whole vessel. Weak dispersion is found at the lowest point in the bottom of the vessel and at the cylindrical walls at the top near the free surface, suggesting the lowest intensity of dissipation energy regions. ASM is very suitable to predict the flow field, density and cyclohexane volume fraction distribution in a stirred vessel with RTI in a wide rage of velocities.

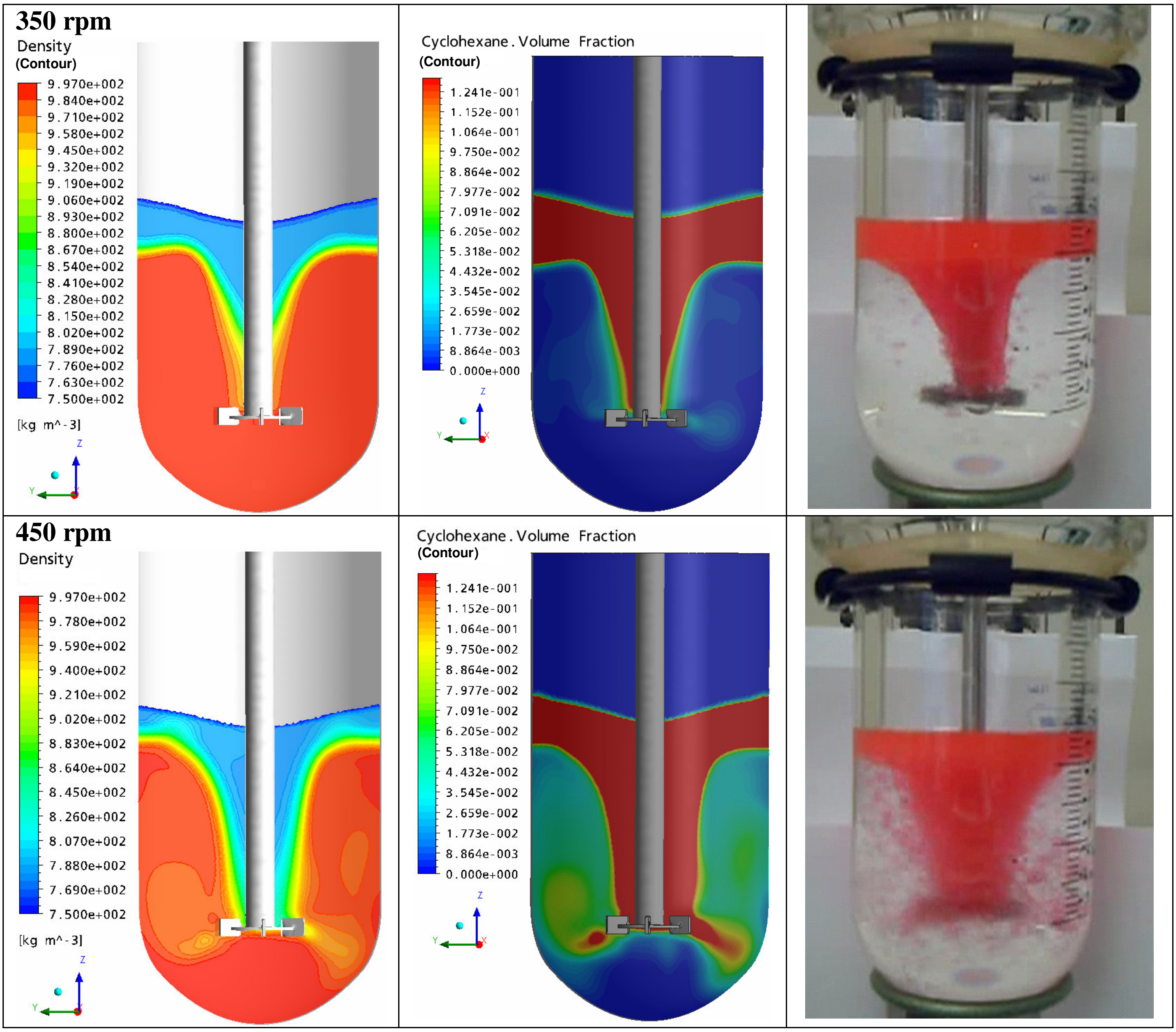

Figure 5.43-a: Dispersion behaviour of cyclohexane in water, experimentally (right) and CFD simulations of the density (left) and volume fraction (mid) at RTI velocity of 350 and 450 rpm by using contour plots.

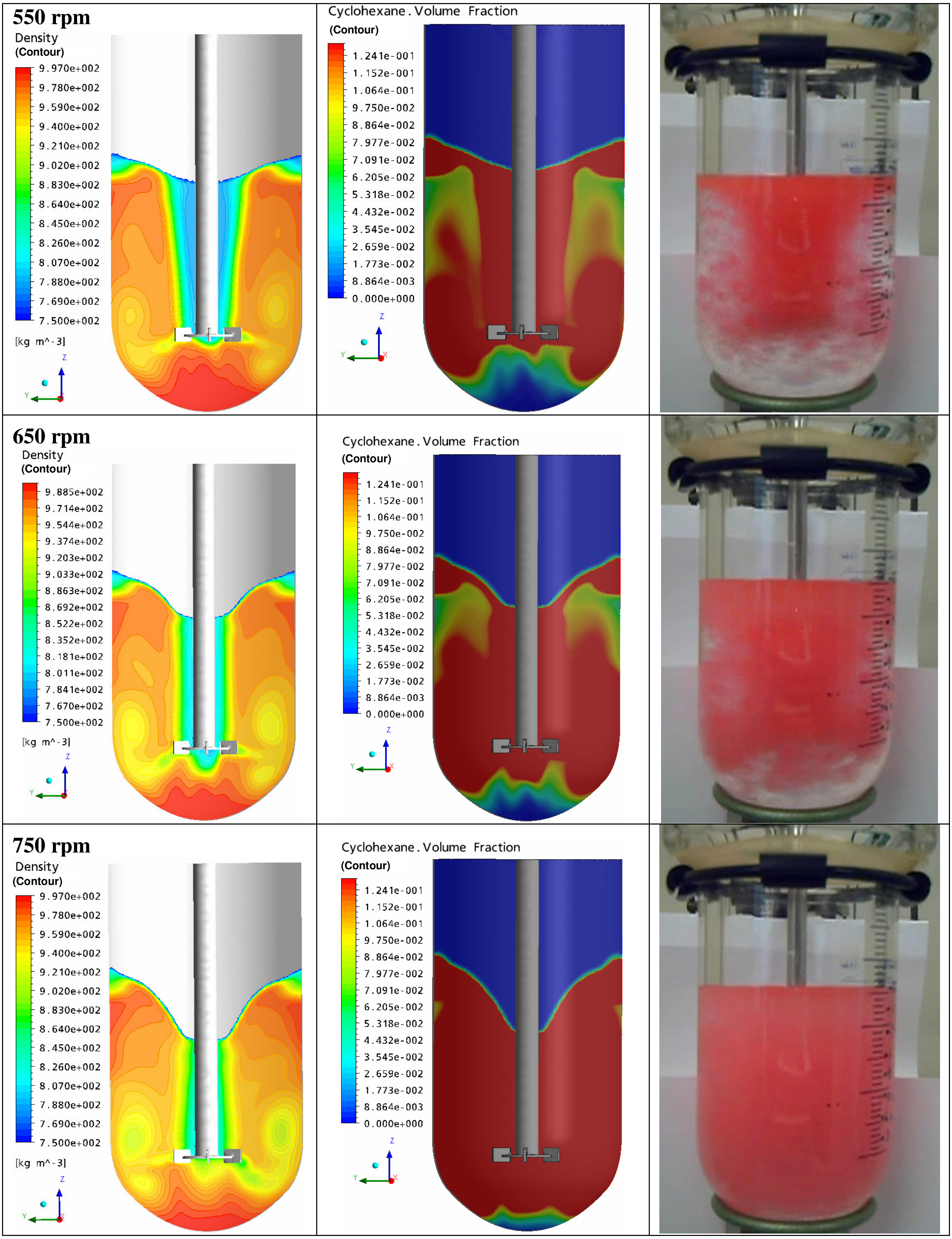

Figure 5.43-b: Dispersion of cyclohexane in water, experimentally (right) and CFD simulations of the density (left) and volume fraction (mid) at RTI velocity of 550, 650 and 750 rpm using contours.

5.4.2.1.1 Algebraic slip model in comparison with Ishii-Zuber model for different grid size

The cyclohexane volume fraction distribution is predicted with the CFD simulation by using two different drag force models such as ASM and Ishii-Zuber model at RTI velocity of 550 rpm, the used cell size is 0.001 m. The measured dispersion behaviour of cyclohexane is compared with that obtained from the CFD simulations as illustrated in Fig. 5.44. The calculated drag forces from Ishii-Zuber model that exerts on the dispersed phase is not enough to push the total cyclohexane volume at the top into water phase. Only cyclohexane is concentrated around the shaft of the impeller and does not reach the blades of the impeller which enhance the dispersion (Fig. 5.44-c). This model considers the surface tension between the two phases, see chapters 5.3.6 and 5.3.1 for further explanation. Whereas the calculated drag force from the ASM enhance the dispersion of cyclohexane in the radial direction due to the increased slip velocity, the drop velocity relative to the surrounding velocity, and shear rates. For that the calculated distribution of cyclohexane volume fractions in the vessel in Fig. 5.44-b is very similar to the visualized dispersion behaviour of cyclohexane in Fig. 5.44-a. These results coincide well with the axial and radial profiles of cyclohexane volume fraction that described in details in chapter 5.3.6.

The cell size has a great effect on the distribution of cyclohexane volume fractions in the vessel. Detailed explanation and discussion about this can be seen in chapter 5.3.7. Reducing the cell size 4 times from 0.004 m (Fig. 5.44-d) to 0.001 m (Fig. 5.44-c) by using Ishii-Zuber model, reduces the thickness of cyclohexane layer at the top and enhance the dispersion towards the shaft of the impeller consequently. Whereas a large layer of unmixed cyclohexane can be seen at the top, with few dispersion near the impeller (Fig. 5.44-d) due to the inconsistent of the grid between the stirrer and the vessel. This is not the case with the anchor impeller which has larger cell size of 0.003 m and gives accurate results, due to its large size compared with the small size RTI.

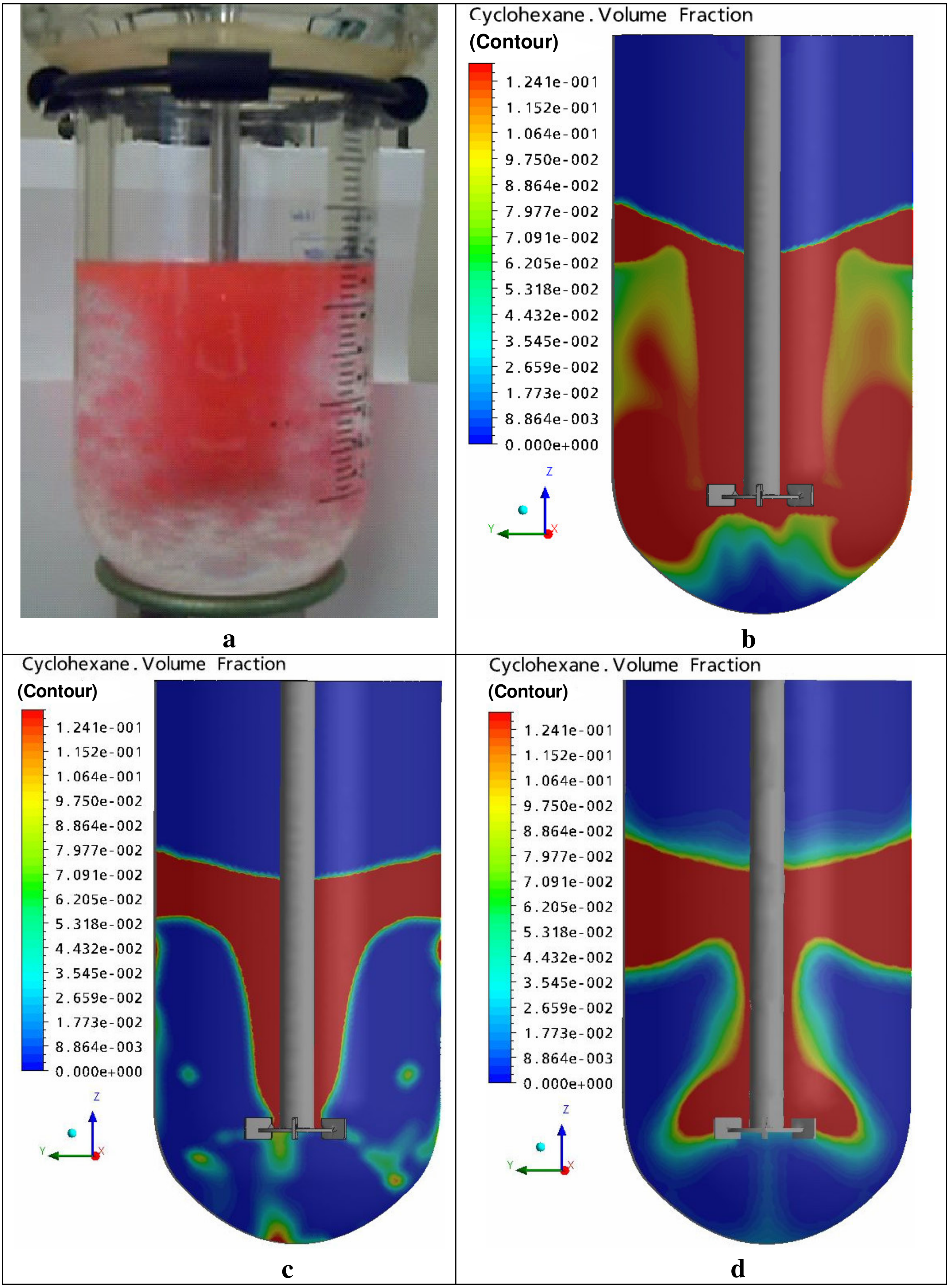

Figure 5.44: Dispersion of cyclohexane in water: (a) Experimentally and with CFD simulations at RTI velocity of 550 rpm by using (b) ASM with cell size of 0.001 m, (c) Ishii-Zuber model with cell size of 0.001 m and (d) Ishii-Zuber model with cell size of 0.004 m.

5.4.2.2 Transient predicted dispersion behaviour

Cyclohexane is dispersed gradually as a function of time at RTI velocity of 350 rpm into water from the cylindrical walls towards the shaft, forming a symmetric vortex around the shaft as can be seen in Fig. 5.45. This coincides well with the experimental visualization and steady simulation predictions in Fig. 5.43-a. The steady flow field is obtained at t = 30 s and it coincides with that obtained from the steady simulations and with that from visualization method. The interface between cyclohexane/water and air/cyclohexane at t = 0 is sharp due to the used very fine grid. When the RTI velocity increased to 750 rpm, cyclohexane disperses around the shaft quickly at t = 1 s from the middle distance between the shaft and the walls of the vessel at r = 2 cm, see Fig 5.46.

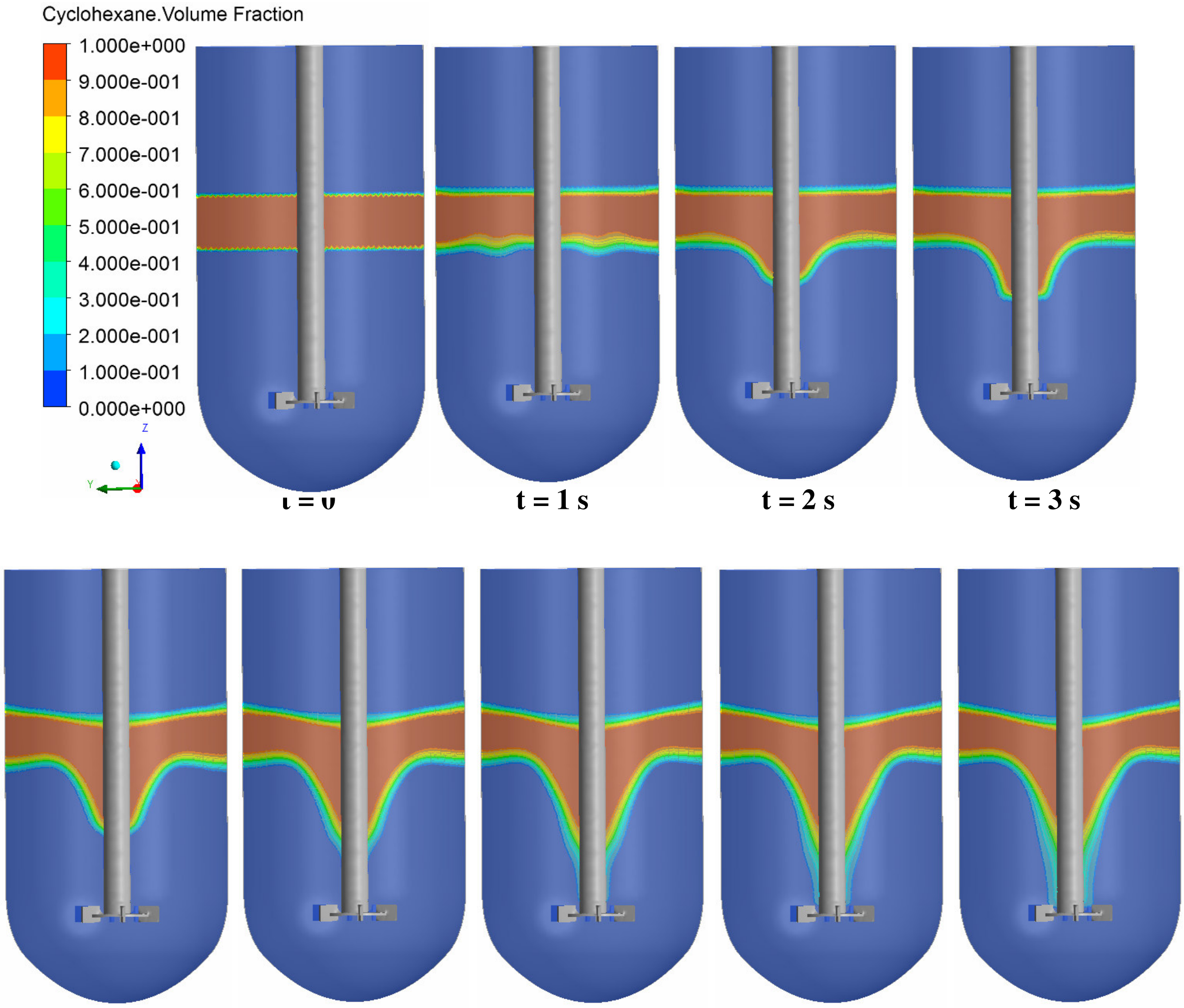

t = 0 t = 1 s t = 2 s t = 3 s

t = 10 s t = 15 s t = 20 s t = 25 s t = 30 s

Figure 5.45: Transient dispersion behaviour of cyclohexane/water system at RTI velocity of 350 rpm by using the contour plots of cyclohexane volume fraction.

Cyclohexane disperses gradually as a function of time from the impeller towards the cylindrical walls, resulting in the upper and lower vortices at t = 3 s. The dispersion is continued in the region above the impeller as can be seen between t = 10 s and 50 s. So it needs longer time to get uniform distribution in the vessel above and below the impeller, and this requires longer time for calculations, thus steady simulations with very fine grid is preferred in such cases. Also at high RTI velocity of 750 rpm, the transient flow field is very similar to that obtained from steady simulations in Fig. 5.43-b, see the contour plot of the density distribution. This dispersion behaviour emphasizes the axial and radial profiles of CHVF obtained from the sampling method.

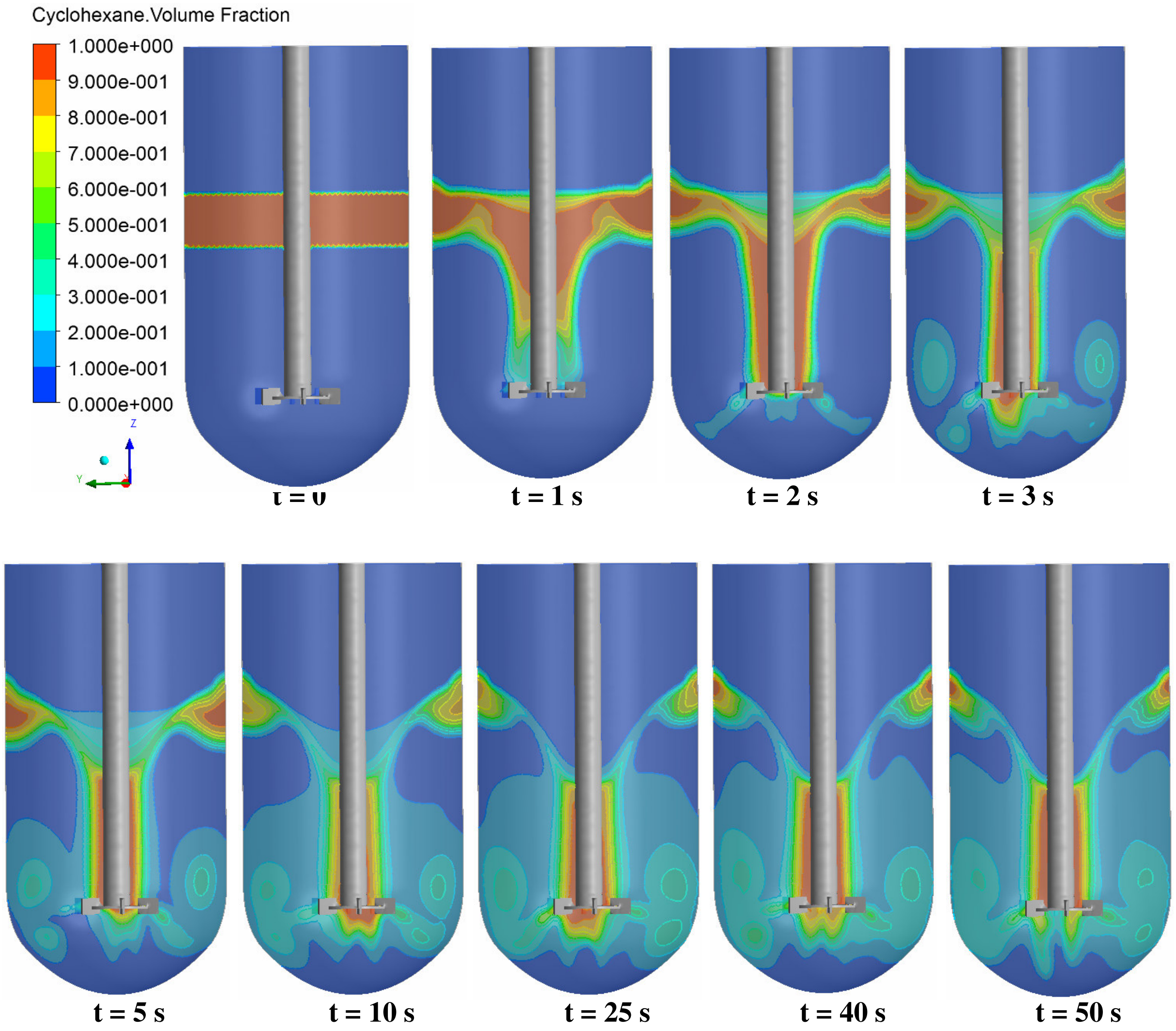

t = 0 t = 1 s t = 2 s t = 3 s

t = 5 s t = 10 s t = 25 s t = 40 s t = 50 s

Figure 5.46: Transient dispersion behaviour of cyclohexane/water system at RTI velocity of 750 rpm by using the contour plots of cyclohexane volume fraction.

5.5 Mass transfer of benzoic acid in cyclohexane/water system at different stirrer velocities and dispersion times

This chapter contains the experimental results of the mass transfer of benzoic acid (solute) from water (continuous phase) to cyclohexane (dispersed phase) in a stirred batch vessel. The measured concentration values of the benzoic acid in water and cyclohexane are drawn as a function of time and stirrer velocity. Different stirrers are used such as anchor, RTI, propeller and PBT. The volumetric mass transfer coefficients (k_c A) are calculated at different stirrer velocities. The rate of mass transfer values are also calculated as a function of time and stirrer velocity. The effect of the percentage volume of cyclohexane on the mass transfer in case of the anchor impeller is investigated. The effect of the RTI clearance is also studied. The predicted averaged CHVF into water from CFD simulations is used to calculate separately the interfacial area (A) between the two phases and the mass transfer coefficient in the continuous phase k_c.

5.5.1 Anchor impeller with 20 vol% cyclohexane

5.5.1.1 Concentration of benzoic acid in water

The measured concentration of benzoic acid in water as a function of time can be seen in Fig. 5.47 for anchor velocities from 150 rpm to 400 rpm. When the dispersion time increases, the concentration of the benzoic acid in water decreases until reaching the equilibrium concentration, where there is no further change in the concentration. This can be obtained at t = 25 min for anchor velocity of 150 rpm and 250 rpm. At these nearly slow velocities, the flow is approximately laminar, thus the surface is continuously renewed as a function of time and enhance the mass transfer of the solute from water to cyclohexane gradually. For higher anchor velocities of 300, 350 and 400 rpm (Fig. 5.48), an instantaneous equilibration occurs at t = 20, 10 and 1 min, respectively. The concentration of the benzoic acid reaches the minimum value at these times then they increase again to reach the real equilibrium concentration of 0.017 mol/L at t = 40, 20 and 10 min for anchor velocity of 300, 350 and 400 rpm, respectively.

The inverse of the mass transfer of benzoic acid occurs at anchor velocity two to three times the minimum velocity. This behaviour may be due to large interfacial areas of a dispersion in a mixing vessel and the high driving forces for mass transfer resulting from the high solute solubility in either or both of the two phases. Also the high velocity of the continuous phase results in high concentration gradient of the solute close to the interface that could cause the development of roll cells (small eddies) at the interface, which enhance the mass transfer by mixing of fluid elements close to the interface between the two phases due to the high turbulence and flow convection.

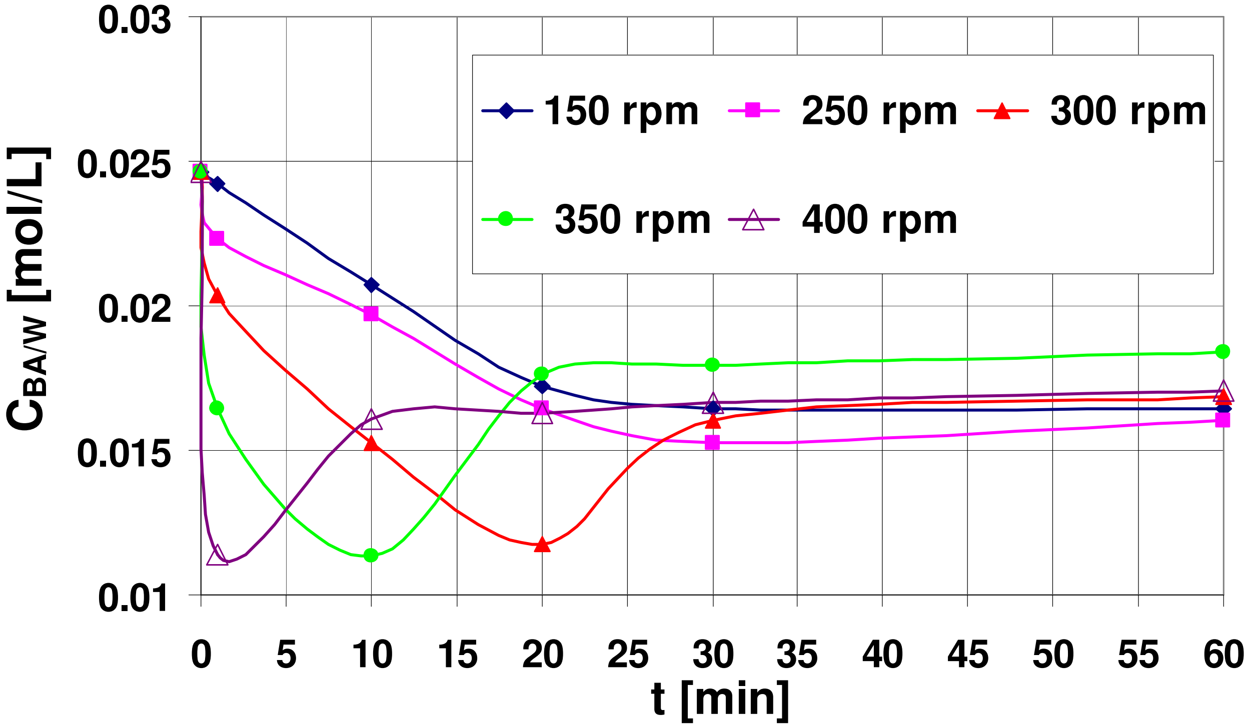

Figure 5.47: Concentration of benzoic acid in water as a function of time for anchor velocities of ω = 150 rpm, 250 rpm, 300 rpm and 350 rpm.

At high anchor velocities, the centrifugal forces become dominant due to the high interfacial tension between the two phases, resulting in several eddies (see chapter 5.1.1). The interaction between the cyclohexane eddies and water phase leads to several collisions, coalescence and breakup of cyclohexane droplets at the interface, resulting in surface renewal between the two phases, and thus increasing the rate of mass transfer. The large mass transfer of benzoic acid in water occurs at t = 1 min for all anchor velocities, because there is a continuous decrease of the solute concentration with time when the anchor velocity increases as can be seen in Fig. 5.48. For t ≥ 30 min, there will be no effect of the anchor velocity on the mass transfer of benzoic acid because the two phases become saturated with the solute and reach the equilibrium concentration.

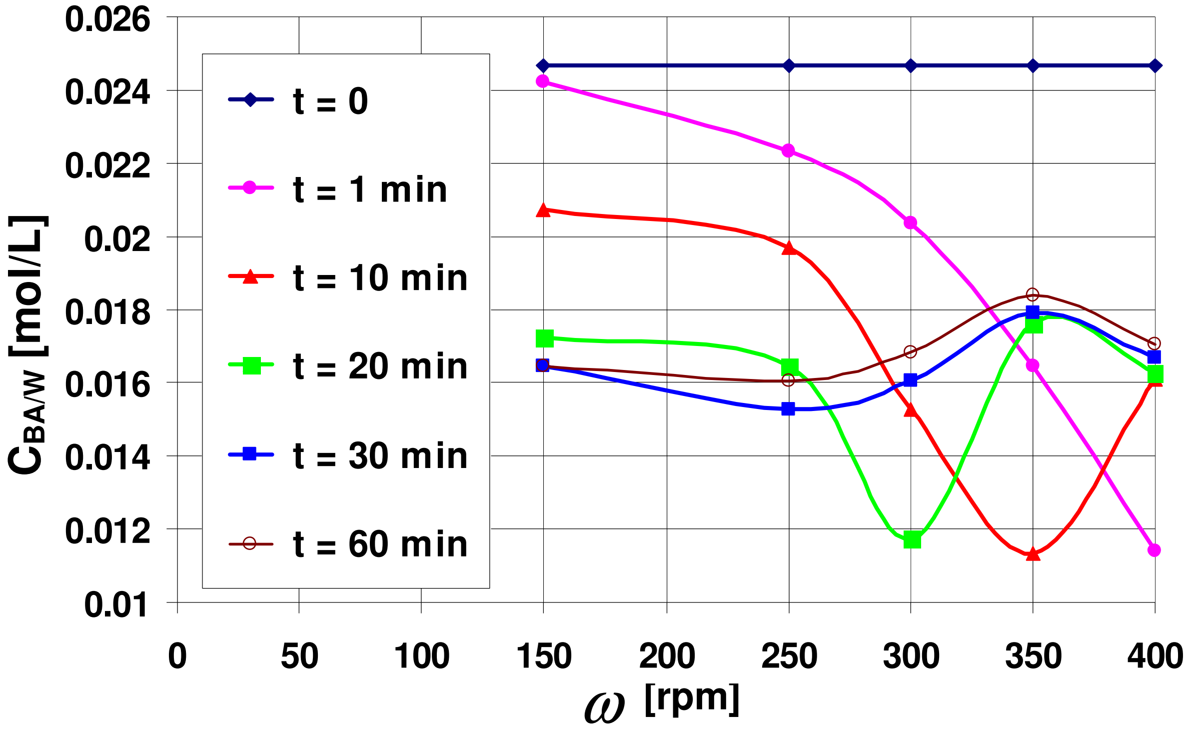

Figure 5.48: Concentration of benzoic acid in water as a function of anchor velocity at mixing times of t = 0, 1 min, 10 min, 20 min, 30 min and 60 min.

5.5.1.2 Concentration of benzoic acid in cyclohexane

The concentration of benzoic acid in cyclohexane is calculated from the conservation mass balance equation and is drawn as a function of time for anchor velocities from 150 rpm to 400 rpm as can be seen in Fig. 5.49. At low anchor velocities of 150 and 250 rpm (approximately laminar flow), there is a gradual increase of the benzoic acid concentration with time until the organic phase reaches the saturation and the equilibrium concentration of 0.008 mol/L at t = 30 min. It can be seen a maximum concentration of 0.013 mol/L at t = 1, 10 and 20 min is obtained at anchor velocities of 300, 350 and 400 rpm, respectively. The system always tends to reach the equilibrium concentration and the steady state. For that the benzoic acid transfers inversely from cyclohexane to water until the equilibrium concentration is attained at t = 10, 20 and 30 min for anchor velocities of 400, 350 and 300 rpm, respectively.

When the anchor velocity is increased above 250 rpm, large eddy is formed, thus larger interfacial area between the cyclohexane/water phases is obtained due to the formation of a highly turbulent and unsteady state system, which may causes the inverse mass transfer of the benzoic acid from cyclohexane to water. The irregular velocity field that caused by the surface tension gradient at the interface between the two phases, and thus it affects the concentration profiles of the solute through the small eddies that exist at the interface to enhance the mass transfer as suggested by Sylvia and Eugeny [56]. The surface tension gradient is caused by the concentration gradient at the interface.

At high velocities of the continuous phase, fluid elements with strong concentration inhomogeniety are instantaneously replaced by fluid elements rich in the solute. So the highest mass transfer rate can be reached at high Reynolds number of the continuous phase, with mass transfer direction from the dispersed phase to the continuous phase. When the anchor velocity increases from 150 to 400 rpm, the system reaches the equilibrium concentration 3 times faster from t = 30 to 10 min, respectively.

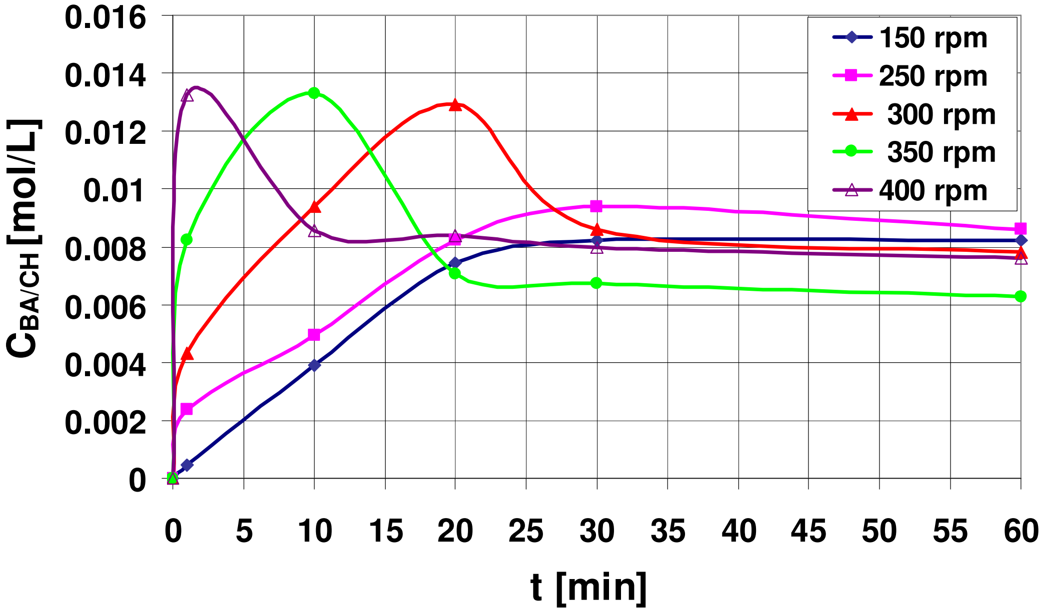

Figure 5.49: Concentration of benzoic acid in cyclohexane as a function of time for anchor velocity of ω = 150 rpm, 250 rpm, 300 rpm and 350 rpm.

The mass transfer of benzoic acid from water to cyclohexane increases always when the anchor velocity increases at t = 1 min as shown in Fig. 5.50. Whereas at t = 10 and 20 min, the concentrations of benzoic acid show maximum at anchor velocity of 350 and 300 rpm, respectively then it decreases for the same mentioned reasons. There is no significant effect of the anchor velocity on the mass transfer of benzoic acid for t ≥ 30 min.

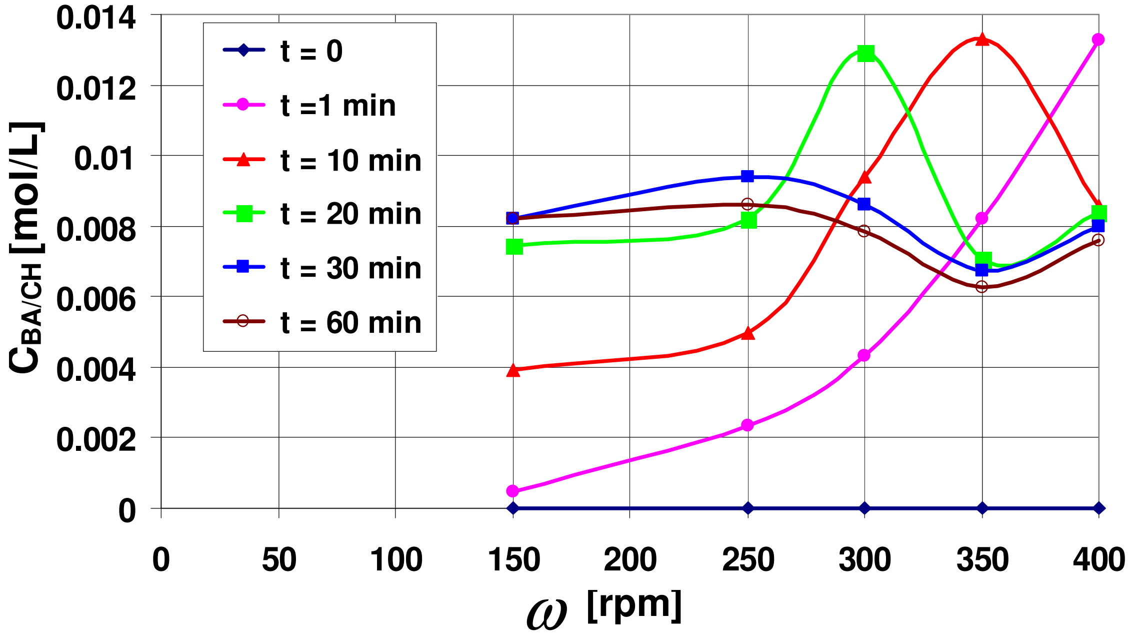

Figure 5.50: Concentration of benzoic acid in cyclohexane as a function of anchor velocity at mixing times of t = 0, 1 min, 10 min, 20 min, 30 min and 60 min.

5.5.1.3 Equilibrium time and concentration of benzoic acid

The equilibrium time is defined as the required time for the benzoic acid to reach the equilibrium concentration at which there is no further change in the benzoic acid concentration in the both continuous and dispersed phases. It is found from Fig. 5.51 a very small variation of the equilibrium concentration of benzoic acid with the increase of the anchor velocity from 150 rpm to 400 rpm. The required time to reach the equilibrium concentration in Fig. 5.52 decreases when increasing the anchor velocity from 150 rpm to 350 rpm. For the anchor velocity greater than 350 rpm, it has no effect on the equilibrium concentration and equilibrium time.

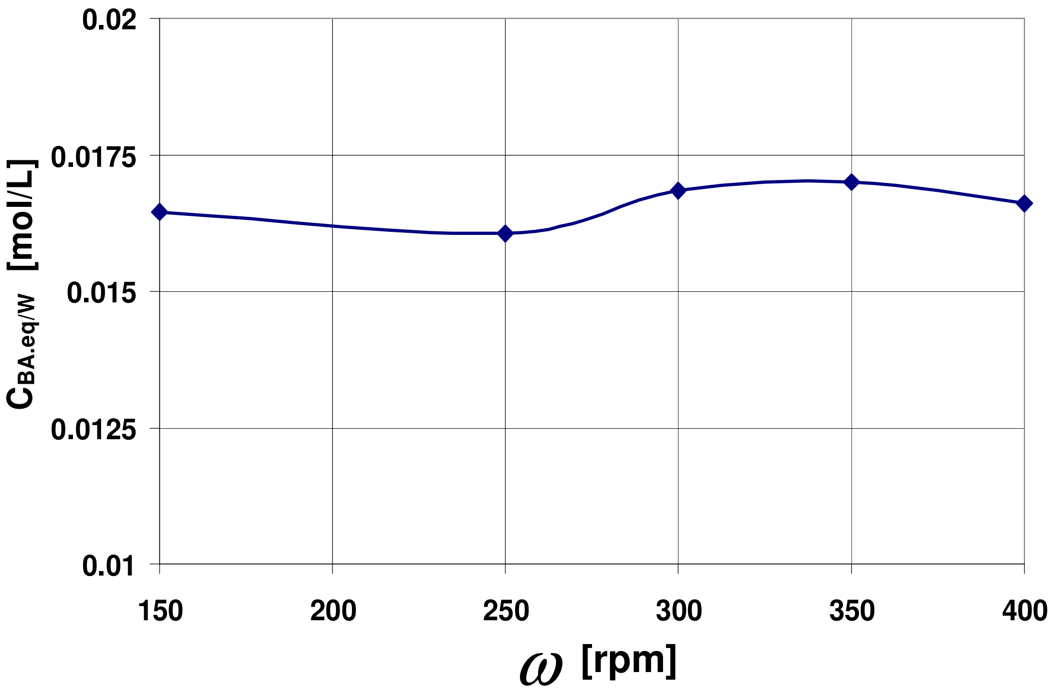

Figure 5.51: The equilibrium concentration of benzoic acid in water as a function of anchor velocity.

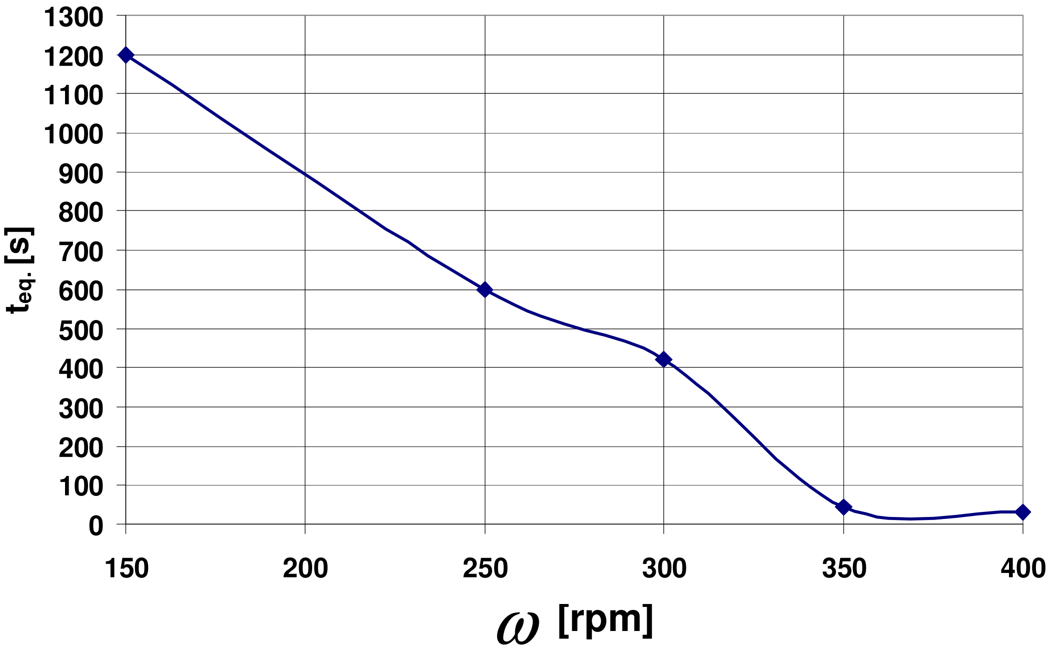

Figure 5.52: The equilibrium time as a function of anchor velocity.

5.5.1.4 Volumetric mass transfer coefficient

From the measured concentration values of benzoic acid in water as a function of time, it is possible to calculate the volumetric mass transfer coefficient of benzoic acid (k_cA) at different anchor velocities by using the derived equation 2.3 from the material balance on benzoic acid as described in section 2.5. It is required to draw ln $((C_{eq.} - C_t) / (C_{eq.} - C_{t0}))$ as a function of time for anchor velocity from 150 rpm to 400 rpm to calculate k_c A as shown in Fig. 5.53. A straight line whose slope is proportional to the volumetric mass transfer coefficient $(- k_c A / V_c)$ is obtained, and then k_c A can be calculated, i.e. for anchor velocity of 150 rpm, the slope is – 0.0019 1/s, but k_c A = – V_c slope, where:

V_c = ((400 mL • 1 L / 1000 mL) • (1 m^3 / 1000 L)) = 0.0004 m^3.

Then, k_c [m/s] A [m^2] = – 0.0004 m^3 • (– 0.0019 s^{-1}) = 7.6 e^{-7} m^3 /s.

The variation of k_c A with stirrer velocity may be due to the variation of k_c or A or both with stirrer velocity. The absolute value of the slope increases from 0.0019 to 0.0596 s^{-1} when the anchor velocity increases from 150 to 400 rpm, but the slopes are close at anchor velocities of 350 and 400 rpm. Suggesting there is no further increase in the mass transfer.

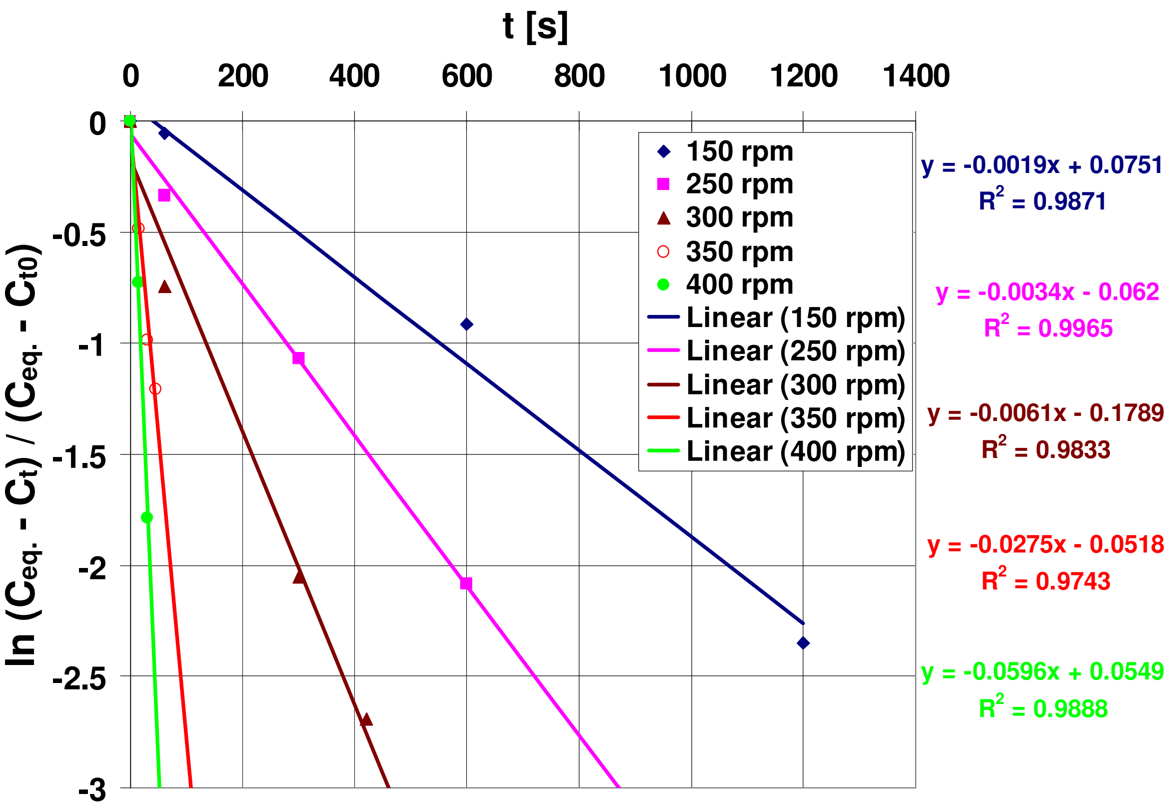

Figure 5.53: ln $((C_{eq.} - C_t) / (C_{eq.} - C_{t0}))$ as a function of time for anchor velocities of 150 rpm, 250 rpm,300 rpm, 350 rpm and 400 rpm.

The volumetric mass transfer coefficient of benzoic acid increases slowly when the anchor velocity increases from 150 to 300 rpm as illustrated in Fig. 5.54. That means a small amount of benzoic acid is transferred to cyclohexane. At low anchor velocities (low Reynolds number) the surface renewal at the interface by diffusion is responsible for mass transfer. For anchor velocities greater than 300 rpm, larger values of $k_c A$ are obtained. This may be due to the increase of the mass transfer coefficient in water and/or increase the mass transfer area between the two phases. At high Reynolds number, large eddies are formed. The interfacial area between the two phases stretches deforms and folds, as well as the surface renewal velocity is enhanced, making the interphase mass transfer more efficient and increase the $k_c A$ values. Thus the convective effects and the enlargement of the interfacial area between the two phases play the dominant role on the mass transfer. A power function of 3.96 of the anchor velocity can describe the effect of the anchor velocity on the volumetric mass transfer coefficient of benzoic acid.

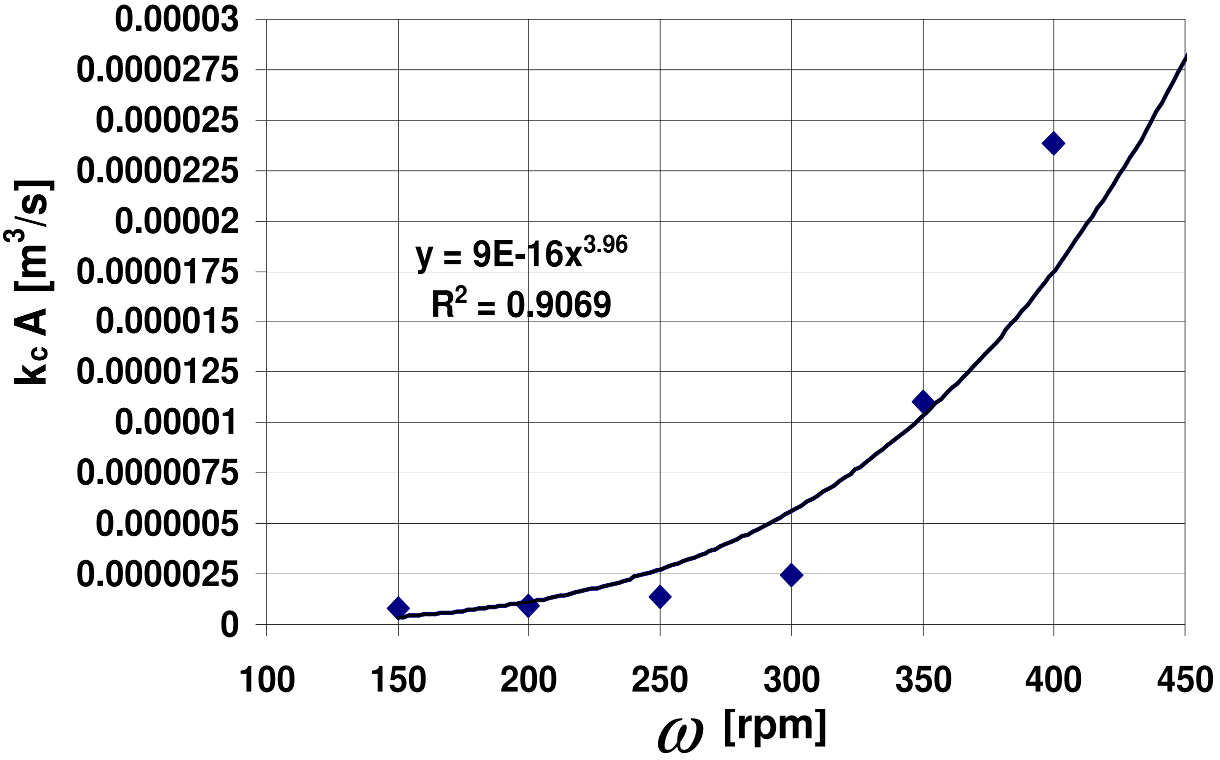

Figure 5.54: The volumetric mass transfer coefficient as a function of anchor velocity by using the power function.

5.5.1.5 Rate of mass transfer of benzoic acid

The rate of mass transfer of benzoic acid from water to cyclohexane ($ROMT_{BA/CH}$) is drawn as a function of time in Fig. 5.55 for different anchor velocities. It is found that the maximum rate of mass transfer of benzoic acid can be obtained at dispersion time of 1.0 min for the all anchor velocities, where the rate of mass transfer increases from 0.0006 to 0.0132 mol/L min when the anchor velocity increases from 150 to 400 rpm, and then it decreases up to t = 10 min. The anchor velocity has no effect on the rate of mass transfer of benzoic acid above t = 10 min. In the beginning of the mixing process until t = 1 min, the concentration difference of the benzoic acid between the continuous and dispersed phases is large, thus the driving force is also large and the rat of mass transfer will be large. After this time, the rate of mass transfer of benzoic acid decreases because the driving force decreases, and the both phases tend to reach the equilibrium conditions.

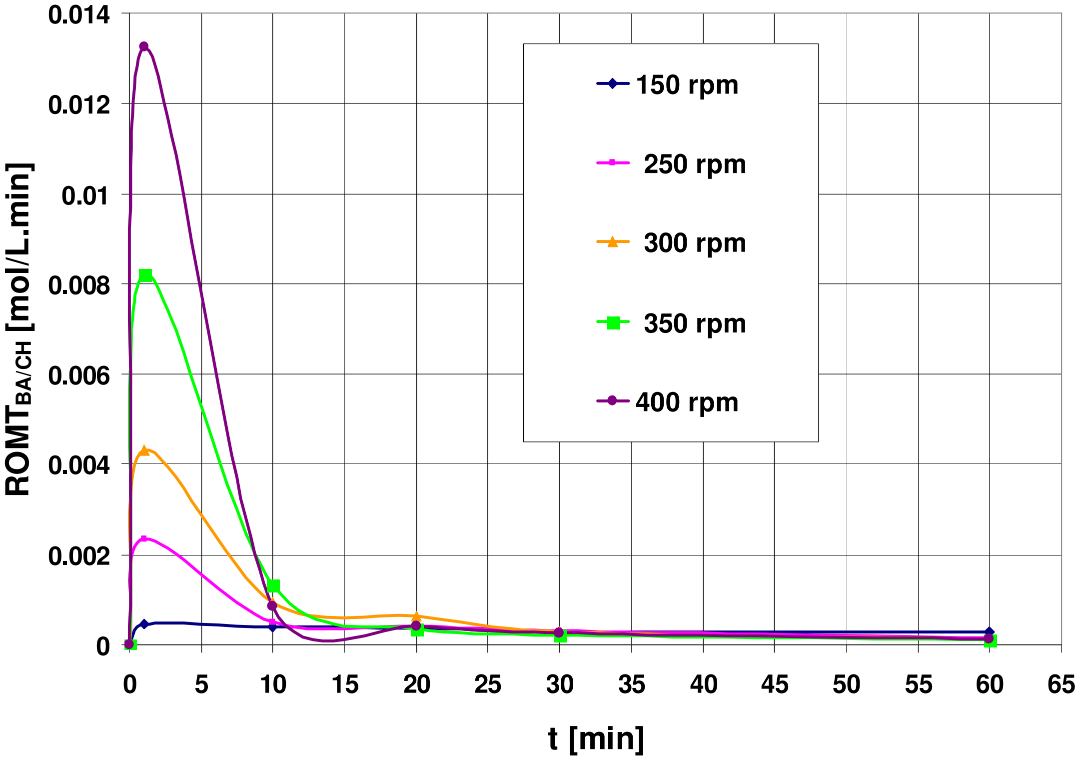

Figure 5.55: The rate of mass transfer of benzoic acid from water to cyclohexane as a function of time at different anchor velocities.

The rate of mass transfer of benzoic acid at t = 1.0 min increases as a power function with anchor velocity of order 3.42 as illustrated in Fig. 5.56. If two drops coalescence, the energy release due to surface reduction is equivalent to a kinetic energy for the resulting large drop. It may be suggested that the strong coalescence action at high anchor velocities is able to renew the shell of the continuous phase surrounding the dispersed phase, thus enhance the rate of mass transfer. There is no significant increase of the ROMT of benzoic acid at t = 10 min. Lower rates of mass transfer are caused by lower driving forces.

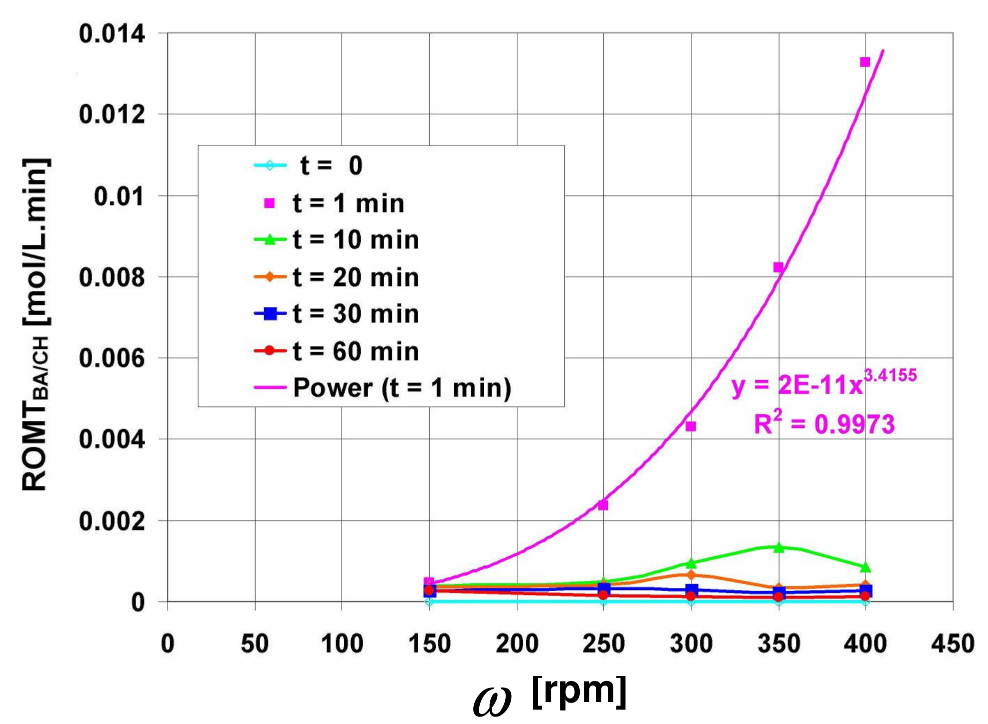

Figure 5.56: The rate of mass transfer of benzoic acid from water to cyclohexane as a function of anchor velocity at different dispersing times.

5.5.2 Anchor impeller at 150 rpm with 10 - 30 vol% cyclohexane

5.5.2.1 Concentration of benzoic acid in water

The concentration of the benzoic acid in water decreases when the percentage of the dispersed phase increases from 10 vol% to 30 vol% at anchor velocity of 150 rpm as can be seen in Fig. 5.57. That means the transported amount of benzoic acid from water to cyclohexane increases, because the higher volumetric fractions of the dispersed phase results in higher rates of collisions, coalescence, breakup and formation of the roll cells at the interface between the two phases, causing the formation of more new surface areas as well as redistribution of the solute (benzoic acid) in the dispersed phase. Thus larger mass transfer of benzoic acid into cyclohexane by diffusion is obtained. At low initial volumetric fraction (10 vol%) of cyclohexane, the concentration of benzoic acid in water decreases slowly and takes very long time to reach the equilibrium concentration at t = 120 min. This is 4 times greater than that required when using large initial volume fraction of 20 vol% and 30 vol% cyclohexane. This is may be due to the small contact area between the two phases at 10 vol% cyclohexane caused by the small holdup of cyclohexane into water at this low velocity, the velocity of the layer at the interface is also smaller because it is away from the tip of anchor impeller and thus lower shear forces affect on the film deformation and breakage at the interface. Thus the mass transfer by diffusion will be the predominant effect at low 10 vol%, whereas at a high 20 vol% and 30 vol% of cyclohexane both diffusion and convective mass transfer exist, thus larger mass transfer is obtained where larger volume of cyclohexane is incorporated in the water phase, leading to a larger contact area between the two phases.

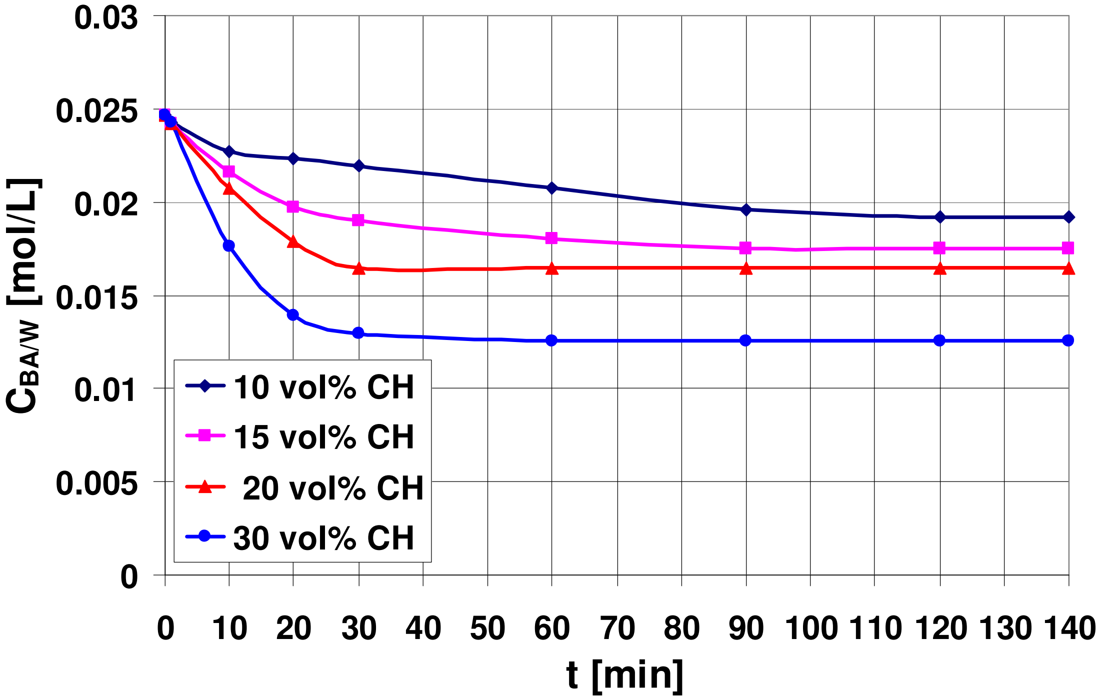

Figure 5.57: The transient concentration of benzoic acid in water for anchor velocity of 150 rpm and cyclohexane volume percentage of 10 vol%, 15 vol%, 20 vol% and 30 vol%.

It is found that increasing the initial percentage volume of cyclohexane at t = 1 min in Fig. 5.58 has no effect on the concentration of benzoic acid in water and similar small amount of mass transfer of benzoic acid occurs. The concentration of benzoic acid in water decreases when the percentage volume of cyclohexane increases at t = 10, 20 and 30 min. A small decrease of the solute concentration (small mass transfer) is found at t > 30 min for 10 and 15 vol% of cyclohexane, whereas there is no further decrease of the concentration for 20 and 30 vol% of cyclohexane (no mass transfer).

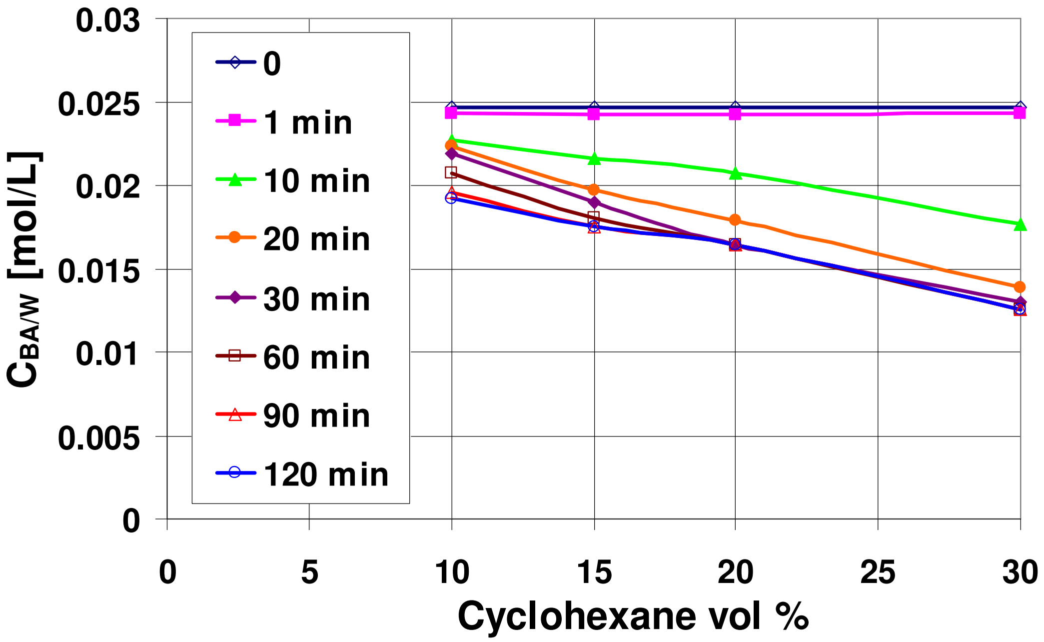

Figure 5.58: The concentration of benzoic acid in water for anchor velocity of 150 rpm as a function of cyclohexane volume percentage at different dispersion time.

5.5.2.2 Concentration of benzoic acid in cyclohexane

A remarkably strong increase of the concentration of the benzoic acid in cyclohexane as a function of time is found in Fig. 5.59 for 20 vol% and 30 vol% of cyclohexane at anchor velocity of 150 rpm until reaching the equilibrium concentration at t = 30 min. Whereas a gradual and slowly increase is found for 10 vol% and 15 vol% of cyclohexane until reaching the equilibrium concentration at longer time of t = 120 and 90 min, respectively. This behaviour occurs for the same reasons explained in the previous section 5.5.2.1. The concentration of benzoic acid in cyclohexane is drawn against the percentage volume of cyclohexane at different dispersion times in Fig. 5.60. The mass transfer of the solute is directly proportional to the initial volume fraction of cyclohexane. Lower time is required to reach the equilibrium concentration at high volumetric fractions of cyclohexane because the surface renewal by diffusion is larger due the formation of larger eddy and contact area between the two phases, thus improves the mass transfer of benzoic acid.

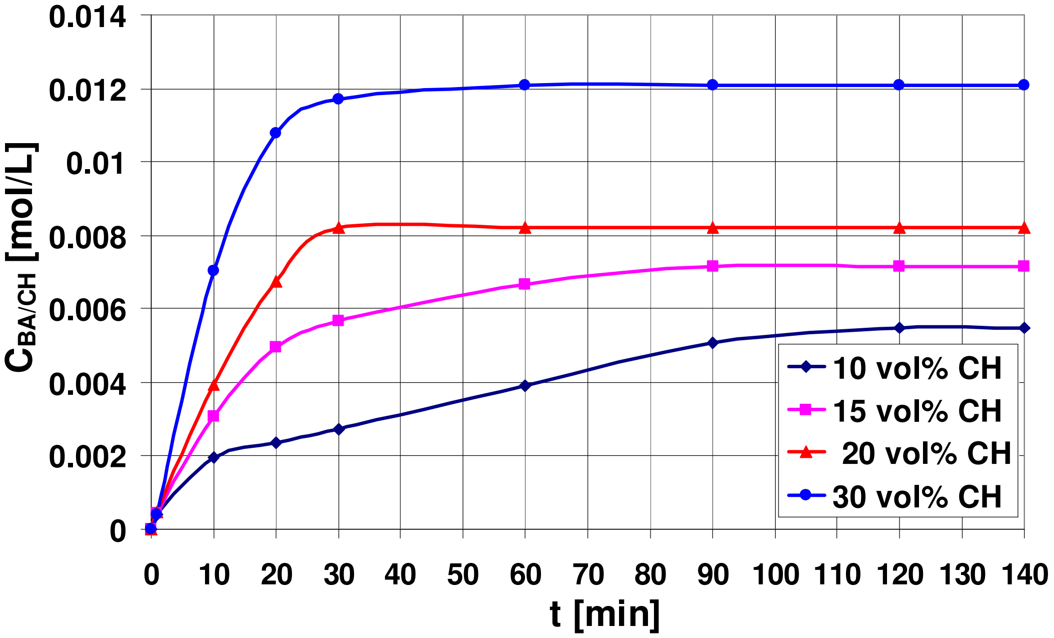

Figure 5.59: The transient concentration of benzoic acid in cyclohexane for anchor velocity of 150 rpm and cyclohexane volume percentage of 10 vol%, 15 vol%, 20 vol% and 30 vol%.

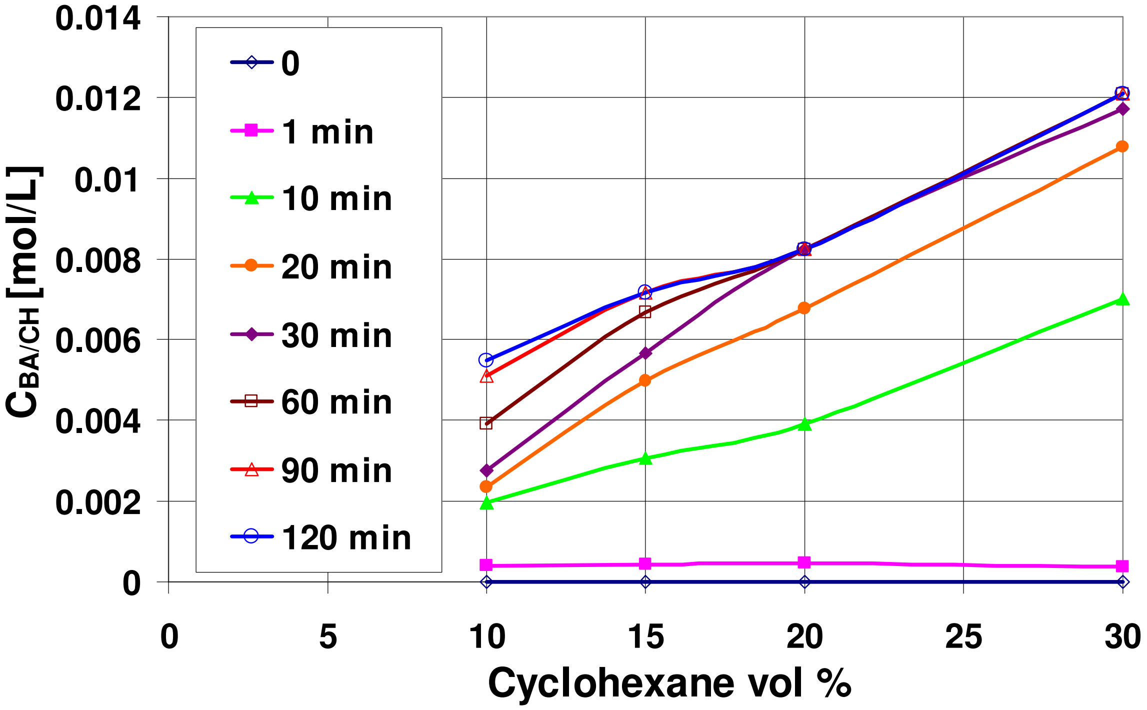

Figure 5.60: The concentration of benzoic acid in cyclohexane for anchor velocity of 150 rpm as a function of cyclohexane volume percentage at different dispersion times.

5.5.2.3 Volumetric mass transfer coefficient

From the slopes of the straight lines in Fig. 5.61, for different initial volume percentages of cyclohexane, the volumetric mass transfer coefficients k_c A are calculated as illustrated in section 5.1.1.4. It is found that the absolute value of the slope increases when the cyclohexane percentage volume increases from 10 vol% to 20 vol%. The slope remains approximately constant above 20 vol% of cyclohexane. The volumetric mass transfer coefficient k_c A increase with increasing the volume percentage of cyclohexane up to 20 vol% as can be seen in Fig. 5.62, and there is no significant effect on the k_c A values when the percentage volume of cyclohexane is greater than 20 vol% for the same reasons illustrated before. The volumetric mass transfer coefficient shows a polynomial function with a second degree of the volume percentage of cyclohexane.

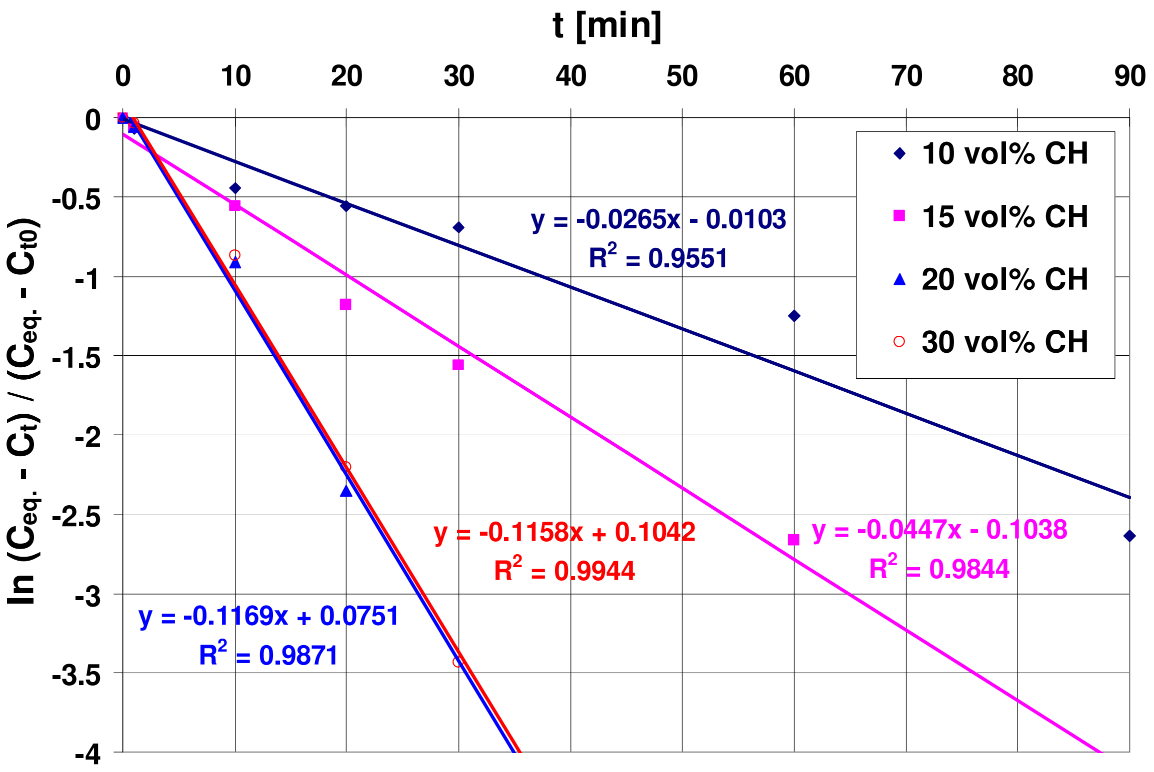

Figure 5.61: ln $((C_{eq.} - C_t) / (C_{eq.} - C_{t0}))$ as a function of time for anchor velocity of 150 rpm and cyclohexane volume percentage of 10 vol% , 15 vol%, 20 vol% and 30 vol%.

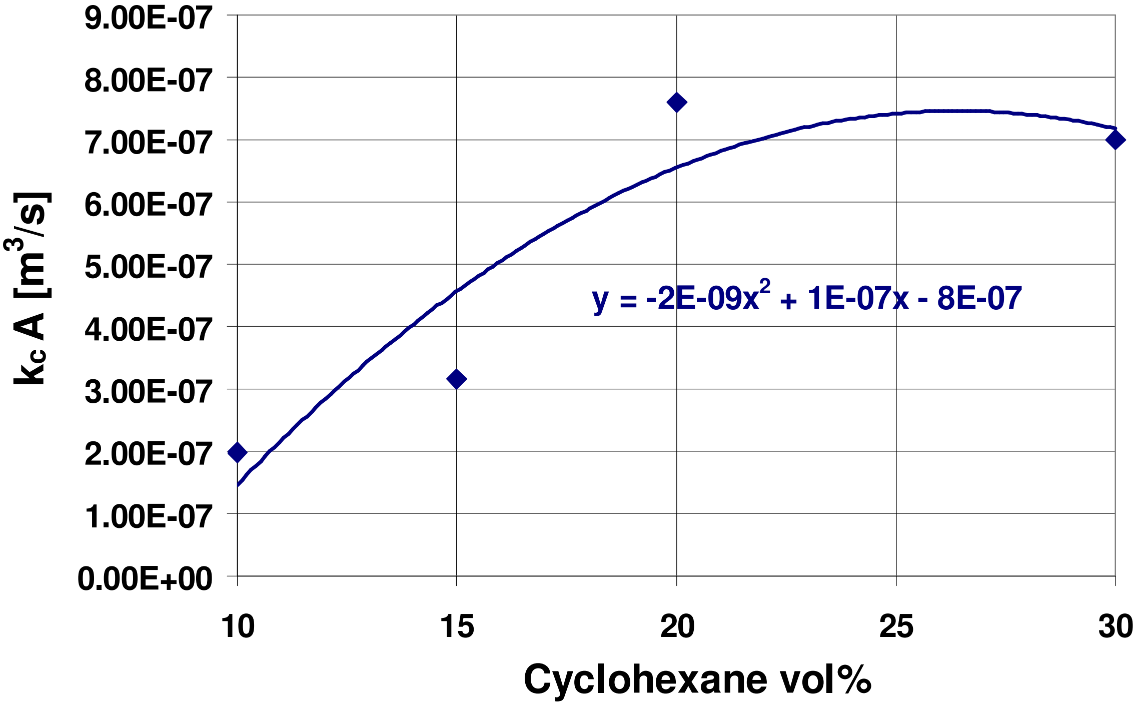

Figure 5.62: The volumetric mass transfer coefficient as a function of the cyclohexane percentage volume at anchor velocity of 150 rpm.

5.5.2.4 Rate of mass transfer of benzoic acid

The rate of mass transfer of benzoic acid from water to cyclohexane ($ROMT_{BA/CH}$) is direct proportional to the initial volumetric fractions of cyclohexane (see Fig. 5.63). It shows a maximum value at t = 1 min for 10 vol%, 15 vol% and 20 vol% and at t = 10 min for 30 vol% of cyclohexane because the concentration gradient at the interface between the two phases is large, thus the driving forces are high. Then it decreases slowly because the two phases reach the equilibrium conditions and steady state. Above t = 60 min, there is no significant effect for the high percentage volume of cyclohexane on the rate of mass transfer of benzoic acid. The rate of mass transfer of benzoic acid values at t = 1 min in Fig. 5.64 are close with very small difference for all percentage volumes of cyclohexane.

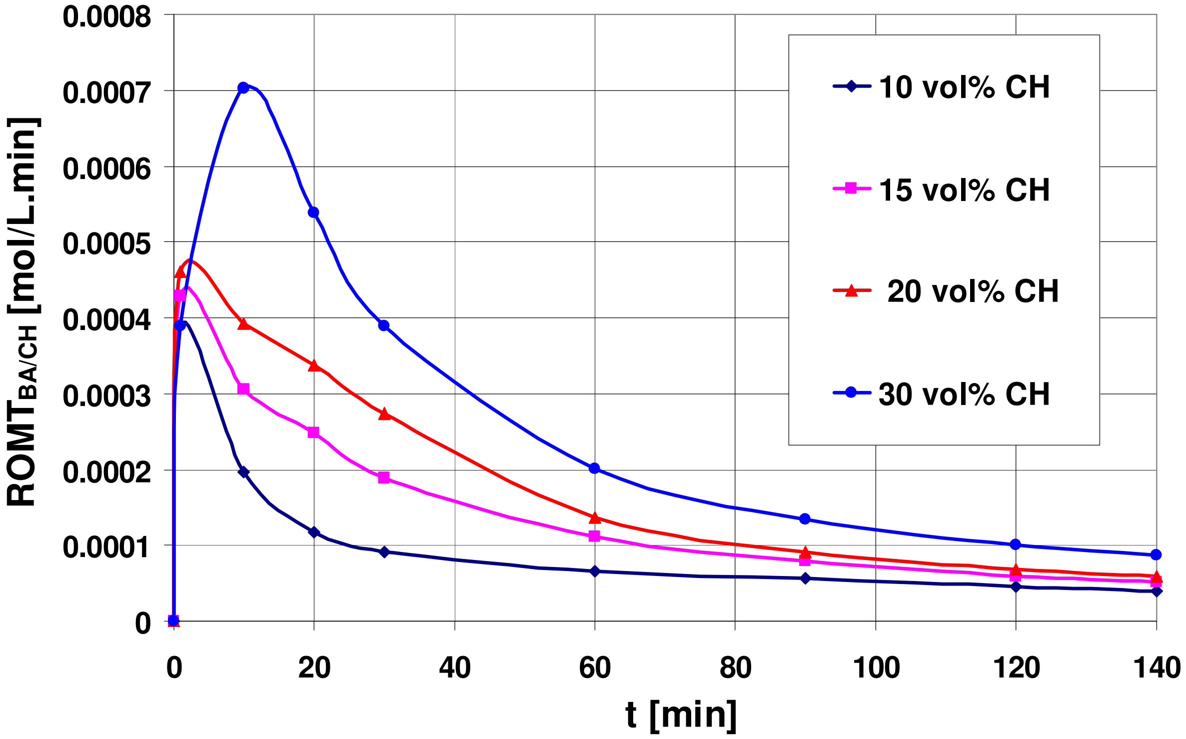

Figure 5.63: The rate of mass transfer of benzoic acid from water to cyclohexane as a function of time at different cyclohexane percentage volume of 10 vol%, 15 vol%, 20 vol% and 30 vol%.

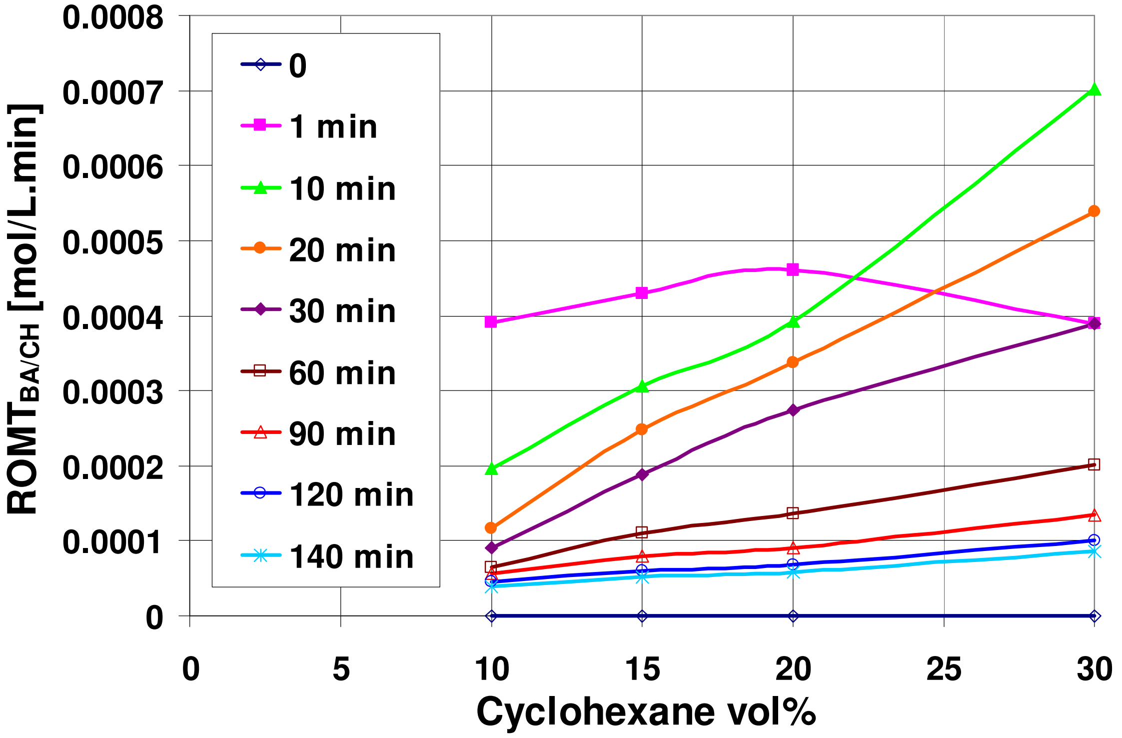

Figure 5.64: The rate of mass transfer of benzoic acid from water to cyclohexane as a function of cyclohexane percentage volume at different dispersing times.

5.5.3 Rushton turbine impeller with 20 vol% cyclohexane

5.5.3.1 Clearance effect on benzoic acid concentration in water

The measured concentration of benzoic acid in water as a function of time is indicated in Fig. 5.65 for different RTI velocities at bottom clearances of 3.2 and 4.1 cm. The decrease of the concentration of benzoic acid in water at RTI velocity of 350 and 400 rpm and clearance of 3.2 cm is smaller and slower than that for clearance of 4.1 cm. For RTI velocity ≥ 450 rpm, there is no significant effect of its clearance on the concentration of benzoic acid and mass transfer. The energy produced at lower RTI velocities of 350 and 400 rpm and clearance of 3.2 cm is not enough to push the cyclohexane layer towards the turbine blades, which can deform and break the cyclohexane layer into droplets and disperse them into water phase as a result of the collisions with the blades of the impeller. For RTI clearance of 4.1 cm, the cyclohexane layer reaches the turbine blade before that at clearance of 3.2 cm due to the shorter distance between the impeller and cyclohexane layer at the top, thus the kinetic energy is transported faster from the impeller to the cyclohexane phase and the interaction between the two phases becomes higher. Thus more droplets of cyclohexane are formed around the impeller and larger contact area is obtained, leading to larger mass transfer of benzoic acid from water to cyclohexane at RTI clearance of 4.1 cm and velocity of 350 or 400 rpm. This behaviour can be also confirmed by the comparison with the flow pattern obtained by the RTI at clearances of 3.2 and 4.1 cm as can be seen in section 5.1.2 (Figs. 5.2 and 5.3).

At high Reynolds number, the effect of the buoyancy and shear forces in the radial flow RTI are dominant. Thus RTI creates a complex flow in the vicinity of the vessel. The periodic unsteadiness of this flow and existence of a pair trailing vortices behind the impeller blades (small eddies below and above the impeller) make it easy for drops to deform and breakup. Thus enhance the collisions between the two phases through recirculation and redispersion of the cyclohexane droplets, thus enhance the mass transfer of the solute.

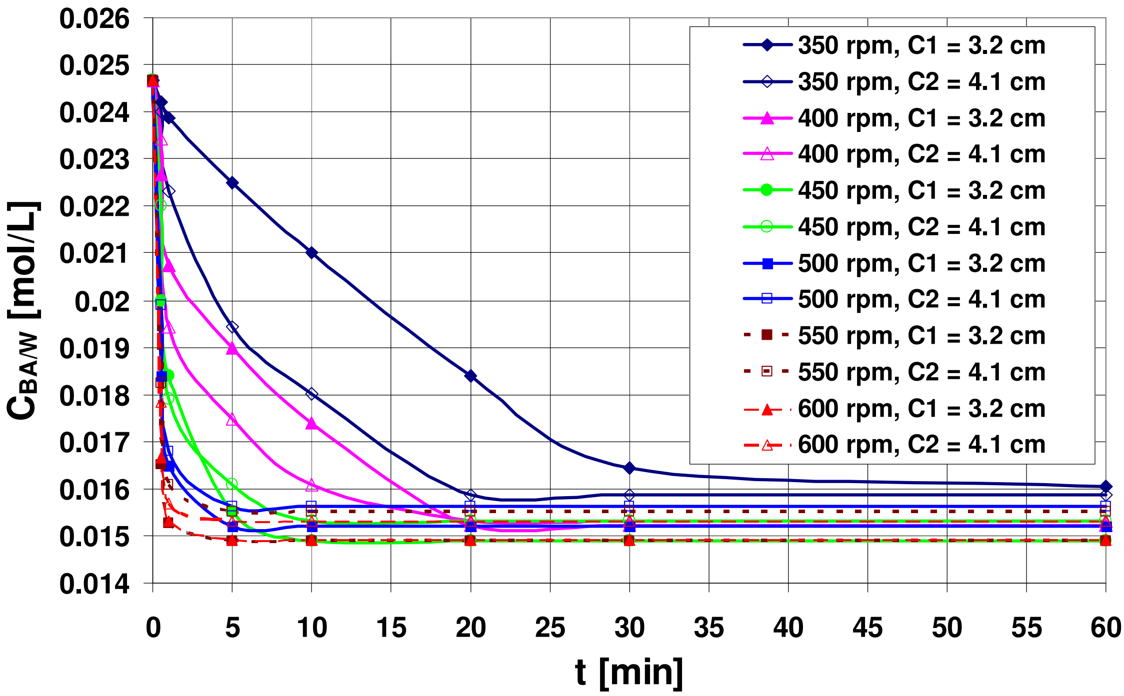

Figure 5.65: The concentration of benzoic acid in water as a function of time for rushton turbine velocity of 350 rpm to 600 rpm and bottom clearance of 3.2 cm and 4.1 cm.

The concentration of benzoic acid in water decreases when the dispersion time increases (see Fig. 5.66) because this allows the two phases to be in a contact for a longer time and allows for a lager mass of benzoic acid to transfer from water to cyclohexane. At t = 0.5 min, the concentration of benzoic acid in water at clearance of 3.2 cm is lower than that at 4.1 cm for all RTI velocities. The minimum RTI velocity to reach the equilibrium concentration is 550 rpm. The mass transfer of benzoic acid from water to cyclohexane at RTI clearance of 4.1 cm is higher than that at 3.2 cm for RTI velocity up to 450 rpm at t = 1 min and 400 rpm at t = 5, 10 and 20 min. The minimum velocity to reach the equilibrium concentration of benzoic acid in water decreases from 550 at t = 0.5 and 1 min to 500 at t = 5 and 10 min and to 400 rpm at t = 20 min. For t ≥ 30 min, there is no effect of the RTI velocity on mass transfer of benzoic acid to cyclohexane. The equilibrium concentration is independent on the dispersion time at RTI velocity ≥ 600 rpm.

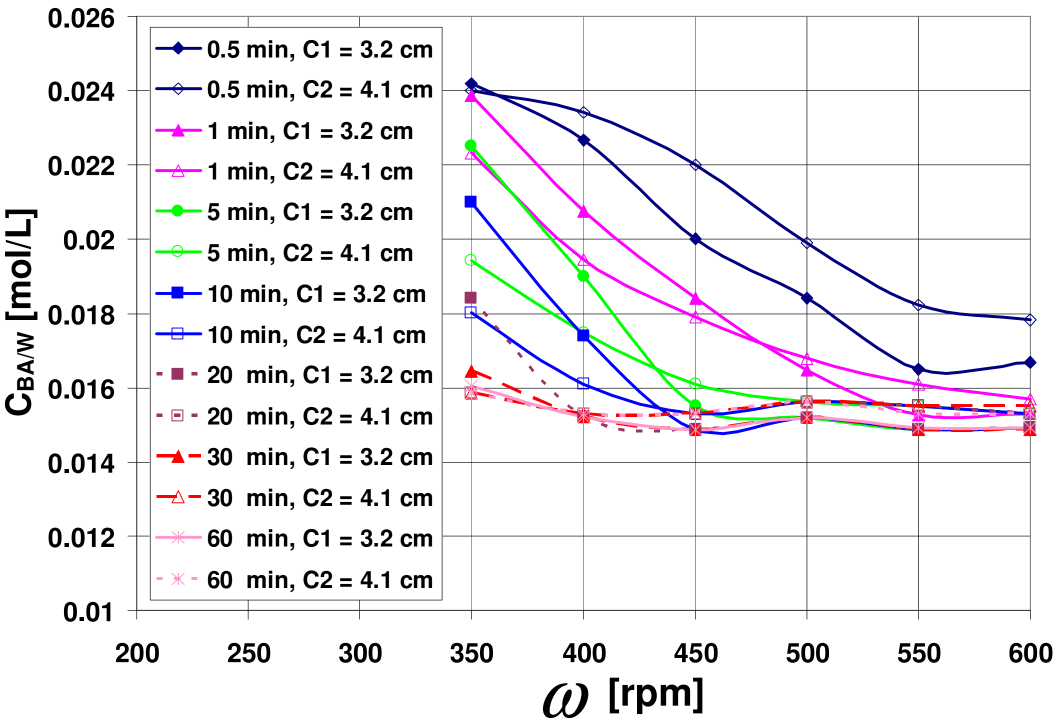

Figure 5.66: Concentration of benzoic acid in water as a function of RTI velocity at different dispersion times from t = 0.5 min to 60 min at clearance of 3.2 cm and 4.1 cm.

5.5.3.2 Clearance effect on benzoic acid concentration in cyclohexane

The mass transfer is affected by the rates of surface renewal associated with droplets circulation through varying degrees of turbulence, which depends on the location in the vessel. The concentration of benzoic acid in cyclohexane increases when the dispersion time increases for both RTI clearances as shown in Fig. 5.67. A small and slow increase is found at RTI velocities of 350 and 400 rpm, whereas a remarkable strong increase is found at RTI velocities ≥ 450 rpm, because the high kinetic and dissipation energy are converted into a turbulent motion through the collisions and circulations, leading to more surface renewal of the dispersed phase and thus enhance the mass transfer of the solute. Low RTI velocities ≤ 400 rpm with clearance of 4.1 cm give higher concentrations of benzoic acid in cyclohexane (larger mass transfer) than that at clearance of 3.2 cm, whereas at RTI velocities ≥ 450 rpm, very close values with a small difference are obtained. Increasing the RTI velocity increases the concentration of benzoic acid in cyclohexane until reaching to the saturation, depending on the dispersion time for each velocity (see Fig. 5.68). That means for longer dispersion time t≥ 30 min, minimum RTI velocity of 350 rpm is satisfied to reach the equilibrium. RTI velocity of 550 rpm is required to reach the equilibrium concentration at short dispersion time of 0.5 min.

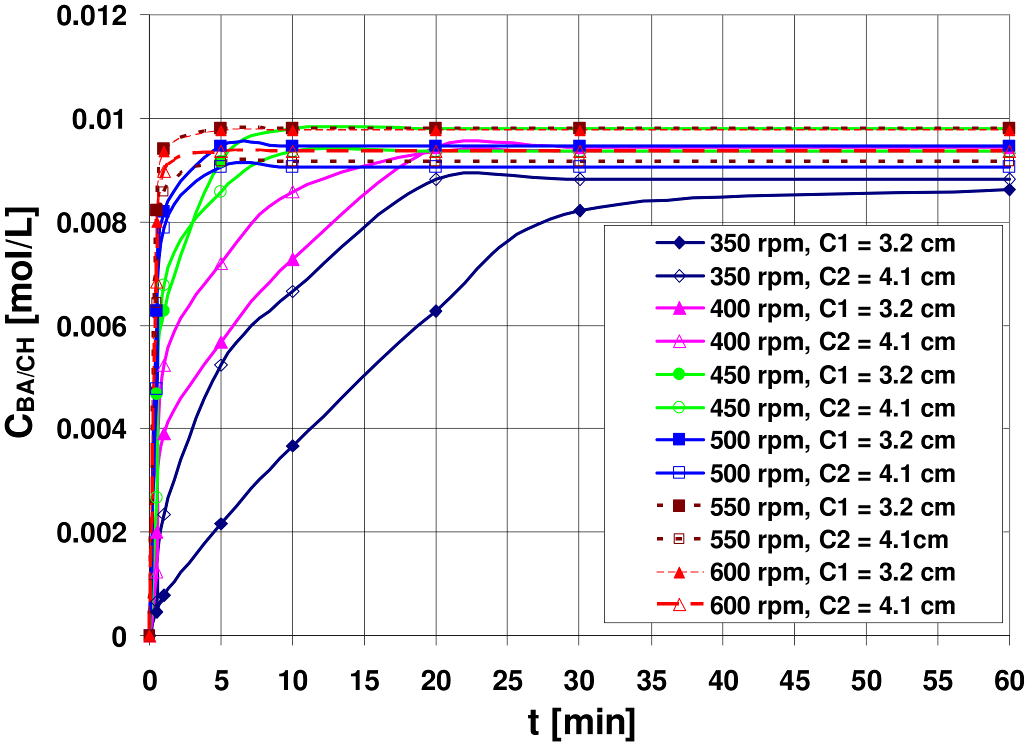

Figure 5.67: The concentration of benzoic acid in cyclohexane as a function of time for rushton turbine velocity from 350 rpm to 600 and bottom clearance of 3.2 cm and 4.1 cm.

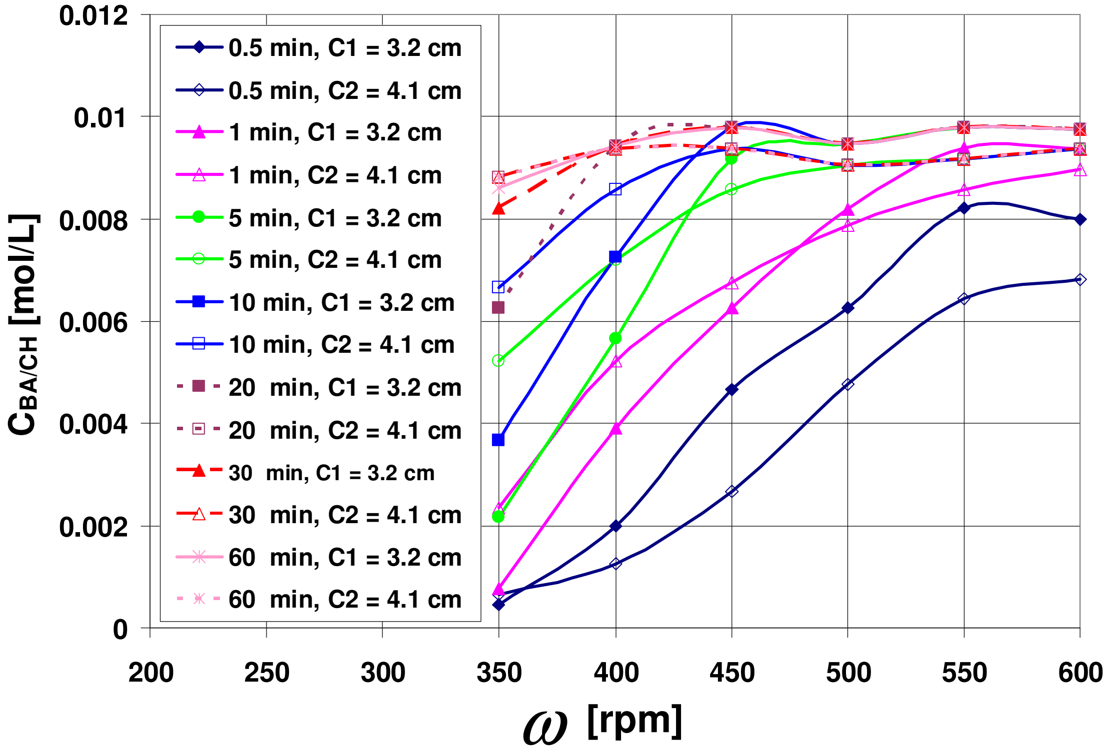

Figure 5.68: Concentration of benzoic acid in cyclohexane as a function of RTI velocity at different dispersion times from t = 0.5 min to 60 min at clearance of 3.2 cm and 4.1 cm.

5.5.3.3 The equilibrium time and concentration of benzoic acid

The required time to reach the equilibrium concentration in Fig. 5.69 decreases when the RTI velocity increases from 350 rpm to 500 rpm for RTI clearance of 3.2 and 4.1 cm with similar values except at RTI velocity of 350 rpm, because a slower mass transfer of benzoic acid is found and illustrated in Fig. 5.65. The minimum RTI velocity to reach the equilibrium conditions is 500 rpm. There is no more change on the equilibrium time and concentration for both RTI clearances at velocities > 500 rpm (see Fig. 5.69). The final equilibrium concentrations of benzoic acid in water at different RTI velocities are very close (around 0.0155 mol/L) for both RTI clearances as can be seen in Fig. 5.70. The RTI velocity has no significant effect on the equilibrium concentration values but only on the time required to reach the equilibrium concentration.

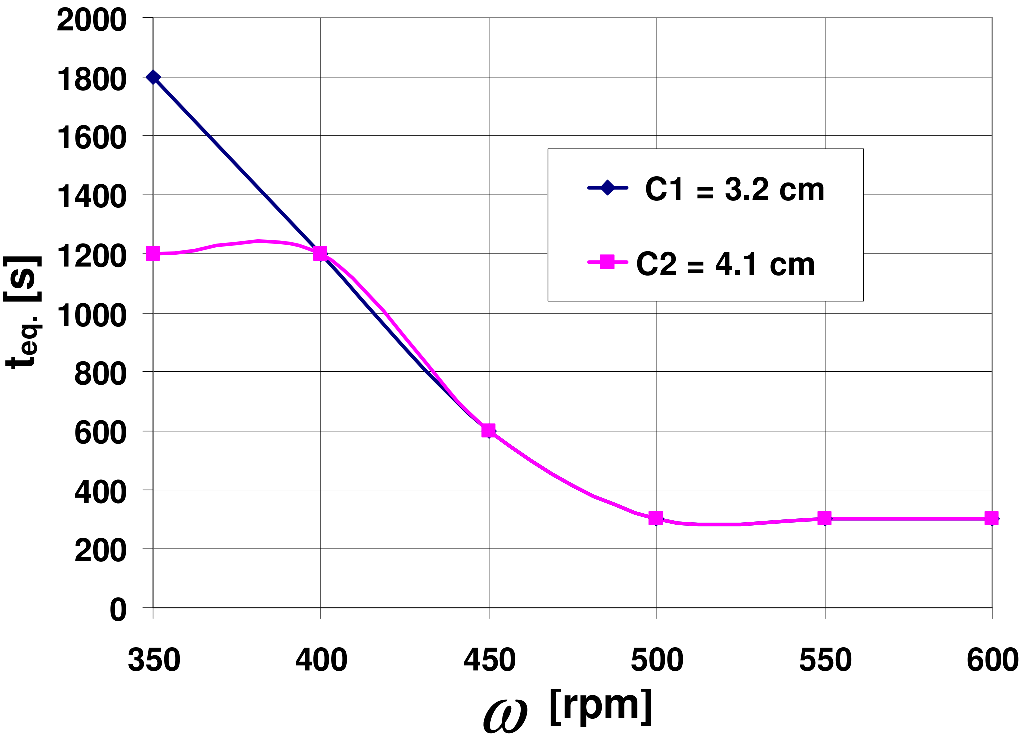

Figure 5.69: The equilibrium time as a function of RTI velocity for bottom clearances of 3.2 cm and 4.1 cm.

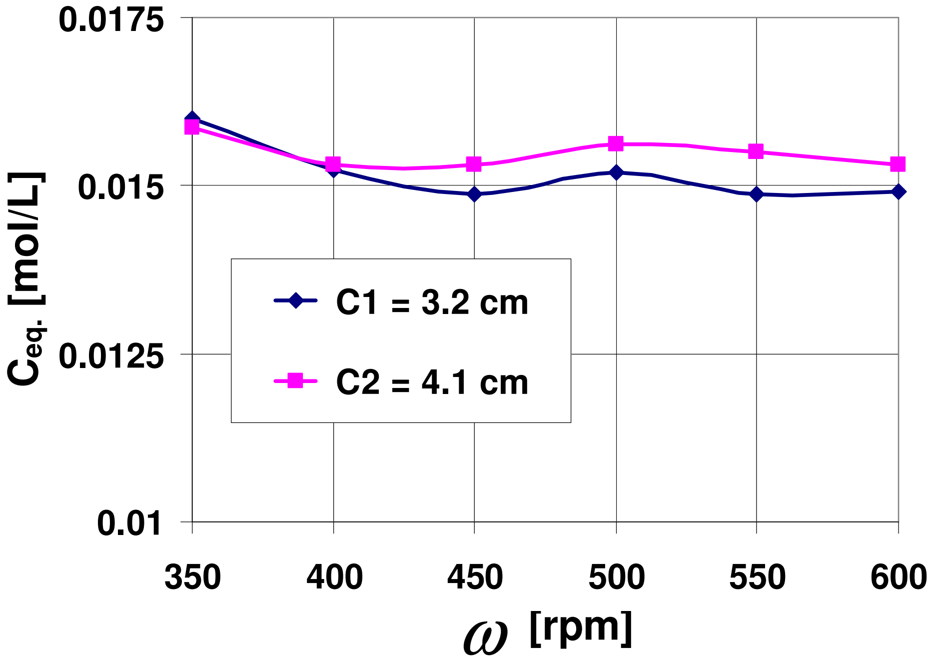

Figure 5.70: The equilibrium concentration of benzoic acid as a function of RTI velocity at bottom clearances of 3.2 cm and 4.1 cm.

5.5.3.4 Volumetric mass transfer coefficient

ln $((C_{eq.} - C_t) / (C_{eq.} - C_{t0}))$ values are drawn as a function of time for RTI velocities from 350 rpm to 600 rpm at clearances of 3.2 and 4.1 cm in Figs. 5.71 and 5.72, respectively. It is found that the absolute values of the slopes are similar with very small difference for both clearances at all RTI velocities as well as the volumetric mass transfer coefficient in Fig. 5.73. The turbulence generated in the impeller discharge affect the values of k_c A, turbulence is greater near the impeller, least at the walls of the vessel near the free surface and in the bottom of the vessel and intermediate strength between these locations. At high RTI velocities, the dissipation energy is high near the impeller as well as the mass transfer coefficient and the interfacial area. For that the rate of surface renewal is greater near the impeller. This occurs due to the breakup, redispersion of drops and diffusion. The mass transfer of benzoic acid to water is slow at RTI velocity of 350, 400 and 450 rpm, it takes long time to reach the equilibrium concentration because the driving force at the interface is low. This results in low volumetric mass transfer coefficients as it can be seen in Fig. 5.73, whereas at RTI velocities greater than 450 rpm, the fast mass transfer of benzoic acid from water to cyclohexane gives high absolute values of the slopes because it takes shorter time to reach the equilibrium concentration because the concentration difference is high. This gives high volumetric mass transfer coefficients as illustrated in Fig. 5.73. The minimum RTI velocity to get maximum volumetric mass transfer coefficient is 550 rpm. It is found that k_c A increases as 6.5 power of the RTI velocity. The clearance of the RTI has no significant effect on the volumetric mass transfer coefficients.

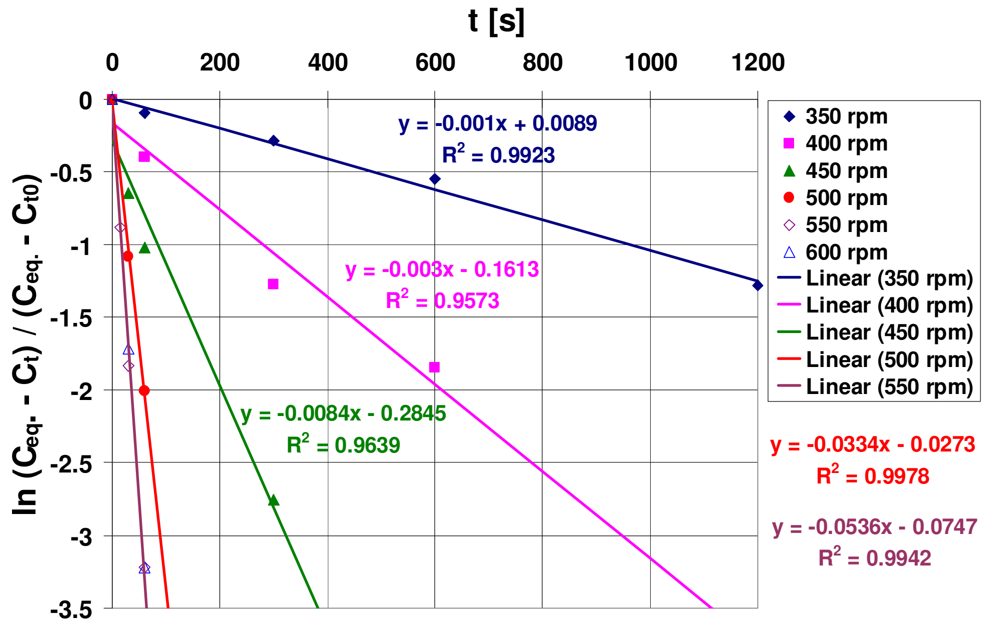

Figure 5.71: ln $((C_{eq.} - C_t) / (C_{eq.} - C_{t0}))$ as a function of time for RTI with clearance of 3.2 cm at velocity from 350 rpm to 600 rpm.

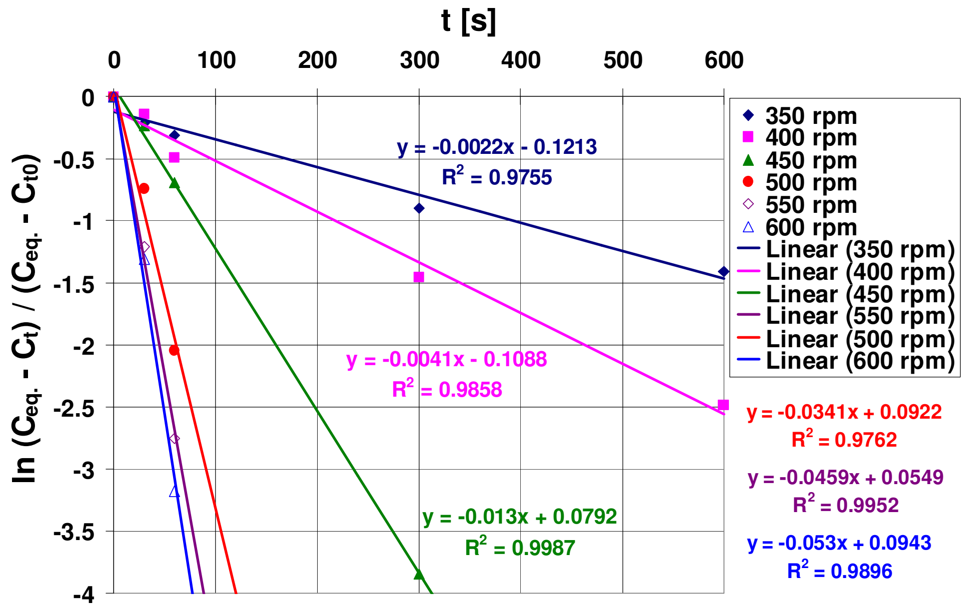

Figure 5.72: ln $((C_{eq.} - C_t) / (C_{eq.} - C_{t0}))$ as a function of time for RTI with clearance of 4.1 cm at velocity from 350 rpm to 600 rpm.

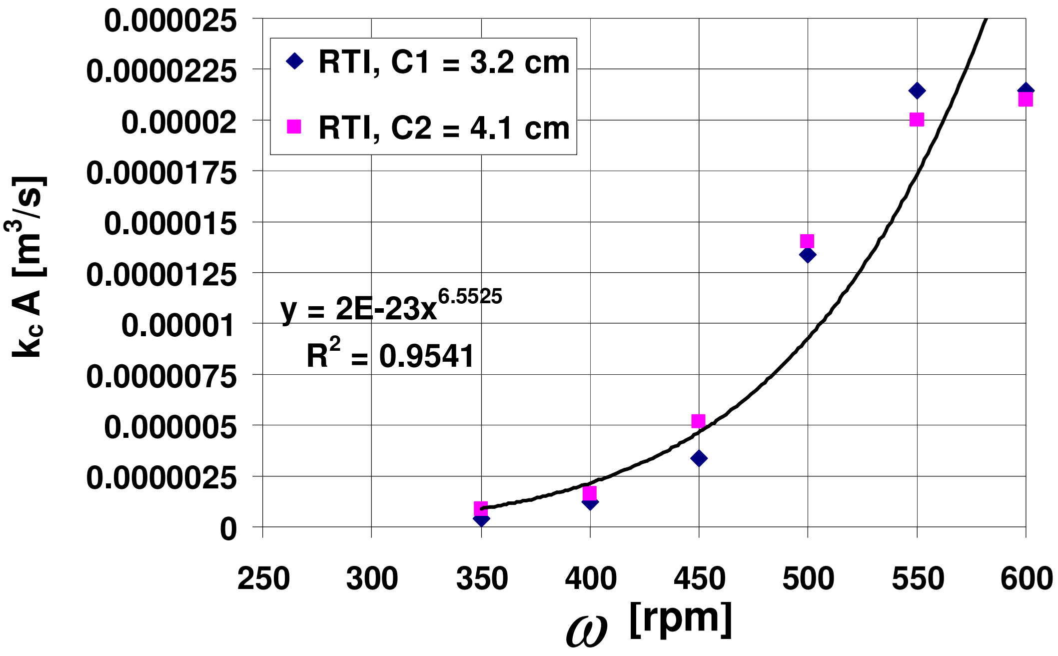

Figure 5.73: The volumetric mass transfer coefficient as a function of the RTI velocity for bottom clearances of 3.2 cm and 4.1 cm.

5.5.3.5 Rate of mass transfer of benzoic acid

The rate of mass transfer depends on surface renewal by diffusion and turbulence in the continuous phase. It is found in Fig. 5.74 that the rate of mass transfer of benzoic acid from water to cyclohexane increases to reach the maximum at t = 1.0 min for low RTI velocities of 350 and 400 rpm, but its value is higher in case of RTI clearance of 4.1 cm than that in case of 3.2 cm. For RTI velocities $\geq$ 450 rpm, the maximum rate of mass transfer is obtained at t = 0.5 min, but its value is higher in case of RTI clearance of 3.2 cm than that in case of 4.1 cm. This behaviour may be due to the fact that at the low RTI velocities, cyclohexane layer reaches to the turbine blades at RTI clearance of 4.1 cm faster than that at 3.2 cm, but at high RTI velocities the major dispersion of cyclohexane occurs in the upper part above the RTI blades and smaller amount of cyclohexane goes to the bottom of the vessel below the RTI blades at RTI clearance of 4.1 cm, whereas larger amount of cyclohexane disperses in the lower part of the vessel at RTI clearance of 3.2 cm gives higher rate of mass transfer. For 0.5 min < t < 1 min, a strong decrease of the ROMT of benzoic acid is obtained forming a narrow distribution. A slow decrease of the ROMT of benzoic acid is obtained for 1 min < t < 5 min. The maximum rate of mass transfer of benzoic acid can be obtained at RTI velocity of 550 rpm, clearance of 3.2 cm and t = 0.5 min as illustrated in Fig. 5.75. RTI velocity and clearance has no effect on the $ROMT_{BA/CH}$ for t > 5 min.

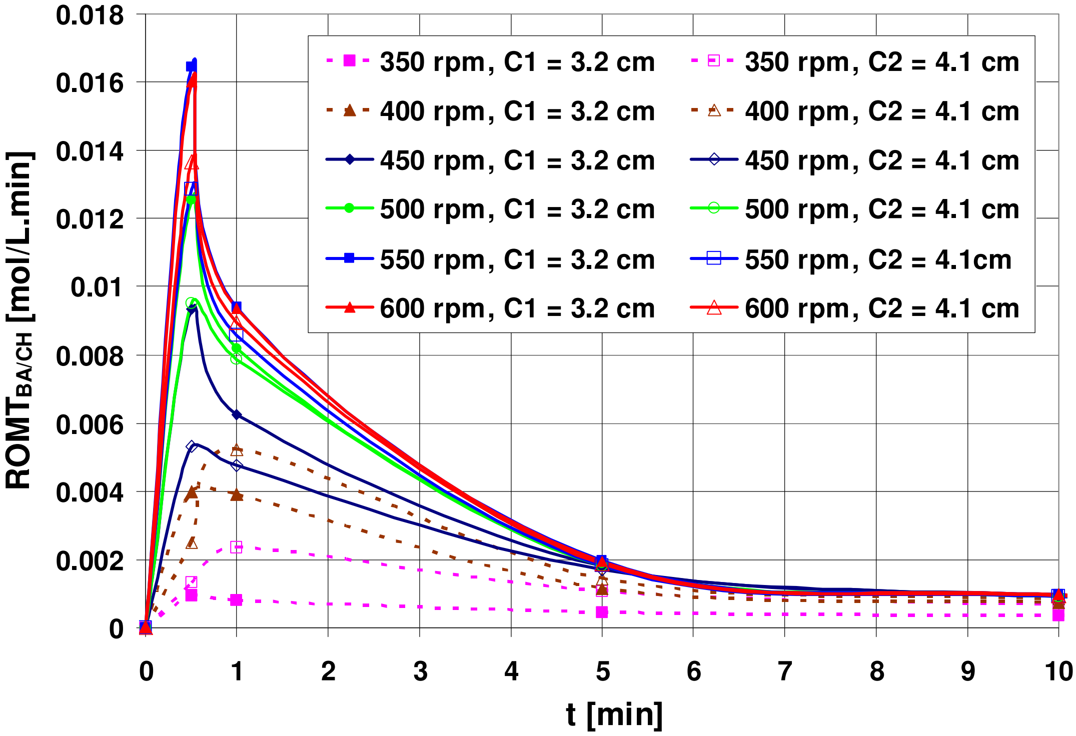

Figure 5.74: The rate of mass transfer of benzoic acid from water to cyclohexane as a function of time at RTI velocity from 350 rpm to 600 rpm.

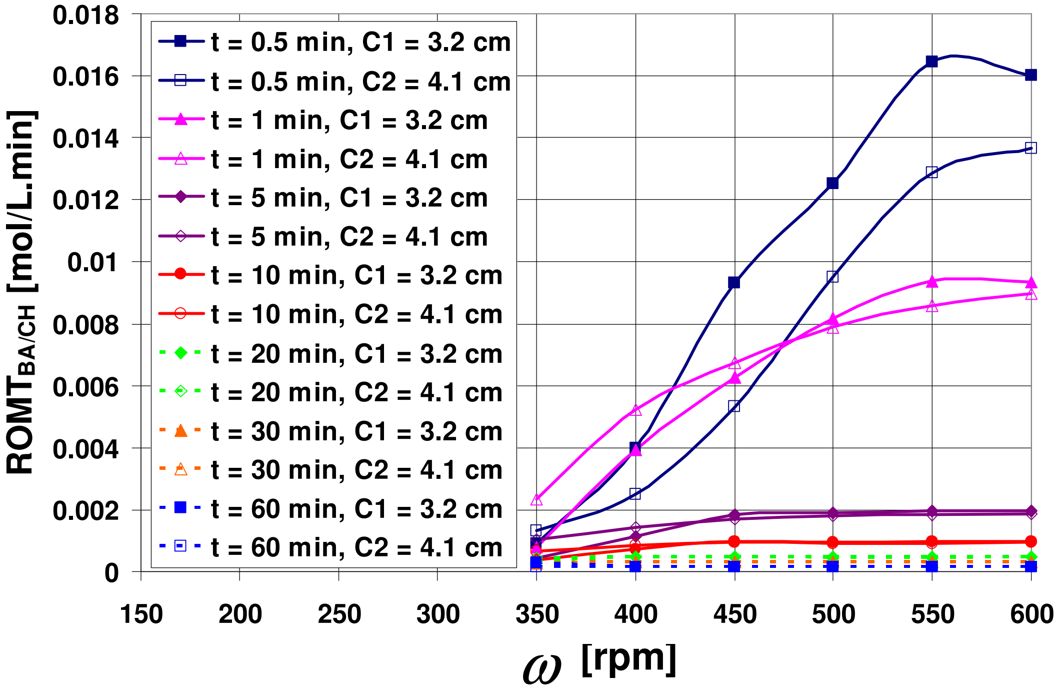

Figure 5.75: The rate of mass transfer of benzoic acid from water to cyclohexane as a function RTI velocity for dispersion times from 0.5 min to 60 min.

5.5.4 Propeller impeller with 20 vol% cyclohexane

5.5.4.1 Concentration of benzoic acid in water

The concentration of benzoic acid in water is drawn as a function of time in Fig. 5.76 for propeller velocity from 350 rpm to 600 rpm and bottom clearance of 4.1 cm. At low propeller velocity of 350 rpm, the mass transfer of benzoic acid from water to cyclohexane is slow and small compared to that at higher velocities. For propeller velocities greater than 400 rpm, a strong and fast decrease of the benzoic acid concentration occurs at t = 1 min to reach the equilibrium concentration.

The strong axial flow of the liquids vertically away from the impeller to the top and bottom of the vessel enhances the coalescence and breakup of the cyclohexane droplets through the redispersion and recirculation along the axis of the vessel, thus increase the dissipation and kinetic energy in the path of recirculation and enhance the mass transfer strongly due to the surface renewal by turbulence and diffusion. The high turbulence in the region of the impeller and the centrifugal forces leading to several eddies improve the mass transfer.

The concentration of benzoic acid in water deceases at t = 0.5 and 1 min significantly as illustrated in Fig. 5.77 when the propeller velocity increases until reaching the equilibrium concentration at a velocity of 550 and 500 rpm, respectively. The minimum velocity to get the equilibrium conditions for all dispersion times $\geq$ 1 min is about 500 rpm, this may be due to the complete dispersion of cyclohexane into water and nearly uniform distribution in the region of the impeller is obtained as found in section 5.1.3. Increasing the dispersion time until t = 5 min results in a significant decrease of the concentration of benzoic acid in water. For t > 10 min, it has no effect on the mass transfer of the solute for all propeller velocities.

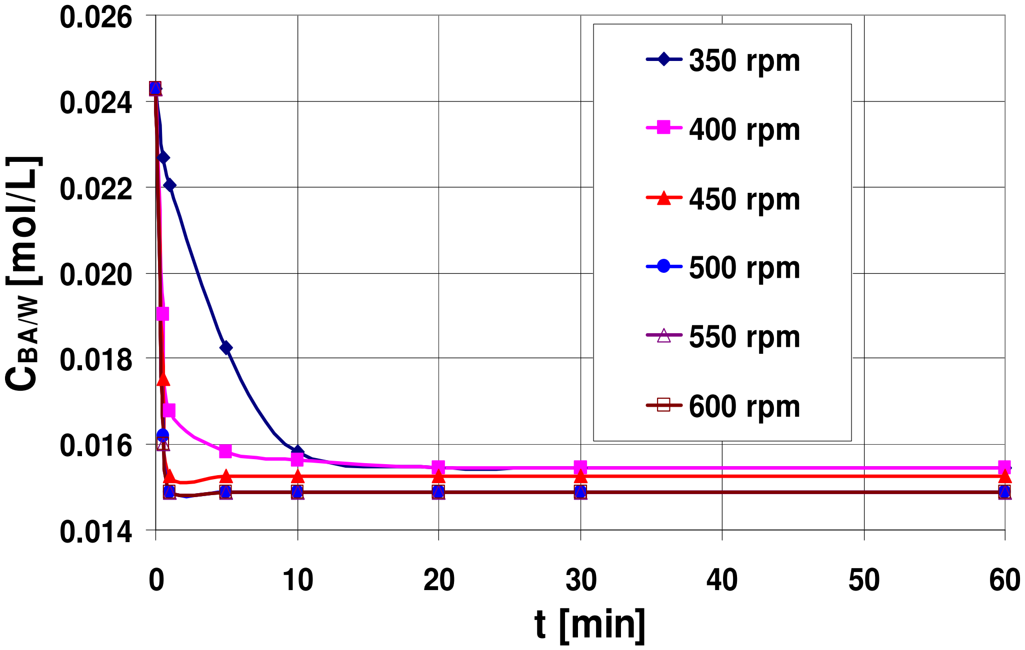

Figure 5.76: Concentration of benzoic acid in water as a function time for propeller velocities from 350 rpm to 600 rpm and bottom clearance of 4.1 cm.

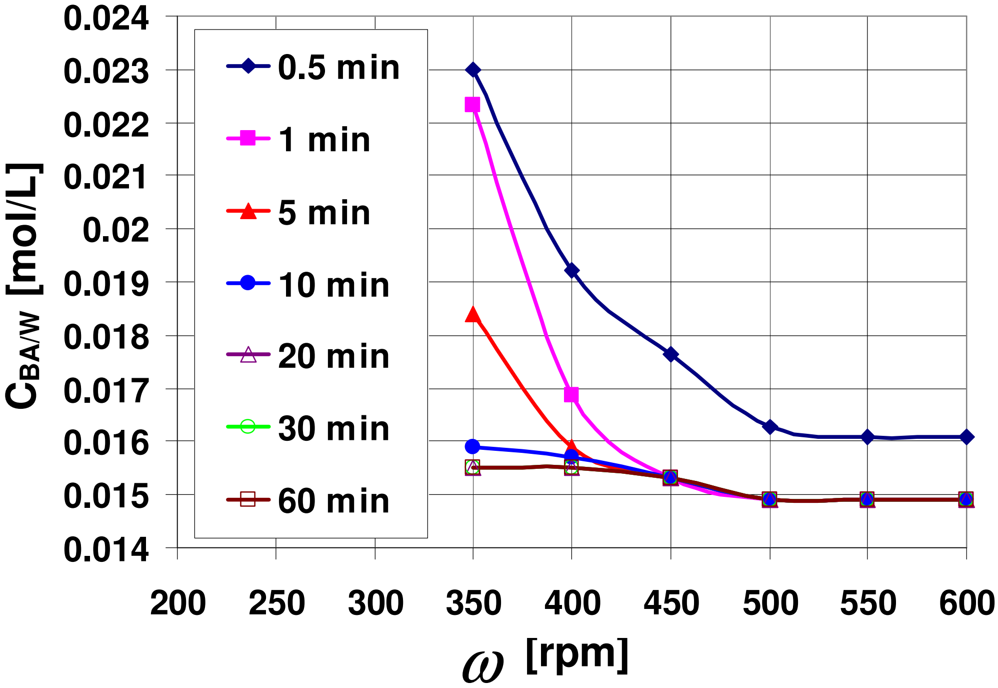

Figure 5.77: Concentration of benzoic acid in water as a function of propeller velocity at dispersion time from 0.5 min to 60 min and bottom clearance of 4.1 cm.

5.5.4.2 Concentration of benzoic acid in cyclohexane

The concentration of benzoic acid in cyclohexane increases when the dispersion time increases until the equilibrium and saturation concentration is obtained as can be seen in Fig. 5.78. The maximum concentration of benzoic acid in cyclohexane is obtained at t = 1 min at propeller velocity of 500 rpm or at t = 10 min at propeller velocity of 350 rpm as shown in Fig. 5.79 because the turbulence around the impeller is high as can be seen in Fig. 5.4-a, where the flow pattern and the distribution of cyclohexane in the vessel (see section 5.3.3) emphasize these results. Propeller velocity greater than 550 rpm has no effect on the mass transfer of benzoic acid from water to cyclohexane or on the equilibrium concentration of benzoic acid.

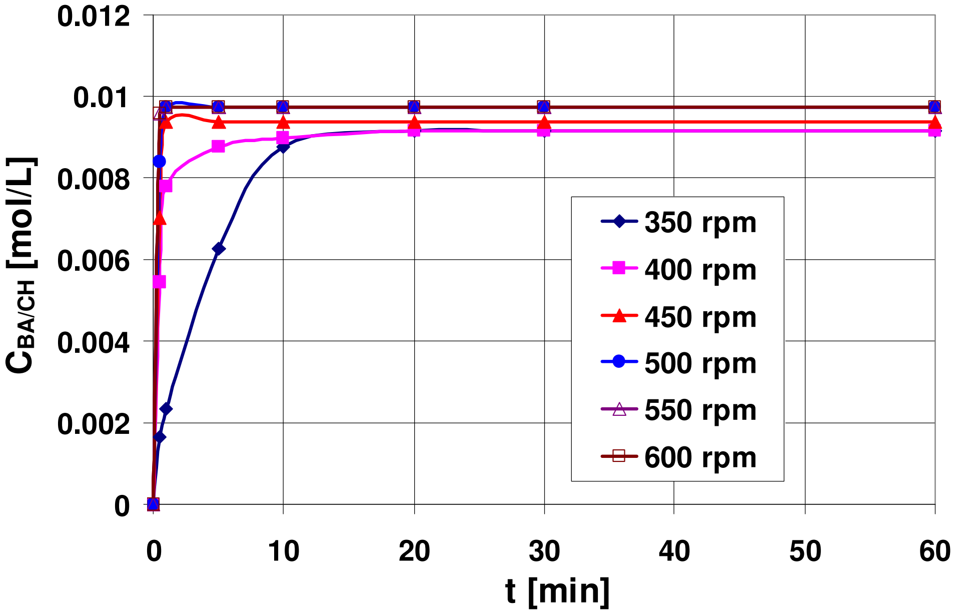

Figure 5.78: Concentration of benzoic acid in water as a function time for propeller velocities from 350 rpm to 600 rpm and bottom clearance of 4.1 cm.

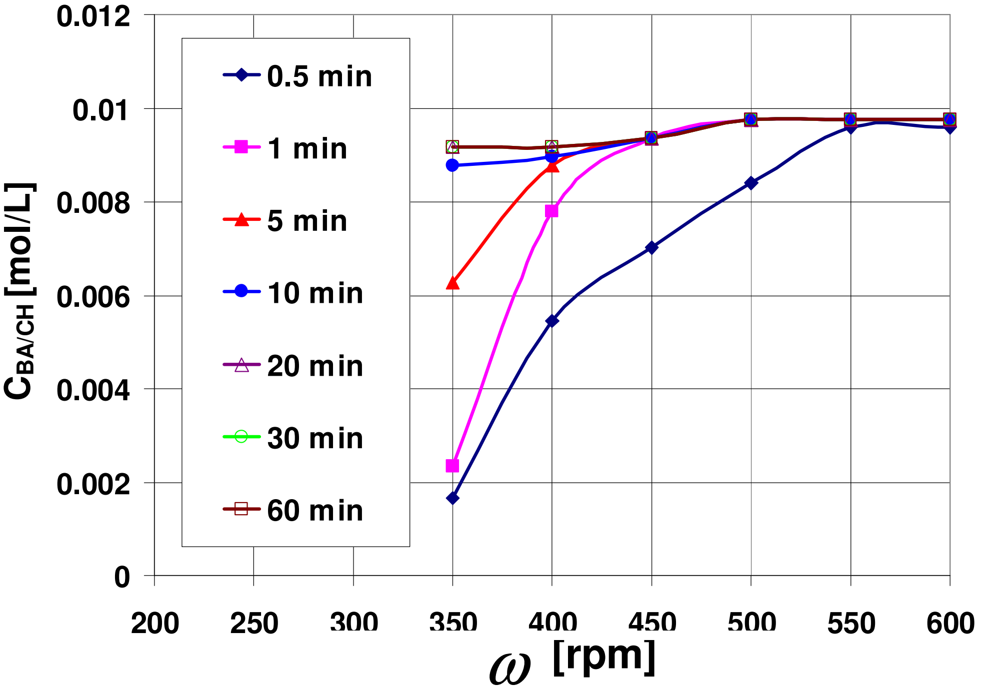

Figure 5.79: Concentration of benzoic acid in cyclohexane as a function of propeller velocity at dispersion times from 0.5 min to 60 min and bottom clearance of 4.1 cm.

5.5.4.3 The equilibrium time and concentration of benzoic acid

The required time to reach the equilibrium concentration of benzoic acid depends on the propeller velocity as can be seen in Fig. 5.80. When the propeller velocity increases, then the equilibrium time required to reach the equilibrium concentration of 0.0149 mol /L decreases until $t_{eq.} = 60$ s at propeller velocity of 500 rpm. Propeller velocity greater than 500 rpm has no effect on the equilibrium time.

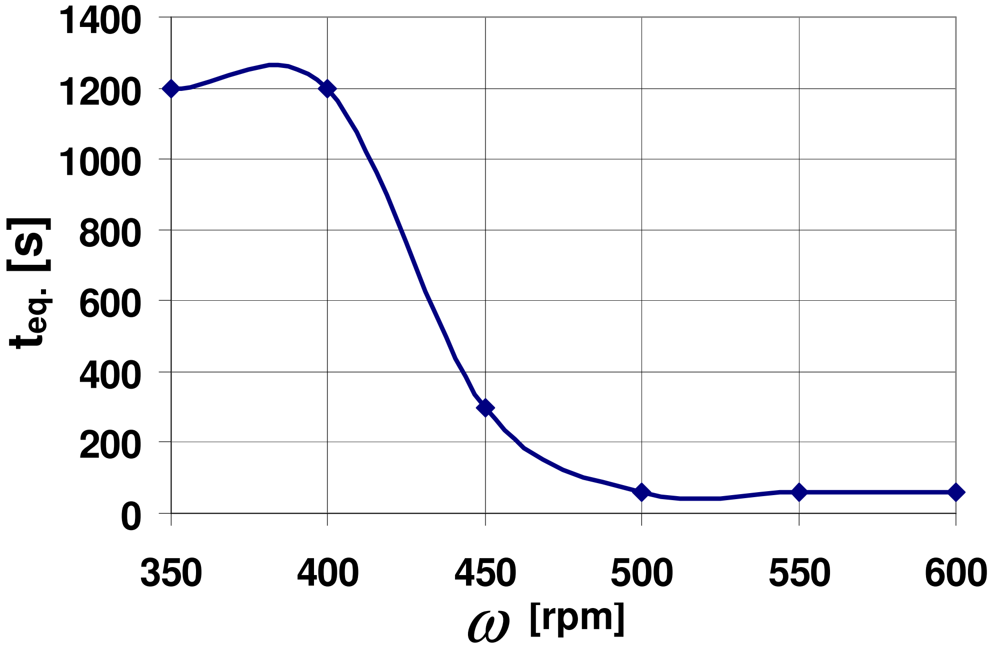

Figure 5.80: The equilibrium time as a function of propeller velocity.

5.5.4.4 Volumetric mass transfer coefficient

The volumetric mass transfer coefficient k_cA of benzoic acid in water is calculated by drawing ln $((C_{eq.} - C_t) / (C_{eq.} - C_{t0}))$ as a function of time which can be seen in Fig. 5.81. A clear and big difference is found between the low absolute value of the slope of the straight line at propeller velocity of 350 rpm and those high absolute values at velocities $\geq$ 400 rpm. The volumetric mass transfer coefficient values in Fig. 5.82 increases when the propeller velocity increases from 350 rpm to 500 rpm, then it remains constant for propeller velocity greater than 500 rpm because there will be no further mass transfer of benzoic acid from water and the system of cyclohexane/water-benzoic acid solution reaches the steady state and equilibrium conditions. This may be also due to the fact that the interfacial area between the two phases does not change and the droplet size of cyclohexane reaches the equilibrium droplet size at propeller velocity ≥ 500 rpm. The volumetric mass transfer coefficient is a polynomial function with the propeller velocity of the fourth degree (see Fig. 5.82).

The highly increase of the k_cA at high Reynolds numbers is due to the axial flow effect and high shear forces of the propeller, which enhance the rate of collisions, breakup, coalescence and redispersion of cyclohexane droplets, resulting in surface renewal at the interface between the two phases, thus enhance the mass transfer. This case is close to that when using anchor impeller.

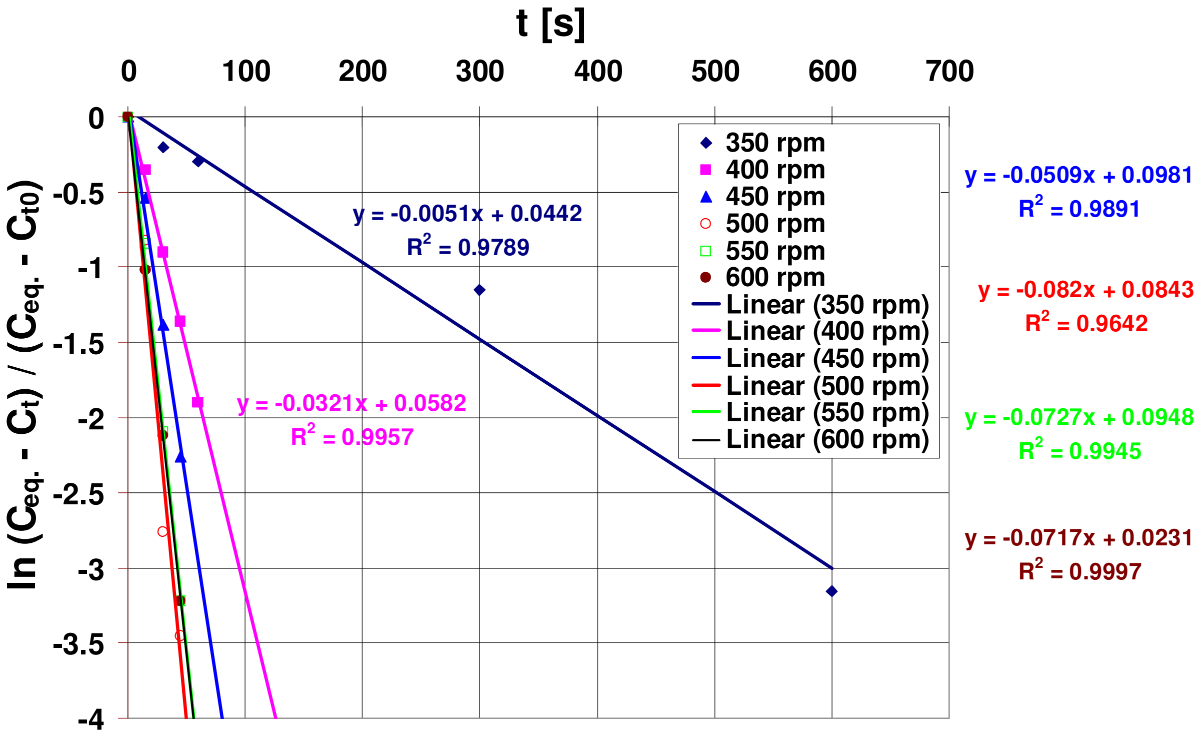

Figure 5.81: ln $((C_{eq.} - C_t) / (C_{eq.} - C_{t0}))$ as a function of time for propeller velocities from 350 rpm to 600 rpm.

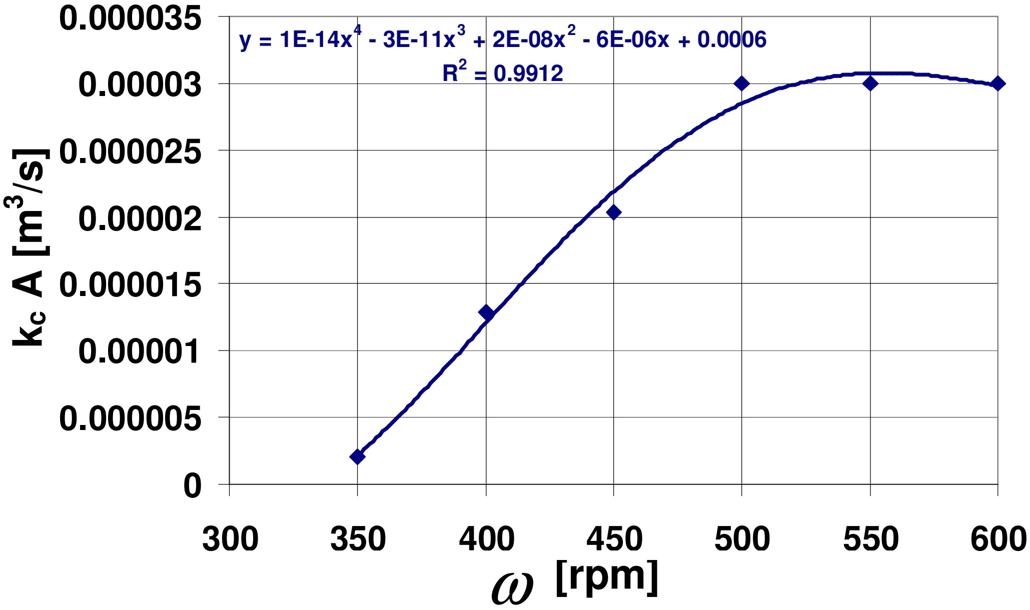

Figure 5.82: The volumetric mass transfer coefficient as a function of propeller velocity.

5.5.4.5 Rate of mass transfer of benzoic acid

The rate of mass transfer of benzoic acid from water to cyclohexane increases when the dispersion time increases to reach its maximum at t = 0.5 min as illustrated in Fig. 5.83. A strong decrease is found between 0.5 min < t < 1 min forming a narrow distribution in this period of time. A small decrease in the rate of mass transfer is found at 1 min < t < 5 min. For t > 5 min, the rate of mass transfer of benzoic acid remains constant and similar for all propeller velocities.

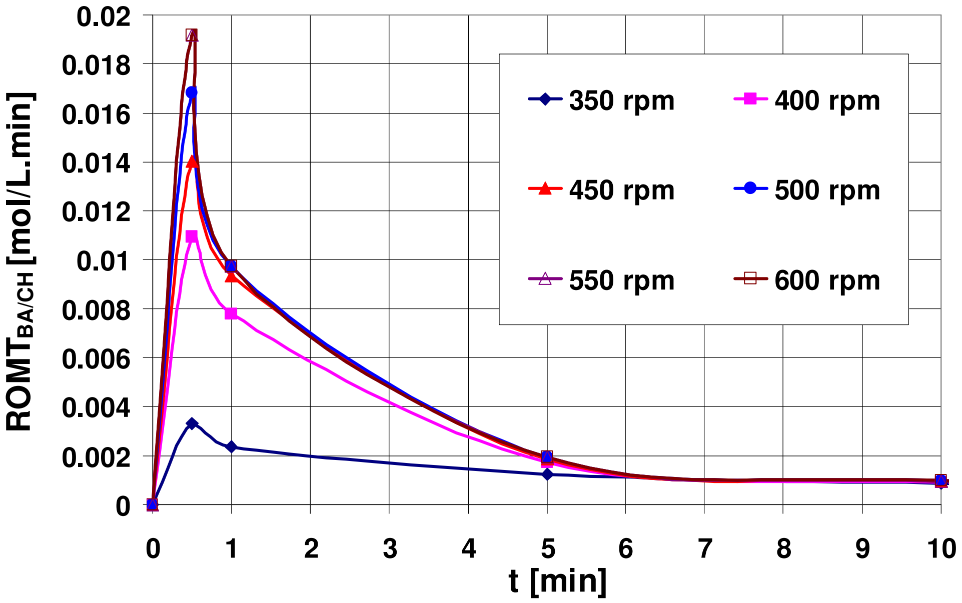

Figure 5.83: The rate of mass transfer of benzoic acid from water to cyclohexane as a function of time at propeller velocity from 350 rpm to 600 rpm.

The maximum rate of mass transfer of 0.019 mol/L.min is obtained at t = 0.5 min at propeller velocity of 550 rpm as it is found from Fig. 5.84, whereas at t = 1 min, a maximum rate of mass transfer of 0.01 mol/L.min can be obtained at minimum propeller velocity of approximately 450 rpm. These results coincide well with that obtained from the radial and axial profiles of cyclohexane volume fraction. The minimum velocity required to get complete dispersion is about 450 rpm, and to get a nearly uniform dispersion is about 550 rpm. So when the distribution of cyclohexane is uniform, then the required time to reach the equilibrium concentration is lowered. For t ≥ 5 min, minimum rates of mass transfer values are obtained, and there is no effect of the propeller velocity on the rate of mass transfer of benzoic acid, because the system reaches the steady state and saturation conditions.

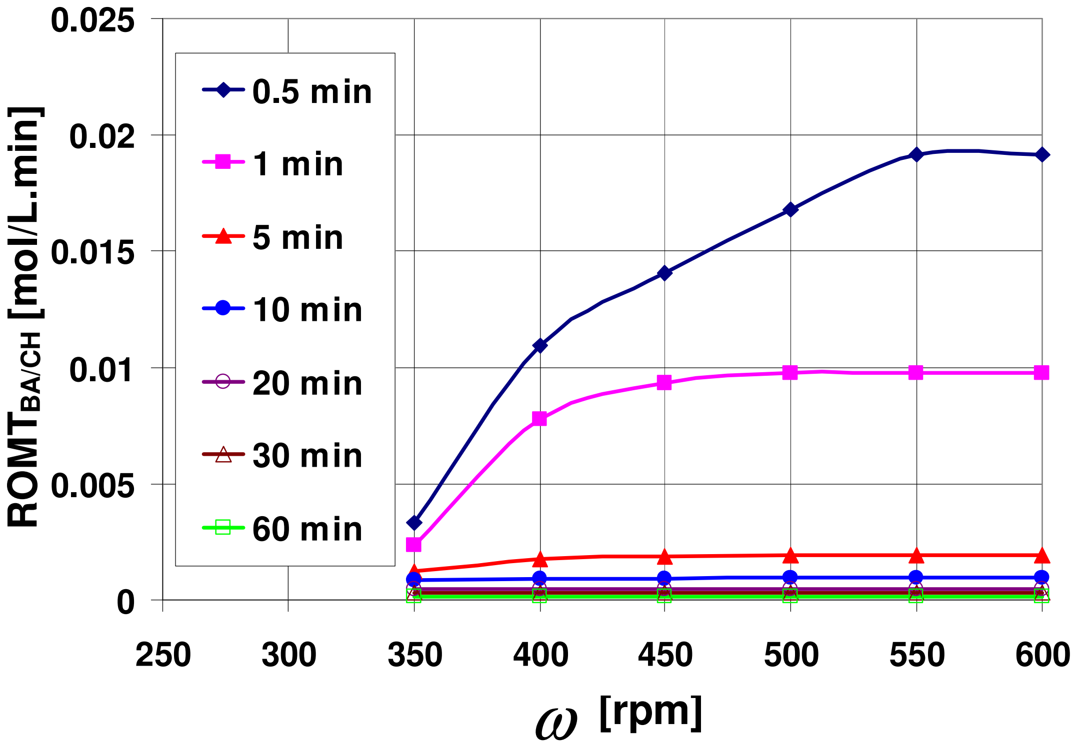

Figure 5.84: The rate of mass transfer of benzoic acid from water to cyclohexane as a function Propeller velocity for dispersion times from 0.5 min to 60 min.

5.5.5 PBT impeller with 20 vol% cyclohexane

5.5.5.1 Concentration of benzoic acid in water

The concentration of benzoic acid in water depends on the dispersion time and PBT velocity. The measured concentration of benzoic acid in water is drawn as a function of time for PBT velocity from 350 rpm to 600 rpm as can be seen in Fig. 5.85. It is found a small decrease of the benzoic acid concentration in water when the dispersion time increases at PBT velocity of 350 and 400 rpm until the equilibrium concentration of 0.017 mol/L is obtained at $t = 10$ min, whereas a strong and fast decease of the benzoic acid concentration is obtained at PBT velocity $\geq$ 450 rpm, the equilibrium concentration is achieved at $t = 1$ min. This behaviour is close to that obtained by the RTI, because PBT impeller produces combined radial and axial flow, but mainly radial. At low PBT velocity, a wide symmetric vortex is formed around the shaft (see Fig. 5.5) due to the high shear forces which allow the surface renewal at the interface and enhance the mass transfer by diffusion. At high Reynolds numbers, the strong radial discharge stream, enhance the collisions with walls, blades of the impeller and the bulk liquid to produce large axial circulations above and below the impeller, that improve strongly the mass transfer due to the surface renewal by turbulent and diffusion at a velocity of 550 rpm, where a uniform distribution of cyclohexane is obtained (Fig. 5.33 in section 5.3.4).

For a given dispersion time in Fig. 5.86, the concentration of benzoic acid decreases when the PBT velocity increases until reaching the minimum concentration of benzoic acid in water at velocity of 550, 500 and 450 rpm for $t = 0.5$, 1 and 5 min, respectively. For $t > 5$ min, the dispersion time has no effect on the mass transfer of benzoic acid; therefore there is no change on the concentration values of benzoic acid in water (see Fig. 5.86).

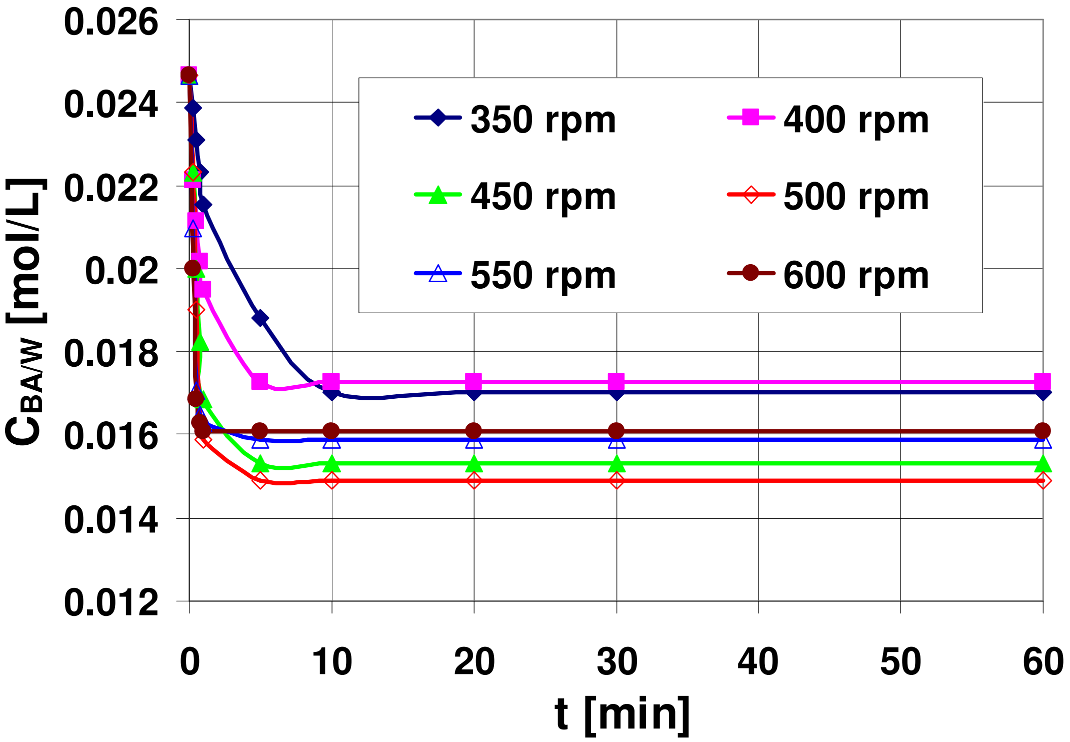

Figure 5.85: Concentration of benzoic acid in water as a function of time for PBT velocity from 350 rpm to 600 rpm and bottom clearance of 4.1 cm.

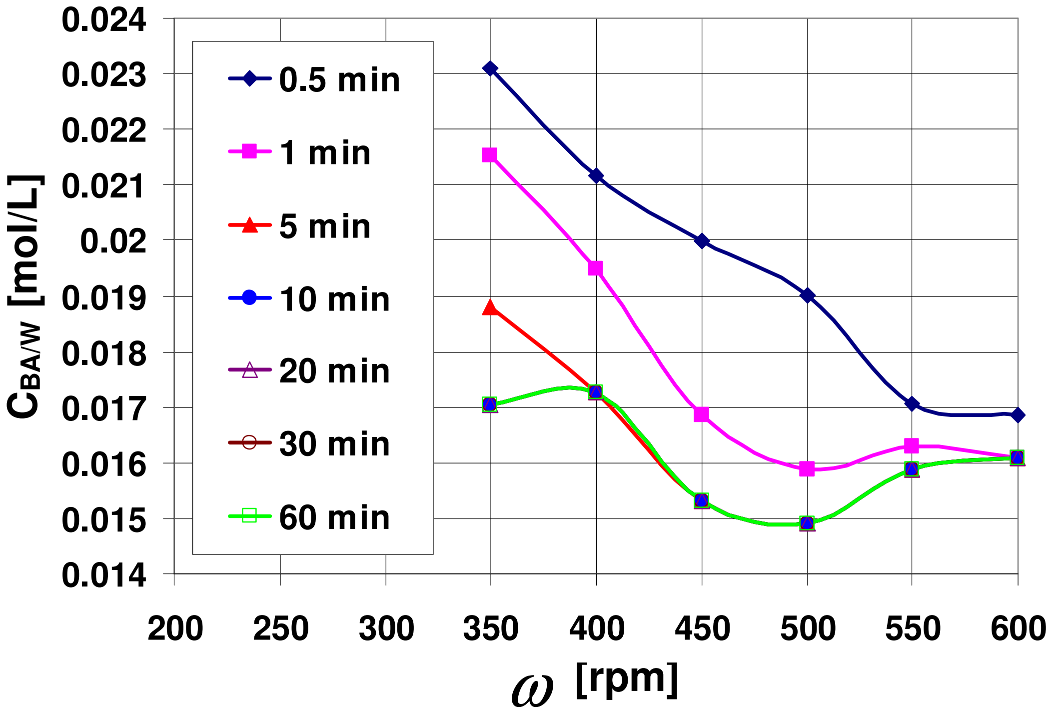

Figure 5.86: Concentration of benzoic acid in water as a function of PBT velocity at dispersion time from 0.5 min to 60 min.

5.5.5.2 Concentration of benzoic acid in cyclohexane

The decrease in the concentration of benzoic acid in the continuous phase is accompanied with an increase of its concentration in the dispersed phase when the dispersion time increases as illustrated in Fig. 5.87. The maximum concentration of benzoic acid in cyclohexane (0.01 mol/L) is found at t = 5 min and PBT velocity of 500 rpm as shown in Fig. 5.88. The dispersion time has no effect on the mass transfer beyond t = 5 min and PBT velocity of 400 rpm.

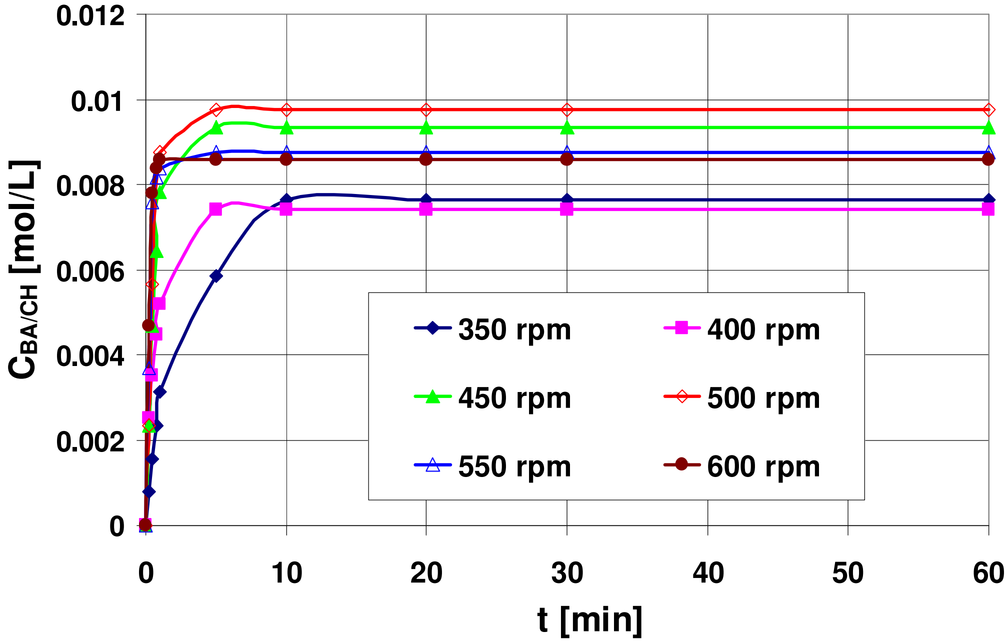

Figure 5.87: Concentration of benzoic acid in cyclohexane as a function of time for PBT velocity from 350 rpm to 600 rpm and bottom clearance of 4.1 cm.

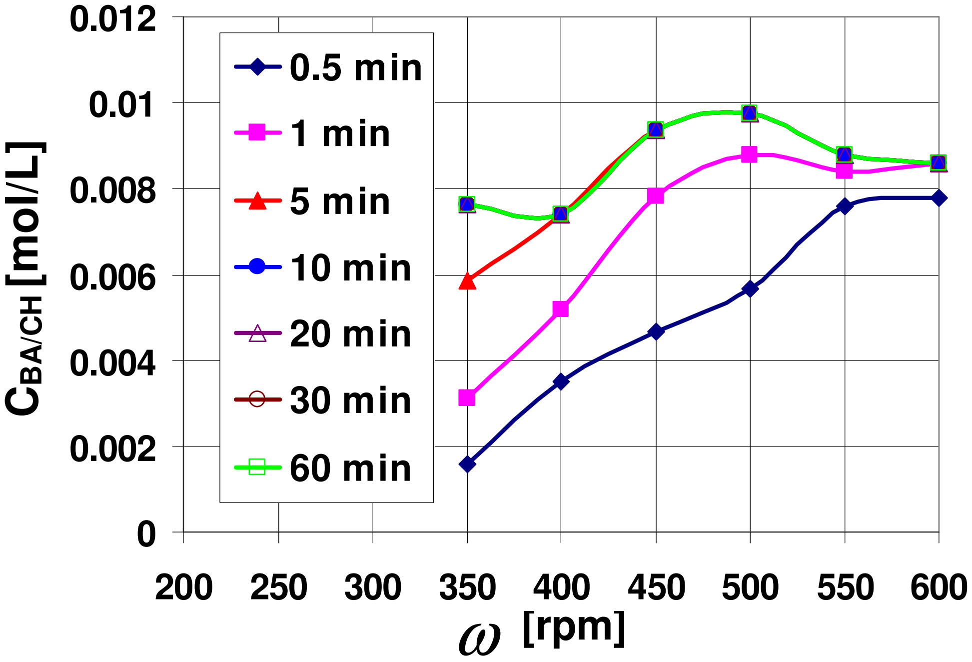

Figure 5.88: Concentration of benzoic acid in cyclohexane as a function of PBT velocity at dispersion time from 0.5 min to 60 min.

5.5.5.3 The equilibrium time and concentration of benzoic acid

The equilibrium time decreases when the PBT velocity increases from 350 to 400 rpm as shown in Fig. 5.89. The minimum velocity of the PBT impeller required to reach the equilibrium concentration of benzoic acid in water of about 0.0161 mol/L is found to be 400 rpm. This low value is due to the significant effect of the axial and radial flow of the PBT impeller that improves the rate of breakup, coalescence and redispersion through the continuous recirculation process. The corresponding equilibrium time is 300 s (5 min). There is no effect of the PBT velocity on the equilibrium time when the PBT velocity is greater than 400 rpm.

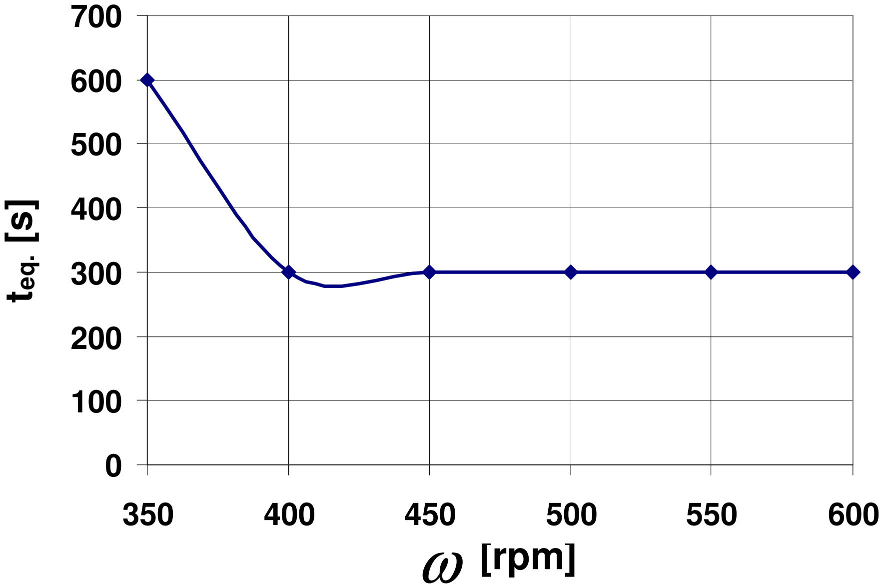

Figure 5.89: The equilibrium time as a function of PBT velocity.

5.5.5.4 Volumetric mass transfer coefficient

ln (($C_{eq.}$ – C_t) / ($C_{eq.}$ – C_{t0})) is drawn as a function of time at PBT velocities from 350 rpm to 600 rpm as illustrated in Fig. 5.90. Straight lines with slopes proportional to the k_cA are obtained. When the PBT velocity increases, the absolute values of these slopes increase smoothly and steadily from 0.0088 at PBT velocity of 350 rpm to 0.0727 at 600 rpm. The effect of the PBT velocity on the volumetric mass transfer is shown in Fig. 5.91. Increasing the stirrer velocity increases the mass transfer of benzoic acid in the continuous phase as a 3.79 power function of the PBT velocity. This is due to the effect of the turbulence generated in the impeller discharge stream. This result agrees with that obtained by Rushton et al. [138], they found that in a mixing vessel the energy input is proportional to the cube of the impeller velocity and to the fifth power of the impeller diameter. The variation of k_c A with the velocity may be due to the variation of k_c or A or both with the velocity, and hence with the power imposed by the impeller.

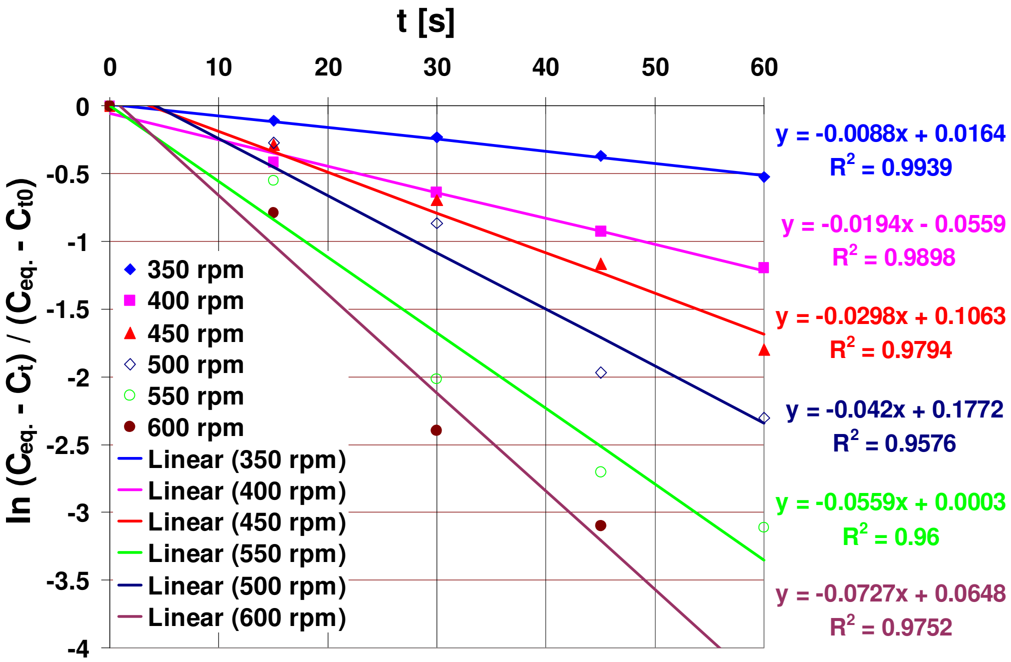

Figure 5.90: ln $((C_{eq.} - C_t) / (C_{eq.} - C_{t0}))$ as a function of time for PBT velocities from 350 rpm to 600 rpm.

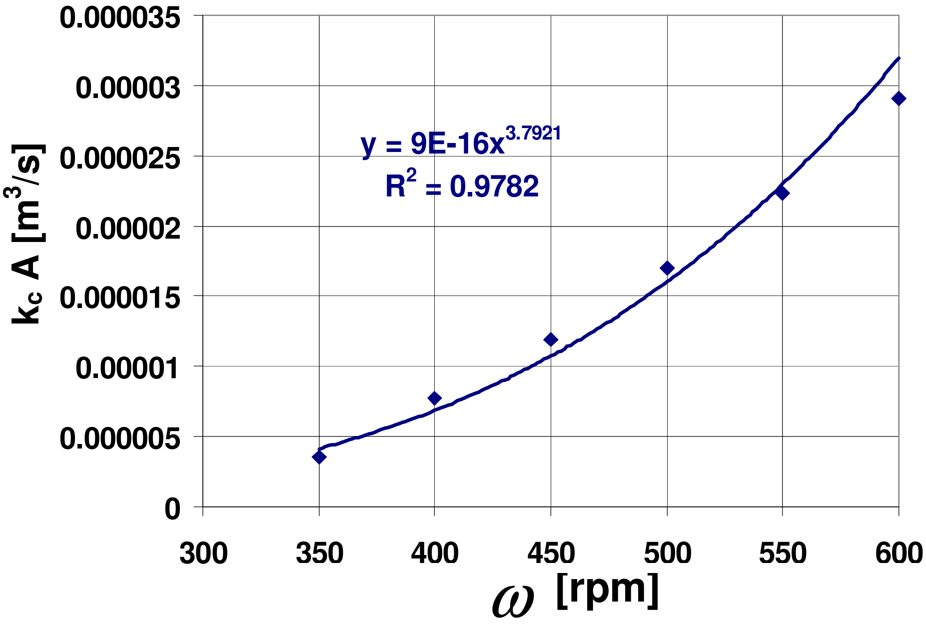

Figure 5.91: The volumetric mass transfer coefficient as a function of the PBT velocity.

5.5.5.5 Rate of mass transfer of benzoic acid

The rate of mass transfer of benzoic acid from water to cyclohexane in Fig. 5.92 shows the strong increase of its value to reach the maximum when the dispersion time increases to t = 0.5 min for all PBT velocities. Then it decreases slowly until t = 5 min. When the PBT velocity increases in Fig. 5.93, the rate of mass transfer increases especially at t = 0.5 and 1 min to reach its maximum at PBT velocity of 550 and 500 rpm, respectively. The maximum rate of mass transfer of benzoic acid is found at t = 0.5 min and PBT velocity of 550 rpm, because a uniform distribution of cyclohexane is obtained, resulting in low droplet sizes (see Fig. 5.12 in chapter 5.2) and large interfacial area for mass transfer. After t > 5 min there will be no effect of the dispersion time and PBT velocity on the rate of mass transfer.

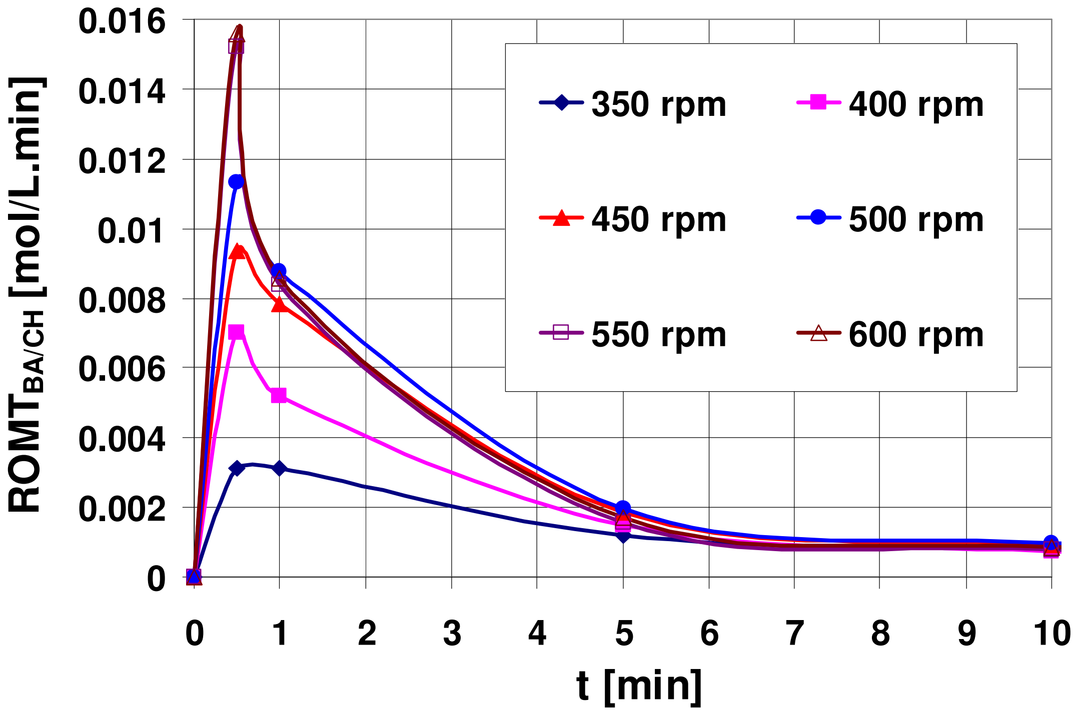

Figure 5.92: The rate of mass transfer of benzoic acid from water to cyclohexane as a function of time for PBT velocity from 350 rpm to 600 rpm.

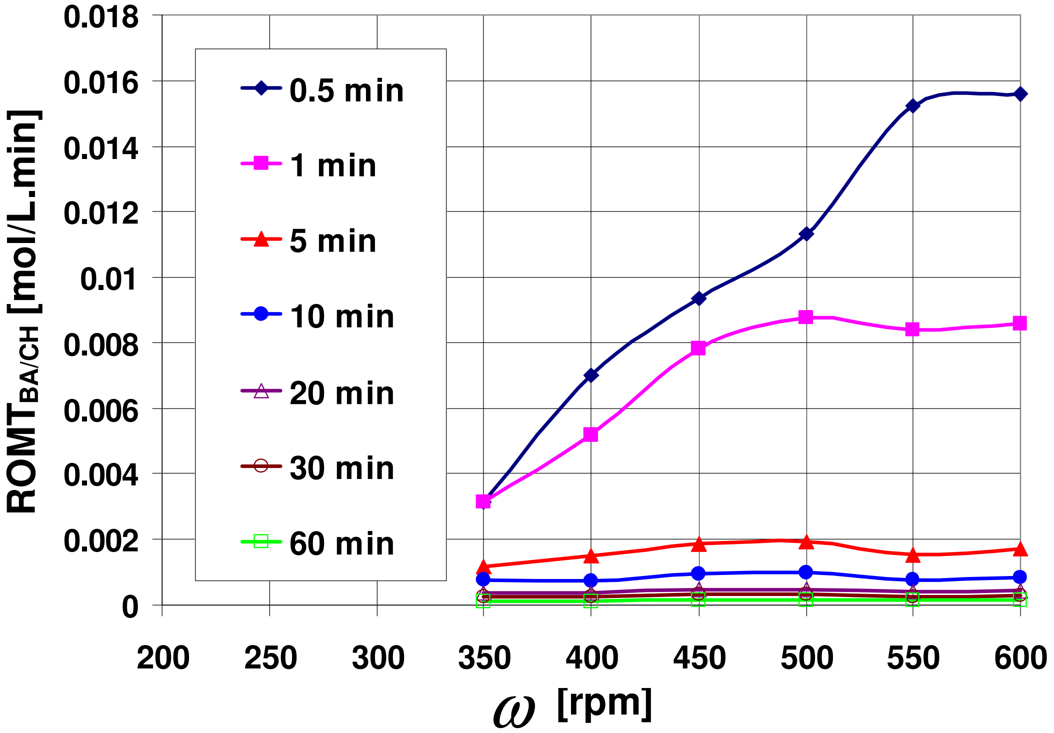

Figure 5.93: The rate of mass transfer of benzoic acid from water to cyclohexane as a function PBT velocity for dispersion times from 0.5 min to 60 min.

5.5.6 Comparison the effect of stirrer type on the mass transfer

5.5.6.1 The equilibrium time and concentration of benzoic acid

The minimum dispersion time required to reach the equilibrium concentration depends on several parameters such as the stirrer type and its velocity. Fig. 5.94 describes the effect of stirrer type and velocity on the equilibrium time. The anchor impeller -which gives high interfacial area with a large film of the dispersed droplets of cyclohexane at the interface between the two phases- gives the minimum equilibrium time of 30 s at a minimum velocity of 350 rpm, whereas the RTI and PBT reach the equilibrium concentration at the same equilibrium time of 300 s at velocities of 500 and 400 rpm, respectively. The RTI and propeller reach the equilibrium concentration at the same velocity of 500 rpm but different equilibrium times of 300 s and 60 s, respectively. The behaviour of anchor and propeller impellers is close because both of them produce intensive axial flow, results in strong centrifugal forces that enhance the mass transfer at a lower dispersion time in comparison with the radial impellers.

The existence of the combined radial and axial flow in case of the PBT reduces the PBT velocity to reach the equilibrium concentration.

The equilibrium concentration of benzoic acid in water is measured after allowing the two cyclohexane/(water-benzoic acid) phases to be stirred for one hour for a given stirrer velocity. The equilibrium concentration values in Fig. 5.95 are similar with a very small difference for anchor, RTI and propeller i.e. the stirrer velocity has no significant effect on the equilibrium concentrations but only the dispersion time. For PBT, there is an inflection velocity of about 500 rpm, the equilibrium concentration decreases from PBT velocity of 350 rpm to 500 rpm and then increases to reach the final equilibrium concentration; this may be due to the sudden change in the uniformity of the dispersion as illustrated in section 5.1.4 through the visualisation with the red tracer.

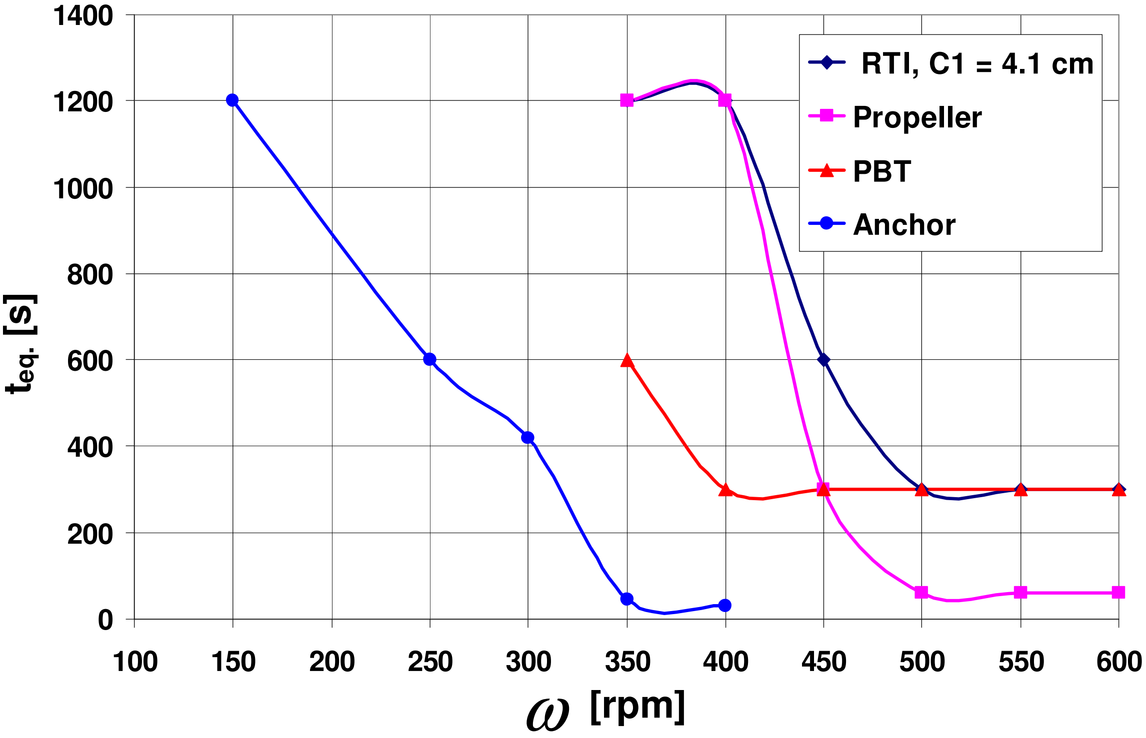

Figure 5.94: The equilibrium time as a function of velocity for RTI, propeller, PBT and anchor impellers.

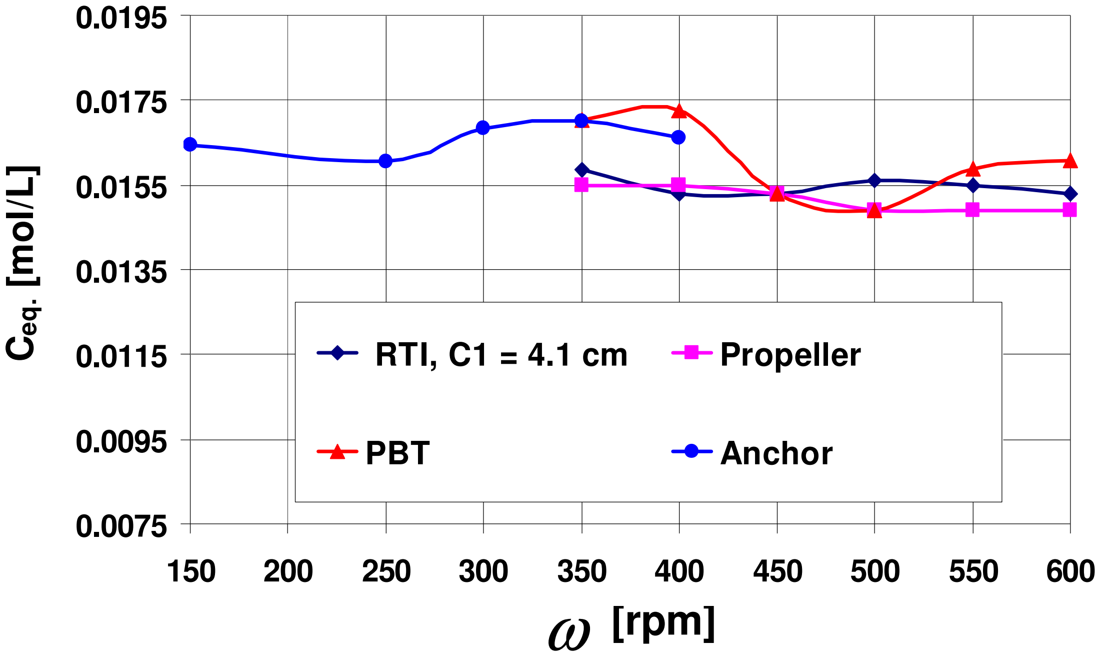

Figure 5.95: The equilibrium concentration as a function of velocity for RTI, propeller, PBT and anchor impellers.

5.5.6.2 Rate of mass transfer of benzoic acid

The dispersion of the droplets and coalescence in the mixing vessel as well as the diffusion and turbulence has a great effect on the rate of mass transfer of the benzoic acid in the continuous phase. Thus the surface renewal of the dispersed phase is affected by these factors and affects the rate of mass transfer [49].

It is found in Fig. 5.96 that the rate of mass transfer increases to reach the maximum at t = 1 min for all types and velocities of the stirrers. Then it decreases until t = 10 min. There is no significant effect of the stirrer type and velocity on the mass transfer for t > 10 min.

The rate of mass transfer with the anchor > propeller > PBT > RTI at stirrer velocities of 350, 450, 500 and 550 rpm. The flow pattern produced by the stirrer (see chapter 5.1) affect the mass transfer. The large formed eddy by the anchor impeller cause the droplets to rotate in the eddy, not break only deform, whereas in small eddies produced by the rest of the stirrers, especially the RTI and PBT they breakup, and thus the symmetric vortex around the impeller is broken at high velocities.

The centrifugal forces have much more effect in case of the axial flow anchor (which forms an axial vortex in agitated liquids with low viscosity [14]) and propeller impellers, thus affect the intensity of turbulence and degree of collisions, coalescence, breakup and eddies formation which enhance the mass transfer more than in the other radial (RTI) or combined flow (PBT) stirrers. The effect of the centrifugal forces in case of the anchor impeller is stronger than that in case of the propeller, because the anchor impeller is larger than the propeller, thus the energy input (large turbulent) is large, resulting in larger rates of mass transfer in case of the anchor impeller which pushes larger amount of cyclohexane towards the impeller near the bottom of the vessel and increases the contact area between the two phases.

The propeller, RTI and PBT impellers gives similar trend and magnitudes of the rates of mass transfer of benzoic acid at stirrer velocity of 350 rpm with a very small difference, this may be due to the fact that the cyclohexane layer forms a symmetric vortex around the shaft at this low velocity, and few droplets are formed around the impeller, thus the interfacial area approximately is very close and therefore the rate of mass transfer are similar.

At a velocity of 450 rpm, the PBT impeller gives higher rates of mass transfer than RTI because the vortex around the shaft is wider and thus larger volume of cyclohexane is dispersed in water, resulting in larger interfacial area and mass transfer. For velocities $\geq$ 500 rpm, Propeller impeller always gives the highest rate of mass transfer, whereas the RTI and PBT impeller give similar rate of mass transfer values with a very small difference. This behavior may be due to the fact that the RTI forms a radial flow and the PBT impeller forms a combined flow in the axial and radial directions which enhance the homogeneity of the cyclohexane distribution in the vessel at lower velocity than that in case of RTI. The results of the mass transfer highly affected with the flow field obtained from the visualization method with red tracer (chapter 5.1) and in a good agreement with the axial and radial profile distribution of cyclohexane volume fractions (chapter 5.3).

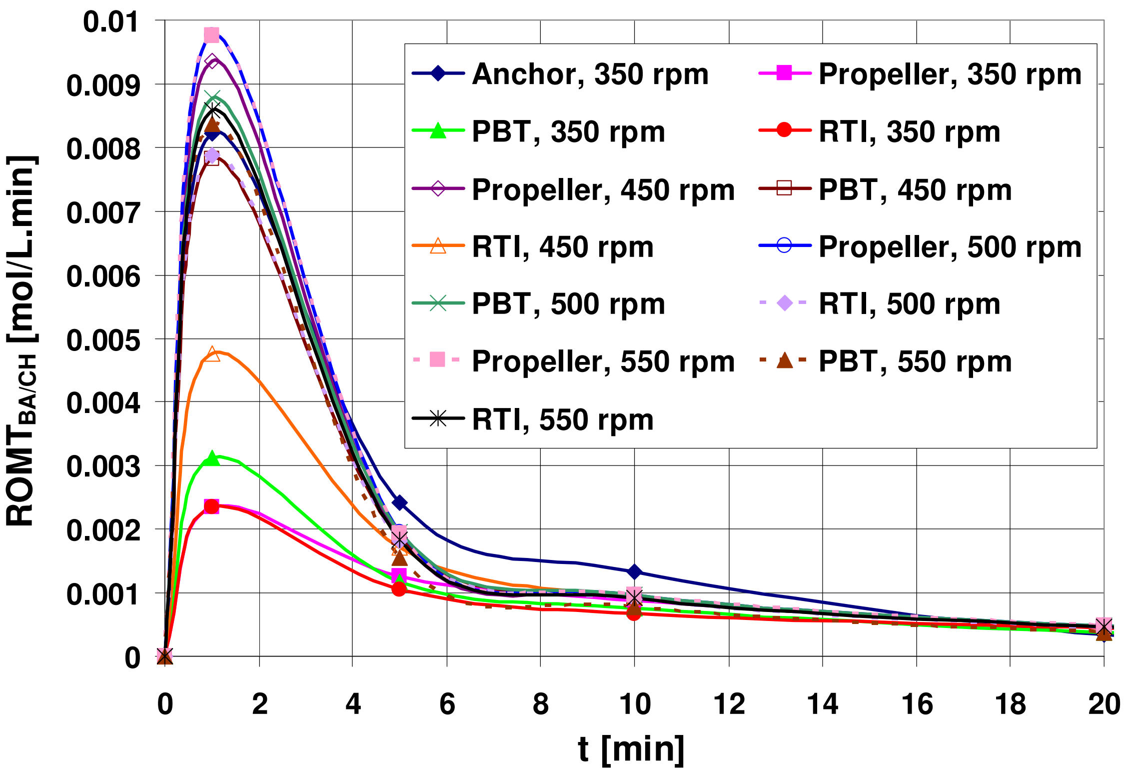

Figure 5.96: The rate of mass transfer of benzoic acid from water to cyclohexane for different stirrers at 350 rpm, 450 rpm, 500 rpm and 550 rpm and clearance of 4.1 cm.

5.5.6.3 Volumetric mass transfer coefficient

The effect of stirrer type and its velocity on the volumetric mass transfer coefficient is illustrated in Fig. 5.97. The anchor gives low volumetric mass transfer coefficient for anchor velocities from 150 and 300 rpm. This may be due to the low turbulence and small number of droplets is formed at the interface film between the two phases. For velocity$\geq$ 350 rpm, anchor impeller gives the highest rate of mass transfer and thus highest volumetric mass transfer coefficients compared with the propeller and turbine impellers.

It is found that $(k_cA)_{propeller} > (k_cA)_{PBT} > (k_cA)_{RTI}$ for stirrer velocity$\geq$ 350 rpm. This results due to the higher turbulence and input energy from the propeller which affects the breakup, coalescence of the cyclohexane droplets, re-dispersion of the coalescence droplets and diffusion. Thus these parameters affect on the surface renewal of the dispersed phase, the interfacial area between the two phases and the volumetric mass transfer coefficients. The values of k_cA for RTI and propeller impeller increase when the stirrer velocity increases to reach its maximum of 0.00002 and 0.00003 m^3/s at velocity of 550 and 500 rpm, respectively. Above these velocities k_cA values remain constant. That means the propeller impeller gives the maximum volumetric mass transfer coefficient at a minimum stirrer velocity of 500 rpm, whereas the PBT impeller gives the same value of k_cA at 600 rpm.

The values of k_cA vary as the 3.96 power of the anchor velocity, 3.7 power of the PBT velocity, 4 power of the propeller velocity and 6.5 power of the RTI velocity. k_c and A are affected similarly but not equally by the stirrer velocity as announced by Rushton et al. [49].

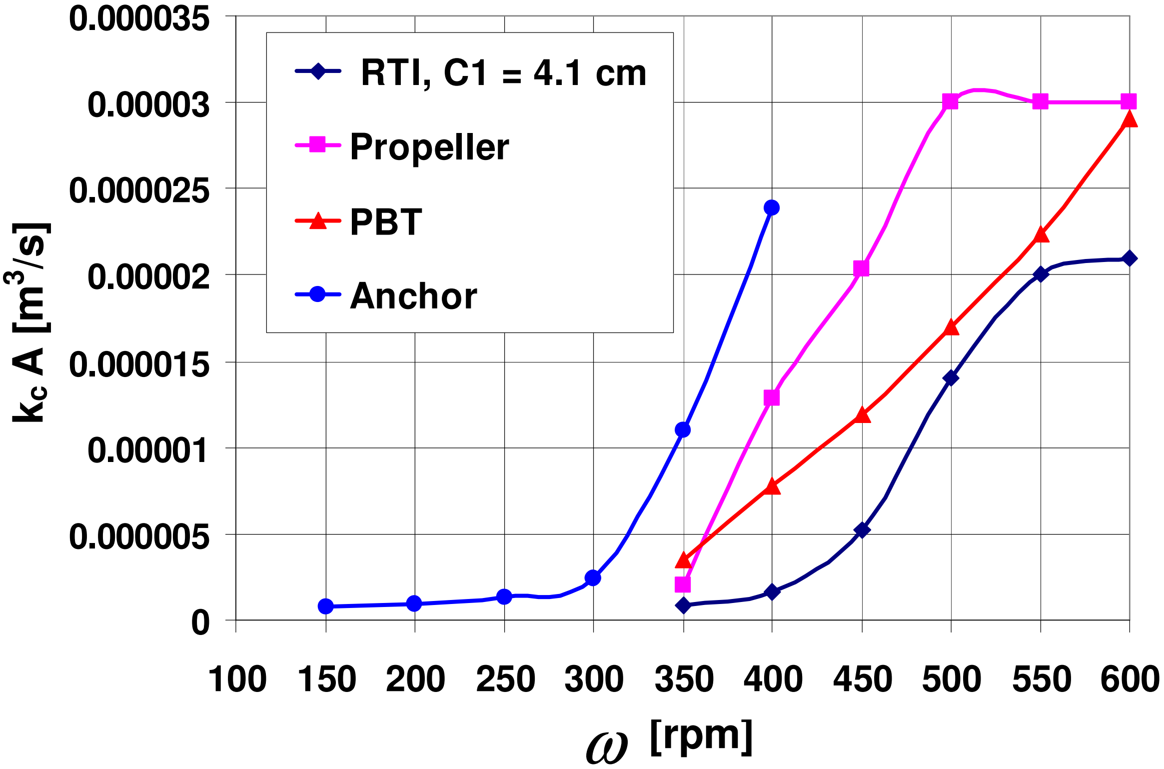

Figure 5.97: The volumetric mass transfer coefficient as a function of stirrer velocity for RTI, propeller, PBT and anchor impellers.

5.5.7 Calculation of the interfacial area and mass transfer coefficient

The interfacial area (A) between the two phases is calculated based on the CFD calculated averaged volume fraction of cyclohexane into water for a wide range of stirrer velocities, and the measured Sauter mean droplet diameter of cyclohexane regarding to equation 2.2.

The area A is the product of the specific area (a) and the volume of the continuous phase. It is found that the interfacial area varies as the 2.6 power of the RTI velocity and 0.75 of the anchor velocity as can be seen in Fig. 5.98. It is found by Rodger et al. [63] that the interfacial area varies as the 1.4 power of the stirrer (flat turbine impeller) velocity.

Anchor impeller gives interfacial area between the two phases higher than that given by the RTI, and they become close at stirrer velocity greater than 600 rpm. A minimum RTI velocity of 550 rpm is required to get similar maximum interfacial area that is given by the anchor impeller at a velocity of 350 rpm. To get a maximum interfacial area, the power consumption by the RTI should be higher than that consumed by the anchor impeller because the intensive turbulence in the bulk liquid occurs at a minimum RTI velocity of 550 rpm. The energy input in case of anchor impeller at low velocity of 350 rpm is high because its diameter is large in comparison with the small diameter RTI, suggesting that the stirrer size affects the minimum stirring velocity.

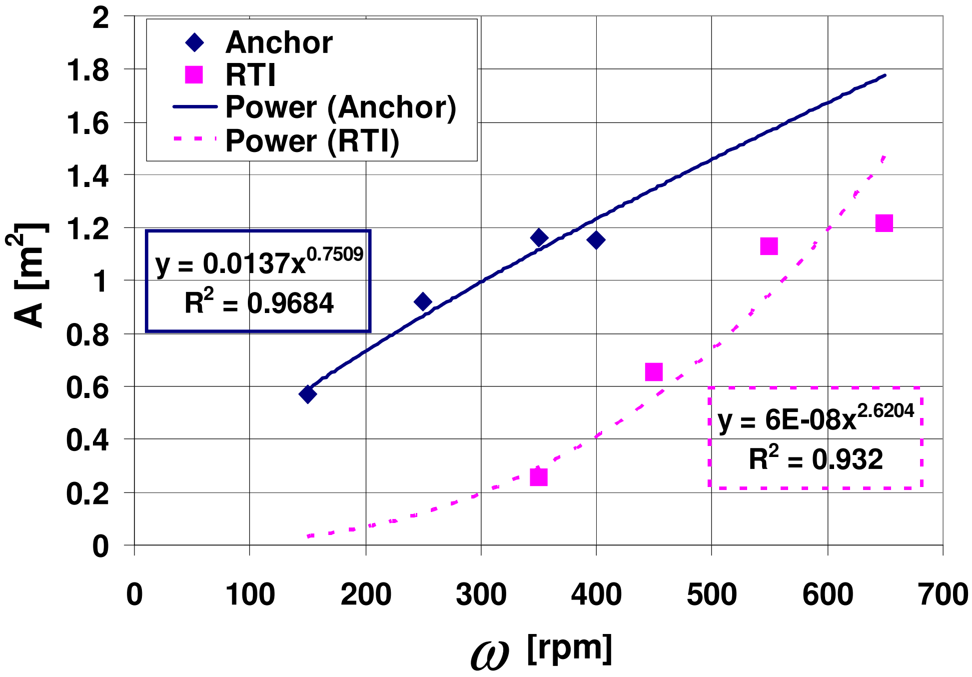

Figure 5.98: Interfacial area as a function of stirrer velocity for RTI and anchor impeller.

The large interfacial area in case of the anchor impeller may be caused by the large interface, results from the large eddy, and swirling eddies that exist at the interface between the phases, whereas in case of RTI it is caused by the small droplets, results from the strong radial discharge stream and the existed vortices above an below the impeller which enhance the collisions and the rate of droplets breakup leading to large interfacial area between the two phases.

Mass transfer coefficient k_c of the benzoic acid in the continuous phase is affected by the turbulence generated in the impeller region. It is found that k_c increases as the 4.2 power of the RTI velocity and 2.95 of the anchor velocity as can be seen in Fig. 5.99. The mass transfer occurs may be due to the surface renewal of the dispersed phase. It occurs due to the diffusion, coalescence and dispersion of the droplets. Mass transfer coefficient k_c in case of the anchor impeller is higher than that for the RTI because the anchor impeller produces high turbulence in the continuous phase, leading to higher gradient velocities between the two phases.

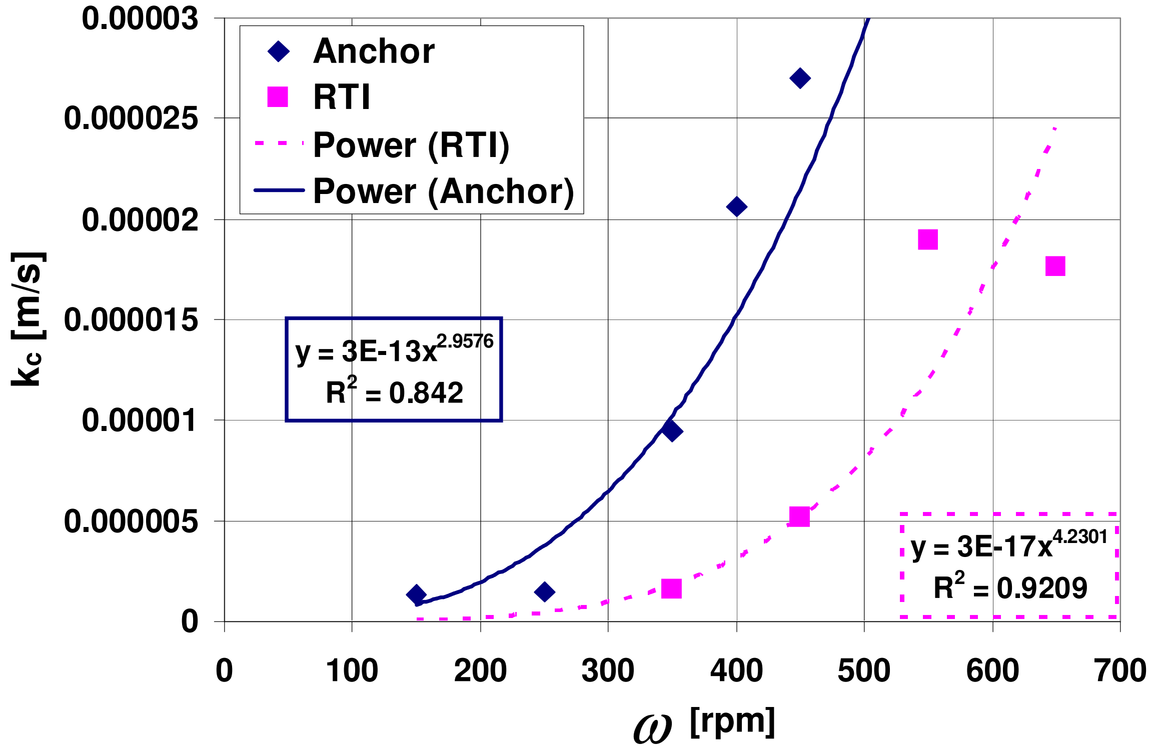

Figure 5.99: Mass transfer coefficient as a function of stirrer velocity for RTI and anchor impeller.

The values of A are higher than that of k_c for both stirrers. For that the dependence of k_c A values on stirrer velocity is highly affected by the variation of the area with the stirrer velocity rather than the variation of k_c. This may be because the stable drop size under the hydrodynamic conditions is used in the calculations of the interfacial area. This result agrees with that obtained by Nagata [139]. The volumetric mass transfer coefficient k_c A varies as 3.96 power of the anchor velocity as can be seen in Fig. 5.54, it may be close to the sum of the velocity power of 2.95 for the k_c and 0.75 for the A. Whereas k_c A varies as 6.5 power of the RTI velocity as shown in Fig. 5.73, it may be near to the sum of the velocity power of 4.2 for the k_c and 2.6 for the interfacial area A.

5.6 Flow velocity fields

The flow fields are measured experimentally by tracking the movement of the Redoxharz II particles in the stirred vessel with 3-blades propeller and 6-blades RTI. The velocities and the number of the particles corresponding to these velocities are measured and classified into four groups: Very low velocity range from 0 - 20 mm/s represents the dead zone. The slow motion of the particles represents the velocity range from 20 - 40 mm/s without meaningful flow movement. Normal movement of the particles are classified in the velocity range from 40 - 80 mm/s, which are distinguished as lines that can be well followed, thus the magnitude and direction of the flow can be determined easily. Rapid motion of the particles is found when the stirrer velocities are higher than 80 mm/s, where the particles are clearly visible and well recognized over the time. The distribution of the particles and their corresponding velocities in a stirred vessel with the propeller and RTI at velocities of 400, 600 and 800 rpm are investigated.

5.6.1 Propeller and rushton turbine impellers

An axial flow is formed in a stirred vessel with propeller impeller, whereas a radial flow by the RTI is obtained, the intensity of the flow depends on their velocities. The flow field visualization and velocity distribution of the particles by using the light cut method at propeller and RTI velocity of 400 rpm are shown in Figs. 5.100 and 5.101, respectively.

For the propeller impeller, particles with a velocity between 0-20 mm/s are present in the upper part of the vessel in the distance between 0 - 1000 pixels on the vertical y-coordinates, large number of particles with a very small movement (dead zone) can be seen in Fig. 5.100. It is clear that all the particles are distributed in the upper part of the vessel above the propeller which ensures the existence of the strong axial flow even at low propeller velocity. Whereas there are small number of particles with a velocity between 0-20 mm/s above and below the RTI in the vessel as can be seen in Fig. 5.101, caused by the collision of the radial discharge stream with the cylindrical walls, resulting in two vortices above and below the RTI, but they are very weak at low velocity of 400 rpm and has no significant effect on the particles distribution, and this agree well with distribution of cyclohexane by visualization with red tracer as can be seen in chapter 5.1, where few droplets of cyclohexane are found below and above the RTI.

For propeller impeller, slow particles move at a velocity between 20 and 40 mm/s are more widely distributed in the vessel mainly in the upper part of the vessel. The corresponding particle distances are between 500 and 2000 pixel on the y-axis (vertical coordinate). Particles in the normal velocity range from 40 to 80 mm/s and the fast one whose velocity greater than 80 mm/s are visible and can be seen in the vicinity of the stirrer and near the cylindrical walls in the distances between 1500 and 2700 pixels on the vertical coordinates and 800 to 1800 pixels on the x-axis (horizontal coordinate).

For the RTI, most of the particles can be seen only in the vicinity around the RTI. The rapid movement of the particles takes place on the vertical coordinates between 1500 to 2500 pixel and 100 to 2500 pixels on the horizontal coordinate at a velocity greater than 40 mm/s. Thus the flow obtained by RTI is radially, where most of the particles are distributed around the RTI impeller, thus the travelled distance by the particles in the radial direction (horizontal coordinate) is higher in case of RTI. Whereas the travelled distance in the axial coordinate (vertical coordinate) is higher in case of the propeller impeller.

Increasing the velocity of propeller to 600 rpm in Fig. 5.102 increases the velocities of the particles to reach the normal and fast velocity ranges. The particles are distributed in the vicinity of the propeller but mostly above the propeller up wards in the axial direction, the particles possess high kinetic and turbulent energy, thus enhance the rate of collisions which helps the particles to reach the free surface at the top of the vessel. This is the reason that cyclohexane droplets are completely dispersed in water at lower velocity than that in case of

RTI. The clear visible particles move in the vertical coordinates between 1500 and 2750 pixel in the upper area of the vessel.

The particles in the dead zone and with almost no movement become much less and they are distributed below the propeller. The particles with velocities exceed 80 mm/s can be pushed up for longer distance upward by the propeller and begin the visible axial flow field in Fig. 5.102.

For RTI, the state of the flow at 600 rpm in the vessel is radial as shown in Fig. 5.103. The particles are much more visible and the flow field can be traced. No particles have velocity in the range of 0 - 20 mm/s, few particles with a slow velocity between 20-40 mm/s are found below the RTI and many particles with velocities between 40 - 80 mm/s and higher than 80 mm/s are well distributed, but mostly above the RTI as can be seen in Fig. 5.103.

All of the above results describe well the turbulence and velocity distribution in a stirred vessel with RTI and propeller impeller at different locations in the vessel. They explain and agree with the results of the complete and uniform dispersion of cyclohexane through the axial and radial profiles of cyclohexane volume fraction (sections 5.3.2.and 5.3.3), and thus their effects on the mass transfer process (section 5.5.6).

Increasing the propeller velocity to 800 rpm in Fig. 5.104, results in a complete distribution of the particles. The particles move in long distances during the exposure time of 1/30 seconds with velocities from 80 mm/s to 300 mm/s. The propeller impeller gives clearly strong axial flow at this velocity. No dead zone with particles velocity less than 20 mm/s is formed. The velocities of the particles start from 20 mm/s. Many particles have fast velocities from 80 to 300 mm/s and are distributed well throughout the vessel.

RTI at a velocity of 800 rpm gives clear and strong radial flow as can be seen in Fig. 5.105. RTI transmits and distributes its energy in the vessel uniformly with almost normal velocity of the particles between 40-80 mm/s, but there are small numbers of particles with slow velocity between 20-40 mm/s below the

RTI in the lower part of the vessel. The flow field, velocities and particles trajectories can be visualised and measured earlier, clearly and completely distributed in a stirred vessel with propeller rather than that stirred with RTI with 6 blades.

The distances travelled by the particles in the axial direction with propeller impeller are much longer than that in case of the RTI which push the particles in the radial direction then they will be divided to two parts, above and below the RTI.

5.6.2 Histograms of the flow velocities

The number frequency distribution of the particles velocity in a stirred vessel with propeller and RTI at velocity of 400, 600 and 800 rpm is shown in Fig. 5.106. The velocity of the particles is directly proportional to the stirrer velocity.

At low velocity of 400 rpm, the number of particles which have a very low velocity between 0-20 mm/s in the dead zone (approximately no movements) are less in case of the RTI than that in case of the propeller impeller. Approximately the same numbers of the particles with velocity of 20-40 mm/s, 40-80 mm/s and 80-135 mm/s are obtained for both stirrers. RTI gives few particles with a velocity higher than 135 mm/s. Almost the number frequency of the particles velocity at stirrer velocity of 400 rpm is similar for propeller and RTI.

Increasing the velocity of the stirrer to 600 rpm shows that the RTI gives higher number frequency of the particles with velocities between 40-80 mm/s and 80- 135 mm/s in comparison with the propeller impeller, whereas few particles with a very high velocity in the range between 180-220 mm/s exist around the propeller impeller. RTI velocity of 600 rpm gives much more uniformly distributed particles in the vessel than that obtained by the propeller, in addition to the absence of the dead zones of very low velocities between 0-20 mm/s.

At stirrer velocity of 800 rpm, the number frequency of the particles velocity between 20-40 mm/s, 40-80 mm/s and 80- 135 mm/s is approximately similar for both RTI and propeller. The particles with very low velocity between 0-20 mm/s disappeared in the vicinity of the both stirrers. The maximum velocity of the particles in a stirred vessel with propeller impeller is 300 mm/s, whereas it is found to be 150 mm/s in case of the RTI. This indicates that the propeller impeller gives higher turbulence in the vessel and thus gives higher rates of mass transfer as it is found in section 5.5.6 due to the surface renewal by turbulence, caused by the effect of the centrifugal forces in case of propeller impeller.

The maximum turbulence is found near the impellers, minimum in the bottom of the vessel and at the top near the walls of the vessel and intermediate between these locations. This turbulence distribution confirms the CHVF distribution in the stirred vessel with RTI and propeller impeller.

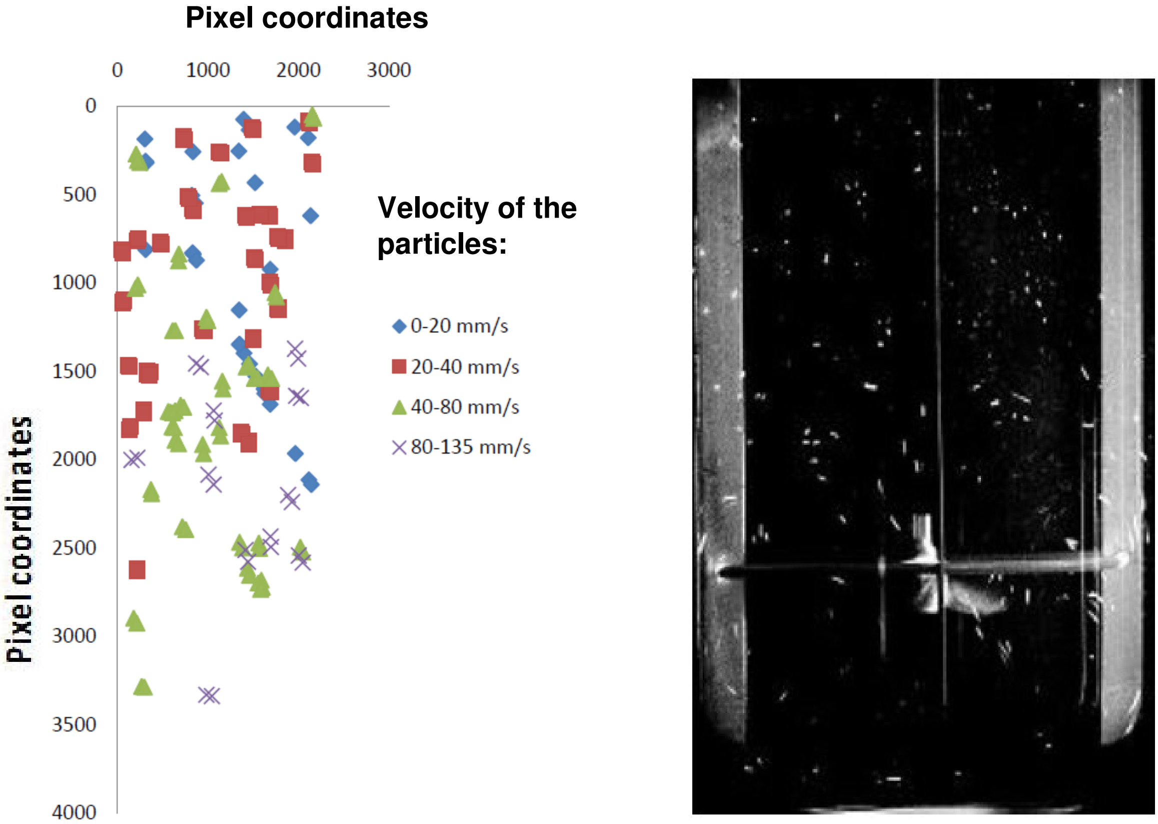

Figure 5.100: Flow field (right) and velocity distribution (left) with propeller impeller at a velocity of 400 rpm.

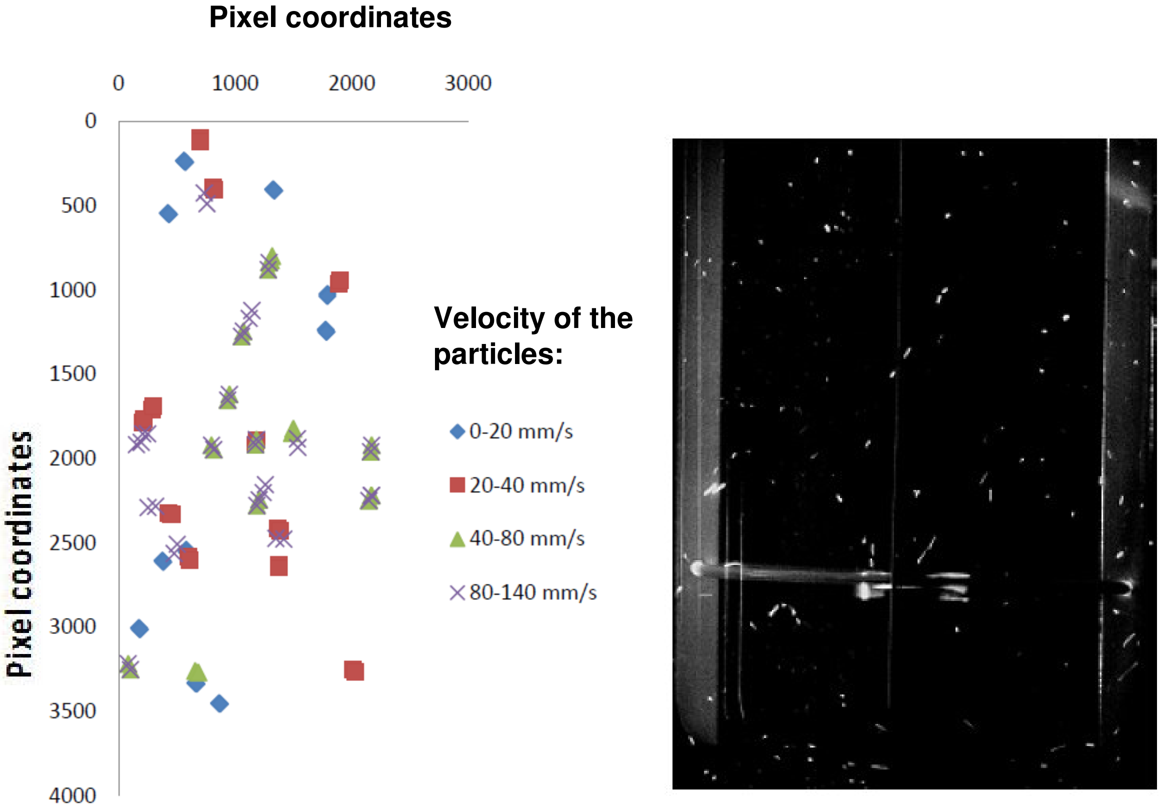

Figure 5.101: Flow field (right) and velocity distribution (left) with RTI at a velocity of 400 rpm.

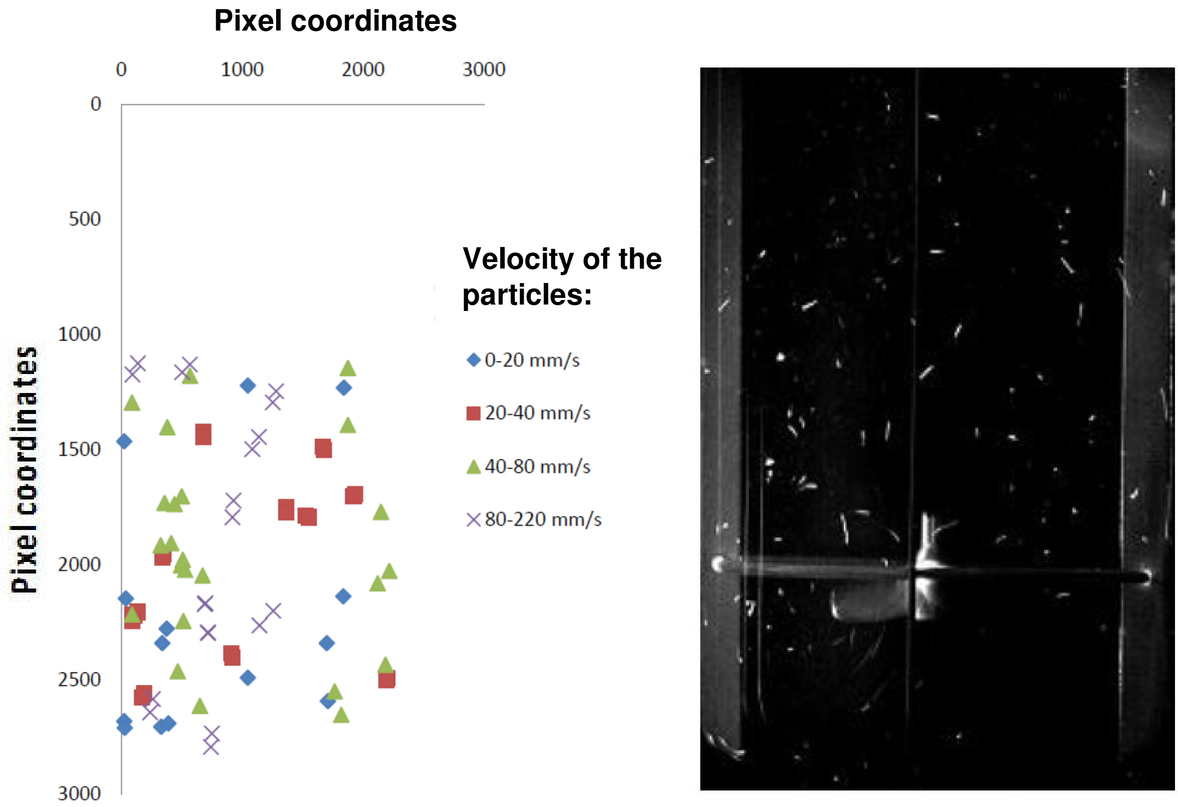

Figure 5.102: Flow field (right) and velocity distribution (left) with propeller impeller at a velocity of 600 rpm.

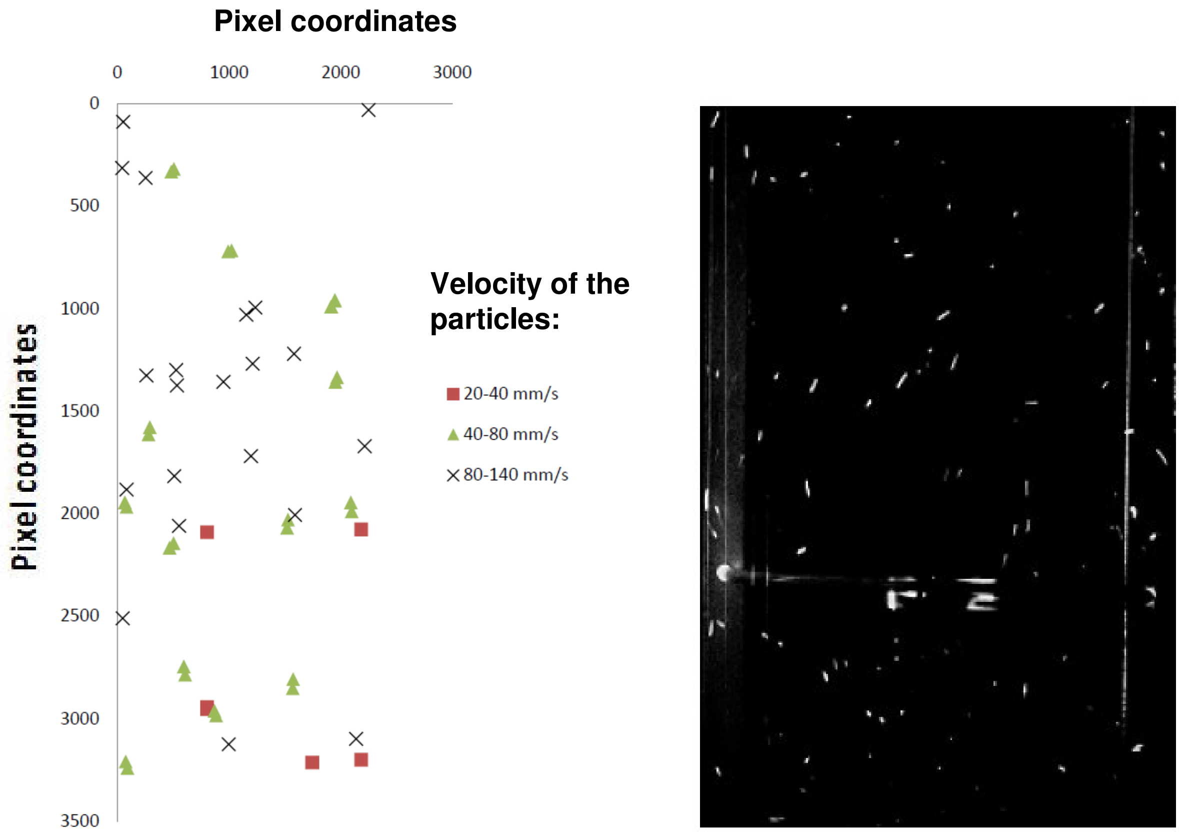

Figure 5.103: Flow field (right) and velocity distribution (left) with RTI at a velocity of 600 rpm.

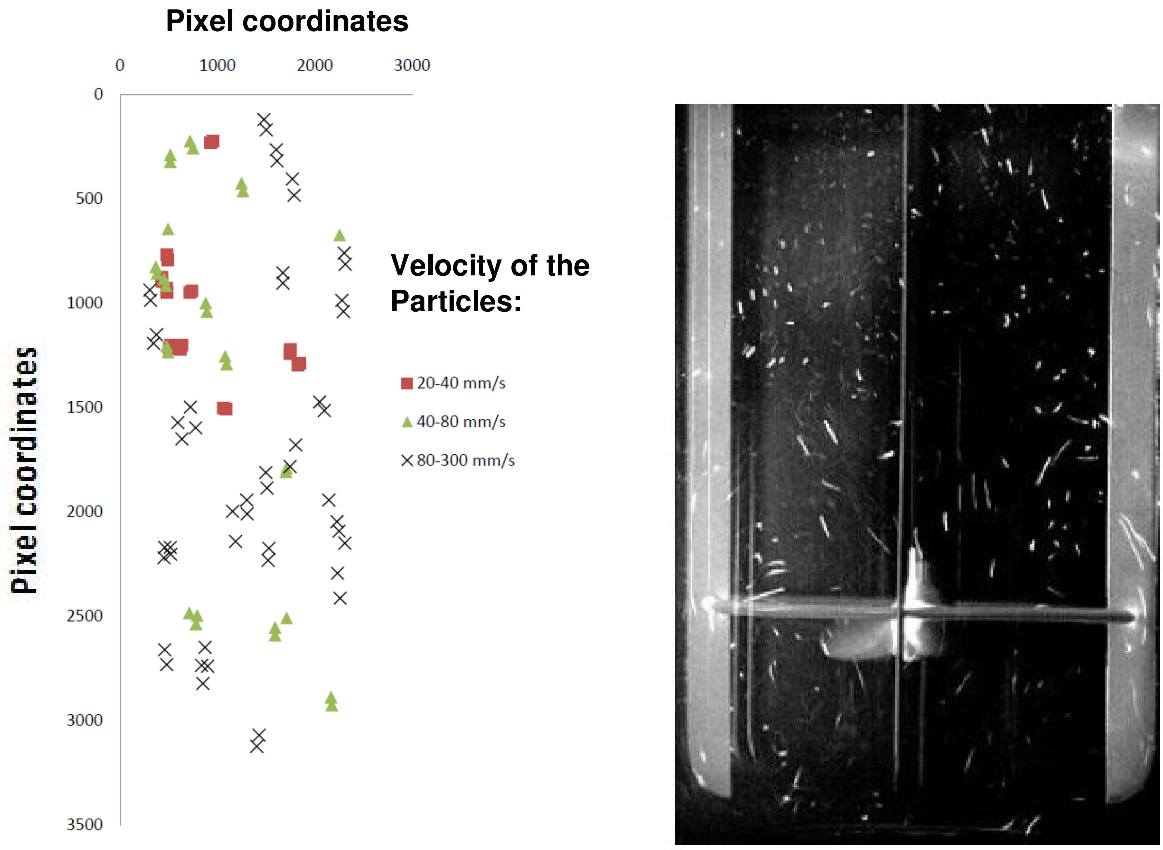

Figure 5.104: Flow field (right) and velocity distribution (left) with propeller impeller at a velocity of 800 rpm.

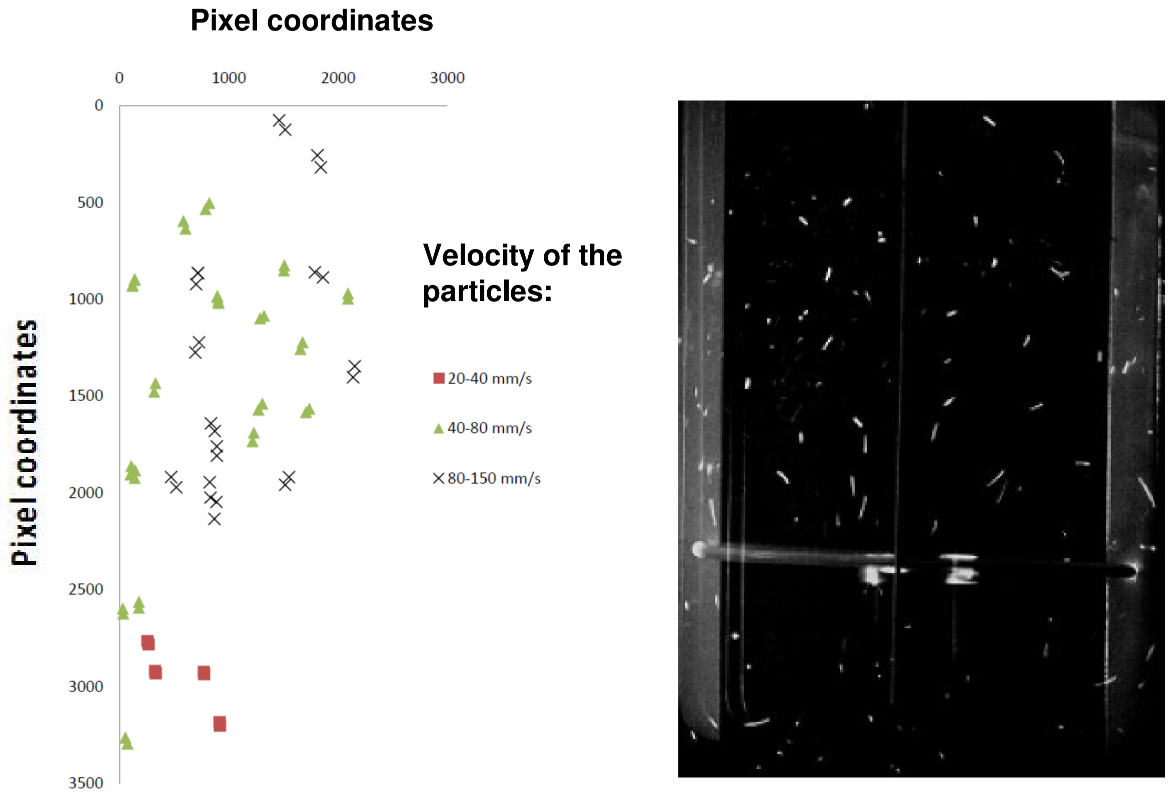

Figure 5.105: Flow field (right) and velocity distribution (left) with RTI at a velocity of 800 rpm.

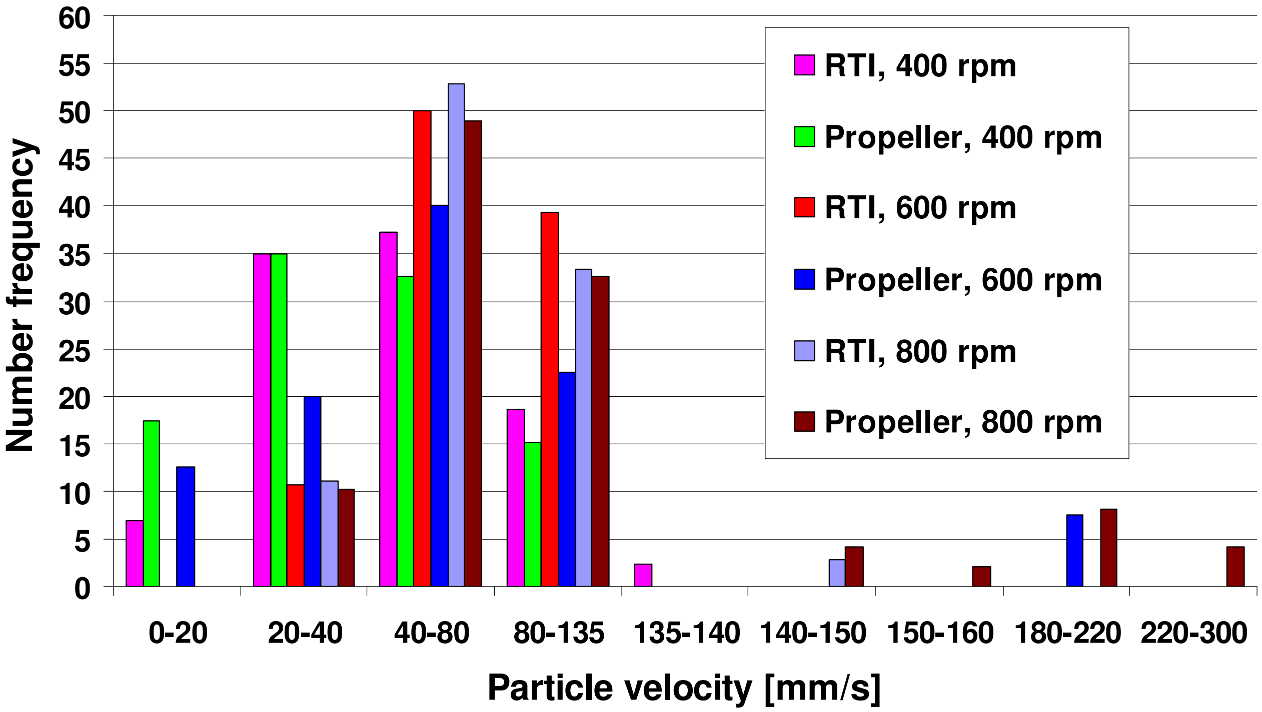

Figure 5.106: Influence of stirrer type and velocity on the number frequency distribution of the particles velocities.

5.7 CFD simulation of the flow velocity fields

5.7.1 Anchor impeller

The axial predicted velocity flow fields of cyclohexane and water phases are represented by the vector plots onto vertical (y,z) coordinate plane near the shaft as shown in Figs. 5.107-a and b at anchor velocities from 150 to 400 rpm. The vectors show regions of high and low liquid velocity and are useful to predict the overall convective bulk mixing. The velocity flow fields create forces leading to drop deformation and breakage which are related to energy dissipation and turbulence intensity.

For anchor velocity of 150 rpm, cyclohexane flows towards the bulk of the liquid leading to a wide vortex between the shaft and the impeller. Two small eddies possess the higher velocities are formed near the tip of the impeller, where the energy dissipation is the highest. In contrast the water is pushed upwards by the convection forces of the anchor impeller from the shaft to the walls of the vessel and then back downwards leading to a small vortex near the cylindrical walls at the top. These interacting vortices formed by the two phases enhance the mass transfer of the solute because the interface between the two phases is continuously renewed. The velocity of the water phase is higher than that of cyclohexane especially near the walls and the tip of the anchor impeller, the level of the liquid phases remains constant at $z = 0.11$ m.

Increasing the anchor velocity to 250 rpm in Fig. 5.107-a, causes turbulent flow with high velocity fluctuations. The velocities of the water phase are higher than that for cyclohexane phase, may be due to the high inertia of water phase, due to the high centrifugal forces resulted from the eddy motion of cyclohexane downwards, and because water phase is heavier than cyclohexane. This behaviour leads to a large axial vortex (top to bottom circulation) near the walls of the vessel which acts like a pump, drafting cyclohexane to the lower part of the vessel to occupy the place of the water phase, and push water phase upwards near the walls of the vessel. The level of the water phase increases to $z = 0.12$ m.

The cyclohexane phase is pulled down into the bulk liquid forming a symmetrical vortex around the shaft of the impeller. Interacting turbulent eddies with different sizes are formed at the interface between the two phases, leading to the droplets deformation and breakup with time. The higher velocities and intensive turbulence are found at the interface between cyclohexane/water phases, near the tip of the impeller and near the cylindrical walls of the vessel along the vertical arm of the impeller.

Further increase of the anchor velocity to 400 rpm in Fig. 5.107-b shows further increase of the water level near the walls of the vessel to $z = 0.14$ m due to the stronger centrifugal forces and circulating vortices at the interface between the two phases, leads to high surface tension gradient and thus pressure and concentration gradients at the interface, thus leads to higher rates of mass transfer (see chapter.5.5.1). This axial flow occurs due to the low viscosity of the both phases. The maximum velocity of water and cyclohexane phases increases 4 and 2 times that at 150 rpm, respectively, when the anchor velocity increases to 400 rpm. The relative velocities between the two phases are high, for that it is difficult to get a uniform dispersion of cyclohexane.

Cyclohexane volume fraction distribution and flow pattern by visualization (chapter 5.1) and from the axial and radial profiles (chapter 5.3) are consistent with the magnitude and direction of the flow velocity field given in Figs. 5.107-a and b.

The predicted velocities of the two phases are in a good agreement with the results of the volumetric mass transfer coefficient, where a significant increase in the volumetric mass transfer coefficient occurs at anchor velocity $\geq$ 350 rpm as can be seen in chapter 5.5.1 (Fig. 5.54).

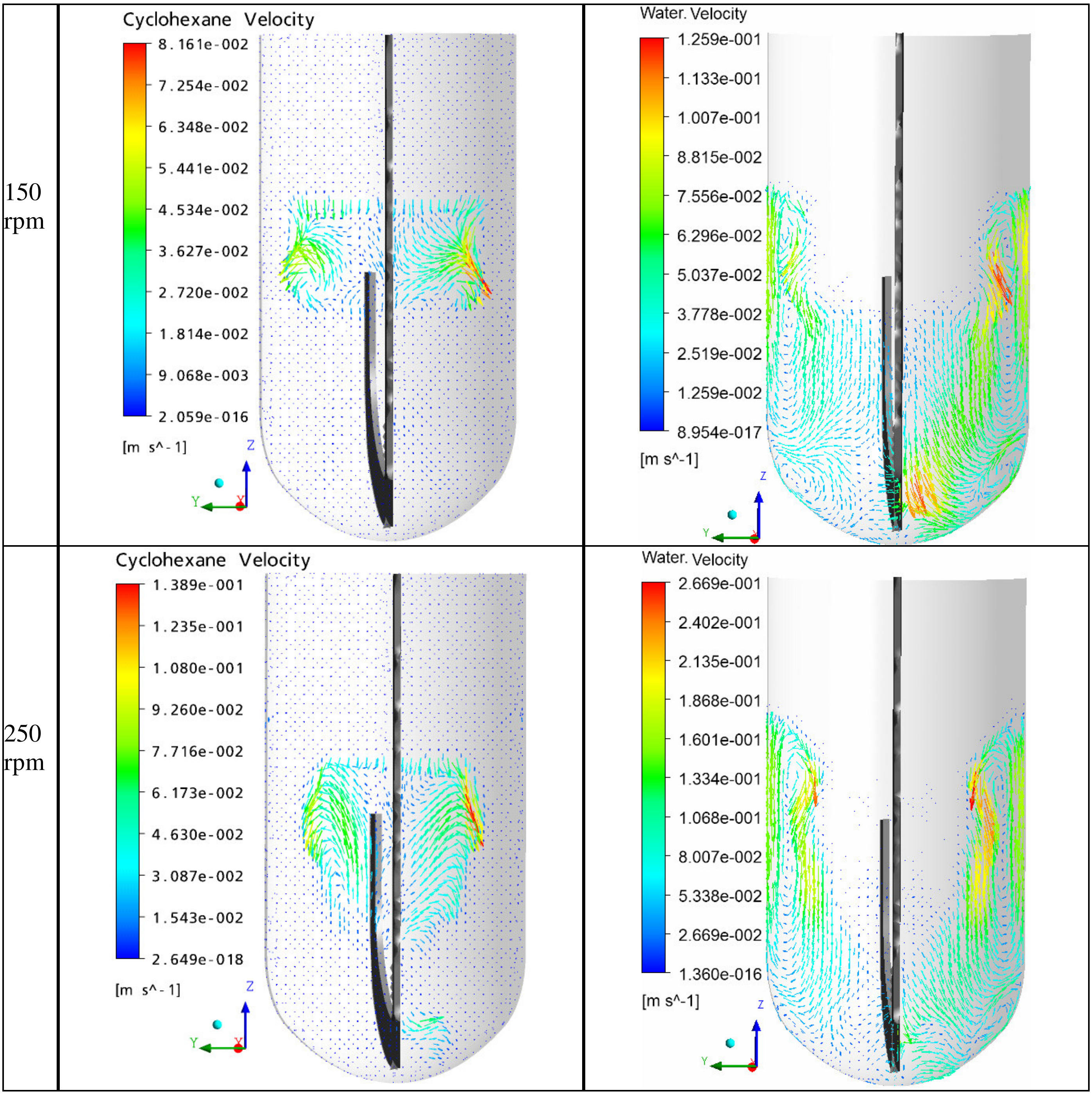

Figure 5.107-a: CFD predicted velocity profiles of cyclohexane (left) and water (right) as a function of anchor velocity of 150 rpm and 250 rpm at x = 0.0045 m.

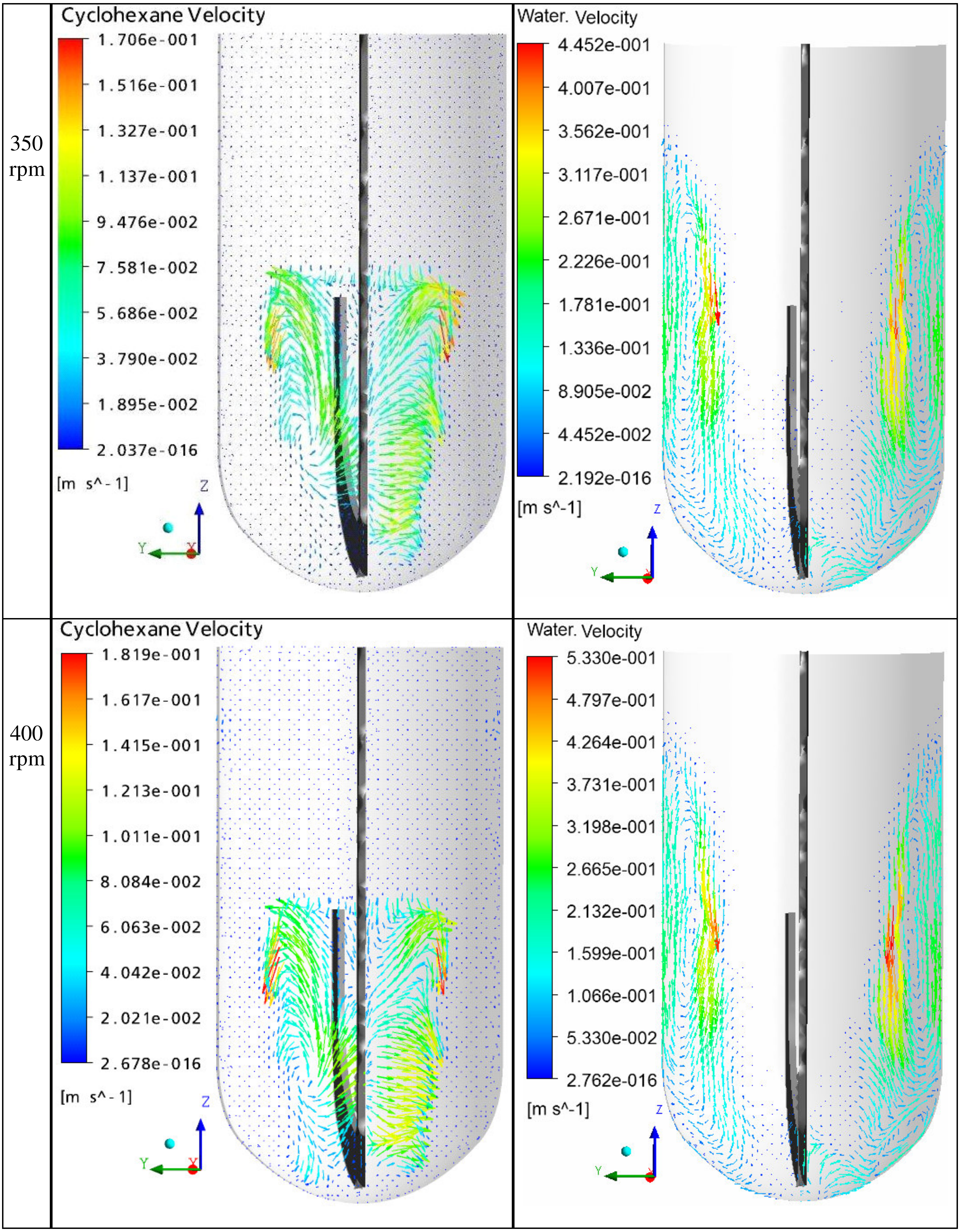

Figure 5.107-b: CFD predicted velocity profiles of cyclohexane (left) and water (right) as a function of anchor velocity of 350 rpm and 400 rpm at x = 0.0045 m (near the shaft).

The velocity flow field in the radial distances (x) between the shaft and the impeller vertical blades is shown in Figs. 5.108-a and b at anchor velocity from 150 to 400 rpm. The radius of the cyclohxane eddy at anchor velocity of 150 rpm is about x = 0.03 m. It is wide and occupies the space in the upper side between the two vertical arms of the impeller. This eddy contains a small vortex caused by the shear forces near the tip of the anchor moves from the free surface of the cyclohexane eddy at x = 0.02 m near the impeller to the lower part of the eddy at x = 0.0045 m near the shaft.

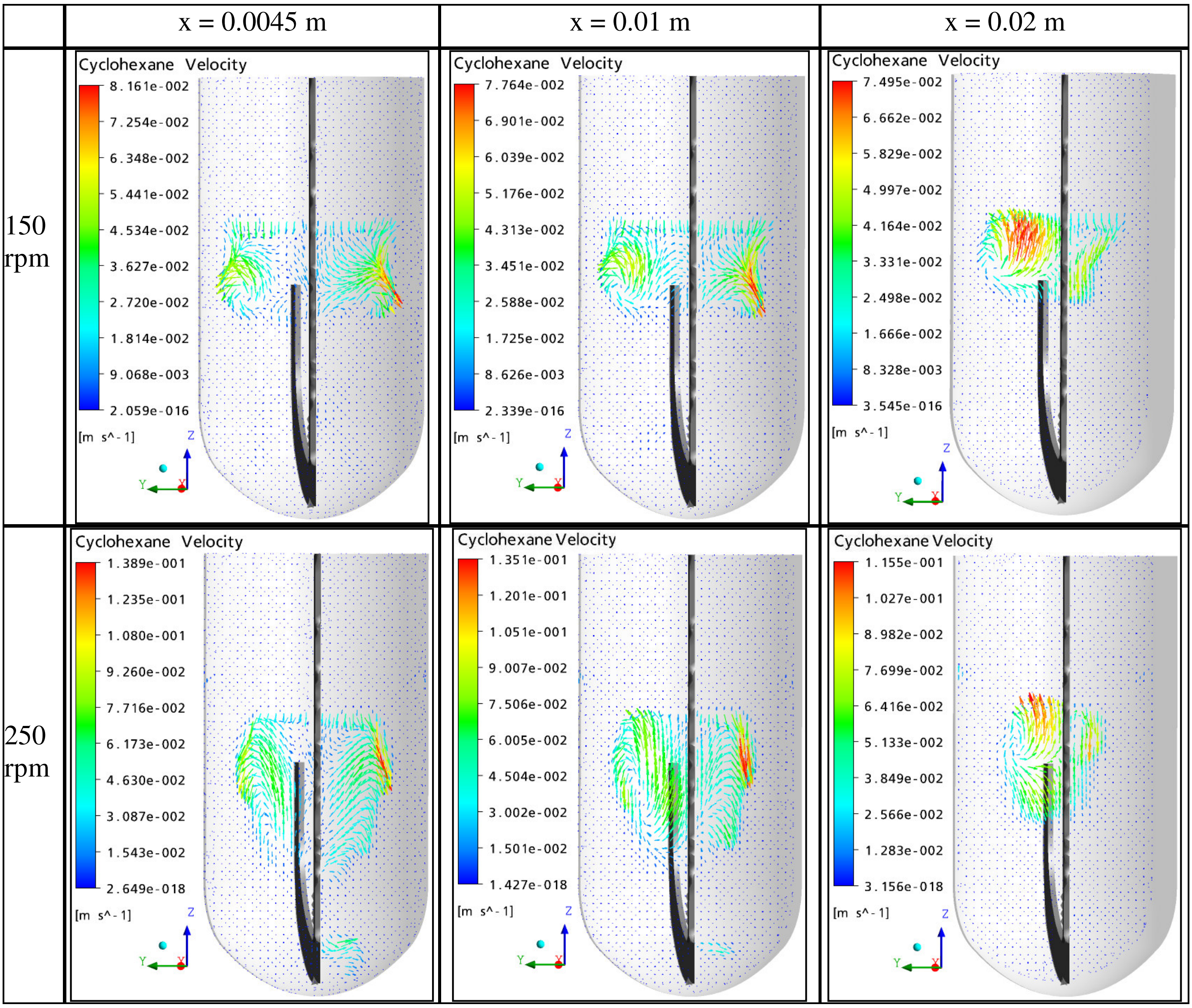

Figure 5.108-a: CFD predicted axial cyclohexane velocity profiles as a function of anchor velocity of 150 rpm and 250 rpm at x = 0.0045 m (left), x = 0.01 m (middle) and x =0.02 m (right).

Increasing the anchor velocity to 250 rpm increases the centrifugal forces that push water out to the walls of the vessel upwards to a higher distance. Cyclohexane eddy enlarges and moves downwards around the shaft. The flow of cyclohexane is from the inside to the outside of the eddy, leading to roll cells at the interface which have the highest velocity in the eddy, see Fig. 5.108-a.

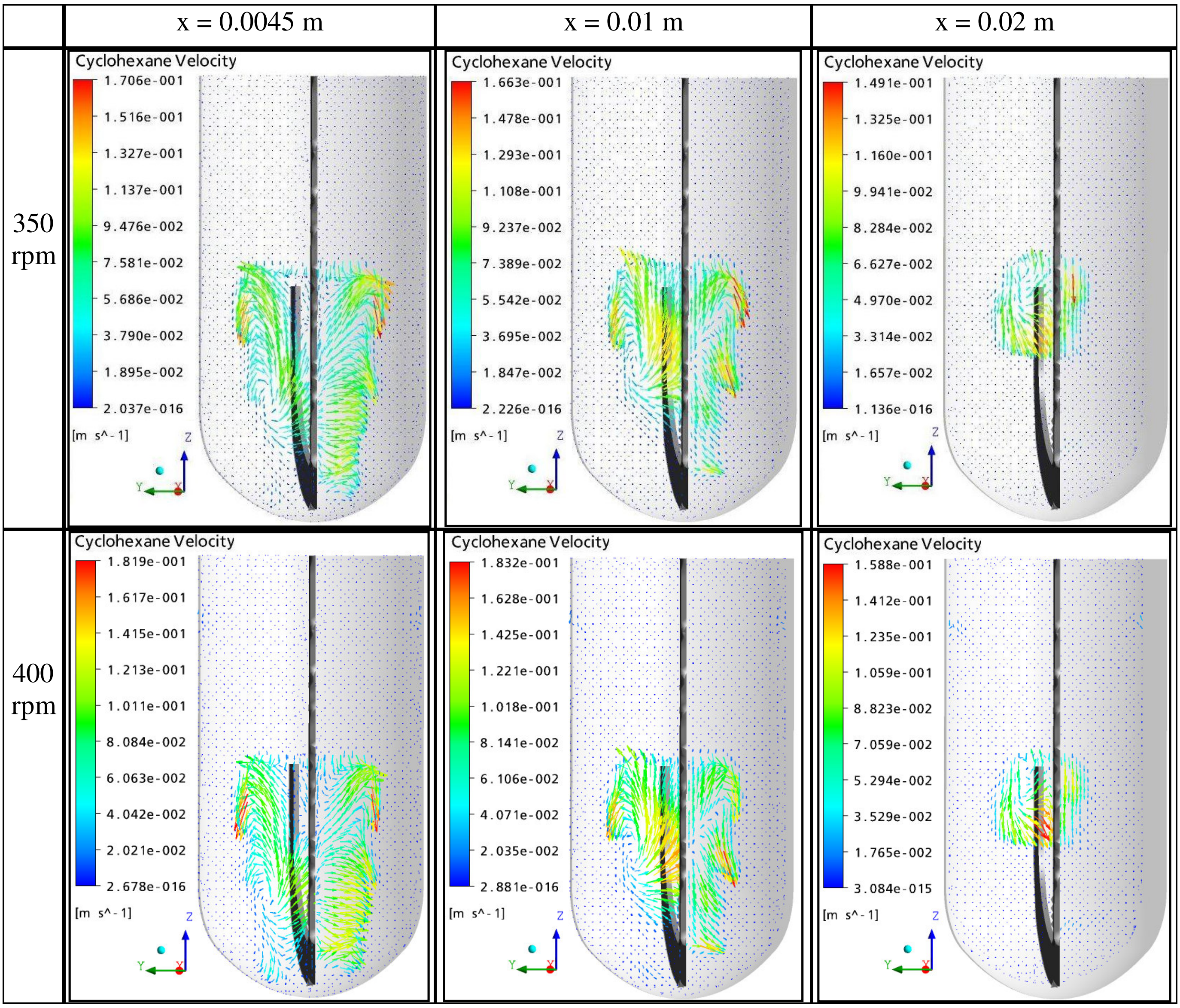

Figure 5.108-b: CFD predicted axial cyclohexane velocity profiles as a function of anchor velocity of 350 rpm and 400 rpm at x = 0.0045 m (left), x = 0.01 m (middle) and x =0.02 m (right).

Further increase of the anchor velocity increases the turbulence and vortices in the large cyclohexane eddy, which reaches to the bottom of the vessel at anchor velocity of 400 rpm. This eddy starts near the tip of the impeller as a one large circulation, and swirls in a conical form down towards the shaft of the impeller as can be seen in Fig. 5.108-b. The development of the roll cells at the interface affects the velocity distribution as found by Sylvia et al. [56].

The radial velocity profile of cyclohexane is represented on horizontal (x,y) coordinate planes at different axial distances (z) in Fig. 5.109-a and b at anchor velocity from 150 to 400 rpm. Initially at $t = 0$, the total height of the liquid phases is 0.11 m. At anchor velocity of 150 rpm, the cyclohexane is pulled down to a height of about $z = 0.07$ m, below the tip of the impeller. Two vortices with high velocities are formed near the tip of the impeller at $z = 0.09$ m.

The velocity flow field in the axial direction (z) is identical when the anchor velocity increases to 400 rpm. The magnitudes of the velocities increase due to the increased turbulent forces and eddy dissipation. When the anchor velocity increases to 250 rpm, more amount of cyclohexane is pulled down in the eddy to a depth of $z = 0.08$ m. Few droplets of cyclohexane can be found also at a level below $z = 0.07$ m, see Fig. 5.109-a. The velocity values increase significantly at anchor velocity $\geq$ 350 rpm. The maximum height of the cyclohexane eddy is a little bit above the tip of the impeller at $z = 0.095$ m. Whereas at anchor velocity of 400 rpm, its height reaches to a level below the tip of the impeller because cyclohexane spread more in the radial distances between the impeller blades. Tracer amounts of cyclohexane can be seen at $z = 0.09$ m as can be seen in Fig. 5.109-b. This behaviour is confirmed experimentally by visualization with red tracer in chapter 5.1 (Fig. 5.1-a and b).

The velocity flow fields of cyclohexane are in a good agreement with that obtained from the visualization and distribution profiles of CHVF. Cyclohexane volume fractions are consistent with the magnitude and direction of the velocity field. The velocity flow fields illustrate the effect of the turbulent flow, flow pattern and velocity distribution on the rate of mass transfer.

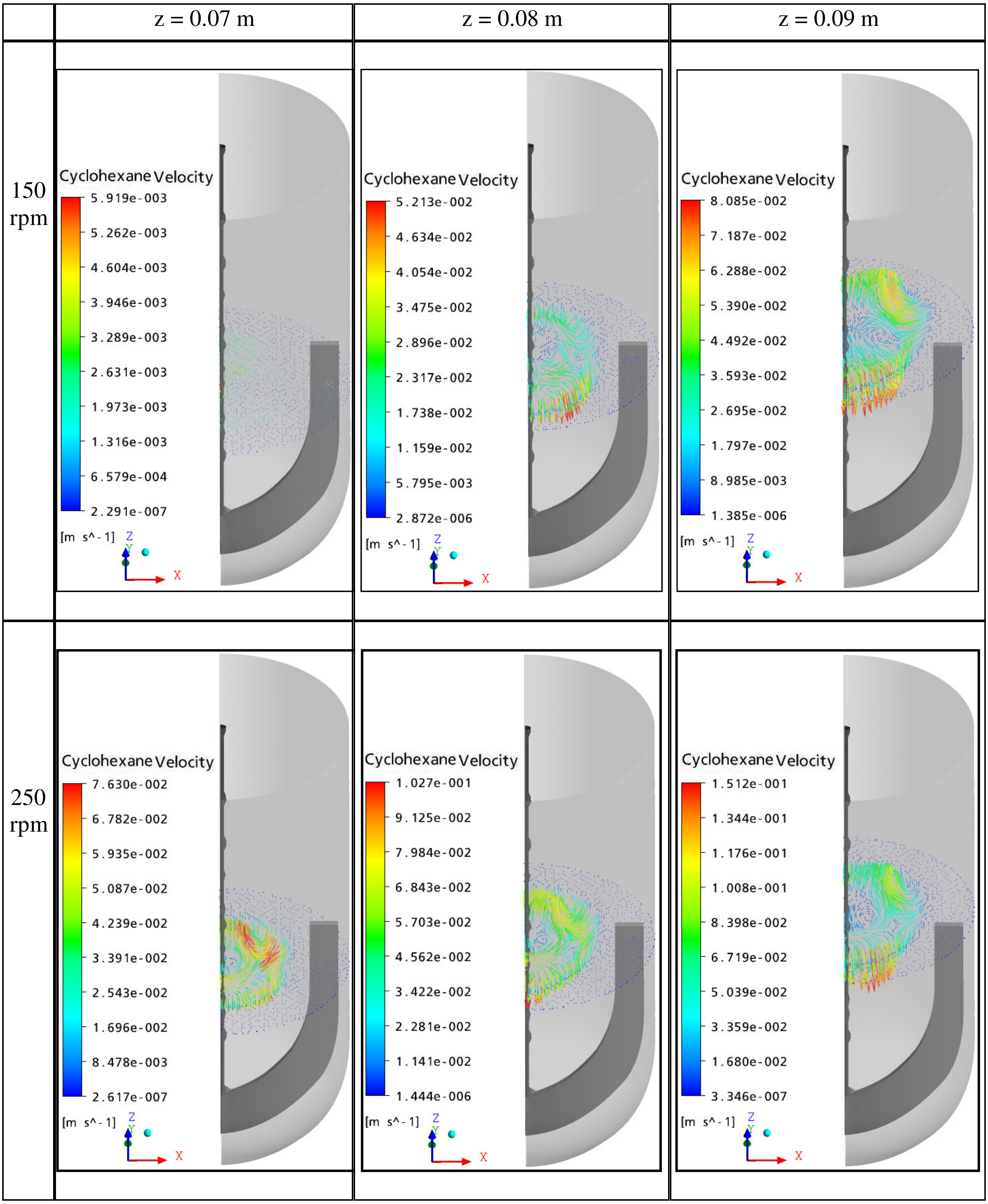

Figure 5.109-a: CFD predicted radial cyclohexane velocity profiles as a function of anchor velocity of 150 rpm and 250 rpm at z = 0.07 m (left), z = 0.08 m (middle) and z =0.09 m (right).

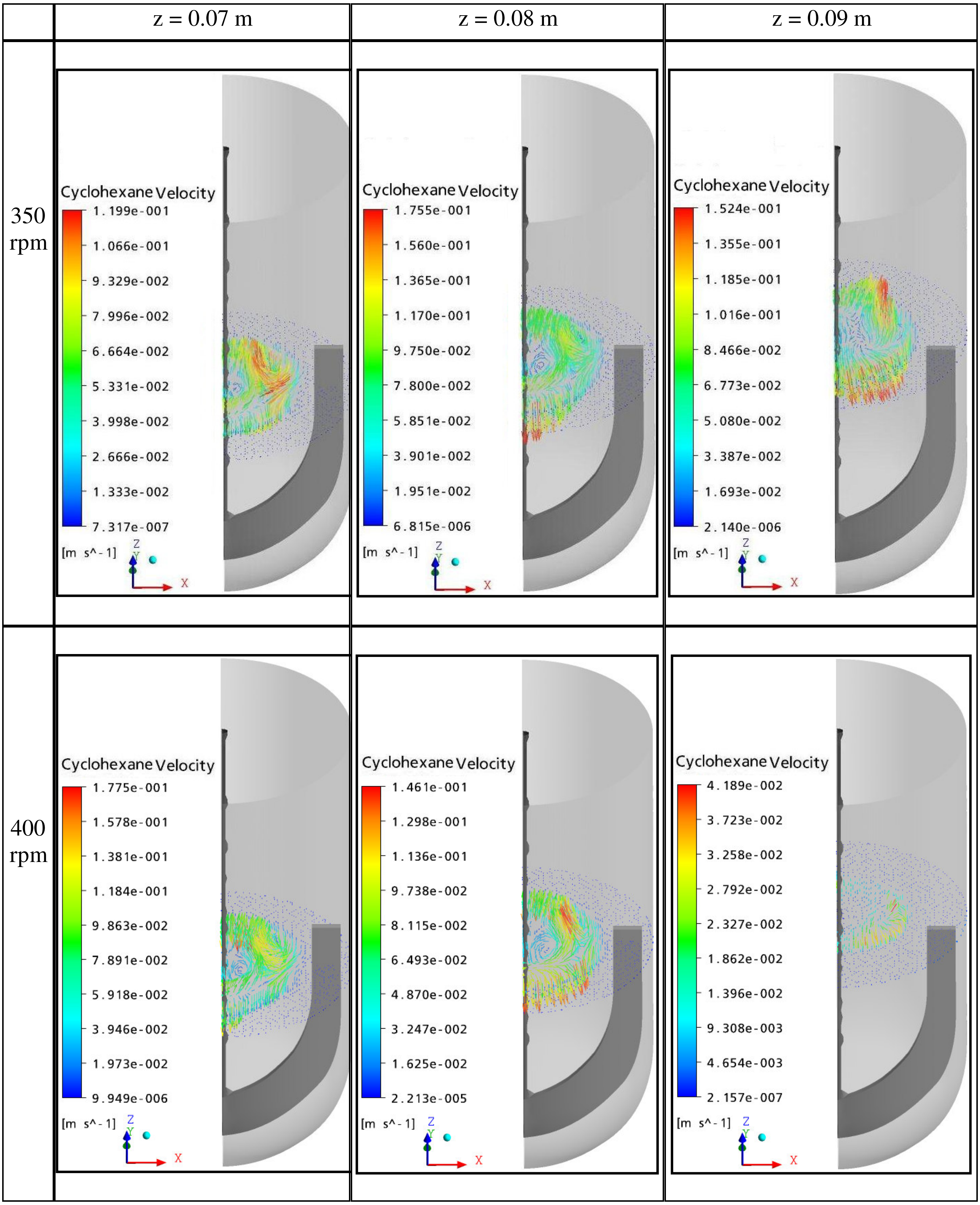

Figure 5.109-b: CFD predicted radial cyclohexane velocity profiles as a function of anchor velocity of 350 rpm and 400 rpm at z = 0.07 m (left), z = 0.08 m (middle) and z =0.09 m (right).

The axial velocity profiles of cyclohexane at anchor velocity of 150 rpm in Fig. 5.110-a show maximum values near the free surface at $z = 0.11$ m for the radial distances between $0.015 \text{ m} \leq x \leq 0.03$ m and near the tip of the impeller for $0.005 \text{ m} \leq x \leq 0.01$ m. A maximum velocity of 0.29 m/s is found near the free surface at $x = 0.03$ m (the maximum radius of the eddy). Cyclohexane eddy presents in the region between $0.065 \text{ m} < z < 0.12$ m, $0.0045 \text{ m} < x < 0.03$ m at anchor velocity of 150 rpm. This emphasize the flow path of cyclohexane in Fig. 5.109-a, where the vortex of high velocity is formed at the free surface in radial distance near the tip of the impeller and then moves to the bottom in the corners of the eddy near the shaft. The velocity of this vortex decreases in the order from 0.25, 0.15 and 0.1 m/s when it moves from $x = 0.025$, 0.018 and 0.014 m, respectively as can be seen at anchor velocity of 150 rpm in Fig. 5.110-a, left. This decrease is due to the low turbulent energy in the central area of the shaft.

Increasing the velocity of the anchor increases the turbulent intensity and the pressure forces in the region of the impeller, resulting in higher velocities of cyclohexane, whereas the trend of the axial and radial velocity profiles is identical. At anchor velocity of 250 rpm, the cyclohexane eddy exists in the region between $0.04 \text{ m} < z < 0.095$ m and $0.0045 \text{ m} < x < 0.025$ m, see the axial and radial velocity profiles in Fig. 5.110-a. Whereas the eddy exists in the region $0.02 \text{ m} < z < 0.09$ m and $0.0045 \text{ m} < x < 0.025$ m at anchor velocity of 350 rpm, more uniform velocity can be found near the shaft at $x = 0.0045$ and 0.01 m, see Fig. 5.110-b. For anchor velocity of 400 rpm, the cyclohexane eddy exists in the region between $0.015 \text{ m} < z < 0.085$ m and $0.0045 \text{ m} < x < 0.025$ m. Small volume of cyclohexane is found at $z = 0.09$ m, but with lower velocity than that at $z = 0.08$ m. At low anchor velocity of 150 rpm, the radial velocity profile is wide, because the eddy of cyclohexane is wide, whereas the axial velocity profile is narrow. At anchor impeller velocity $\geq$ 350 rpm, the cyclohexane eddy becomes narrow and the axial velocity becomes uniform inside the cyclohexane eddy, see Fig. 5.110-a and b.

	Axial cyclohexane velocity	**Radial cyclohexane velocity**
150 rpm	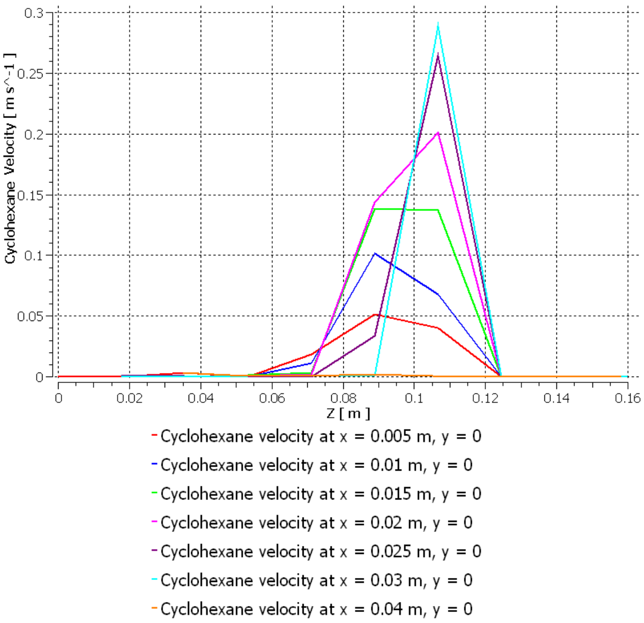	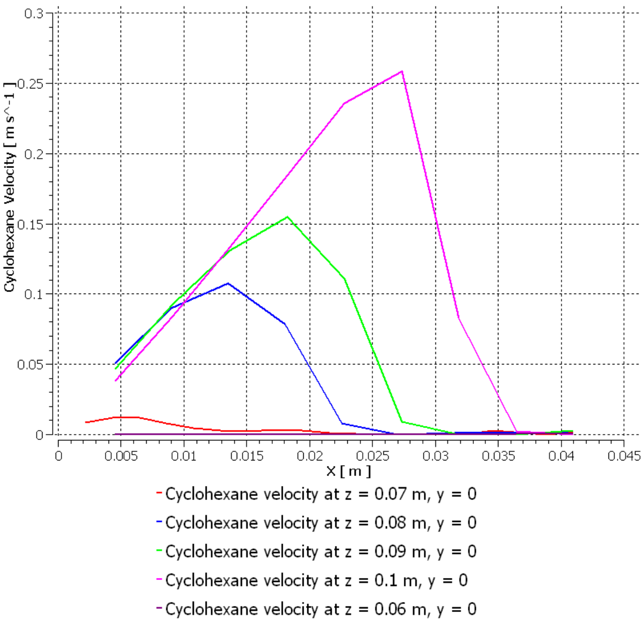
250 rpm	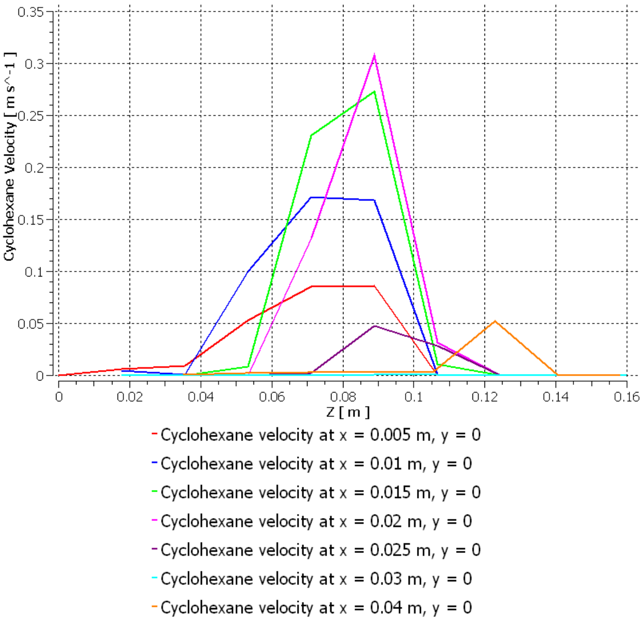	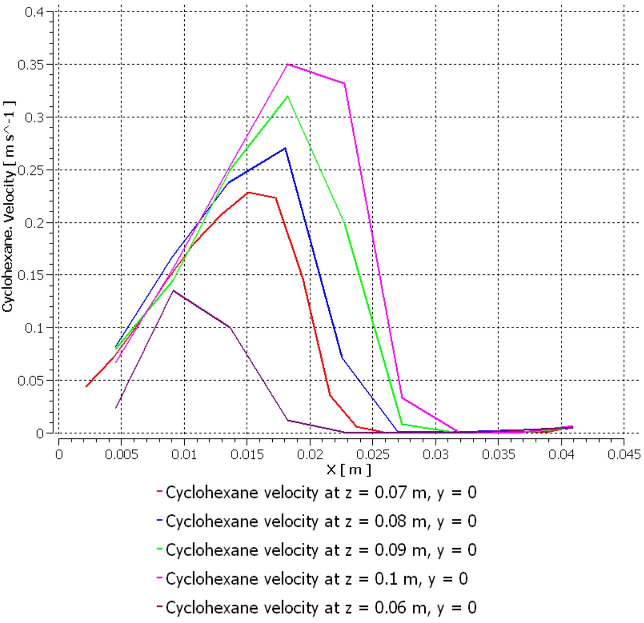

Figure 5.110-a: CFD predicted axial and radial velocity of cyclohexane as a function of anchor velocity of 150 rpm and 250 rpm.

	Axial cyclohexane velocity	Radial cyclohexane velocity
350 rpm	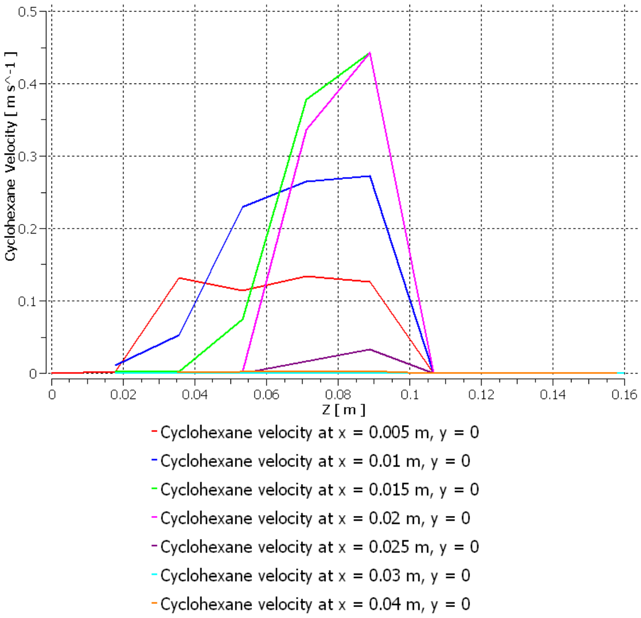	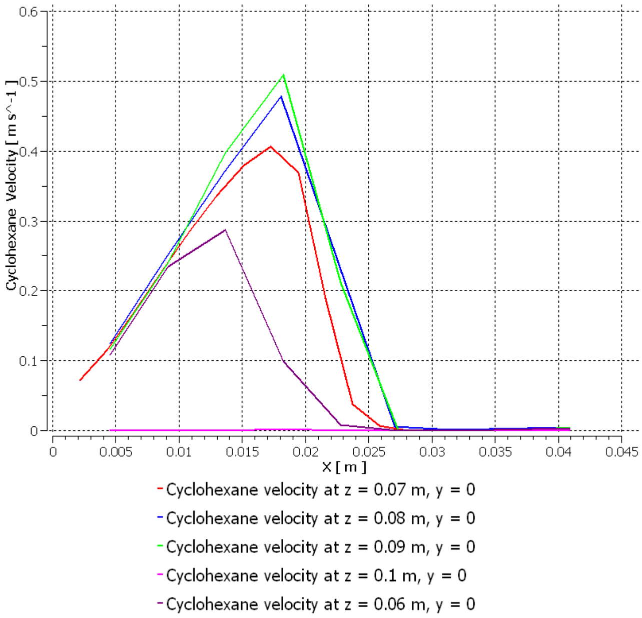
400 rpm	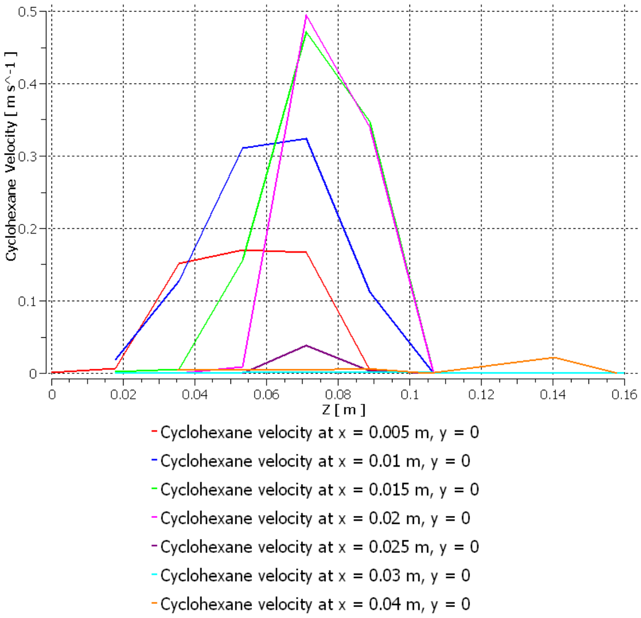	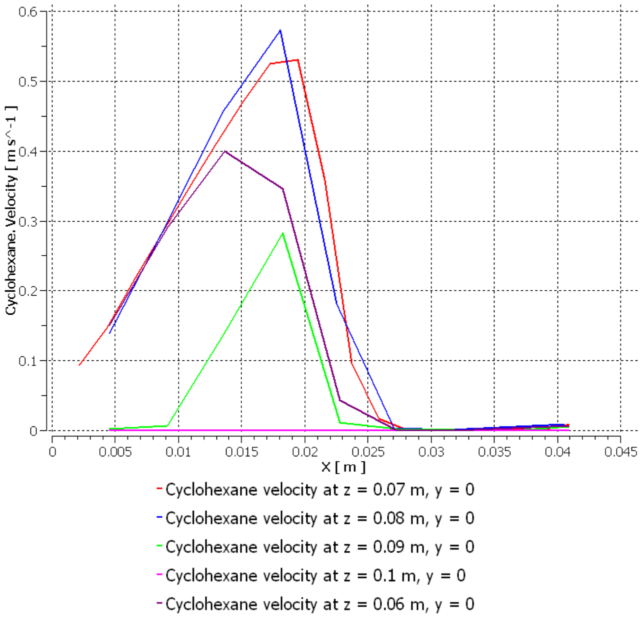

Figure 5.110-b: CFD predicted axial and radial velocity of cyclohexane as a function of anchor velocity of 350 rpm and 400 rpm.

5.7.2 Rushton turbine impeller

The path of the cyclohexane/water flow field in the stirred vessel with RTI are represented by the vectors at RTI velocities from 350 to 750 rpm in Fig. 5.111 a, b and c on a vertical plane (y,z) at different radial positions.

At low RTI velocity of 350 rpm, two small circulations are formed near the cylindrical walls of the vessel near the free surface at the top layer of cyclohexane, and two circulations are formed above and below the impeller. This is due to the centrifugal forces which pull the cyclohexane layer from the walls of the vessel between 0.02 m $< x <$ 0.04 m towards the shaft of the impeller leading to symmetrical vortex. This may be due to the high turbulence occurs in the domain of the impeller which contains large volume percentage of water. Similar flow field is obtained in the radial distance at $x = 0.01$, 0.02 m and 0.03 m in Fig. 5.111-c.

The output flow from the impeller is apparent radial and has the highest velocity due to the high turbulent intensity and kinetic energy caused by the impeller. It collides with the cylindrical walls to be divided into two circulations as can be seen at RTI velocity $\geq$ 450 rpm, the larger and stronger one is formed above the impeller and the second one is found below the impeller, the downwards flow is due to the gravity forces. The impeller discharged stream is inclined upward by the buoyant action of the light dispersed phase. The free surface is nearly still flat, see Fig. 5.111-a.

Further increase of the impeller velocity, increases the percentage of the dispersed phase in water and decreases the turbulent (fluctuating velocity) in the domain and the number of circulations especially above the impeller. Thus diminishes the circulations at the free surface, see Fig. 5.111-b. Most of cyclohexane is dispersed into water at RTI velocity of 550 rpm, and very thin layer is still found in the top at the interface. The air vortex is very small at the free surface. The density of the vectors increases especially near the shaft at $x = 0.01$ m because cyclohexane is concentrated around the shaft. The velocity of the dispersion increases when cyclohexane is completely incorporated into water phase, because cyclohexane is lighter than water, thus the density of the dispersion is lowered.

The highest velocity is found in the region of the impeller between the impeller blades and the cylindrical walls. The depth of the air vortex increases at RTI velocity ≥ 650 rpm, because the centrifugal forces appear at high Reynolds numbers. The axial flow field in the radial position at $x = 0.03$ m in Fig. 5. 111-c is similar to that at RTI velocity ≥ 550 rpm, where the maximum velocity regions are found in the output streams below the impeller and near the cylindrical walls forming a U-shape, but the density of the vectors in the bottom of the vessel at RTI velocity of 750 rpm are higher, because the concentration of cyclohexane in that region becomes high. Strong turbulent includes high velocity fluctuations is caused by the jet like flows on the walls and impeller blades, leads to eddies of different sizes in the impeller region. Whereas at RTI velocity of 450 rpm, cyclohexane is almost exists above the impeller near the walls and then spreads along the walls of the vessel to the top and bottom, see Fig. 5. 111-c.

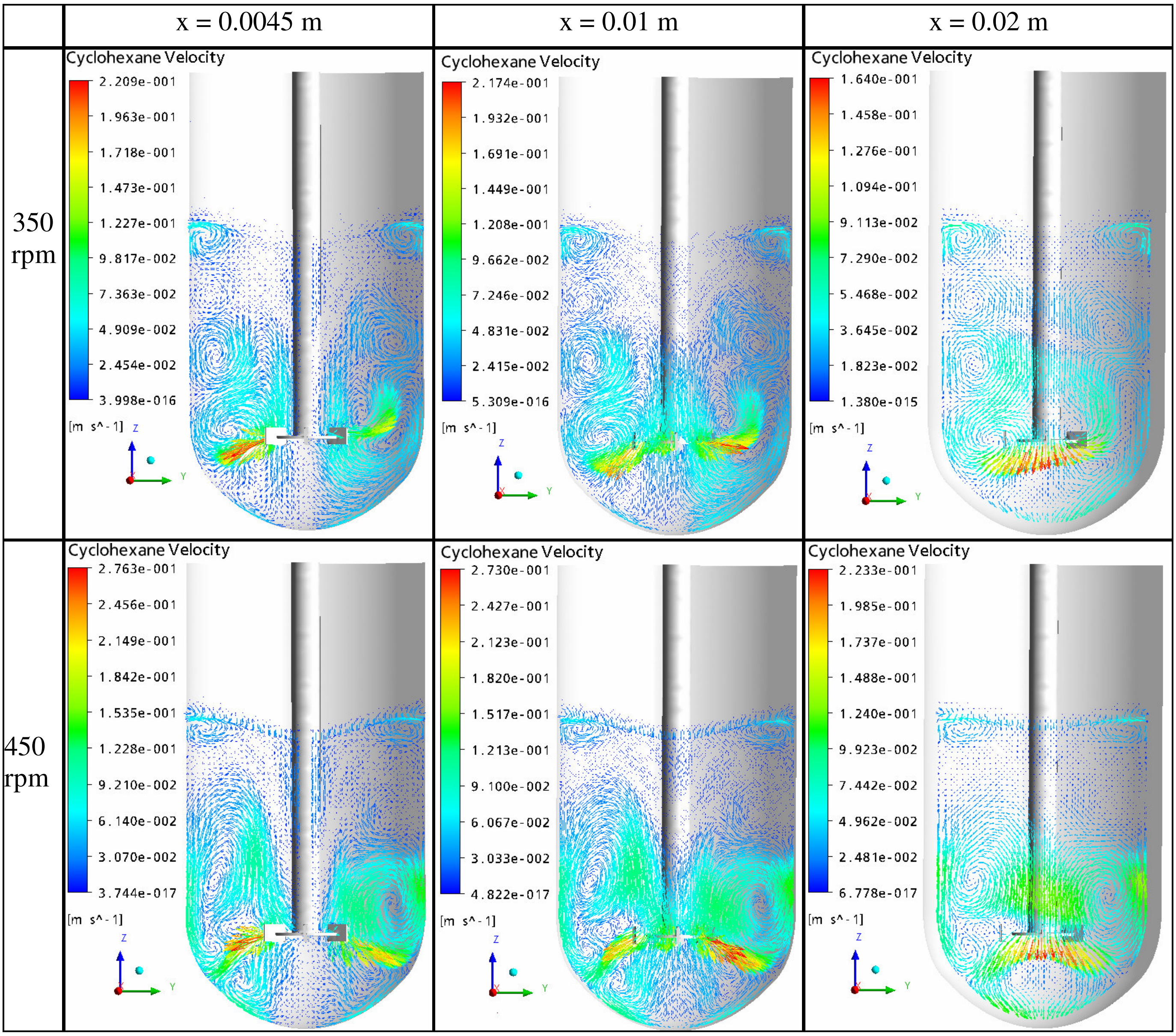

Figure 5.111-a: CFD predicted axial cyclohexane velocity profiles as a function of RTI velocity of 350 rpm and 400 rpm at x = 0.0045 m (left), x = 0.01 m (middle) and x =0.02 m (right).

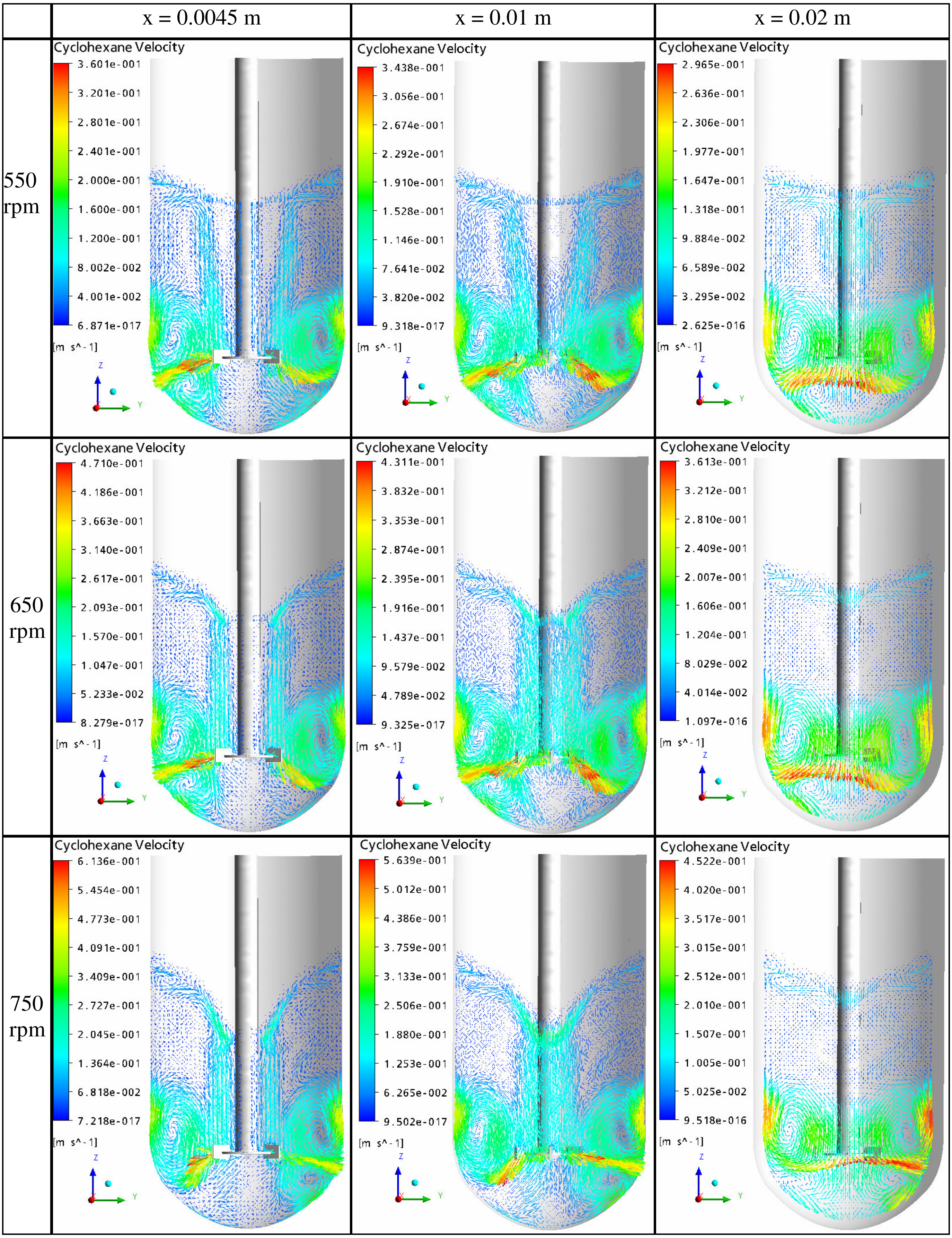

Figure 5.111-b: CFD predicted axial cyclohexane velocity profiles as a function of RTI velocity of 550 rpm, 650 rpm and 750 rpm at x = 0.0045 m (left), x = 0.01 m (middle) and x =0.02 m (right).

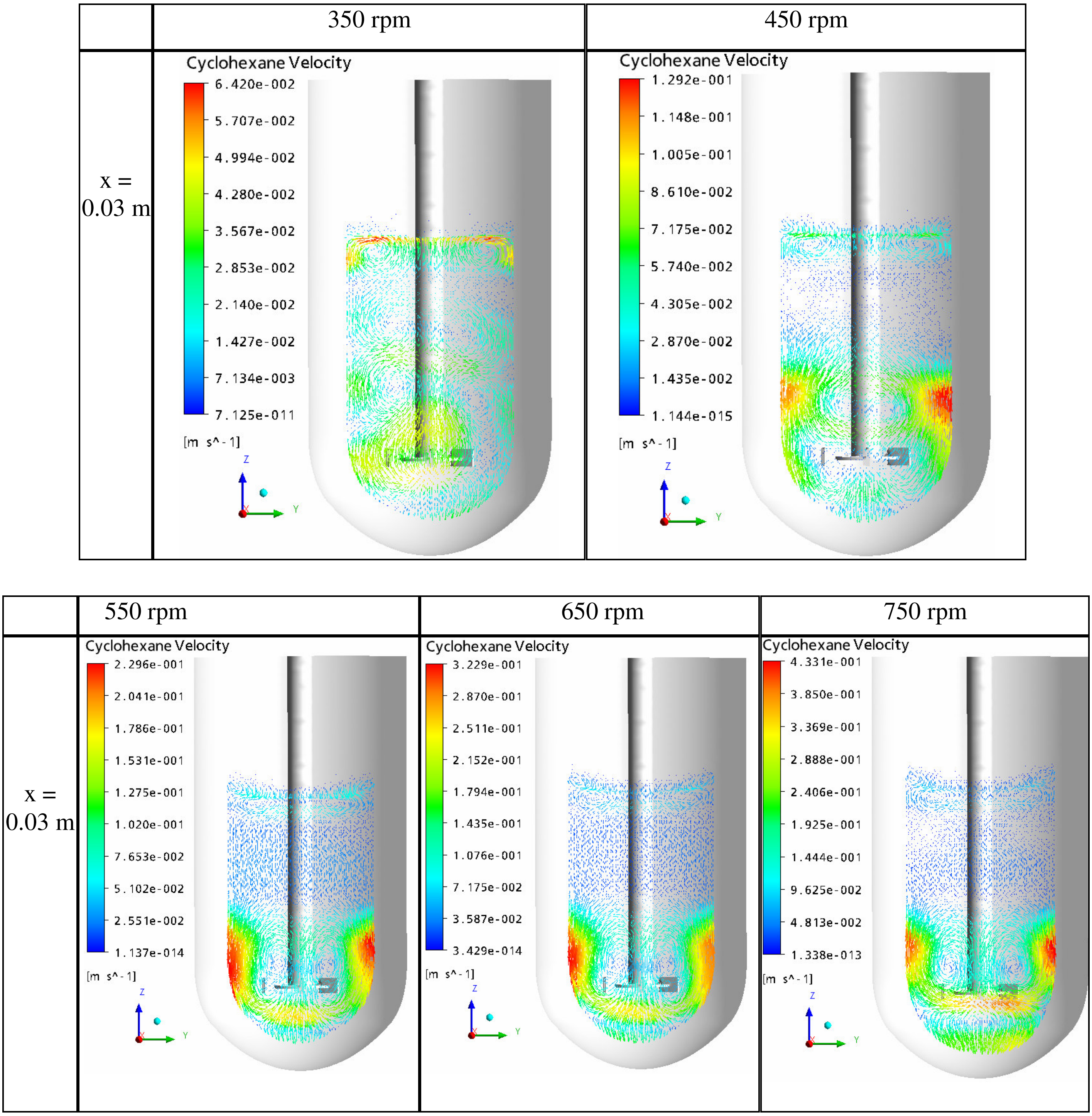

Figure 5.111-c: CFD predicted axial cyclohexane velocity profiles as a function of RTI velocity of 350 rpm to 750 rpm at x = 0.03 m.

The radial flow field of cyclohexane/water system at different axial distances from z = 0.01 m below the impeller level to z = 0.11 m at the free surface is illustrated in Figs. 5.112-a to f at RTI velocities from 350 to 750 rpm. At z = 0.01 m, the radial flow from the walls of the vessel towards the RTI in Figs. 5.112-a and b caused by the counter clockwise motion of the circulation below the impeller. At RTI velocity of 350 rpm, the surrounding of the impeller is only water, thus the velocity distribution is uniform, but its magnitude is low due to the low input energy of the small RTI. Cyclohexane reaches the blades of the RTI at a minimum velocity of 450 rpm and disperses into water, so the velocity distribution becomes inhomogeneous. Thus the length of the velocity vectors is not identical. The magnitudes of the velocity increase to 0.198 m/s when the RTI velocity increases to 750 rpm at z = 0.01 m. They become uniform at a minimum velocity of 650 rpm, where the values of the velocity become close with very small difference, see Fig. 5.112-a and b.

The intensity of the turbulence and energy dissipation is the highest in the level of the RTI impeller at z = 0.032 m. The strong radial flow from the RTI makes strong collisions with the cylindrical walls of the vessel that divides the output stream in two circulations below and above the impeller. The strength of the collisions increases with increasing the velocity of RTI, due to the increased concentration of cyclohexane in the impeller domain. A complete dispersion of cyclohexane occurs at a RTI velocity of about 550 rpm, thus the uniform velocity distribution can be obtained at a minimum velocity of 650 rpm, where the slip velocity of cyclohexane goes to zero, and both cyclohexane and water phases moves with similar velocities. The maximum dispersion velocity of 0.357 m/s is obtained at z = 0.032 m and RTI velocity of 750 rpm, see Fig. 5.112-a and b.

At z = 0.04 m above the impeller in Figs. 5.112-c and d, the flow remains radial out of the impeller from one side and into the impeller from the other side. The high velocity region is found near the cylindrical walls, where the flow becomes tangential in the circumference of the vessel, due to the high pressure forces caused by the collisions between the output stream from the impeller and the cylindrical walls. The magnitude of the velocity increases when the RTI velocity increases and it decreases a way from the impeller to the top or bottom. Uniform velocity distribution is obtained at minimum RTI velocity of 550 rpm.

Maximum velocity between 0.39 and 0.438 is obtained at RTI velocity of 750 rpm, see Figs. 5.112-c and d.

At z = 0.06 m, the direction of the flow is radial towards the cylindrical walls of the vessel, but it does not reach the cylindrical walls like that in the case at z = 0.04 m because of the decreased turbulent intensity there. The maximum velocity of 0.172 m/s is obtained at RTI of 750 rpm.

The velocity of the liquid phases decreases a way from the impeller and near the free surface at z = 0.08 and 0.11 m as can be seen in Figs. 5.112-e and f. When the cyclohexane dispersion into water becomes uniform, then the velocity distribution also becomes uniform at a RTI velocity of 750 rpm. The maximum velocity of 0.14 m/s is obtained at z = 0.08 m.

At z = 0.11 m and low RTI velocity of 350 rpm, cyclohexane exists at the top layer and small proportion disperses into water. The highest velocity region is that near the cylindrical walls, the position at which cyclohexane is pulled down into water. Increasing the RTI velocity increases the dispersion intensity of cyclohexane down into the vessel until it is distributed uniformly in the whole vessel at a minimum RTI velocity of 650 rpm. The maximum velocity of 0.14 m/s is obtained at RTI velocity of 750 rpm, see Figs. 5.112-e and f.

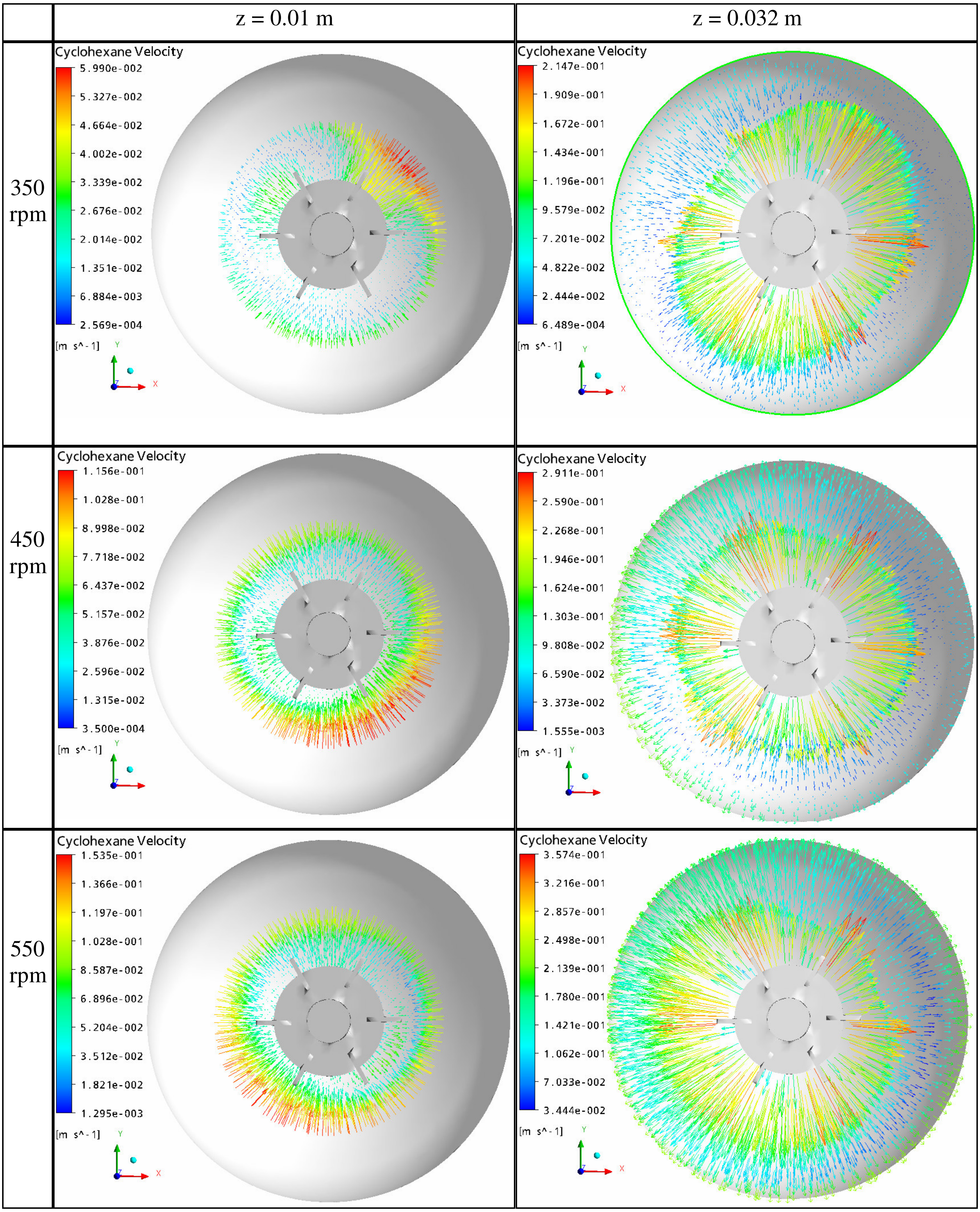

Figure 5.112-a: CFD predicted radial cyclohexane velocity profiles as a function of RTI velocity of 350 rpm, 450 rpm and 550 rpm at z = 0.01 m (left) and z = 0.032 m (right).

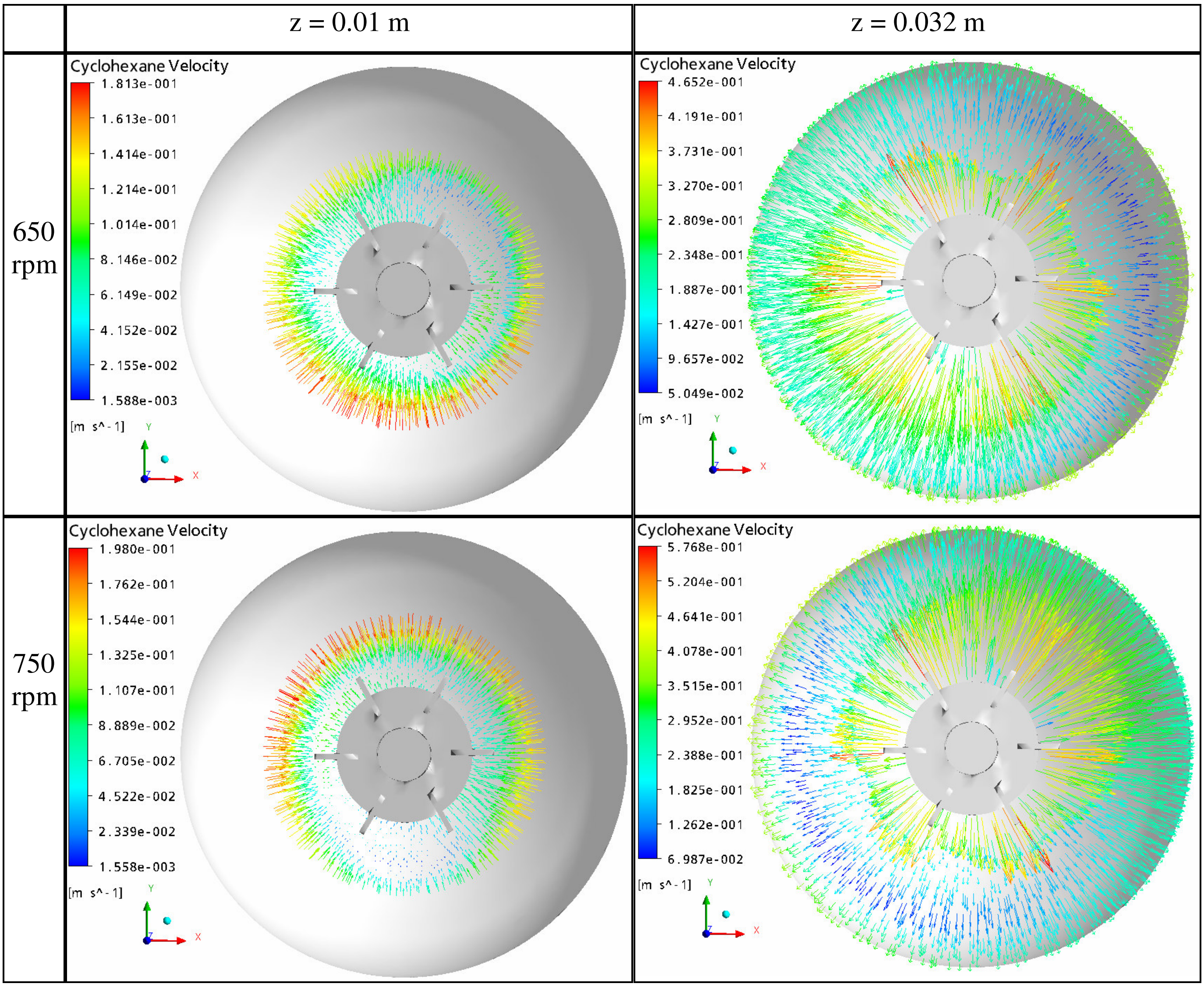

Figure 5.112-b: CFD predicted radial cyclohexane velocity profiles as a function of RTI velocity of 650 rpm and 750 rpm at z = 0.01 m (left) and z =0.032 m (right).

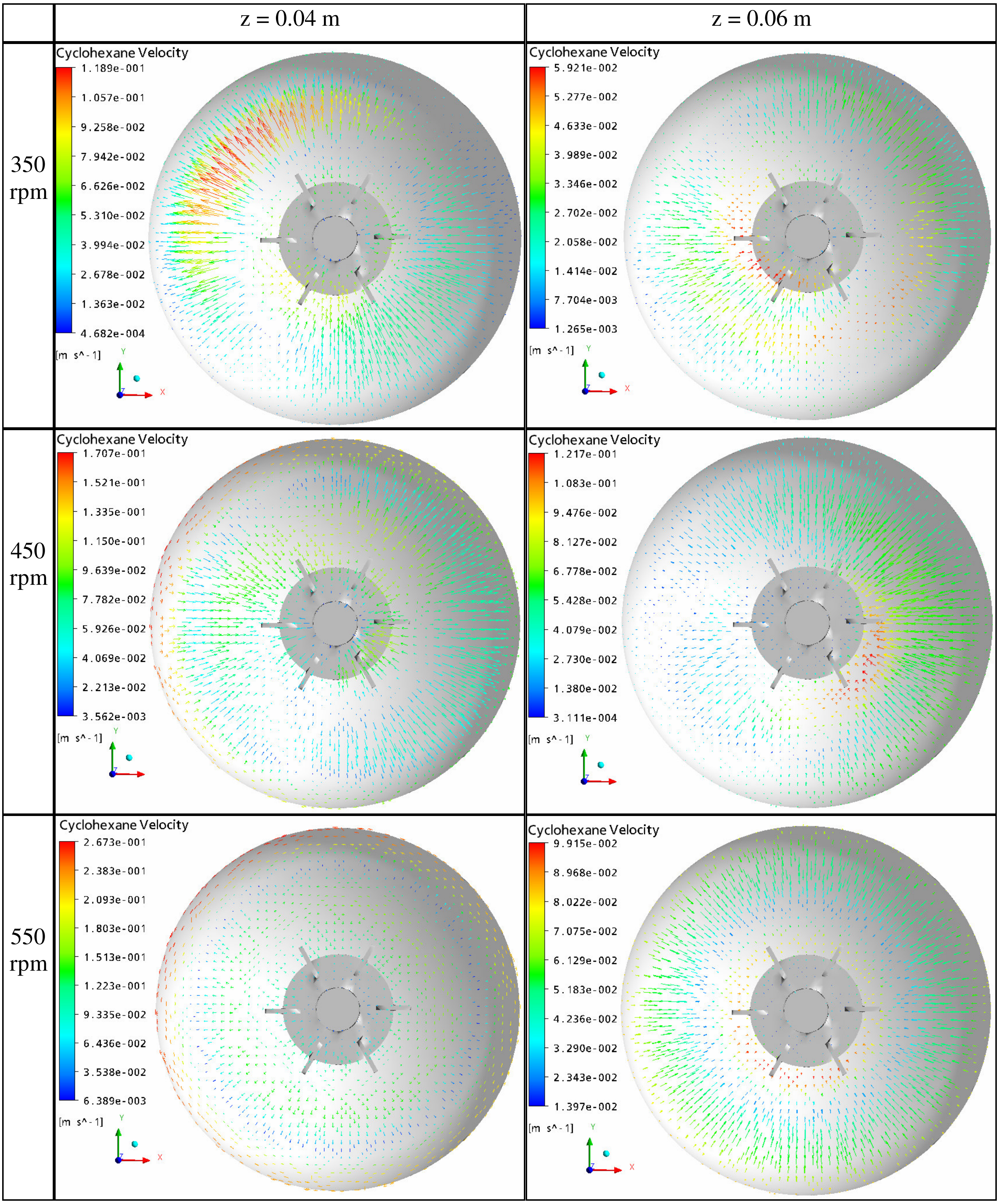

Figure 5.112-c: CFD predicted radial cyclohexane velocity profiles as a function of RTI velocity of 350 rpm, 450 and 550 rpm at z = 0.04 m (left) and z =0.06 m (right).

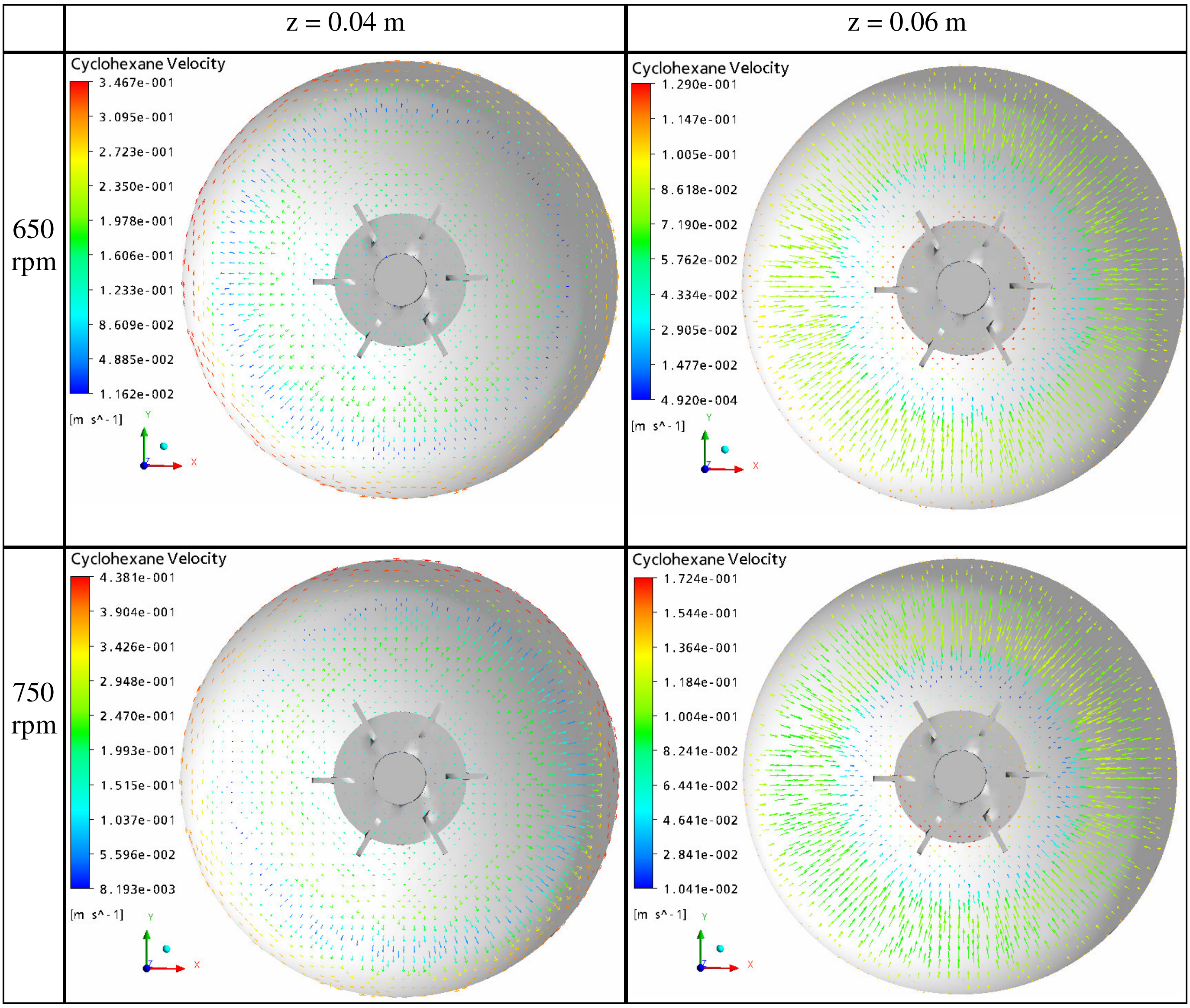

Figure 5.112-d: CFD predicted radial cyclohexane velocity profiles as a function of RTI velocity of 650 rpm and 750 rpm at z = 0.04 m (left) and z =0.06 m (right).

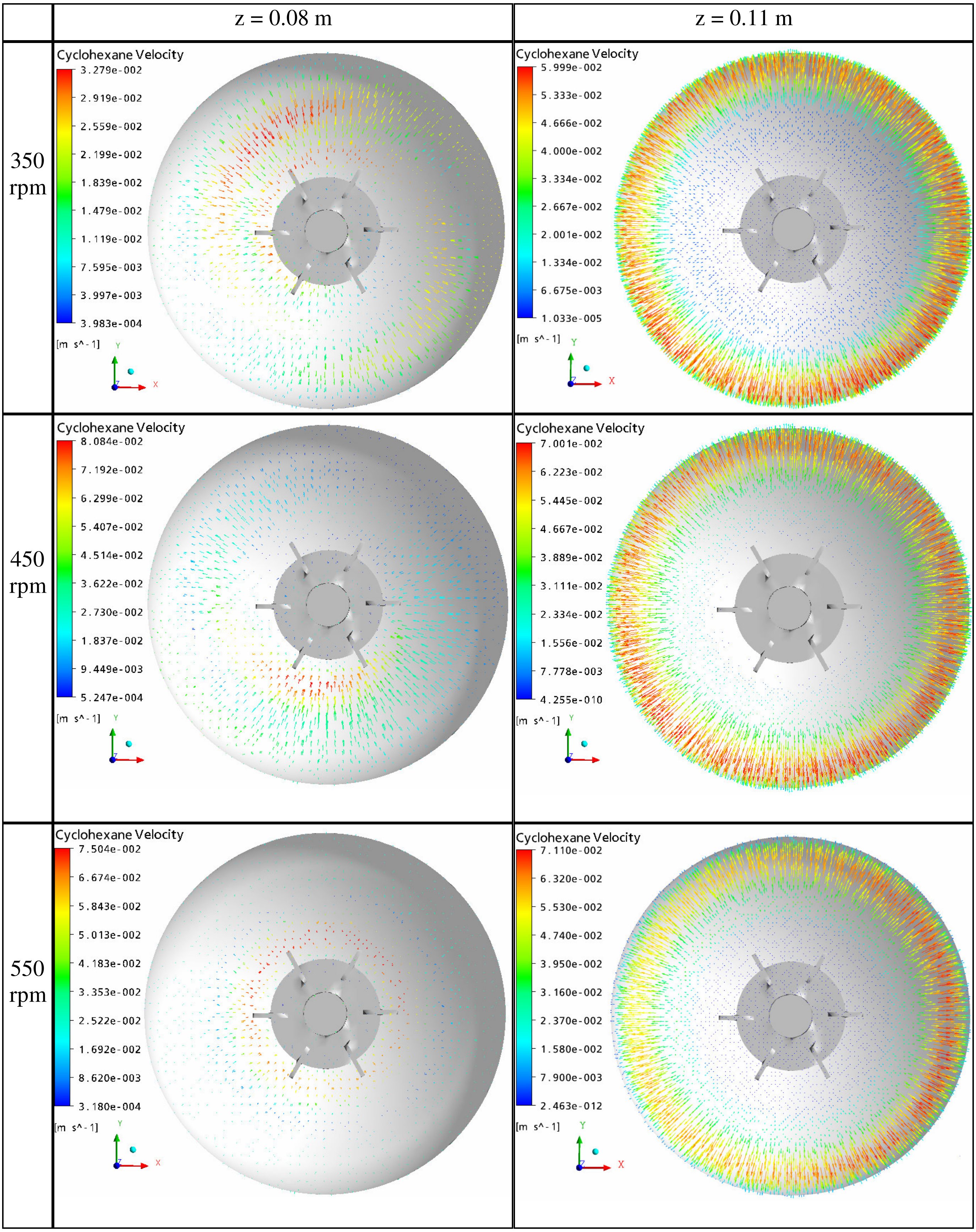

Figure 5.113-e: CFD predicted radial cyclohexane velocity profiles as a function of RTI velocity of 350 rpm, 450 rpm and 550 rpm at z = 0.08 m (left) and z = 0.11 m (right).

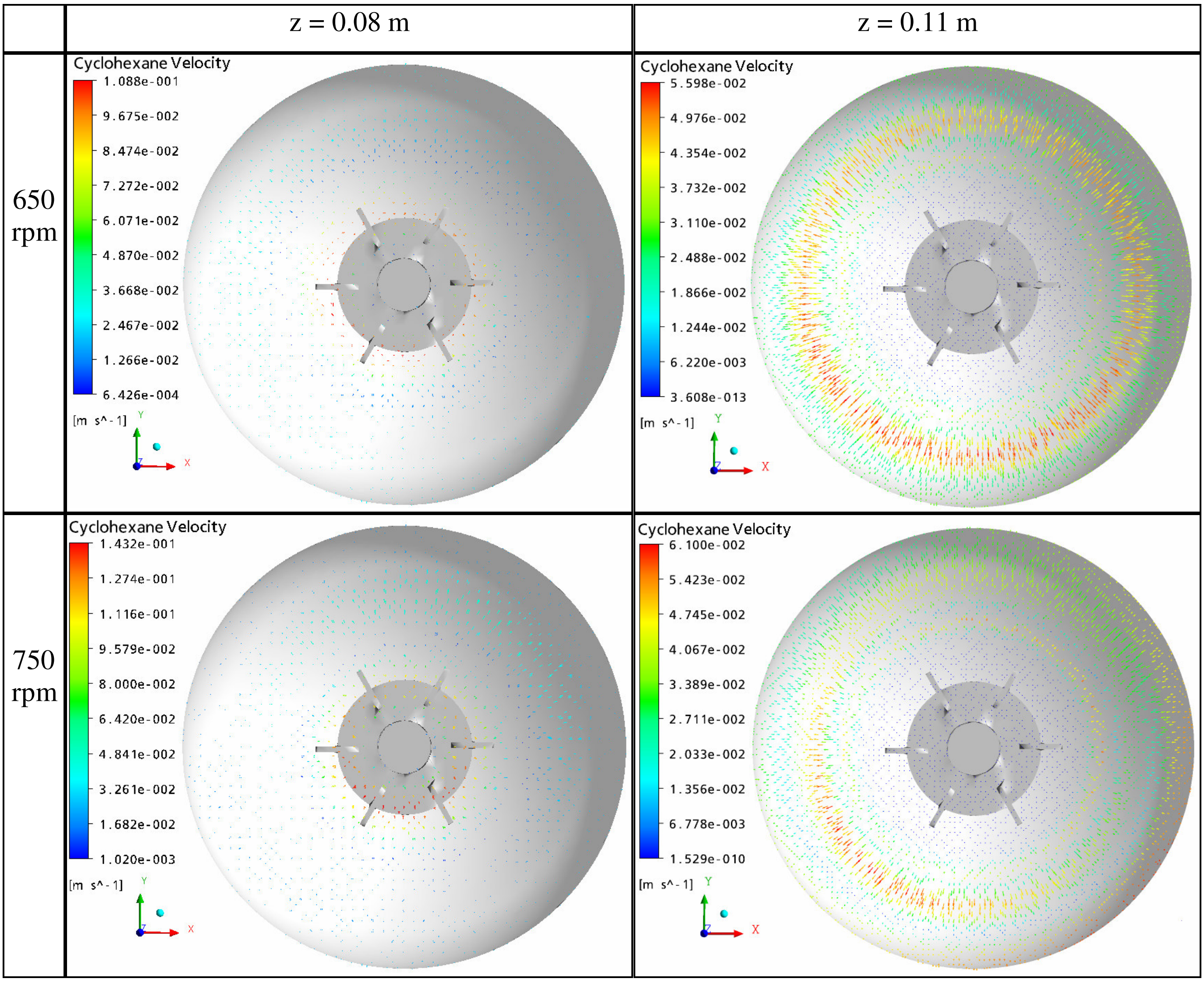

Figure 5.113-f: CFD predicted radial cyclohexane velocity profiles as a function of RTI velocity of 650 rpm and 750 rpm at z = 0.08 m (left) and z =0.11 m (right).

The axial and radial profiles of the cyclohexane velocity are illustrated in Figs. 5.114-a, b and c. For RTI velocity of 350 rpm, It can be seen the maximum axial velocity of 0.08 m/s at the level of the RTI at z = 0.032 m, and near the blades of the impeller at x = 0.01 and 0.015 m, because the turbulent intensity and kinetic energy there are the highest, except near the walls at x = 0.04 m, where the axial velocity is 0.02 m/s. A symmetrical radial velocity distribution with small differences around the shaft of the impeller is obtained. This is consistent with the symmetrical vortex that formed around the shaft of the RTI. The maximum radial velocity of 0.12 m/s is obtained near the impeller at the radial distance y = 0.015 m and axial distance z = 0.032 m. It decreases above the impeller towards the free surface at $z = 0.11$ m, but the velocity near the wall at $y = 0.04$ m is higher than that near the shaft, where cyclohexane is pulled down into the bulk at RTI velocity of 350 rpm. The radial flow caused by the RTI makes the radial velocities higher than the axial one. The flow below the impeller is weak and the velocities are low. Increasing the RTI velocity to 450 rpm, increases the intensity of the turbulence and shear forces around the impeller, thus the axial and radial velocities increase to 0.12 and 0.17 m/s, respectively especially at $z = 0.032$ m, $0.015\text{m} \leq x \leq 0.025$ m and $y = \pm 0.018$ m, see Fig. 5.114-a. Further increase of the RTI velocity to 650 rpm has a significant effect on the radial velocity rather than the axial velocity (Fig. 5.114-b), but the axial velocity near the wall at $x = 0.04$ m in the level of the impeller shows a significant increase due to the high collision and interacting forces between the cylindrical walls and the radial output stream from the impeller, which results in two axial circulations below and above the impeller. The lower velocities and turbulence are found below the impeller and near the free surface. The distribution of cyclohexane in water becomes more uniform, thus the velocity distribution becomes more symmetric around the shaft and more uniform, see Fig. 5.114-b. The maximum cyclohexane velocity of 0.2 and 0.3 m/s are obtained at RTI velocity of 550 and 650 rpm, respectively at the impeller level at $z = 0.032$ m, $y = 0.04$ m near the wall and $y = 0.017$ m (near the RTI blades). Increasing the RTI velocity to 750 rpm increases the cyclohexane velocity to nearly 0.4 m/s. Both cyclohexane and water phases transport with the same velocity, because the slip velocity of cyclohexane –the relative velocity of cyclohexane droplets to water velocity– becomes zero, because the dispersed phase flow follows the continuous phase flow closely until the velocities of the two phases are close, especially a way from the impeller. The axial velocity becomes nearly uniform at RTI velocity of 750 rpm at $0.02 \text{ m} < z < 0.06$ m and $0.01 \text{ m} < x < 0.03$ m (vortex region). A significant increase of the bulk velocity is found below the impeller caused by the turbulence and gravitational forces which increase the degree of cyclohexane dispersion in the bottom of the vessel below the impeller until a uniform and complete distribution of cyclohexane into water is attained.

	Axial cyclohexane velocity	**Radial cyclohexane velocity**
350 rpm	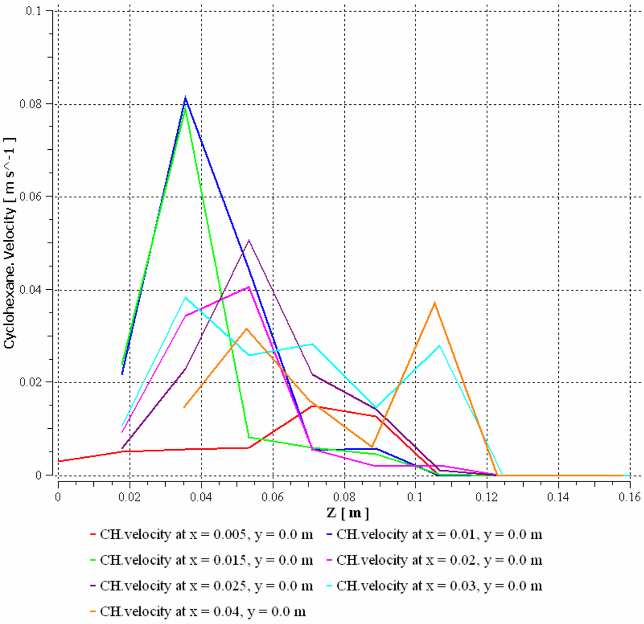	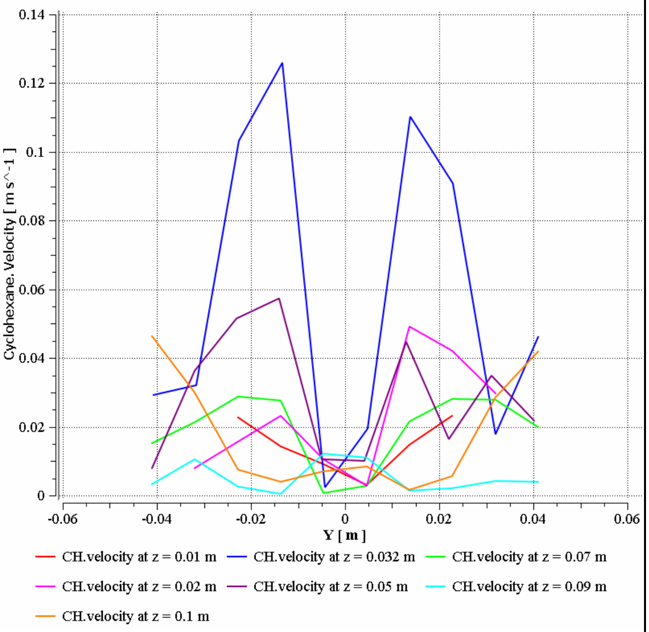
450 rpm	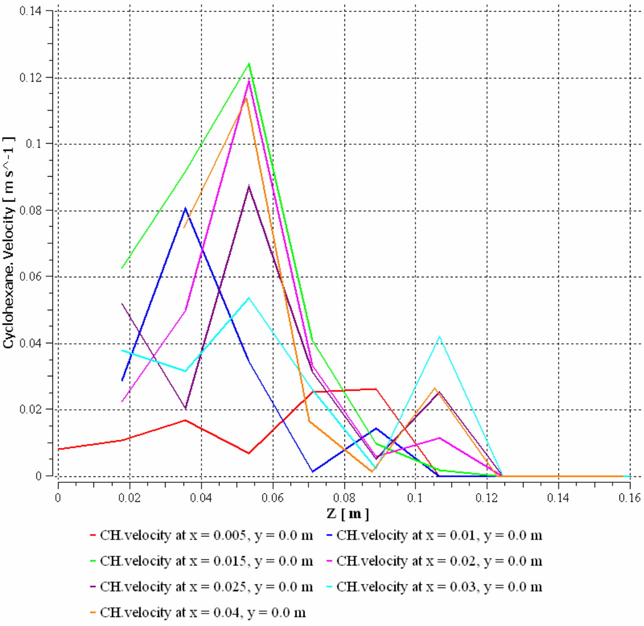	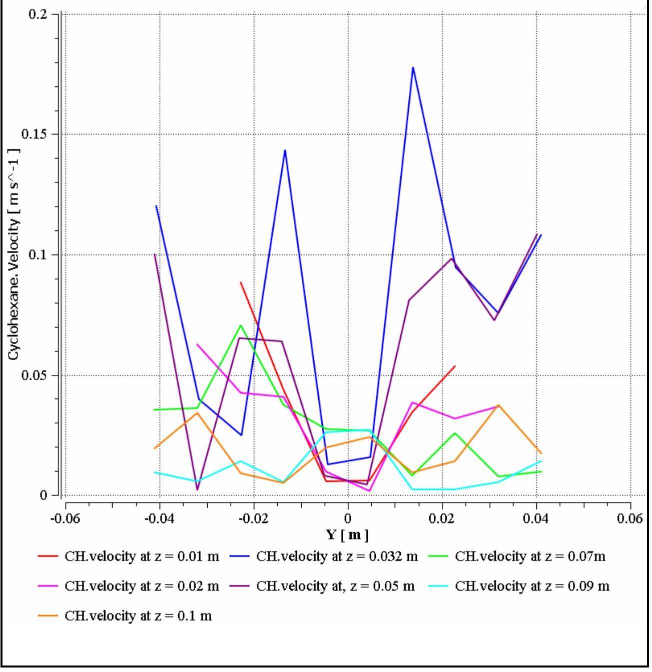

Figure 5.114-a: CFD predicted axial and radial velocity of cyclohexane as a function of RTI velocity of 350 rpm and 450 rpm.

	Axial cyclohexane velocity	Radial cyclohexane velocity
550 rpm	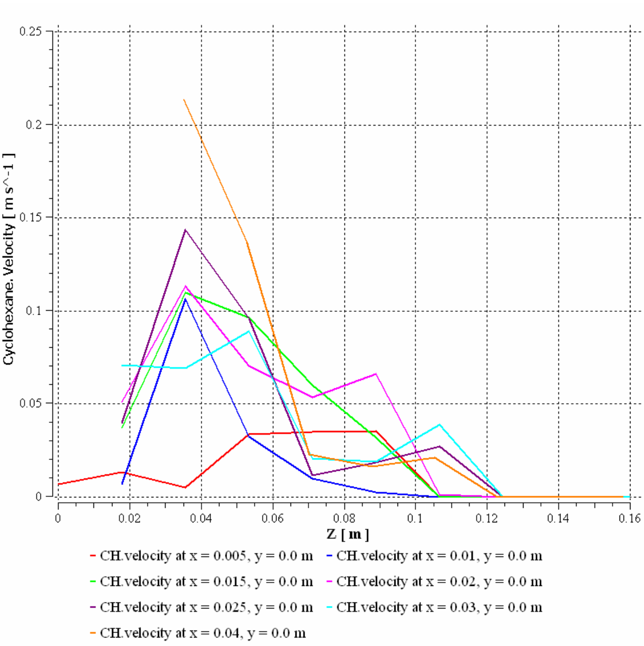	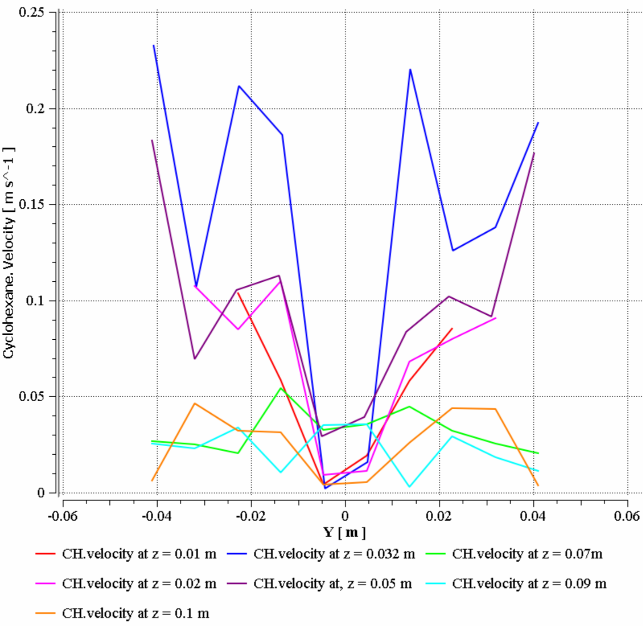
650 rpm	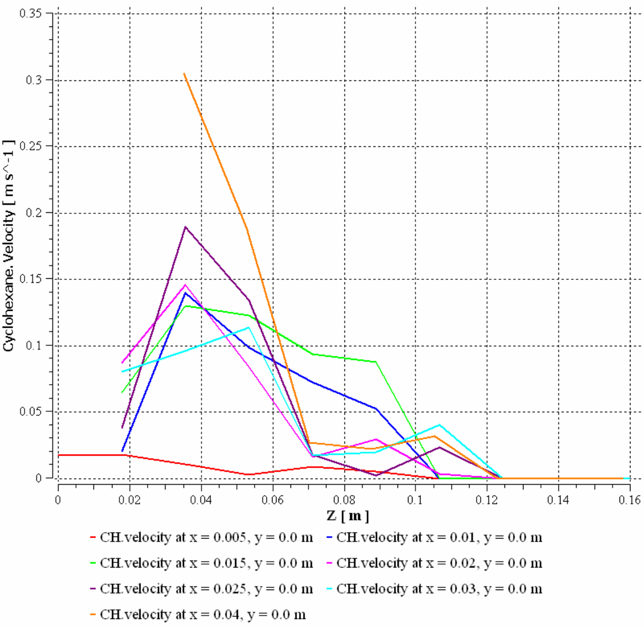	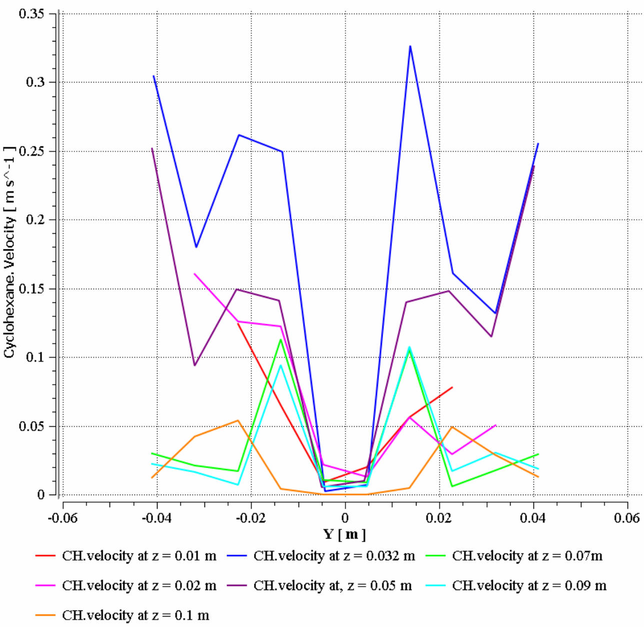

Figure 5.114-b: CFD predicted axial and radial velocity of cyclohexane as a function of RTI velocity of 550 rpm and 650 rpm.

	Axial cyclohexane velocity	**Radial cyclohexane velocity**
750 rpm	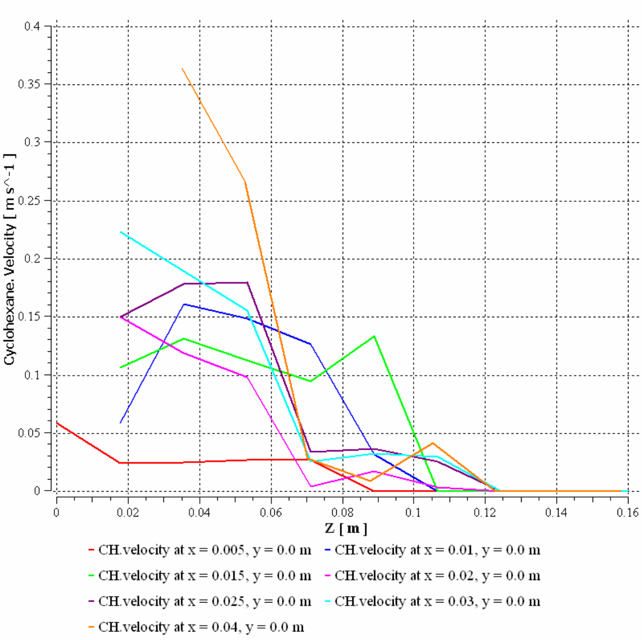	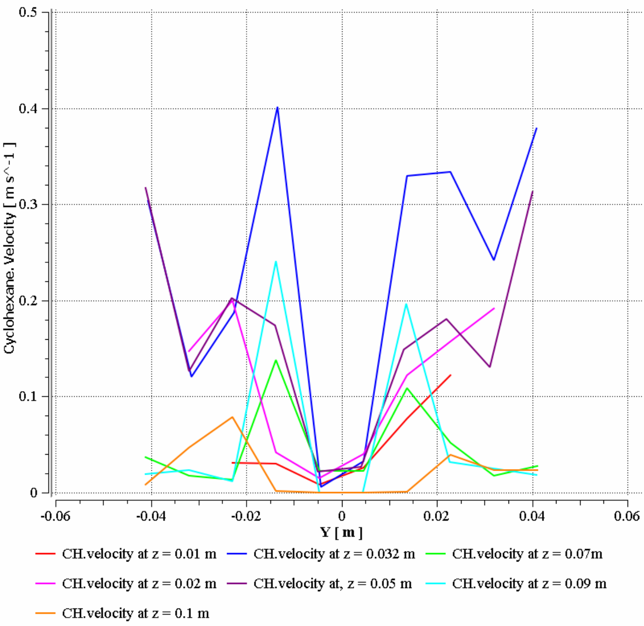

Figure 5.114-c: CFD predicted axial and radial velocity of cyclohexane as a function of RTI velocity of 750 rpm.

The magnitudes of the predicted axial velocities are very close to the experimental data obtained from the light cut method by using tracer particles as can be seen in chapter 5.6. They are in good agreement with the CHVF distribution profiles, the velocity for complete and uniform distribution and the rates of mass transfer.

The predicted velocities vary, according to the strength of the turbulence and the RTI velocity, between 0.14-0.22 m/s (maximum), 0.05-0.1 m/s (intermediate) and 0.02-0.04 m/s (minimum). The predicted velocities with CFD give detailed and precise description of the velocity flow field in different locations in the vessel, which can not be measured experimentally.

6. CONCLUSIONS AND OUTLOOKS

1. The mass transfer coefficient, interfacial area, dispersed phase holdup, the minimum velocity for complete and uniform dispersion should be known to enable efficient design of the stirred vessel.
2. CFD modelling allows prediction the flow pattern, the turbulent dispersed phase flow field, the interfacial area, the local phase velocities and volume fractions. There is a good agreement with the experimental data for a wide range of stirrer velocity.
3. Eulerian-Eulerian model with the ASM and the k-ε models are able to predict the dispersion behaviour of cyclohexane/water system with RTI. Whereas Ishii-Zuber model is the suitable to predict the dispersion behaviour with anchor impeller.
4. The accuracy of the simulations results is influenced by the design of the grid as well as the drag model applied.
5. Assumption of a constant droplet diameter and spherical shape of the droplets in the CFD simulations is consistent with the experimental photographs for the dispersed droplets of cyclohexane.
6. The dispersion efficiency of the cyclohexane/water can be investigated on the basis of the local volume fraction distribution for the dispersed phase.
7. The actual sampling method can be used in the industrial situations to measure the volumetric fraction distribution of cyclohexane in the vessel, where in which the visual observation method impossible to use.
8. The minimum stirring velocities, to get complete and uniform dispersion, obtained visually is found to be close to that obtained from the axial and radial profiles of cyclohexane volume fractions.
9. Bottom clearance of RTI has an effect on the minimum velocity for complete dispersion, but it has no effect on the minimum RTI velocity to get a uniform dispersion.

10. Water/benzoic acid/cyclohexane is a suitable system to study the interphase mass transfer.
11. Anchor impeller gives mass transfer and interfacial area between the two phases higher than that given by the RTI.
12. The mass transfer coefficient and interfacial area between cyclohexane and water depend different on the stirrer velocity.
13. The mass transfer of the benzoic acid is highly affected by the flow field obtained from different types of stirrers.
14. The CFD predicted density and cyclohexane volume fraction distribution describe well the dispersion of cyclohexane /water system for a wide range of stirrer velocity.
15. The CFD predicted flow velocity fields of cyclohexane/water are consistent with that obtained by photographic light-cut and visualization with red tracer methods.
16. The impellers that give high flow and low shear such as the propeller and anchor are more efficient than that give low flow and high shear like the RTI.

Outlooks

1. The present work is necessary as a first step towards the goal of design and scale up of liquid-liquid dispersion vessels by means of CFD.
2. It is recommended to study the mass transfer coefficient, interfacial area, holdup distribution, the minimum velocity for complete and uniform dispersion in a stirred vessel with a new stirrer design that combines the RTI and the anchor impeller on the same shaft.

7. REFERENCES

[1] Wang, F., Mao, Z. S. Numerical and experimental investigation of liquid-liquid two phase flow in stirred tanks. Ind. Chem. Res. 44 (2002) 5776-5787.

[2] Fredrik, J. E. Svenss, Rasmuson, A. LDA measurements in a stirred tank with liquid-liquid system at high volume percentage dispersed phase. Chem. Eng. Technol. 27, No. 3 (2004) 335-339.

[3] Alban, F. B., Sajjadi, S., Yianneskis, M. Dynamic tracking of fast liquid-liquid dispersion processes with a real time in-situ optical technique. Trans. IChemE, Part A, Chem. Eng. Res. Des. 82 (2004) 1054-1060.

[4] Skelland, A. H. P., Lee, J. M. Agitator speeds in baffled vessels for uniform liquid-liquid dispersions. Ind. Eng. Chem. Process Des. Deu. 17 (1978) 473-478.

[5] Piero, M. Armenante, Huang, Y. T. Experimental determination of the minimum agitation speed for complete liquid-liquid dispersion in mechanically agitated vessels. Ind. Eng. Chem. Res. 31 (1992) 1398-1406.

[6] Wang, F., Mao, Z. S., Wang, Y., Yang, C. Measurement of phase holdups in liquid-liquid-solid three-phase stirred tanks and CFD simulation. Chem. Eng. Sci. 61 (2006) 7535-7550.

[7] Skelland, A. H. P., Moeti., L. T. Mechanism of continuous phase mass transfer in agitated liquid-liquid systems. Ind. Eng. Chem. Res. 29 (1990) 2258-2267.

[8] Eckert, R. E., McLaughlin, C. M., Rushton, J. H. Liquid-Liquid interfacial areas formed by turbine impellers in baffled, cylindrical mixing tanks. AIChE J. 31 (1985) 1811-1820.

[9] Edward, L.P., Victor, A.A.-O., Suzanne, M.K. Handbook of industrial mixing science and practice. U.S. (2004).

[10] Calabrese, R. V., Chang, T. P. K., Dang, P. T. Drop breakup in turbulent

stirred-tank contactors. Part I. Effect of dispersed phase viscosity. AICHE J. 32 (1986) 657-666.

[11] Zhou, G., Kresta, S. M. Correlation of mean drop size and minimum drop size with the turbulence energy dissipation and the flow in an agitated tank. Chem. Eng. Sci. 53 (1998) 2063-2079.

[12] Feng, W., Weijing, W., Zaisha, M. Numerical study of solid liquid tow-phase flow in stirred tanks with rushton impeller. Part I. Formulation and simulation of flow field. Chin. J. Chem. Eng. 10 (2004) 1-20.

[13] Weijing, W., Zaisha, M. Numerical simulation of gas-liquid flow in a stirred tank with rushton impeller. Chin. J. Chem. Eng. 10 (2002) 385-395.

[14] Al-Qaessi, F. Mixing of two miscible liquids with high viscosity and density difference in semi-batch and batch reactors – CFD simulations and experiments. Ph.D. Thesis, University Duisburg-Essen, Germany (2007).

[15] Haiyan, S., Weijing, W., Zaisha, M. Numerical simulation of the whole three-dimensional flow in a stirred tank with anisotropic algebraic stress model. Chin. J. Chem. Eng., 10 (2002) 15-24.

[16] Pasteur. Reactor behaviour. (2005) online in the internet: http://www.che.boun.edu.tr/che302/Chapter%2011.pdf

[17] Bouwmans, I., Van den Akker, H. E. A. The influence of viscosity and density differences on mixing times in stirred vessels. IChemE. Symp. Ser. 121 (1990) 1-12.

[18] Wikipedia. Miscible. (2005) online in the internet: http://en.wikipedia.org/wiki/Miscible

[19] Action energy. Blending miscible liquids. (2006) online in the internet: http://www.actionenergy.org.uk

[20] Van De Vusse, J.G. Mixing by agitation of miscible liquids-Part I. Chem. Eng. Sci. 4 (1955) 178-200.

[21] Clevelandmixer. Mixing glossary of terms. (2006) online in the internet: http://www.clevelandmixer.com/files/pdf

[22] Paul, Hong O., James, Lee M. Unsteady state liquid-liquid dispersions in agitated vessels. Ind. Eng. Chem. Process Des. Dev. 22 (1983) 130-135.

[23] Skelland, A. H. P., Seksaria, R. Minimum impeller speeds for liquid-liquid dispersion in baffled vessel. Ind. Eng. Chem. Process Des. Dev. 17 (1978) 56-61.

[24] Ritter, J., Kraume, M. On-line measurement technique for drop size distribution in Liquid/liquid systems at high dispersed phase fractions. Chem. Eng. Technol. 23 (2005) 579-581.

[25] Tsung Chen, H., Middlenman, S. Drop size distribution in agitated liquid-liquid systems. AIChE J. 13 (1967) 989 - 994.

[26] Musgrove, M., Ruszkowski, S. Influence of impeller type and agitation conditions on the drop size of immiscible liquid dispersions. Proc. of the 10th European Conf. on Mixing Delft Netherlands (2000) 165.

[27] Eckert, R. E., McLaughlin, C. M., Rushton, J. H. Liquid-liquid interfacial area formed by turbine impeller in baffled, cylindrical mixing tank. AIChE J. 31 (1985)1811-1820.

[28] Smith, T. N. Measurement of drop size in liquid-liquid dispersions. Chem. Eng. Sci. 29 (1974) 583-587.

[29] Wille, M., Langer, G., Werner, U. PDA measurement of drop size distribution for liquid-liquid dispersing in agitated tanks. Chem. Eng. Technol. 24 (2001) 475-479.

[30] Bae, J. H., Tavlarides, L. L. Laser capillary spectrophotometry for drop-size concentration measurement. AIChE J. 35 (1989) 1073-1084.

[31] Van Woezik, B. A. A., Westerterp, K. R. Measurement of interfacial areas with the chemical method for a system with alternating dispersed phases. Chem. Eng. Process. 39 (2000) 299-314.

[32] Bouyatiotis, B. A., Thonton, J. D. Liquid-liquid extraction studies in stirred tanks. Part I: Droplet size and holdup measurements in a seven inch diameter baffled vessel. IChemE. Symp. Ser. 26 (1967) 43-51.

[33] Lovick, J., Mouza, A. A., Paras, S. V., Lye, G. J., Angeli, P. Drop size distribution in highly concentrated liquid-liquid dispersions using a light back scattering method. J. Chem. Technol. Biotechnol. 80 (2005) 545-552.

[34] Kraume, M., Gäbler, A., Schulze, K. Influence of physical properties on drop size distributions of stirred liquid-liquid dispersions. Chem. Eng. Technol. 27 (2004) 330-334.

[35] Skelland, A. H. P., Jeffrey, S. Kanel. Simulation of mass transfer in a batch agitated liquid-liquid dispersion. Ind. Eng. Chem. Res. 31 (1992) 908-920.

[36] Johansson, A. C., Godfrey, J. C. The influence of the impeller geometry on liquid-liquid mixing in agitated tank. Recents Progres en Genie des Procedes, 11 (1997) 255-262.

[37] Tsouris, C., Michael, Norato, A., Lawrence, Tavlarides, L. A Pulse-echo ultrasonic probe for local volume fraction measurement in liquid-liquid dispersions. Ind. Eng. Chem. Res. 34 (1995) 3154-3158.

[38] Armenate, P. M., Huang, Y.-T. Experimental determination of the minimum agitation speed for complete liquid-liquid dispersion in mechanically agitated vessels. Ind. Eng. Chem. Res. 31 (1992) 1398-1406.

[39] Skelland, A. H. P., Ramsey, G. G. Minimum agitation speed for complete liquid-liquid dispersion. Ind. Eng. Chem. Res., 26 (1987) 77-81.

[40] Okufi, S., de Ortiz Perez, E. S., Sawistowski, H. Scal-up of liquid-liquid dispersions in stirred tank. Can. J. Chem. Eng. 68 (1990) 400-406.

[41] Gosman, A. D., Lekakou, C., Politis, S., Issa, R. I., Looney, M. K. Multidimensional modelling of turbulent tow-phase flows in stirred vessels. AIChE J. 38 (1992) 1946-1956.

[42] Skelland A. H. P., Seksaria, R. Minimum impeller speeds for liquid-liquid dispersion in baffled vessel. Ind. Eng. Chem. Process Des. Dev. 17 (1978) 56-61.

[43] Gaggero, M., Arato, E., Costa, P. Liquid-liquid mixing: study on the phase

formation in stirred tanks. 6th Euoropean conference on Mixing, Pavia, Italy (1988) 197-204.

[44] Godfrey, J. C., Reeve, R. N. Grilc, V. Minimum conditions for the production of liquid-liquid dispersions in agitated tanks. Inst. Chem. Eng. Symp. Ser. 89 (1984) 107-126.

[45] Bushra, A., Chandra, Y., Bhattacharya, S. D. Studies on multiphase agitation. J. Surf. Sci. Technol. 14 (1998) 157-168.

[46] Alopaeus, V. Calculation of multicomponent mass transfer between dispersed and continuous phases, ACTA Polytechnica Scandinavica. Chem. Technol. Ser. 283 (2001) 1-35.

[47] Cussler, E. L. Diffusion: Mass transfer in fluid systems, Cambridge University Press, New York (1984).

[48] Hines, A. L., Maddox, R. N. Mass transfer: Fundamentals and applications, Prentice Hall, New Jersey (1985).

[49] Rushton, J. H., Nagata, S., Rooney, T. B. Measurement of mass transfer coefficients in liquid-liquid mixing. AIChE J. May (1964) 298-302.

[50] Schindler, H. D., Treybal, R. E. Continuous-phase mass transfer coefficient for liquid extraction in agitated vessels, AIChE J. 14 (1968) 790-798.

[51] Keey, R. B., Glen, J. B. Area-free mass transfer coefficients for liquid-liquid extraction in a continuously worked mixer. AIChE J. 15 (1969) 942-947.

[52] Skelland, A. H., Lee, J. M. Drop size and continuous-phase mass transfer innagitated vessels. AIChE J. 27 (1981) 99-111.

[53] Mok, Y. I. Treybal, R. E. Continuous phase mass transfer coefficients for liquid extraction in agitated vessels: II. AIChE J. 17 (1971) 916-920.

[54] Treybal, R. E. Mass Transfer Operations. 3rd Ed, McGraw-Hill, Singapore (1981).

[55] Hiraoka, S., Yamada, I., Tada, Y., Mori, H., Narita, N., Suzuki, H., Aragaki,

T. Measurement of continuous-phase mass transfer coefficient at droplet surface in liquid-liquid mixing vessel by chemical reaction method. J. Chem. Eng. Jpn. 23 (1990) 166-170.

[56] Burghoff, S., Eugeny Y. Kenig. A CFD model for mass transfer and interfacial phenomena on single droplets. AIChE J. 52 (2006) 4071-4078.

[57] Srivastava, P., Hahr, O., Buchholz, R., Mark Worden, R. Enhancement of mass transfer using colloidal liquid aphrons: Measurement of mass transfer coefficients in liquid-liquid extraction. Biotechnol. Bioeng. 70 (2000) 525-532.

[58] Johnson, A.I., Chen-jung Huang. Mass transfer studies in agitated vessel. AIChE J. September (1956) 412-419.

[59] Boyadzhiev, L., Elenkov, D., Kyuchukov, G. On liquid-liquid mass transfer inside drops in a turbulent flow field. Can. J. Chem. Eng. 47 (1969) 42-44.

[60] Nagata, S., Yamaguchi, I. Mass transfer and chemical reaction in liquid-liquid agitation systems. Mem. Fac. Eng. Kyoto Univ. 22 (1960) 249.

[61] Sung Ahn, B., Lee, W. K. Simulation and experimental analysis of mass transfer in a liquid-liquid stirred tank extractor. Ind. Eng. Chem. Res. 29 (1990) 1927-1935.

[62] Hinze, J. O. Fundamentals of the hydrodynamic mechanism of splitting in dispersion processes. AICHE J. 1 (1955) 289-295.

[63] Rodger, W. A., Trice, Jr., V. G., Rushton, J. H. Effect of fluid motion on interfacial area of dispersions. Chem. Eng. Prog. 52 (1956) 515.

[64] Vermeulen, T., Williams, G. M., Langlois, G.E. Interfacial area in liquid-liquid and gas-liquid agitation. Chem. Eng. Progr. 51 (1955) 85F.

[65] Venkataraman, K., Degaleesan, T. E., Laddha, G. S. Continuous and dispersed phase coefficients for heat and mass transfer involving single-file drops. Proc. Indian Acad. Sci. 3 (1980) 31-36.

[66] Rodger, W. A. Interfacial area in liquid-liquid dispersions related to fluid motion in mixing vessels. U. S. Atomic Energy Comm. ANL-5575 (1956).

[67] Rodger, W.A., Trice, Jr., V. G. Light transmittance as a measure of interfacial area in liquid-liquid dispersions. U. S. Atomic Energy Comm. ANL-5512 (1956).

[68] Roeckl, Single. Agitator types. (2005) online in the internet: http://roeckl-und-single.de

[69] Johansson, A. C., Godfrey, J. C. Influence of impeller type on two-phase liquid-liquid mixing. The 1997 Jubilee Research Event, IChemE (1997) 297-300.

[70] Kraume, M. Mischen und rühren. Wiley-VCH, Weinheim (2003).

[71] Tatterson, G. B. Fluid mixing and gas dispersion in agitated tanks. McGraw-Hill, New York (1991).

[72] Harnby, N., Edwards, M. F., Nienow, A. W. Mixing in the process industries. 2nd ed, Butterworth-Heinemann, Oxford (1992).

[73] Myers, K. J., Reeder, M. F., Ryan, D., Daly, G. Get a fix on high-shear mixing. Chem. Eng. Prog. Nov. (1999) 33-42.

[74] Dickey, D. S., Hemrajani, R. R. Recipes for fluid mixing. Chem. Eng. March (1992) 82-89.

[75] Brauer, H. Stirred vessel reactors. Fundam. Biochem. Eng. 2 (1985) 395-444.

[76] Ohta, M., Kuryama, M., Saito, S. A two-dimensional model for the secondary flow in an agitated vessel with anchor impeller. J. Chem. Eng. Jpn. 18 (1985) 81-84.

[77] Peixoto, S. M. C., Nunhez, J. R., Duarte, C. G. Characterizing the flow of stirred vessels with anchor type impellers. Braz. J. Chem. Eng. 17 (2000) 1-15.

[78] Delaplace, G., Guerin, R., Leuliet, J., Torrez, C., Andre, C., Sliding mesh

method to simulate flow of highly viscous fluid in stirred tank agitated with helical ribbon impeller, Proc.2th International Conference on Simulation in food and Bio industries (2002) 151-157.

[79] Abid, M., Xuereb, C., Bertrand, J. Hydrodynamics in vessels stirred with anchors and gate agitators: Necessity of a 3-D Modelling. Trans. IChemE 70 (1992) 377-384.

[80] Baumann, K. H., Mühlfriedel, K. Mass transfer studies with Laser-Induced fluorescence across liquid/liquid phase boundaries. Chem. Eng. Technol., 25 (2004) 697-700.

[81] Espinosa, T., Brito, E., Thibault, F., Tanguy, P. Power consumption with anchor mixers-effect of bottom clearance. Chem. Eng. Comm. 157 (1997) 65-71.

[82] Ljungqvist, M., Rasmuson A. Numerical simulation of the two phase flow in an axially stirred vessel. Trans. IChemE 79 (2001) 533-545.

[83] Weinstein, B., Treybal, R. E. Liquid-liquid contacting in unbaffled, agitated vessels. AIChE J. 19 (1992) 304-312.

[84] Dieulot, J., Delaplace, G., Guerin, R., Leuliet, J., Brienne, J. Laminar mixing performances of a stirred tank equipped with helical ribbon agitator subjected to steady and unsteady rotational speed. Trans. IChemE 80 (2002) 335-343.

[85] Process equipment globalspec. Mixers. (2006) online in the internet: http://process-equipment.globalspec.com

[86] CFX-5 Documentation. Introduction to CFX-5. (2004) 94-104.

[87] Hartmann, H., Derksen, J. J., Van den Akker, H. E. A. Numerical simulation of a dissolution process in a stirred tank reactor. Chem. Eng. Sci. 61 (2006) 3025–3032.

[88] Khopkar, A. R., Kasat, G. R., Pandit, A. B., Ranade, V. V. CFD simulation of mixing in tall gas-liquid stirred vessel: Role of local flow patterns. Chem. Eng. Sci. 61 (2006) 2921-2929.

[89] Ishii, M. Thermo-fluid dynamic theory of two-phase flow. Eyrolles: Paris (1975).

[90] Huang, S., Mohamad, A., Nandakumar, K. Numerical analysis of a two-phase flow and mixing process in a stirred tank. Int. J. Chem. React. Eng. 6 (2008) 1-17.

[91] Looney, M. K., Gosman, A. D., Issa, R. I., Politis, S. Modelling of the turbulent flow of solid-liquid suspensions in stirred vessels. 5th Inter. Conf. of Mathematical Modelling, Berkeley, CA (1985).

[92] Vikhansky, A., Kraft, M. Modelling of RDC using a combined CFD-population balance approach. Chem. Eng. Sci. 59 (2006) 2597-2606.

[93] Zhu, X. Y., Vigil, R. D. Banded liquid-liquid taylor-couette-poiseuille flow. AIChE J. 47 (2001) 1932-1940.

[94] Jaworski, Z., Pianko-Oprych P., Two-phase laminar flow simulations in a kenics static mixer-standard Eulerian and Lagrangian approaches. Chem. Eng. Res. Des. 80 (2002) 910-916.

[95] Pianko-Oprych P., Jaworski, Z., CFD modelling of two-phase flows in SMX static mixer. Inzynieria Chemiczna I Procesowa, 24 (2003) 449-467.

[96] Pianko-Oprych P., Jaworski, Z., CFD modelling of liquid-liquid two-phase flows in static mixer. Inzynieria Chemiczna I Procesowa, 25 (2004) 341-362.

[97] Micale, G., Montante, G., Grisafi, F., Brucato, A., Godfrey, J. CFD simulation of particle distribution in stirred vessels. Trans. Inst. Chem. Eng. 78A (2000) 435-444.

[98] Montante, G., Micale, G., Magelli, F., Brucato, A. Experiments and CFD predictions of solid particle distribution in a vessel agitated with four pitched blade turbines. Trans. Inst. Chem. Eng. 79A (2001) 1005-1100.

[99] Morud, K. E., Hiertager, B. H. LDA measurement and CFD modelling of gas-liquid flow in a stirred vessel. Chem. Eng. Sci. 51 (1996) 233-249.

[100] Bakker, A., Van den Akker, H. E. A. A computational model for the gas-liquid flow in stirred reactors. Trans. Inst. Chem. Eng. 72A (1994) 594-606.

[101] Kuipers, J. A. M., Swaaij, W. P. M. Application of computational fluid dynamics to chemical reaction engineering. Rev. Chem. Eng. 13 (1997) 1-118.

[102] Tsouris, C., Tavlarides, L. L. Breakage and coalescence model for the drops in turbulent dispersions. AIChE J. 40 (1994) 395-406.

[103] Koh, P. T. L., Xantidis, F. CFD modelling in the scale-up of a stirred reactor for the production of resin beads. 2nd Int. Conf. on CFD in the Miner. Pro. Ind., CSIRO, Australia (1999) 369-374.

[104] Zhang, Y., Yang, C., Mao, Z. S. Large eddy simulation of the gas-liquid flow in a stirred tank. AIChE J. 54 (2008) 304-312.

[105] Calabrese, R. V., Kevala, K. R., Kiger, K. T. Using a dispersed phase model to track particle paths and deformation rates in complex mixing geometries. Proceedings of AIChE Annual Meeting and Fall Showcase, Conference Proceedings, Cincinnati, OH (2005) 3975.

[106] Deen, N. G., Solberg, T., Hjertager, H. Flow generated by an aerated rushton impeller: two phase PIV experiments and numerical. Can. J. Chem. Eng. 80 (2002) 638-652.

[107] Sun, H., Mao, Z. S., Yu, G. Experimental and numerical study of gas hold-up in surface aerated stirred tank. Chem. Eng. Sci. 61 (2006) 4098-4110.

[108] Luchang, H., Yuejin, L., He'an, L. Numerical simulation of gas holdup distribution in a standard rushton stirred tank using discrete particle method. Chin. J. Chem. Eng. 15 (2007) 808-813.

[109] Weijing, W., Mao, Z. S., Yang, C. Experimental and numerical investigation on gas holdup and flooding in an aerated stirred tank with rushton impeller. Ind. Eng. Chem. Res. 45 (2006) 1141-1151.

[110] Hartmann, H., Derksen, J. J., Montavon, C., Pearson, J., Hamill, I. S., Van den Akker, H.E.A. Assessment of large eddy and RANS stirred tank simulations by means of LDA, Chem. Eng. Sci. 59 (2004) 2419–2432.

[111] Feng, W., Zaisha, M., Xiangqian, S. Numerical study of solid-liquid two-phase flow in stirred tanks with rushton impeller part (Ⅱ) prediction of critical impeller speed. Chin. J. Chem. Eng. 12 (2004).

[112] Cranfield. Computational fluid dynamics. (2006) online in the internet: http://www.cranfield.ac.uk/soe/cpd/ate-cfd.htm

[113] Ferziger, J., Perić, M., Computational methods for fuid dynamics, Springer- Verlag Berlin Heidelberg, Germany (1996).

[114] Mathematik. Introduction to computational fluid dynamics. (2005) online in the internet: http://www.mathematik.uni-dortmund.de

[115] Bakker, A., LaRoche, R.D., Wang, M.-H., Calabrese, R.V. Sliding mesh simulation of laminar flow in stirred reactors. The Online CFM Book, February 15 (2000): http://www.bakker.org/cfm

[116] Torrecilla, M. Introduction to numerical simulation of fluid flows. Technical University of Munich, Winter school, Russia (2004) 24-34.

[117] CFX-5 Documentation. Reference guide. (2004) 37-46.

[118] CFX-5 Documentation. Solver theory. (2005) 21-239.

[119] CFX-5 Documentation, Solver manager, (2005) 2-10.

[120] CFX-5 Documentation, Post, (2005) 2-18.

[121] Wörner, M. Computational modelling of multiphase flows. International Summer School on "Computational Modelling of Combustion & Multiphase Flows in Energy Systems", Neptun-Olimp, Romania (2003) 1-35.

[122] Kat Chalmers. The influence of complex rheology on mixing, reaction and control of stirred vessels. (2005) online in the internet: http://www.kat.chalmers.se/cpdc/tvproj.htm

[123] Kvicinsky, S., Kueny, J., Avellan, F., Parkinson, E. Experimental and

numerical analysis of free surface flows in a rotating bucket. Proceeding of the XXIst IAHR Symposium on Hydraulic Machinery and Systems, Lausanne (2002) 1-7.

[124] Kvicinsky, S., Kueny, J.-L., Avellan, F. Numerical and experimental analysis of free surface flow in A 3D non rotating pelton bucket. The 9th International Symposium on Transport Phenomena and Dynamics of Rotating Machinery, Honolulu, Hawaii, USA (2002) 1-8.

[125] Frank, T. Eulerian multiphase flow modelling: Phase interaction models. ANSYS CFX, Otterfing, FZR-Dresden, Germany (2003).

[126] Frank, T. Free surface flow theory. Chapter 1, ANSYS CFX, Otterfing, Germany (2004).

[127] Zwart, P. Numerical methods for multiphase flow models in CFX-5. ANSYS Canada, Waterloo, Canada (2004).

[128] Sveen, J. New insights from Navier-Stockes modelling of free surface flows. Dept. of Mathematics, University of Oslo (2006) online in the internet: http://www.math.uio.no/~jks/work.html

[129] Ansys CFX-10 Documentation. Materials and reactions, (2005).

[130] Ansys CFX-10 Documentation. Fluid-Fluid interfaces, (2005).

[131] Ansys CFX-10 Documentation. GGI and MFR theory, (2005).

[132] CFX-5 Tutorials Documentation, Tutorial 7. Free surface flow over a pump, (2005).

[133] Khopkar, A. R., Rammohan, A. R., Ranade, V. V., Dudukovic, M. P. Gas-liquid flow generated by a rushton turbine in stirred vessel: CARPT/CT measurement and CFD simulations. Chem. Eng. Sci. 60 (2005) 2215-2229.

[134] Jaworski, Z., Pianko-Oprych, P. Two-phase, laminar flow simulations in a kenics static mixer. The standard Eulerian and Lagrangian approaches. Chemical Engineering Faculty, Technical University of Szczecin, Poland (2009).

[135] Ishii, M. One-dimensional drift-flux model and constitutive equations for

relative motion between phases in various two-phase flow regimes. ANL 77 (1977) 47-48.

[136] Manninen, Tavassalo, V. On the mixture models for multiphase flow. VTT Publications (1996).

[137] Al-Qaessi, F., Abu-Farah, L. Prediction of mixing time for miscible liquids by CFD simulation in semi-batch and batch reactors. EACFM J. 3 (2009) 135–146.

[138] Rushton, J. H., Oldshue, J. Y. Mixing: Present theory and practice. Chem. Eng. Prog. 49 (1953) 161.

[139] Nagata, S. Mixing: principles and applications. Halsted Press, New York (1975).

List of Publications and Posters

1. Abu-Farah, L., Al-Qaessi, F., Schönbucher, A. Cyclohexane/water dispersion behaviour in a batch stirred vessel experimentally and with CFD simulation. Procedia Computer Science, 1 (2010) 655-664.
2. Al-Qaessi, F., Abu-Farah, L. Activated carbon production from date stones using phosphoric acid. Energy Sources Part A Journal, 32 (2010) 1316–1325.
3. Al-Qaessi, F., Abu-Farah, L. Prediction of mixing time for miscible liquids by CFD simulation in semi-batch and batch reactors. Engineering Applications of Computational Fluid Mechanics Journal, 3 (2009) 135–146.
4. Abu-Farah, L., Al-Qaessi, F., Schönbucher, A. Mixing times and secondary flow phenomena of glycerol with ethanol in SBR and BR – an experimental and CFD study. Chemie Ingenieur Technik, 79 (2007) 1472–1473.
5. Abu-Farah, L., Al-Qaessi, F., Schönbucher, A. CFD simulation for the dynamic mixing of different density and different viscosity liquids in stirred SBR and BR – A preliminary study for the safety assessment of polymerisation reactions. 8. Fachtagung Anlagen-, Arbeits- und Umweltsicherheit, P04, ISBN 3-936415-48-X, Köthen – Germany (2006).
6. Abu-Farah, L., Al-Qaessi, F., Schönbucher, A. Experiment and CFD-Models. Flyer of the Institute of Chemical Engineering, University of Duisburg-Essen. ACHEMA, Frankfurt – Germany (2006).
7. Abu-Farah, L., Al-Qaessi, F., Sudhoff, P., Schönbucher, A. CFD simulation of multicomponent mixture of ethanol and glycerol in stirred SBR with anchor type impeller. Chemie Ingenieur Technik, 77 (2005) 1058–1059.
8. Al-Qaessi, F., Abu-Farah, L. CFD simulation of velocity profiles for liquids with different viscosities in stirred batch reactor with anchor impeller. Under review, MS0B220, Brazilian Journal of Chemical Engineering.

9. Al-Qaessi, F., Abu-Farah, L. Pan Cake effect on the mixing time of multiphase liquids with high viscosity and density differences. Under review, No: 2010-0068, Chinese Journal of Chemical Engineering.
10. Abu-Farah, L., Schönbucher, A. Drop size distribution of cyclohexane in two-phase liquid-liquid dispersion in a stirred batch vessel. Under preparation, Chemical Engineering Science.
11. Abu-Farah, L., Schönbucher, A. Holdup distribution of cyclohexane/water dispersion in a stirred vessel with anchor impeller: Experiments and CFD simulation. Under preparation, International Journal of Chemical Reaction Engineering.

Posters

1. Abu-Farah, L., Al-Qaessi, F., Schönbucher, A. Mixing times and secondary flow phenomena of glycerol with ethanol in SBR and BR – an experimental and CFD study. DECHEMA and VDI-GVC - ProcessNet-Jahrestagung, Aachen – Germany (2007).
2. Abu-Farah, L., Al-Qaessi, F., Schönbucher, A. CFD simulation for the dynamic mixing of different density and different viscosity liquids in stirred SBR and BR – A preliminary study for the safety assessment of polymerisation reactions. 8. Fachtagung Anlagen-, Arbeits- und Umweltsicherheit, Köthen – Germany (2006).
3. Abu-Farah, L., Al-Qaessi, F., Sudhoff, P., Schönbucher, A. CFD simulation of multicomponent mixture of ethanol and glycerol in stirred SBR with anchor type impeller. DECHEMA/GVC - Jahrestagungen, Wiesbaden, Rhein-Main-Hallen – Germany (2005).

Oral Presentations

2010 Abu-Farah, L. (presented), Al-Qaessi, F., Schönbucher, A. Cyclohexane/water dispersion behaviour in a stirred batch vessel experimentally and with CFD simulation. International Conference on Computational Science, ICCS 2010, Amsterdam-Netherlands.

2007 Abu-Farah, L., Al-Qaessi, F. (presented), Schönbucher, A. CFD-simulation of the dynamic mixing of liquids with different densities and viscosities in semi-batch and batch reactors. Neujahrskolloquium des Fachbereichs Chemie und dem Ortsverband der Gesellschaft Deutscher Chemiker, University Duisburg-Essen, Essen-Germany.

2006 Abu-Farah, L. (presented), Al-Qaessi, F., Schönbucher, A. CFD simulation for the dynamic mixing of different density and different viscosity liquids in stirred SBR and BR – A preliminary study for the safety assessment of polymerisation reactions. 8. Fachtagung Anlagen-, Arbeits- und Umweltsicherheit, Köthen - Germany.

2005 Abu-Farah, L. (presented), Al-Qaessi, F., Sudhoff, P., Schönbucher, A. CFD simulation of multicomponent mixture of ethanol and glycerol in stirred SBR with anchor type impeller. DECHEMA/GVC - Jahrestagungen 2005, Wiesbaden, Rhein-Main Hallen - Germany.

2005 Al-Qaessi, F., Abu-Farah, L., Schönbucher, A. (presented). Experimental work and CFD-Simulation of mixing behavior in chemical reactors. Albaath University, Faculty of Chemical and Petroleum Engineering, Homs-Syria.

2005 Abu-Farah, L., Al-Qaessi, F., Sudhoff, P. (presented), Schönbucher, A. Reaction calorimeter investigations and computations of mixing processes in the SBR. Neujahrskolloquium des Fachbereichs Chemie und dem Ortsverband der Gesellschaft Deutscher Chemiker, University Duisburg-Essen, Essen-Germany.

Conferences, Workshops, Seminars and Scientific Activities

2010- International Conference on Computational Science ICCS 2010, 31.5 - 2.6.2010, Amsterdam-Netherlands.

2008- International Conference on Modelling and Simulation, MS'08 Jordan, 18 - 20.11.2008, Petra-Jordan.

2008- Excursion (Exkursion), Henkel AG & Co. KGaA, 7.2.2008, Düsseldorf-Germany.

2007- ProcessNet - Jahrestagung 2007, DECHEMA and VDI-GVC, 16 - 18.10.2007, Aachen-Germany.

2007- Excursion, Chemiepark Marl (Chemical park in Marl, Germany) for chemical industries of different types of products, 8.2.2007, Marl-Germany.

2007- Neujahrskolloquium des Fachbereichs Chemie, Gesellschaft Deutscher Chemiker (New year colloquium of the specialist area chemistry together with the local federation of the society of German chemists), University Duisburg-Essen, 10.01.2007, Essen-Germany.

2006- 8. Fachtagung Anlagen-, Arbeits- und Umweltsicherheit in Köthen, 9 - 10.11.2006, Köthen-Germany.

2006- CFX Seminar "High- End Gittergenerierung für CFD- und FEM Anwendungen Hybride Vernetzung mit ICEM-CFD", (High ending generation of lattice for CFD- and FEM applications Hybrid cross-linking with ICEM CFD), Hotel Bredeney, 5.10.2006, Essen-Germany.

2006- ACHEMA 2006 "28e Exposure-Congress International of Chemical Engineering", 15.5.2006, Frankfurt-Germany.

2005- GVC/DECHEMA-Jahrestagungen 2005, Wiesbaden, 6 - 8.9.2005, Rhein-Main-Hallen-Germany.

2005- CFX Seminar "ANSYS CFX-10 für CFX Anwender", 2.9.2005, Bochum-Germany.

2005- CFX Seminar "Die ganze Welt der Simulation" ANSYS CFX, Fluid-

Struktur-Kopplung, 20.7.2005, Essen-Germany.

2005- Excursion, Chemiepark Marl (Chemical park in Marl, Germany) for chemical industries of different types of products, 2.2.2005, Marl-Germany.

2005- Neujahrskolloquium des Fachbereichs Chemie, Gesellschaft Deutscher Chemiker (New Year colloquium of the Specialist area chemistry together with the local federation of the society of German chemists), University Duisburg-Essen, 12.1.2005, Essen-Germany.

2003- Training course on CAD2Mesh Program by ANSYS Germany GmbH, 18 - 19.11.2003, Hannover-Germany.

2003- VDI - GVC [Gesellschfat Verfahrenstechnik und Chemieingenieurwesen] (Society of Chemical and Process Engineering), 11th European Conference on Mixing, Konzert und Kongresshalle, 14 - 17.10.2003, Bamberg-Germany.

2003- DECHEMA-2003, 27th International Exhibition, Congress on Chemical Engineering, Environmental protection and biotechnology, 19 - 24.5.2003, Frankfurt-Germany.

2003- Course and Conference “Multiphase flows in industrial applications simulation and experiments”, Forschungs Zentrum Rossendorf e.v. FZR. AEA Technology GmbH CFX, 28 - 30.4.2003, Dresden-Germany.

2003- Training course on CFX-5.6 Program (Computational Fluid Dynamics Software and Service) for Simulation and Modelling different types of problems. AEA Technology GmbH CFX, Otterfing, 15 - 17.4.2003, München-Germany.

Curriculum Vitae

Name	: Laila Mahmod Nabhan Abu-Farah
Place / Date of birth	: Jordan / 24.11.1970

Education

03/2003 – 07/2010	Ph.D. Degree in Chemical Engineering, Department of Chemical Engineering, University Duisburg-Essen, Essen-Germany.
10/1995 – 06/1998	M.Sc Degree in Chemical Engineering with average of 3.57 from 4.0, Department of Chemical Engineering, University of Jordan, Amman-Jordan. Thesis title is “A Study of Paracetamol and Salicylamide Suspensions in Oily and Aqueous Media”.
10/1989 – 06/1994	B.Sc. Degree in Chemical Engineering with average of 75.7%, Department of Chemical Engineering, University of Jordan, Amman-Jordan. Final project is “Production of Vinyl Chloride Monomer“.

Awards

10/1989 – 06/1994	Ministry of Higher Education scholarship for the financial support of my B.Sc. study at the University of Jordan, Chemical Engineering Department, Amman-Jordan.

Work Experiences

03/2003–07/2010	Research and teaching assistant, Department of Chemical Engineering, University of Duisburg-Essen, Essen-Germany.
09/1999–02/2002	Teacher at National Zarqa College, Al-Zarqa-Jordan, for the subjects: General Physics, Biochemistry and its Lab., Organic Chemistry and its Lab., Fluid Mechanics and its Lab.

and Heat Transfer.

10/1999–07/2000 Teacher at Al-Balqa’ Applied University, Al-Zarqa-Jordan, for the subjects: Chemical Industries and Introduction to Environmental Engineering.

09/1998–03/1999 Chemical Engineer and Researcher - Special Projects group-on Formulation and Stability of Liponet and Chitosan (active materials) at Jordanian Pharmaceutical Manufacturing and Medical Equipment Co. (JPM), Amman-Jordan.

10/1997–06/1998 Chemical Engineer at the Jordanian Pharmaceutical Manufacturing and Medical Equipment Co. (JPM) on The quality control, quality assurance, production and laboratory analysis of different products like; Suppositories, Suspensions, Syrups, and Emulsions. Indeed to the drug efficiency. Droplet size analysis is done using Coulter counter and microscopic analysis with specialist software, Amman-Jordan.

10/1996–06/1998 Teaching Assistant in the Chemical Engineering department at the University of Jordan, Amman-Jordan, for the subjects: Computer Aided Design (simulation and modelling). Numerical Methods in Chemical Engineering, Process Modelling by Statistical Methods, Unit Operation for Solid Materials Lab., Heat and Mass Transfer Lab. and Thermodynamics.

01/1996–06/1996 Chemical Engineer at the Ministry of Water and Irrigation (Water Authority) on water analysis (COD & BOD) and treatment using Biological and Chemical methods, Amman-Jordan.

12/1994–05/1995 Chemical Engineer at the Ministry of Energy and Mineral Resources (Natural resources authority) on different laboratory analysis such as oil shale, metals and water analysis by using different equipments like centrifuge, gas and liquid chromatography, Spectrometer, flame photometer…etc, Amman-Jordan.

06/1993–09/1993 Training at the Jordan Petroleum Refinery Co. Ltd on all the operation units such as distillation, catalytic cracking, cooling towers, hydrogen cracking unit, and laboratory analysis of different oil derivatives, Al-Zarqa-Jordan.

05/1993–06/1993 Training at the Methieb Haddad Co. for production of detergents, Shampoos, Soaps and different cosmetic materials, Al-Zarqa-Jordan.

Computer Skills

- Computer literate in two languages (FORTRAN 77 & QBASIC) and other programs (Windows, MS-DOS, MATHLAB, Aspen+, AutoCAD R14, Internet, Microsoft PowerPoint, Microsoft Word, Microsoft Excel, Adobe (Reader and Photoshop), Movie Maker, Media Player, RealPlayer, Dplot and NCSS 2007.
- Computational fluid dynamics programs literate Like ANSYS-CFX and Fluent. Also I have the ability to create different industrial geometries by using ICEM-CFD and Design modeller programs.

Languages

- Arabic (Native).
- English (Very Good).
- German (Good).
- Spanish (Beginner).